Integration of Orbital and Ground Imagery for Automation of Rover Localization

Dissertation

Presented in Partial Fulfillment of the Requirements for the Degree Doctor of Philosophy in the Graduate School of The Ohio State University

By

Ju Won Hwangbo, M.S., B.S.

Graduate Program in Geodetic Science and Surveying

The Ohio State University

2010

Dissertation Committee:

Dr. Rongxing Li, Advisor

Dr. Alan Saalfeld

Dr. Alper Yilmaz

ABSTRACT

Rover localization is essential to the exploration of space. The availability of sub-meter resolution satellite imagery, especially High Resolution Imaging Science Experiment (HiRISE) onboard the Mars Reconnaissance Orbiter (MRO), has opened the possibility of computing rover locations at higher accuracy by making use of detailed features seen in the satellite orbital images. This dissertation describes a new development towards automation of the rover localization process, using orbital and ground image networks.

A HiRISE orbital image network on Mars is constructed based on a rigorous sensor model, bundle adjustment of HiRISE stereo images and absolute positioning using Mars Orbiter Laser Altimeter (MOLA) data. The unique HiRISE sensor configuration consists of 14 CCDs fixed to a focal plane. Due to the complexity of its sensor geometry, two technical issues need to be resolved in HiRISE stereo processing for precision topographic mapping. These technical issues are achieving coherence in the exterior orientation parameters between stereos as well as overlapping CCDs, and accurate geopositioning of HiRISE data without ground-control points. In this research, bundle adjustment strategies based on polynomial function models are applied to improve the exterior-orientation parameters. Disagreement between HiRISE CCDs is handled by the bundle adjustment,

using inter-CCD tie points. HiRISE DTM was matched with MOLA DTM and points data to obtain the absolute position of the stereo model. Performance analysis of this new experiment will be given.

A ground image network is also constructed using matching of Mars Exploration Rover (MER) stereo images. Rocks detected from both orbital and ground imagery serve as tie points for rover localization. From orbital images, rocks are extracted based on brightness values and the shape of dark spots. Rocks in ground images are extracted through dense stereo matching, rock peak and surface point extraction, and rock modeling. To narrow down a precise rover position, terrain matching is performed using DTMs generated from orbital and ground imagery. Finally, distribution pattern matching is implemented for rocks detected from orbital and ground imagery. The rover position is adjusted based on a 2-D affine transformation obtained from rock pattern matching. The proposed method has been tested for the Spirit rover traverse. Selection of optimal parameter values and quality control is discussed. Experimental results show that the orbital/ground rock matching approach has performed successfully for MER rover localization.

Dedication

To God, who makes everything possible

And to my loving parents and my sister

Acknowledgments

I would like to thank my advisor Dr. Rongxing Li, for shaping me to become the professional. It was an honor working with him in the space exploration missions. His insight and continuous pursuit for excellence has been nothing less than inspiration. I wish to express my gratitude to Dr. Kaichang Di. His constructive comments have been invaluable to me in the challenging research. My sincere thanks are due to the committee: Dr. Alan Saalfeld and Dr. Alper Yilmaz. And I also wish to express my gratitude to Dr. Carolyn Merry for personal guidance and showing me how I can contribute to the community.

I wish to thank the past and present colleagues of the Mapping and GIS Laboratory and the Geodetic Science department: Dr. Jue Wang, Dr. Bo Wu, Dr. Xutong Niu, Dr. Fengliang Xu, Leslie Smith, Irene Tesfai, Yunhang Chen, Shaojun He, Lin Yan, I-Chieh lee, Sagar Desphande, Onur karahayit, Boris Skopljak, Yunjae Choung, and Youngjin Lee. I owe my special thanks to Jihye Park and Hyojin Yang without their friendship it would have been impossible for me to finish this work.

Finally, I thank my family for always believing in me.

Vita

2002 .... B.S. in Civil, Urban and Geosystem Engineering, Seoul national University

2004 .... M.S. in Civil, Urban and Geosystem Engineering, Seoul national University

2008 .... M.S. in Geodetic Science and Surveying, The Ohio State University

2004-Present.................................... Ph.D. in Geodetic Science and Surveying, The Ohio State University

Field of Study

Major Field: Geodetic Science

Studies in: Photogrammetry
Computer Vision
Mapping
GIS

Table of Contents

List of Tables

List of Figures

CHAPTER 1

INTRODUCTION

1.1 Background

The main objective of the Mars Exploration Program is to discover and understand the possibility for life on the red planet. The effort to find out the habitability of Mars in the past, present or future, can be divided into the four science goals: determination of the presence of life, characterization of the climate, characterization of the geology and preparation for human exploration of Mars. Therefore, the scientific investigations on Mars are not limited to simple detection of living organisms or water, but include gaining knowledge about the spatial and temporal patterns and interactions of global-scale geologic and climatic processes on Mars, especially how these processes have affected geochemical cycles of biological importance (Squyres et al., 2003). Since Mariner 9 first circled around the planet in the 1970’s, a series of orbiters, landers and rovers have been deployed to gather data and conduct investigations to comprehend the evolution of Mars and its hydrologic cycle.

Orbital mapping is the fundamental element in planetary exploration programs, providing global and local maps of the Martian surface that are utilized for identifying and registering the target of scientific investigation. Detailed three-dimensional (3-D) topographic information of the terrain produced from stereo photogrammetry not only gives insights about geomorphology of the planet, but also provides significant supports to planetary surface missions. Mars orbital data have been used to generate global and local topographic information for landing-site selection, precision landing and surface operations in Mars Exploration landed missions. For example, steep slopes and topographic obstructions should be avoided since tipping over can cause mechanical damage. Route planning for rovers relies heavily on the topographic maps from orbital imagery to track the location of the rovers, find targets, avoid hazards and select the efficient path possible (Li et al., 2004, 2005, 2006, 2007a, 2008c).

In the past a few decades, there has been great progress in the resolution of the orbiter sensors. Before the sub-meter resolution (0.25 m/pixel) imagery from High Resolution Imaging Science Experiment (HiRISE) became available, the maximum resolution achieved by orbital camera was 1.5 m/pixels from Mars Orbiter Camera (MOC) Narrow Angle (NA) images. Majority of MOC NA images were obtained in the resolution of 3 m/pixels, which can produce high quality DTMs (10 m grid spacing). However, overlapping images suitable for stereo mapping were rare (Li et al., 2004). As of October 2009, several hundred HiRISE stereo pairs have been acquired, making meter-scale topographic mapping of Mars possible for locations where high-resolution stereo images were not available previously. To achieve the full potential of such advanced sensor and its vast coverage, it is of paramount importance to build a HiRISE image network with the best possible precision and accuracy.

The current Mars Exploration Rover (MER) mission has far exceeded its initial goals in terms of distance traveled and operational lifetime (Arvidson et al., 2004; Li et al., 2004, 2005). In future planetary surface robotic operations, a rover would be expected to drive more than the 18 km accomplished by the Opportunity rover by sol 2062 (November 11, 2009). To achieve as much exploration as possible within the lifetime of a rover, it is desirable to travel longer distances within each command cycle, an interval between the commands by human operator. For the MER mission and the past Mars Pathfinder mission, high-level rover decision making is performed on Earth through a predominantly manual, time-consuming process. For MER, a ground-based planning and scheduling tool was used to support a science plan evaluation (Estlin et al., 2005). However, a command sequence was still manually generated on Earth and uplinked to the rovers (Maimone et al., 2007). The MER vehicles have performed over 60,000 coordinated motions (the powering of either steering or drive motors continuously) by sol 1090, activities that demand nearly constant attention (Maimone et al., 2007). The round-trip communication latency between Earth and Mars of 20 minutes or more prevents quick decisions needed when unexpected situations happen. Therefore, the automation of rover navigation is highly desired. Autonomous navigation increases the possibility of achieving as many of the science and engineering objectives as possible, by reducing the idle time and dynamically handling opportunistic science events without human interaction. Considering the larger amount of data to be collected and processed, it is practically impossible to have humans heavily involved in real-time interaction (Gor et al., 2001). For quicker and better decision, effective use of power and improvement in performance, the future space exploration missions should be based on independent space vehicle operation with full autonomy.

The success of autonomous mobile robot navigation depends on the accurate determination of position and attitude information of a rover. Without highly detailed information about the terrain to be explored, autonomous navigation may be jeopardized and little drive progress can be made. With the availability of sub-meter resolution HiRISE imagery, it is now possible to obtain highly detailed topography of the Martian surface. In rover navigation, it is crucial to locate the rover in the context of topographic maps, whose main source is orbital images. Without topographic information, it is impossible to find safe routes, and the rover may drive toward possible hazard or obstacles. Since uncertainty of the surrounding topography means little drive progress could be made in challenging terrain, rover localization in the context of orbital dataset is key to the success of autonomous rover navigation in the future.

The close-range ground imagery from Viking, Pathfinder, MER, and Phoenix missions has a much higher resolution than orbital imagery. Although MOC NA images could be used to distinguish landmarks such as big craters and ridges, the precision was limited to the pixel resolution. The resolution of orbital and ground imagery determines the level of supports orbital topographic products could provide to Martian surface mission. Due to the discrepancies in resolution and viewing direction, orbital and ground images have been processed separately in their own image network, which is a connected set of images based on stereo tie points and geodetic control points. HiRISE offers a comparable image resolution of 25 cm/pixel, which is enough to distinguish small features that can be used as tie points between orbital and ground imagery. The high resolution of HiRISE imagery opens a new possibility of integration of orbital and ground image networks.

The objectives in this research are twofold. The first is to develop photogrammetric sensor model and bundle adjustment system for the construction of HiRISE orbital image networks. The second is to develop a new methodology for integration of orbital and ground image networks using rocks as tie points. In the following section, the past and current Mars exploration missions are discussed, focusing on the mapping capabilities of sensors, the technologies used and related researches. Next, key challenges that need to be resolved to achieve those objectives are outlined. In the last section of this chapter, the overview of this dissertation is given. However, it is not the scope of this dissertation to develop a new stereo matching method. In this research, the stereo matching is conducted using generic area-based matching to create quick orthophotos without manual editing. There are commercial photogrammetric suites with sophisticated matching algorithms designed for high-quality topographic products generation (Chapter 5).

1.2 Literature Review

1.2.1 Mapping of Mars

The mapping of Mars is based on orbital, descent and ground imagery. Mariner 9, launched in 1971, was the first spacecraft orbiter to circle another planet. It took more than 7,300 images of Mars, covering the entire surface at a resolution ranging from 1 to 3 km and selected areas at resolutions down to 100 meters. A global map of Mars was created using topographic information obtained from Mariner 9 and Earth-based radar, compiled at a scale of 1:25,000,000 with a contour interval of 1 km (Wu, 1979).

In 1975, NASA launched two spacecrafts: Viking 1 and Viking 2. Each spacecraft consisted of an orbiter and a lander. The Viking orbiter's images covered the entire surface of Mars and were used to generate a controlled network, contour-maps and DTMs with scales ranging from 1:2,000,000 to 1:25,000. Contour intervals range from 1 km to as small as 20 m. Cameras on the Viking lander have a resolution of 2.1 mrad/pixel for color mode and 0.7 mrad/pixel for monochrome high-resolution mode (Smith et al., 1997). Maps of the terrain surrounding the two Viking landers were compiled at scale of 1:10 with a contour interval of 1 cm (Wu, 1979). The elevation and slope information of Mars topography was determined by a photogrammetric method using Viking orbiter stereo images. The errors in elevation were as large as a number of kilometers (Abshire et al., 2000). The first version of Mars Digital Image Model (MDIM) was created by the U.S. Geological Survey (USGS) using roughly 4600 Viking Orbiter images. The global mosaic, MDIM 1.0, was distributed in 1991 at a scale of 1/256 degree or ~231 m/pixel. The MDIM has been widely used as a control network and continually is updated using new orbital data ever since.

After almost 20 years, Mars Global Surveyor (MGS) was sent to Mars in 1996. Its imaging system, MOC, consists of three cameras. Two wide angle (WA) cameras with 140° fields of view can acquire horizon-to-horizon images of the planet at the best nadir scale of 230 m/picture element (pixel) and the limb scale of 1.5 km/pixel. The NA camera can provide imagery at 1 m/pixel to 12 m/pixel resolution (Malin and Edgett, 2001). MOC images were used for mapping and selection of landing sites. The topographic maps generated from MOC NA stereo images have a horizontal resolution of 5 m and an expected vertical precision of 1 m (Kirk et al., 2003).

The Mars Orbiter Laser Altimeter (MOLA), an instrument on the MGS orbiter, obtained measurements of topography, surface reflectivity, and backscattered laser pulse width. MOLA provided profiles of Martian surface at a maximum vertical resolution of 30 cm and along-track spatial resolution of 300 to 400 m (Smith et al., 1998). MOLA elevation point data is known as the Precision Elevation Data Records, or PEDR (http://pds-geosciences.wustl.edu/missions/mgs/pedr.html). Currently, the best global Mars terrain model was acquired by MOLA. The MOLA terrain model with a spatial resolution of about 1 degree (or 59 km at the equator) has an absolute vertical accuracy of 13 m with respect to the Mars center of mass (Smith et al., 1999). It is estimated that accuracy of elevations derived from MOLA data is 30 to 40 m and the precision of the MOLA measurement approaches 30 cm on smooth level surfaces and increases to 20 m on 30° slopes (Smith et al, 1998). This precise terrain model has many applications in geophysical, geological and atmospheric circulation studies of Mars. The higher-resolution MOLA digital terrain model (DTM) known as Mission Experiment Gridded Data Record (MEDGR) is available at resolutions of 4, 16, 32, 64 and 128 pixels per degree. In the polar region, the resolutions are 128, 256 and 512 pixels per degree. Most importantly, from the mapping perspective, MEDGR provides a global geodetic control for registering orbital images from current and future missions. Shan et al. (2005) reported their efforts in photogrammetric registration of MOC NA imagery to MOLA profiles and automatic DTM generation from MOC NA stereo images.

With a ground resolution of 213 m, the latest version of MDIM (version 2.1) has the accuracy (RMS error of the control network) of about 250 m (Archinal et al., 2003, Kirk et al., 2001). The accuracy of the new image network is improved primarily as the result of constraining all 37,652 control points to radii from MOLA data and adding 1,232 ground control points whose horizontal coordinates are also constrained by MOLA, 1,054 Mariner 9 and 5,317 Viking Orbiter images (Archinal et al., 2004).

Mars Pathfinder landed on Mars in July 1997 and released a rover named as Sojourner to conduct various scientific experiments. It was the first successful mission to send a rover to a planet. The Mars Pathfinder lander was equipped with the Imager for Mars Pathfinder (IMP), a stereo imaging system with color capability provided by a set of selectable filters for each of the two camera channels. The angular resolution is 1 mrad/pixel, approximately same as the Viking lander cameras (Smith et al., 1997). From the panoramic images, the USGS, the German Aerospace Center (DLR), as well as the Ohio State University conducted the landing site mapping based on the photogrammetric processing and topographic modeling (Graddis et al., 1999; Kirk et al., 1999; Kuschel et al., 1999; Di et al, 2002). Sojourner carried the alpha proton X ray spectrometer (APXS), which was used to analyze the chemical elements in Martian soil and rocks near the landing site (Rieder et al., 1997). The rover also had an imaging system consisting of two black and white cameras and one color camera with an angular resolution of 3.1 mrad/pixel to take close-up images for all samples analyzed by the APXS.

In 2001, NASA launched Mars Odyssey orbiter. Its Thermal Emission Imaging System (THEMIS) camera collects data including visible images in 5 bands at 20 m/pixel spatial resolution and thermal infrared (TIR) images at 100 m/pixel spatial resolution using 9 different spectral bands (Christensen et al., 2004).

In 2003, the European Space Agency (ESA) launched the Mars Express mission, which is consisted of the Mars Express (MEX) Orbiter and the lander Beagle 2. The High Resolution Stereo Camera (HRSC) on MEX operates as a multi-line push broom scanning instrument with 9 CCD line detectors mounted in parallel in the focal plane of the camera. HRSC has the unique capability of simultaneous acquisition of stereo imagery using five panchromatic channels under different observation angles and four color channels. The maximum resolution of HRSC images is about 10 m/pixel at 250 km pericenter altitude. The Super Resolution Channel (SRC) of HRSC, a framing camera, provides an even higher resolution images of up to 2.3 m/pixel in small segments of the Martian surface (Albertz et al., 2005, Scholten et al., 2005, Heipke et al., 2007, Gwinner et al., 2009).

In 2004, the Mars Exploration Rover mission landed two rovers, Spirit and Opportunity, on the surface of Mars. In the Entry, Descent and Landing (EDL) phase, a vision system called the Descent Image Motion Estimation System (DIMES) was used to estimate horizontal velocity during the last 2,000 meters of descent by tracking the features on the ground from the DIMES sequential images. The main purpose of the descent images was to control retro-rocket firing and automatically reduce horizontal velocity for precision landing (Maimone et al. 2004). The Descent camera has an angular resolution of 0.82 mrad/pixel and 45º square FOV. At both landing sites, three downward-looking pictures were taken at around 2,000 m, 1,700 m and 1,400 m above Martian surface (Cheng et al., 2005). The ground resolution of the DIMES images was about 1 m. They were also used for trajectory reconstruction of the spacecraft EDL and consequently served as a very important data set for landing site localization (Li et al., 2004, 2005, 2006, 2007a, 2008c).

Each Mars Exploration Rover carries an integrated suite of scientific instruments and tools: the Athena Science Payload (Squyres et al., 2003). The scientific instruments include: Alpha Particle Xray Spectrometer (APXS) for analyzing the composition of rocks and soil; Mössbauner Spectrometer (MB) for investigating mineralogy of iron-bearing rocks and soils; Microscopic Imager (MI) for obtaining high-resolution images of rocks and soils; and Rock Abrasion Tool (RAT) for removing the outer surface of rock and exposing the interior material.

Rovers have four pairs of stereo cameras: panoramic cameras (Pancam), navigation cameras (Navcam), forward-looking hazard cameras (Hazcam) and rear-looking Hazcam. Pancam, Navcam, and Hazcam cameras are used for imaging the terrain far range, middle range and close range, respectively. They are all 1024×1024-pixel frame digital cameras and utilize broadband visible filters. The spectral range of Navcam and Hazcam is 600 to 800 nm, while Pancam uses eight bandpass filters ranging from 400 to 1,000 nm (Maki et al., 2003). The Pancam has 16º field of view (FOV) and 0.28 mrad/pixel angular resolution. The Navcam has 45º FOV and 0.82 mrad/pixel angular resolution. The Hazcam has a much broader FOV of 124º and an angular resolution of 2.1 mrad/pixel. Pancams and Navcams are installed on a Pancam Mast Assembly (PMA), which can rotate in 360° azimuth angle and ±90° elevation angle. A panoramic image with 10% overlap needs 10 pairs of Navcam images or 27 pairs of Pancam images. A Navcam panorama consists of 20 images configured as one vertical row (tier) and can be generated within 30 minutes; a Pancam panorama often consists of three tiers and takes several days to complete. Pancam is also used as a sun sensor finder. Hazcams are installed just under the solar panel. They can perform real-time feature matching and build up the terrain slope in the close range, so as to help the rover to select a safe route (Xu, 2004; Matthies et al., 2007).

In 2005, the Mars Reconnaissance Orbiter (MRO) probe was launched toward the red planet. MRO mounts three cameras: HiRISE, Context Camera (CTX) and Mars Color Imager (MARCI). HiRISE acquires visible images in detail (0.25 to 1.3 m/pixel). CTX provides contexts for high-resolution analysis of key spots on Mars with its wide-area views (swath width of 30 km and pixel resolution of 6 m). MARCI consists of two framing cameras, one with two spectral bands in the ultraviolet and the other with five in the visible. With a 180° FOV, MARCI was designed to conduct the daily global survey of weather on Mars. The availability of HiRISE stereo images from the MRO has made the unprecedented progress in high-resolution imaging and enhanced the capability of topographic and morphological mapping for Mars surface exploration (McEwen et al., 2007; Zurek and Smrekar, 2007).

The most recent mission to Mars was the Phoenix Mars lander, which launched on August 4, 2007 and arrived on the north polar region of Mars on May 25, 2008. Its primary camera is the Surface Stereo Imager (SSI), a stereographic imager with color and near infrared capability. The design of the SSI is based on the IMP on Mars Pathfinder (Smith et al., 1997), but it has been enhanced to four times the resolving power by using the MER CCD detector package. It has the ability to create a complete panorama using a subset of 13 geological filters that span the spectral range from 440 to 1000 nm (Smith et al., 2008).

1.2.2 Planetary Rover Localization

In rover operation, the critical questions that need to be answered at all times are these: where is the rover, how far is it from the target and is it on the designed route? Without external references from GPS systems, rover localization on Mars depends on the combination of various methods, such as two-way Doppler radio positioning technology, cartographic triangulations through landmarks, dead reckoning, and stereo vision, visual odometry and bundle adjustment based on photogrammetry (Li et al., 2004).

The position of the rovers can be measured using the radio transmissions. In the MER mission, the navigation team determined the rover position through fitting direct-to-earth two-way X-band Doppler radio transmissions and two passes of ultra-high frequency two -way Doppler between the rover and the MARS odyssey orbiter (Li et al., 2005).

After the landing, the landmarks seen from the rover can be compared with orbital and decent images to identify the location of the rover in the context of larger-scale topographic products. In the MER mission, when the first panorama was acquired, ground features such as hills and craters were carefully examined in the rover images, the DIMES descent images and MOC images. In the Spirit landing site, several mountain peaks, such as the Columbia Hills and the Grissom Hills, were identified from rover images and also found from orbital images. In the Opportunity landing site, several other craters can be seen through the outside of the rim of Eagle crater, where the rover had fallen right into; these craters are used to identify the Eagle crater from overhead images. A cartographic solution was then given by a least squares adjustment based on the coordinates of mountain peaks measured from orbital images as well as coordinates measured from ground images. At each site, additional MOC NA image was taken to verify if the cartographic solution is consistent with the actual lander position (Li et al., 2008c).

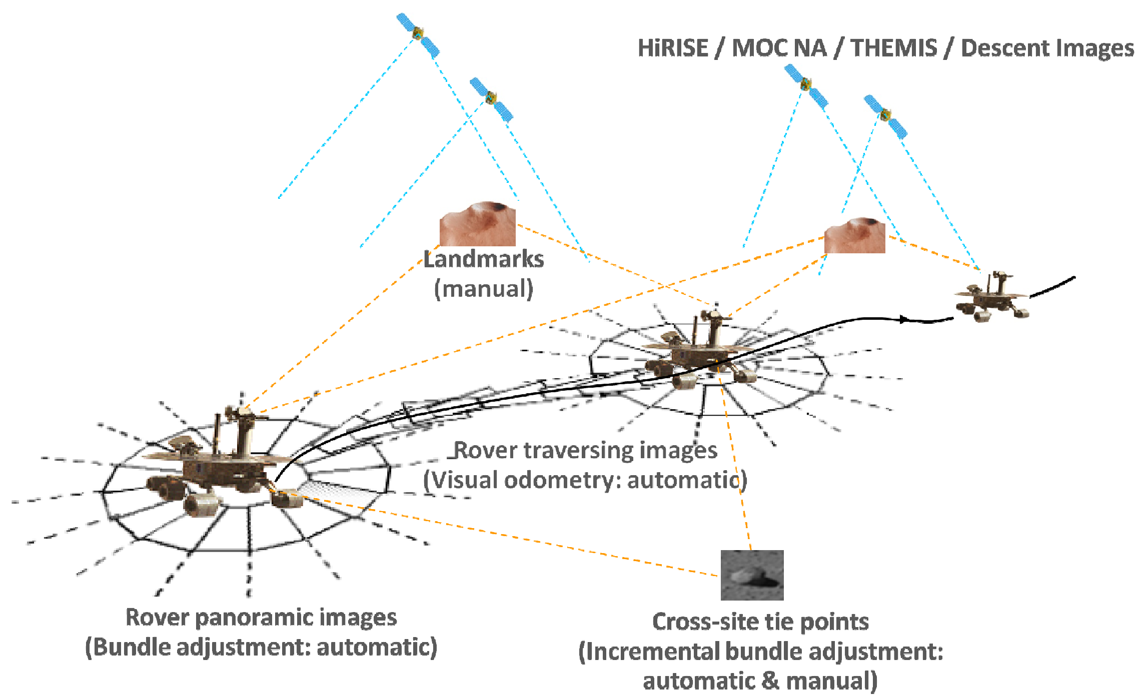

Figure 1.1: Overview of MER rover localization using orbital and ground image networks (Li et al., 2005)

The current MER rover localization is accomplished by a combination of the latest technologies such as photogrammetry, computer vision, and autonomous rover navigation (Figure 1.1). Mars Exploration Rovers are six-wheel drive, four-wheel steered vehicles. The IMU onboard the rover provides three-axis rate and three-axis tilt information. The wheel odometer records wheel turns and orientation information to determine traverse paths relative to the starting position (Li et al., 2008c). The dead reckoning approach uses IMU and odometer to estimate the rover traverse by tracking the integral of accelerations relative to an inertial system. During the surface operations of the MER mission, positions of both rovers are estimated onboard within each sol by dead reckoning. The heading is also updated occasionally by sun-finding techniques using the Pancam images. However, tracking rover traverse with dead reckoning devices is subject to accumulative errors in the measurement of relative pose. IMU and odometer work well most of the time, except when climbing a hill or crossing surfaces covered with soft soil. If slippage occurs, the traverse calculated by IMU and odometer is no longer accurate. In the MER mission, the dead reckoning error has accumulated mainly due to the slippage between the rovers' wheels and the ground. Spirit rover experienced significant wheel slips traversing Husband Hill, with accumulated slippage reaching a maximum of 83.86 m on Sol 648. Particularly on soil-covered terrains with slopes up to 15°, more slippage than the traveled distance occurred for short segments (Li et al., 2008c). Because errors are accumulated as time goes on, the rover position needs to be refined and updated regularly. Thus precision rover localization calls for additional approaches to overcome position errors caused by wheel slippages, azimuthal angle drift, and other navigation errors (Li et al., 2005). In MER mission, the position errors experienced as large as the 10.5 % in the Husband Hill area for Spirit rover and 21% within Eagle Crater for Opportunity rover (Li et al., 2007b).

In rover navigation, stereo vision can be used to avoid possible hazards by building a terrain slope map in real time (Maimone et al., 2004). Goldberg et al. (2002) developed a local, reactive planning algorithm, called Grid-based Estimation of Surface Traversability

Applied to Local Terrain (GESTALT) to choose the best direction for the next move of a rover. Vision-based techniques process stereo images to obtain 3-D environment information and match landmarks, in similar ways to a human's vision system. In the exploration of Mars, the Jet Propulsion Laboratory machine vision group used small-sized cues such as rocks for a fine localization as an improvement to the dead reckoning based approach. The Jet Propulsion Laboratory worked on several advanced methods including probabilistic self-localization (Olson, 2000) and visual odometry algorithms (Olson et al., 2003).

Visual odometry is introduced for reliable long-distance navigation and has been used onboard the MER rovers for precision instrument placement and the correction of slippage (Maimone et al., 2007). Visual odometry processing was performed on both rovers, by taking midpoint survey images using Navcam along the traverse toward another site. By matching features from the traverse images, visual odometry automatically tracks the movement of the rovers. All visual odometry drives were split into small steps to ensure at least 60% overlap between adjacent images. During each step, the rovers are typically commanded to drive no more than 75 cm in a straight line or curved arc (Cheng et al., 2006). In Earth-based tests with ground truth measured by total station, it is shown that visual odometry can achieve a 2% localization error relative to the traverse length (Olson et al., 2003). However, this method also has limitations of requiring small field of view (optimal at 30°) and small traverse intervals (they practiced at 10cm interval), which may not be available during the real situation. In MER operations, visual odometry is applied mainly for a short traverse that is no longer than 10 meters (Li et al., 2005). However, it was not uncommon for the MER rover to drive more than 30 meters without taking any pictures (Xu, 2004). Moreover, the visual odometry process takes approximately two minutes per one pair of stereo images, which is too time-consuming and thus impractical for a long traverse (Li et al., 2006). For that reason, visual odometry has been used only in special circumstances when high slippage is expected or high precision placement is needed.

For relatively long traverses, incremental bundle adjustment based on photogrammetry is used for rover localization (Li et al., 2004, 2005, 2006, 2007a). The photogrammetric approach provides accurate rover positions by building a strong image network along the traverse to maintain consistent overall traverse information. The rover moves to different locations called ‘sites’, where it stops and acquires a full or partial panorama of Navcam and Pancam images. At each rover site, bundle adjustment is conducted based on tie points from stereo matching between the panoramic images. The bundle-adjusted rover position and the panoramic images, linked by tie points, form ground image networks.

The bundle adjustment in MER rover localization is based on three types of stereos. Intra stereos are taken from the left and right stereo cameras at the same position and attitude. Inter-stereo images are also taken at the same site, but the rover’s looking angles are rotated. Intra/inter stereos are used for within-site bundle adjustment to remove the within-site inconsistency. Cross-site stereos are taken at different sites. The performance of bundle adjustment depends on the availability of the sufficient amount of well-distributed tie points that link individual ground images into an image network. The combined visual odometry and bundle adjustment successfully corrected the position errors with an accuracy of 0.5% over a 6 km traverse for Spirit rover (Li et al., 2006). Cross-site bundle adjustment is especially important for reducing position errors between adjacent sites. Visual odometry and within-site bundle adjustment are automatic procedures, while cross-site bundle adjustment has heavily relied on manual operation during MER mission.

For autonomous rover localization, Li et al. (2007b) proposed a new approach for automatic cross-site tie point selection using rock extraction, rock modeling, and rock matching. A peak, the highest point, is the most visible part on a rock regardless of the looking angle. The surface area under the peak is fitted into analytical rock models. Cross-site rocks are matched through two complementary stages: rock model matching and rock distribution pattern matching between the rocks extracted from two adjacent sites. The method worked successfully along with a continuous 1.1 km stretch for the simulated test dataset at Silver Lake (Wang, 2008) and was use for Spirit rover localization since August 2007 (Di et al, 2008b).

1.3 Issues and Significance

The unique HiRISE sensor configuration consists of 14 CCDs fixed to a focal plane. The complexity of the sensor geometry raises technical issues, which need to be resolved in HiRISE stereo processing when used for the generation of high-resolution topographic products such as DTMs or orthophotos. High-frequency random patterns, or “jitter”, in the rotation angles cause disagreements between HiRISE CCDs. To generate seamless topographic products, it is important to achieve coherence in the exterior orientation parameters between multiple CCDs.

Another issue involving construction of orbital image networks is accurate geopositioning of HiRISE data without ground-control points. Due to various measurement errors in terms of timing and star tracker observation, as well as the Doppler shift, the observed trajectories of the orbiters could be affected by systematic shifts and drifts in the magnitude of hundreds or thousands of meters (McEwen et al., 2007; Lefort et al., 2009). To achieve absolute positioning in global scale, new images should be registered to the existing global geodetic control network.

In this dissertation, the orbital image networks on Mars is constructed based on bundle adjustment of multiple HiRISE stereo images and absolute positioning using MOLA control network for precision topographic mapping. Bundle adjustment strategies using polynomial function models are applied to improve the exterior-orientation parameters (Shan et al., 2005; Li et al., 2008b). The MOLA MEDGR gridded product having a resolution of 463 m/ pixel provides the best source of ground control. However, the big difference in planimetric resolution between the HiRISE imagery and MOLA DTM prevents achieving horizontal accuracy better than hundreds of meters when MEDGR is used as direct source of horizontal control. Kirk et al. (2008) used coordinates measured from the 1.5 m/pixel MOC images previously controlled to MOLA for horizontal control points. In this research, HiRISE DTM is matched with interpolated MOLA DTM to obtain an initial estimate of the absolute position of the stereo model. Further terrain matching is conducted using MOLA profile as vertical control.

Due to the sheer volume of HiRISE images, often exceeding 1600 megapixels (McEwen et al., 2007), the stereo mapping could not be completed efficiently unless most of the photogrammetric processing is automated. Stereo matching, which consists of a significant amount of computations, affects the quality of the topographic products directly. There is a fine line between producing as many tie points as possible without sacrificing the quality and eliminating too much or too little possible mismatches. In this research, matching parameters are examined and selected empirically. Performance analysis of this new experiment is given.

In planetary surface exploration, the most critical information that needs to be updated constantly is the location of mission components. Depending on the nature of each mission, these components can be unmanned vehicles (rovers) or astronauts. Without the availability of Global Positioning Systems (GPS) in the outer planets, the localization process is a challenging task that requires a combination of multiple approaches such as wheel odometry, inertial measurement unit (IMU), Sun-finding techniques, visual odometry, incremental bundle adjustment and identification of landmarks from orbital images. Since the current technologies for the MER rover localization methods are limited to the ground image network, the position of the rover is still unidentified in the context of topographic products from orbital imagery. Without identification of landmarks, there is no guarantee that the rover position obtained from the ground image networks could be aligned with the topographic products generated from orbital imagery. Although orbital mapping is very important, it cannot replace the role of ground mapping when considering the resolution, speed, and precision. On the other hand, ground mapping alone does not provide sufficient context information about the unknown territory for the rover navigation and the route planning. Finding a connection between ground and orbital mapping and ultimately integrating both types of image networks would maximize utilization of Mars exploration missions dataset for the success of the autonomous rover navigation in the future space exploration.

To link the orbital and ground image networks, common features should be identified between the two types of imagery. The availability of sub-meter resolution HiRISE imagery has opened the possibility of computing rover locations at higher accuracy by enabling extraction and matching of small features seen in the ground images. In the current MER mission, due to the inconsistencies between the orbital and ground image networks, updating rover positions in the global DTM and orthophotos has been performed by manually identifying common landmarks from both datasets. It is a very time-consuming and labor-intensive procedure. To assist autonomous rover navigation, real-time rover localization on both ground and orbital image networks should be performed automatically. Automatic landmark matching between images typically requires the invariance of features, meaning that the shapes of the features should be similar after image translations and change of scale. In order to establish a correspondence between cross sites or between the ground image data and the global orbital data, this method requires substantial effort to resolve issues of data format, reference systems and cross dataset comparison (Li et al., 2004; 2006a).

For rover localization, visual odometry and bundle adjustment are both performed using tie points between the rover images. In visual odometry, common features are identified between stereo images taken along the traverse within short intervals. Although visual odometry is fully automated onboard the rover, it is only performed when significant slippage is expected due to heavy computational load. Within-site bundle adjustment is also performed automatically, based on tie points selected from the intra- and inter-stereos using the MarsMapper software developed by the OSU Mapping and GIS Lab (Xu, 2004). However, the adjustment of rover traverse still requires manual operation because of difficulties in automatic selection of cross-site tie points (Di et al., 2008a). Cross-site tie point selection has been a labor-intensive procedure due to different viewing angles. On Mars, rocks are the most prominent features and can be used as landmarks. To automate the cross-site tie point selection, Li et al. (2007b) proposed a new approach for automatic cross-site tie point selection using rock extraction, rock modeling and rock matching. Since the resolution of HiRISE is not enough to distinguish shapes of rocks, the rock matching method used for cross-site tie point selection could not be directly applied for rock matching between orbital and ground imagery. Hence, the rock extraction strategy for orbital/ground data integration should be based on different measures to identify rocks visible from both types of images. Since the resolution of HiRISE camera is not high enough to distinguish orbital rocks according to shapes, it is possible to place the rover at the wrong location if the distribution patterns orbital and ground rocks happen to match. Therefore, other measures for quality control are needed, such as variance of local elevation. This dissertation introduces a new method toward integration of orbital and ground image networks using rock extraction, terrain matching and rock distribution pattern matching.

1.4 Overview of the Dissertation

This dissertation aims to improve less-than satisfactory parts of the current technologies, namely generation of high-quality topographic products coherent to the existing control networks and finding correspondence between orbital and ground dataset, automating as much procedures as possible. Accordingly, the contents of this dissertation are divided into two parts. The first part is the construction of orbital image networks with reduced misalignment between stereos as well as control networks. This dissertation focuses on rigorous sensor modeling of HiRISE imagery and bundle adjustment for positional accuracy. The second part is the integration of orbital and ground image networks using terrain matching, rock modeling, and rock pattern matching. Figure 1.2 illustrates the overall workflow for integration of orbital and ground image networks proposed in this dissertation.

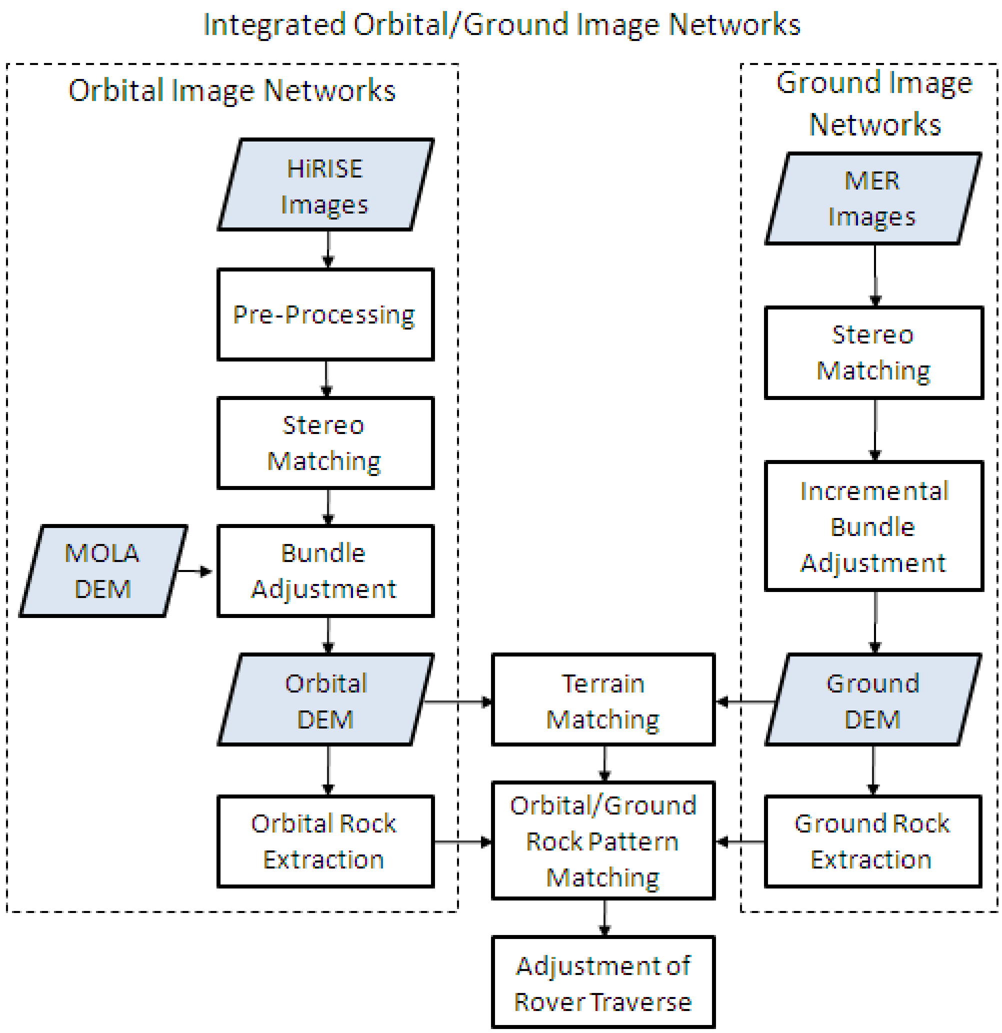

Figure 1.2 Flowchart of the integration of orbital and ground image networks

The organization of the dissertation is as follows: Chapter 2 defines the rigorous HiRISE sensor model, including interior and exterior orientation parameters. Jitter movement in camera pointing angle is analyzed as well. Chapter 3 describes the construction of orbital image networks in detail. The photogrammetric processing of HiRISE stereo images includes image pre-processing, interest point generation, stereo image matching, DTM/orthophoto generation and bundle adjustment. Different types of observation equations in bundle adjustment are presented. They are based on observations such as polynomial models of exterior orientation parameters, stereo tie points, inter-CCD tie points, and MOLA DTM. In chapter 4, a new methodology to find connections between orbital and ground image networks is proposed, using HiRISE and MER dataset. Detailed description about terrain matching, orbital/ground rock extraction and rock pattern matching is given. Chapter 5 discusses parameter selection and quality control for the developed procedures in this research. Empirical analysis is provided in search for the optimal parameter values. Chapter 6 presents implementation results and performance analysis. For the Spirit landing site in Gusev crater, HiRISE stereo images are processed using the MarsMapper: Orbit software developed in this research. The topographic products are compared with USGS products. Also, a rover localization approach using orbital and ground rock matching is tested for Spirit rover traverse. Chapter 7 concludes the dissertation with discussion and future research topics.

CHAPTER 2

ORBITAL (HiRISE) IMAGING GEOMETRY

In order to produce accurate topographic products from HiRISE imagery, its geometry should be modeled to its highest precision. This chapter investigates the relevant coordinate frames, interior orientation and exterior orientation that are needed for processing HiRISE imagery. A rigorous geometric model is presented in which a ground point is transformed to its image point through collinearity equations with the interior and exterior orientation parameters.

2.1 Coordinate System

To calculate the HiRISE exterior orientation parameters, several reference frames are taken into consideration: Mars body-fixed frame, MRO spacecraft frame, and HiRISE frame (Figure 2.1). The relative position and rotation between these frames are recorded in the SPICE kernel, the primary data sets of the space-borne instrument provided by NASA's Navigation and Ancillary Information Facility (Acton, 1999). Mars body-fixed frame is defined based on the Mean Mars Equator and IAU vector of date computed using the IAU 2000 Mars rotation constant (Archinal et al., 2003). The origin of the MRO spacecraft frame is centered on the launch vehicle separation plane. Its Z axis is parallel to the nominal HIRISE boresight, its Y axis is anti-parallel to the Mars Orbit Insertion thrust vector, and its X axis completes the right hand frame. As MRO moves along the Martian orbit, the relative position and rotation angles of MRO spacecraft frame with regard to Mars body-fixed frame are stored in SPICE kernel. The HIRISE frame, fixed to the MRO spacecraft frame, is used to compute the pixel view direction of HiRISE image. Its orientation with respect to the MRO spacecraft frame is provided in the preliminary in-flight alignment results that can be found in the Mars Reconnaissance Orbiter Frames Kernel (Acton, 1999).

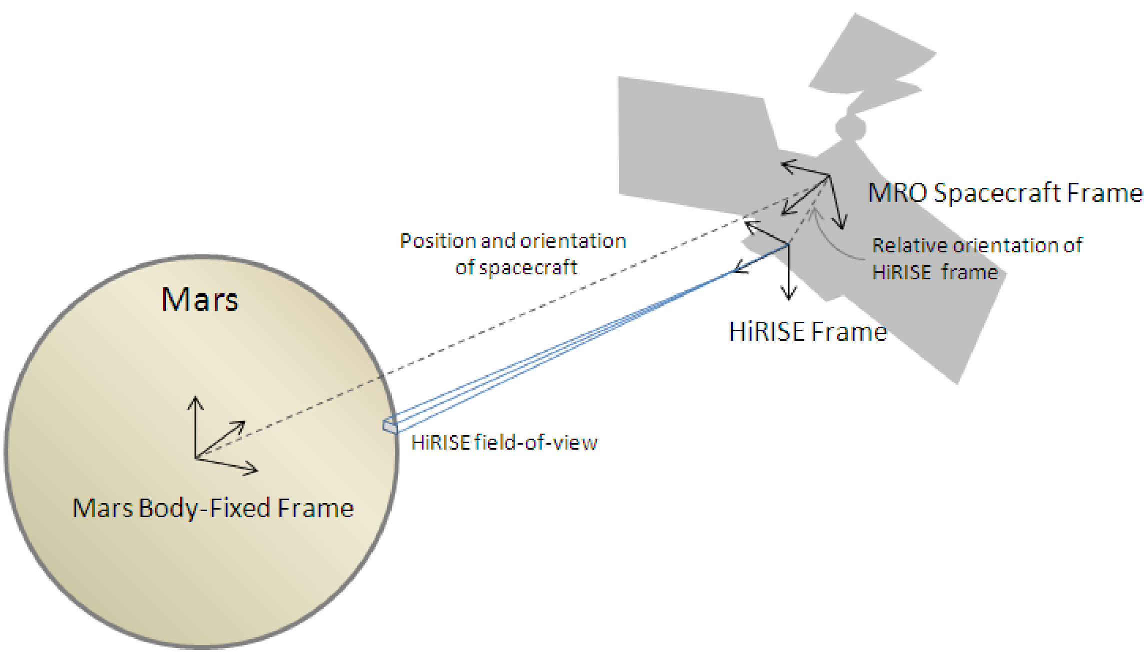

Figure 2.1 Reference frames

The introduced photogrammetric processing of HiRISE imagery is based on the Mars body-fixed frame. At the test regions of the MER (Mars Exploration Rovers) mission landing sites, the HiRISE topographic products are generated using the Landing Site Cartographic (LSC) coordinate frames to facilitate comparison with mapping products generated from rover images. The LSC coordinate frame is an east-north-up (X-Y-Z) right-handed local system with its origin at the lander (Li et al., 2006). For example, the LSC frame at the Gusev Crater landing site is centered on the Spirit lander, or (14.571892ºS, 175.47848ºE) in the Mars body-fixed frame system.

After aerobraking, MRO went into a Primary Science Orbit (PSO) that lasted a bit more than one Mars year, from November 2006 until December 2008. The PSO is a near-circular (250 × 315 km), near-polar (inclination of 92.65º) orbit. With its periapsis fixed over the South Pole, the spacecraft crosses each latitude circle at the same altitude on every orbit (Zurek and Smrekar, 2007). At the altitude of 300 km, the resolution of HiRISE image is 30 cm/pixel.

2.2 Interior Orientation of HiRISE Imaging Geometry

The HiRISE telescope is a 50 cm aperture, f/24 system with folded optics (Figure 2.2). The Cassegrain objective with relay optic and two fold mirrors is optimized to diffraction-limited performance over the long, narrow FOV (McEwan et al., 2007). Due to the folded optics of the camera, the focal plane assembly actually lies perpendicular to the flight direction. However, in the photogrammetric analysis, we treat them as if the optics were unfolded and the focal plane assembly was oriented perpendicular to the incoming rays. In this simpler conceptual model, the layout of HiRISE focal plane assembly is shown in Figure 2.3.

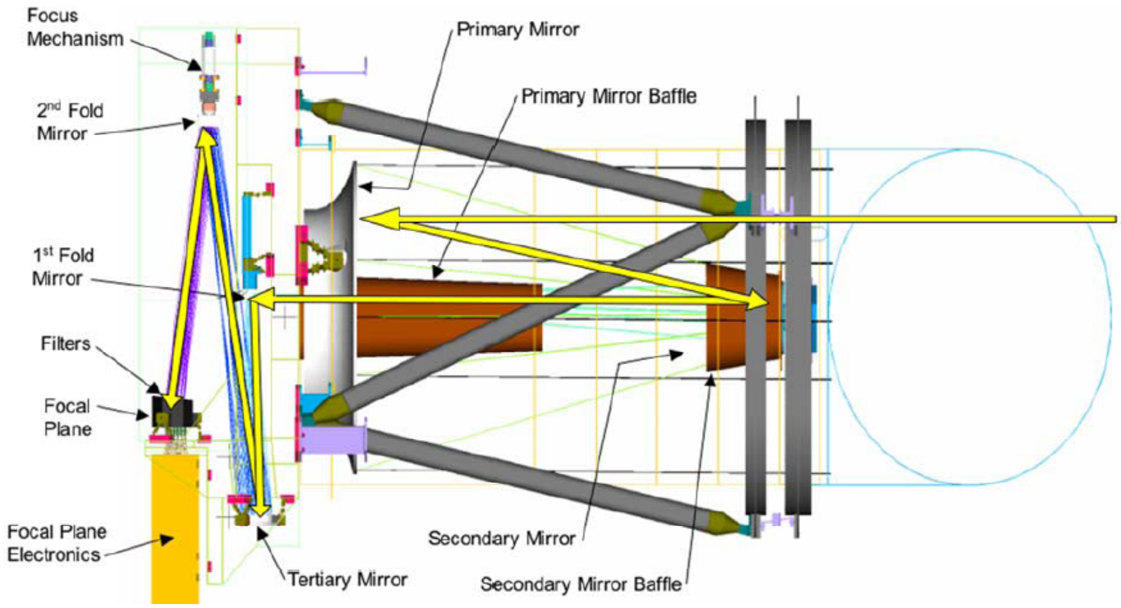

Figure 2.2 Graphical representation of HiRISE telescope, with a sample of ray traces in yellow line (McEwan et al., 2007)

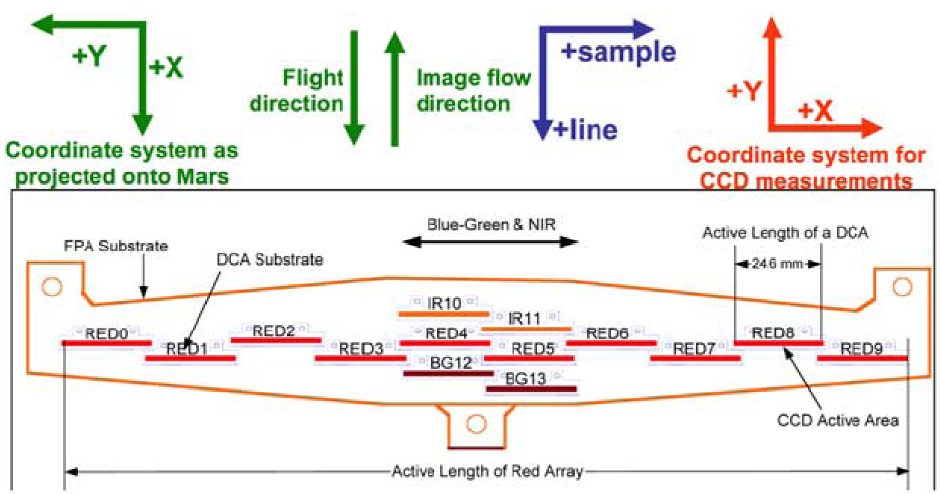

Figure 2.3 HiRISE focal plane assembly layout (Kirk et al., 2008)

HiRISE is a push-broom imaging sensor with 14 CCDs (10 red, 2 blue-green and 2 NIR). Each CCD consists of a block of 2,048 pixels in the across-track direction and 128 pixels in the along-track direction. Ten CCDs covering the red spectrum (570– 830 nm) are located in the center of the focal plane assembly. Blue-green CCD passes <580 nm color band, while near infrared CCD detects >790 nm spectrum. In the across-track direction, the average width of the overlap between adjacent CCDs is about 48 pixels. However, the alignment of the CCDs involves small shifts and rotations with regard to the HiRISE optical axis. After the exclusion of overlapping pixels, HiRISE can generate images with a swath of up to 20,264 pixels (1.14º FOV) in the across-track, which is equivalent to 6 km at 300 km altitude (Delamere et al., 2003; McEwen et al., 2007).

The +X axis of the HiRISE frame is the same as the flight direction and the +Y axis is to the left. In the right-handed coordinate system, the looking direction (+Z axis) to the Martian surface is into the page. The line and sample coordinates is the relative position of image pixels with respect to the center of each 2048×128 CCD. The sample coordinates in the raw image increase in the opposite of the HiRISE frame +Y direction, which is to the right in the page. Since HiRISE is a push-broom scanner, the line coordinates do not change from one row to another. However, they are determined by the number of pixels in the along-track direction collected to store one pixel in time-delay integration (TDI) mode. At the altitude of 300 km, the resolution of HiRISE images is 30 cm/pixel. At such a high resolution, the instantaneous field-of-view (IFOV) is extremely small (1 μrad) and, as a result, the ground track speed is very fast. To improve the signal strength of "fast-moving" objects and to increase the exposure time, time-delay integration (TDI) technology was incorporated in the instrument using 128 CCD lines in the along-track direction. As the

MRO spacecraft moves above the surface of Mars, TDI integrates the signal as it passes across the CCD detector by shifting the accumulated signal into the next line of the CCD at the same rate as the image moves (a line rate of 13,000 lines/sec, or 1 line every 76 microseconds). Signals in each TDI block are transferred from line to line at ground track speed. A single pixel is formed by accumulating signals from the TDI block. HiRISE can use 8, 32, 64 or 128 TDI stages to match scene radiance to the CCD full-well capacity. Figure 2.4 shows how TDI system works in single HiRISE CCD. Depending on the number of TDI stages, a fixed amount of pixels in the along-track direction are used. In any case, the last line always stops at the same position. The observation time of a single pixel is considered to be the ephemeris time when the center of the TDI block is exposed. In SPICE kernel, the ephemeris time is used as time standard to take account of time dilation when calculating orbits of planets, asteroids, comets and interplanetary spacecraft in the Solar system.

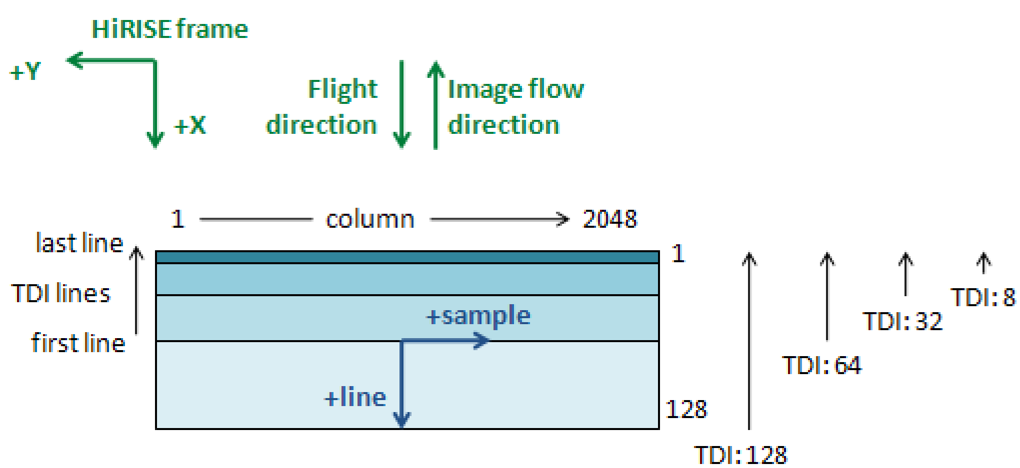

Figure 2.4 Illustration of time-delay integration in single HiRISE CCD

In HiRISE, lower resolution images can be obtained by binning the signal from adjacent lines and pixels, within the CCD, up to a maximum of 16 by 16 pixels. Square pixel binning is available in 6 modes: 1 × 1, 2 × 2, 3 × 3, 4 × 4, 8 × 8 and 16 × 16. Binning is used when desired to reduce data volume and increase coverage of Mars or to increase signal to noise ratio.

Based on the image coordinates, the pixel position in each CCD can be expressed in sample and line coordinates as follows:

$$s = (m - 0.5) \cdot BIN - 1024 \tag{2.1a}$$

$$l = TDI/2 - 64 - (BIN/2 - 0.5) \tag{2.1b}$$

where m is the binned pixel position in column direction with respect to the image corner, s is sample-direction coordinate from CCD center, l is line-direction coordinate from CCD center, TDI is the number of TDI elements in the along-track direction (8, 32, 64 or 128), BIN is binning mode (1, 2, 3, 4, 8 or 16).

If all TDI lines are used ($TDI = 128$) and there is no binning ($BIN = 1$), the center of the TDI block is the midpoint of the CCD, $l = 0$. The sample coordinates range from -1,023.5 to 1,023.5, regardless of the BIN or the TDI mode. The units of sample and line coordinates are in pixels.

The intrinsic setting of the camera system is defined by the elements of interior orientation of the camera, which are carefully determined through camera calibration. Once calibrated, they are assumed to be constant, and all image lines share the same parameters (Wolf, 2000). The calibrated interior orientation parameters are needed to calculate the pixel view direction with respect to the HiRISE frame. The USGS conducted geometric calibration of the HiRISE camera. The complex design and extremely high resolution made the collection of the required calibration information challenging. Even if the calibration in the laboratory was conducted to achieve the best accuracy, substantial changes to the structural dimensions and optical properties of the camera were expected during the flight, as a result of the lack of gravitational distortions, vibrations at launch, and the slow drying of the support structures The relative positions of the detectors in the focal plane and the initial estimate of the focal length and optical distortions were measured directly in the laboratory. After launch, a series of start observations were conducted during the cruise from Earth to Mars to adjust the focal length value (Kirk et al., 2008). The effective focal length derived from these observations was converted to a calibrated focal length shown in Table 2.1.

Focal Length	f (mm)	11995.48
Radial Distortion Coefficients	k_0	-0.004850857
	k_1 (mm^{-2})	$2.41312\cdot10^{-7}$
	k_2 (mm^{-4})	$-1.62369\cdot10^{-13}$

Table 2.1 HiRISE calibrated focal length and radial lens distortion coefficients (Kirk et al., 2008)

The positions of the each CCD detectors in the HiRISE focal plane assembly were measured in the laboratory. The HiRISE boresight is offset by approximately 94 mm from the optic axis. Kirk et al. (2008) reported that the direct measurements of the fiducial marks were made with a nominal precision of 0.1 µm. The pixel spacing is 12 µm in both the line and sample directions, which are assumed to be perpendicular. Based on the calibrated focal length, the coefficients to the optic axis of the camera that translate line and sample coordinates to into the focal plane coordinates are adjusted by 5 mm. These coefficients are shown in Table 2.2.

CCD	x_0 (mm)	dx/ds (mm)	dx/dl (mm)	y_0 (mm)	dy/ds (mm)	dy/dl (mm)
0	-96.3935	0.012	-0.000057	112.9956	-0.012	-0.000057
1	-89.4914	0.012	-0.000042	88.9950	-0.012	-0.000042
2	-96.9459	0.012	-0.000034	65.0469	-0.012	-0.000034
3	-89.4927	0.012	-0.000018	41.0380	-0.012	-0.000018
4	-96.4998	0.012	0.000002	16.9992	-0.012	0.000002
5	-89.4960	0.012	-0.000001	-7.0010	-0.012	-0.000001
6	-96.6811	0.012	0.000019	-30.9996	-0.012	0.000019
7	-89.4935	0.012	0.000031	-55.0034	-0.012	0.000031
8	-96.3954	0.012	0.000049	-78.9990	-0.012	0.000049
9	-89.1039	0.012	0.000056	-102.9997	-0.012	0.000056
10	-110.9610	0.012	0.000000	16.9991	-0.012	0.000000
11	-103.6857	0.012	-0.000001	-7.0010	-0.012	-0.000001
12	-82.2033	0.012	0.000002	16.9993	-0.012	0.000002
13	-74.9334	0.012	0.000003	-7.0007	-0.012	0.000003

Table 2.2 HiRISE focal plane assembly coordinates (Kirk et al., 2008)

In the raw image, the row position of each pixel is related to the ephemeris time, which then determines the position and orientation of the HiRISE frame. The CCD center and the column position are used to calculate the physical position of each pixel in the HiRISE frame. Using the sample and line coordinates calculated from the Equation 2.1a and 2.1b, the following equations can be used to retrieve the focal plane coordinates.

$$x = x_0 + \left(\frac{dx}{ds}\right) s + \left(\frac{dx}{dl}\right) l \tag{2.2a}$$

$$y = y_0 + \left(\frac{dy}{ds}\right) s + \left(\frac{dy}{dl}\right) l \tag{2.2b}$$

where (x, y) is the image coordinates in the HiRISE focal plane in millimeter, (x_0, y_0) is the CCD center coordinates, and dx/ds, dx/dl, dy/ds, dy/dl are Affine transformation coefficients for converting CCD pixel coordinate to the focal plane coordinates.

Finally, ideal focal plane coordinates (x_p, y_p) are obtained using the calibrated radial lens distortion parameters to remove systematic optical distortion.

$$r = (x^2 + y^2)^{\frac{1}{2}} \tag{2.3a}$$

$$\frac{dr}{r} = k_0 + k_1 \cdot r^2 + k_2 \cdot r^4 \tag{2.3b}$$

$$x_p = x - \left(\frac{dr}{r}\right) \cdot x \tag{2.3c}$$

$$y_p = y - \left(\frac{dr}{r}\right) \cdot y \tag{2.3d}$$

where r is the distance from the HiRISE principal point to the image coordinates, k_0, k_1 and k_2 are radial lens distortion parameters (Kirk et al., 2008).

2.3 Exterior Orientation of HiRISE Imagery

Exterior orientation parameters, or the positions of the camera perspective center and pointing angles at a specific time, are provided in the SPICE kernels. The exterior orientation parameters of each image line can be retrieved by interpolating the spacecraft's trajectory and pointing vectors based on the observation time. The observation time of each image line is defined as the exposure time of the center of the TDI block, which can be calculated by the starting time (the exposure time of the first line) of the CCD and the line rate (the speed of line movement). Since each CCD is operated separately, the starting time differs from CCD to CCD. On the other hand, because all CCDs are fixed to the HiRISE focal plane, the line rate is same for every CCD. In order to retrieve exterior orientation parameters for a specific CCD image, the observation time is plugged into the SPICE kernel for interpolation. HiRISE CCDs have different observation time for each line, and as a result, different exterior orientation parameters values. However, they will all share the same exterior orientation parameters at any one moment in time. This significant characteristic makes it possible to uniformly model exterior orientation parameters that can be applied to different CCDs. Thus, images simultaneously acquired by multiple CCD arrays can be processed together under one rigorous sensor model in the bundle adjustment instead of being processed strip by strip separately.

CCD	UTC (second)	ET (second)	DLINE	BIN	TDI	LINE
0	2006-11-22T08:35:24.708	217456589.891075	167	1	128	80000
1	2006-11-22T08:35:24.660	217456589.842522	167	1	128	80000
2	2006-11-22T08:35:24.712	217456589.895043	167	1	128	80000
3	2006-11-22T08:35:24.660	217456589.842522	167	1	128	80000
4	2006-11-22T08:35:24.709	217456589.891747	167	1	128	80000
5	2006-11-22T08:35:24.660	217456589.842522	167	1	128	80000
6	2006-11-22T08:35:24.710	217456589.893013	167	1	128	80000
7	2006-11-22T08:35:24.660	217456589.842522	167	1	128	80000
8	2006-11-22T08:35:24.708	217456589.891075	167	1	128	80000
9	2006-11-22T08:35:24.657	217456589.839821	167	1	128	80000
10	2006-11-22T08:35:24.828	217456590.010384	167	2	128	40000
11	2006-11-22T08:35:24.776	217456589.959206	167	2	128	40000
12	2006-11-22T08:35:24.625	217456589.808067	167	2	128	40000
13	2006-11-22T08:35:24.600	217456589.782570	167	4	32	20000

Table 2.3 Image starting time of HiRISE image PSP_001513_1655 for each CCD

Table 2.3 is the example of image starting time from the HiRISE image PSP_001513_1655 obtained from Experiment Data Record (EDR) provided by the HiRISE Science team. An EDR contains raw image data, observational-related engineering data and information about the instrument commanding parameters used to acquire the image. Based on the image acquisition time, exterior orientation parameters are derived from the SPICE kernels (http://naif.jpl.nasa.gov).

In SPICE kernel, various types of time systems are used. Coordinated universal time (UTC), formerly known as Greenwich Mean Time (GMT), is the basis for the worldwide system of civil time. UTC second is defined in terms of an atomic transition of the element cesium under specific conditions, and is not directly related to any astronomical phenomena. Ephemeris Time (ET), also referred to as Barycentric Dynamical Time, is the time standard used to take account of time dilation when calculating orbits of planets, asteroids, comets and interplanetary spacecraft in the Solar system. It is expressed as a double precision number containing the number of ephemeris seconds past J2000 (noon on January 1, 2000). Ephemeris second corresponded to 9,192,631,770 cycles of the caesium resonance. As can be seen in the arrangement of the HiRISE focal plane assembly (Figure 2.3), odd-numbered CCDs are approximately 7 mm forward from even-numbered CCDs in the flight direction. To compensate this displacement, odd-numbered CCDs start scanning about 0.05 seconds earlier than the CCDs behind them.

To apply the above strategy, one reference CCD strip must be assigned; this strip can be arbitrarily chosen. However, CCD 1, 3, 5 and 7 almost always share the same starting time, and CCD 4 and 5 are placed in the middle of the focal plane assembly between CCD 10, 11, 12 and 13. Considering these factors, CCD 5 is the most preferable choice as a reference CCD. The remaining CCD strips are registered to the reference strip based on the exposure time, which is linearly proportional to the image line (row) index and the line rate. The pixel line time is set to match the ground velocity so that charge from one image region is sequentially clocked into the next corresponding element in the along-track direction. HiRISE uses additional TDI line delay time, specified in HiRISE header as DLINE to adjust the line rate. The ephemeris time of each line is also based on the number of TDI stage and the binning mode as follows.

$$LR = (74 + DLINE/16) \cdot 10^{-6} \tag{2.4a}$$

$$ET_1 = ET_0 - LR \cdot (TDI/2 - 0.5) + LR \cdot (BIN/2 - 0.5) \tag{2.4b}$$

$$ET_n = ET_1 + n \cdot LR \cdot BIN \tag{2.4c}$$

where *LR* is the line rate, *DLINE* is the additional TDI line delay time. ET_0 is the image starting time of the first image line, which is actually the last line of the TDI block. Since the exposure time is defined as the center of the TDI block, the actual ephemeris time of the first image line, ET_1, is obtained by subtracting half the period of the TDI block (second term in Equation 2.4b) and also by adjusting the binning (third term in Equation 2.4b). ET_n is the ephemeris time of the nth line.

Previous research showed that the change in exterior orientation parameters over relatively short trajectories can be modeled using polynomials (Yoon and Shan 2005; Li et al., 2007, 2008). The spacecraft position is stored in SPICE SPK kernel, and the rotation angles are in CK kernel. SPK kernel handles position and velocity of one object relative to another in pieces called segments. A segment represents some arc of the full trajectory of an object. The standard CK kernel is generated by onboard synthesis of data from gyroscopes and star-tracker cameras in sampling interval of 0.1 seconds, or about 1,000 image lines. The pointing angles obtained from the CK data have rather coarse resolution of 35 μrad (Kirk, et al., 2008). In HiRISE, 1 μrad of rotation angle is equivalent to approximately 1 pixel in image space. Overall, the exterior orientation parameters for HiRISE are interpolated from trajectory data not sampled frequently enough nor precise. Therefore, using polynomial functions to model the exterior orientation parameters, instead of the recorded trajectory, would not lead to loss of precision. In practice, second-order polynomials can represent most of the movement in terms of the orbiter trajectory and the pointing direction. Using higher order polynomial functions would increase the ability to model more detailed movement. However, the movement controlled by the terms with orders higher than three have such small magnitude that it is almost negligible. Therefore, in this research, third-order polynomials are used to model the exterior orientation parameters as in Equation 2.5 (Li et al., 2008b).

$$
\begin{aligned}
X_t^c &= a_0 + a_1 t + a_2 t^2 + a_3 t^3 \\
Y_t^c &= b_0 + b_1 t + b_2 t^2 + b_3 t^3 \\
Z_t^c &= c_0 + c_1 t + c_2 t^2 + c_3 t^3 \\
\omega_t &= d_0 + d_1 t + d_2 t^2 + d_3 t^3 \\
\varphi_{\mathrm{t}} &= e_0 + e_1 t + e_2 t^2 + e_3 t^3 \\
\kappa_{\mathrm{t}} &= f_0 + f_1 t + f_2 t^2 + f_3 t^3
\end{aligned}
\tag{2.5}
$$

where X_t^c, Y_t^c, Z_t^c are the coordinates of the perspective centers of the optical system at time *t* in Mars body-fixed frame, ω_t , φ_t , κ_t are the pointing angles at time *t* about the coordinate axes of X, Y, and Z of Mars body-fixed frame, $a_0, \ldots, f_4$ are the polynomial coefficients, and t is the time-dependent image line index number.

The differences between the exterior orientation parameters of the original telemetry from SPICE kernel and the product of the polynomial function from Equation 2.5 can be calculated based on the relations in Equation 2.6.

$$
\begin{aligned}
X_t^{tel} &= X_t^{c} + \nu_{X_t^c} \\
Y_t^{tel} &= Y_t^{c} + \nu_{Y_t^c} \\
Z_t^{tel} &= Z_t^{c} + \nu_{Z_t^c} \\
\omega_t^{tel} &= \omega_t + \nu_{\omega_t} \\
\varphi_t^{tel} &= \varphi_t + \nu_{\varphi_t} \\
\kappa_t^{tel} &= \kappa_t + \nu_{\kappa_t}
\end{aligned}
\tag{2.6}
$$

where X_t^{tel}, Y_t^{tel}, Z_t^{tel}, ω_t^{tel}, φ_t^{tel}, κ_t^{tel} are the telemetry exterior orientation parameters and ν_{X_t}, ν_{Y_t}, ν_{Z_t}, ν_{ω_t}, ν_{φ_t}, ν_{κ_t} are their respective residuals after polynomial fitting.

The third order polynomial fitting of exterior orientation parameters were conducted for three images. The positional residuals of PSP_001513_1655 image are plotted in Figure 2.5. The third order polynomial model can model the trajectory very well with the magnitude of the residuals less than 0.1 mm.

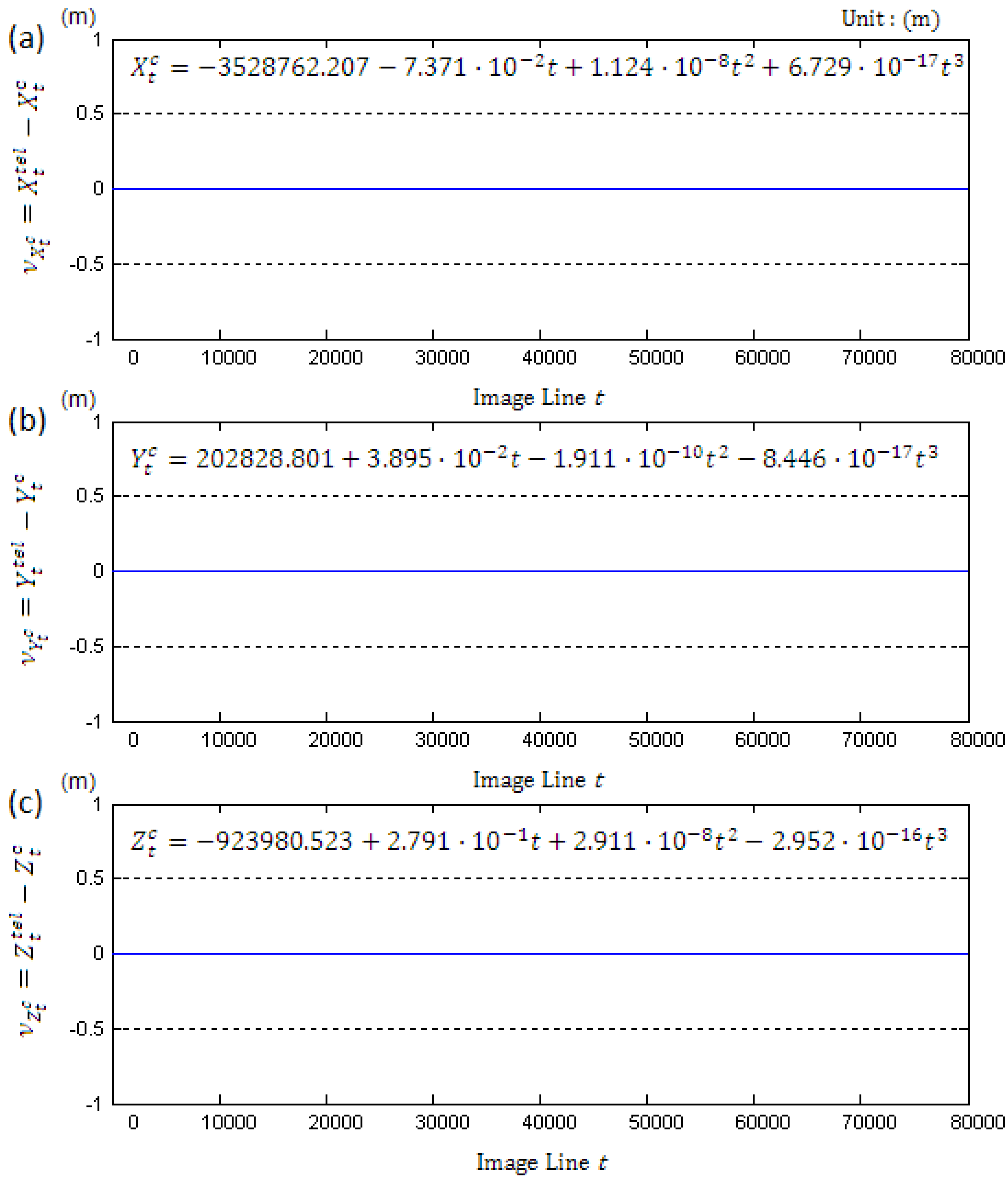

Figure 2.5 Differences between orbiter position from telemetry exterior orientation parameters and calculated position from 3rd-order polynomial fitting for image PSP_001513_1655: residuals in (a) X axis, (b) Y axis, (c) Z axis.

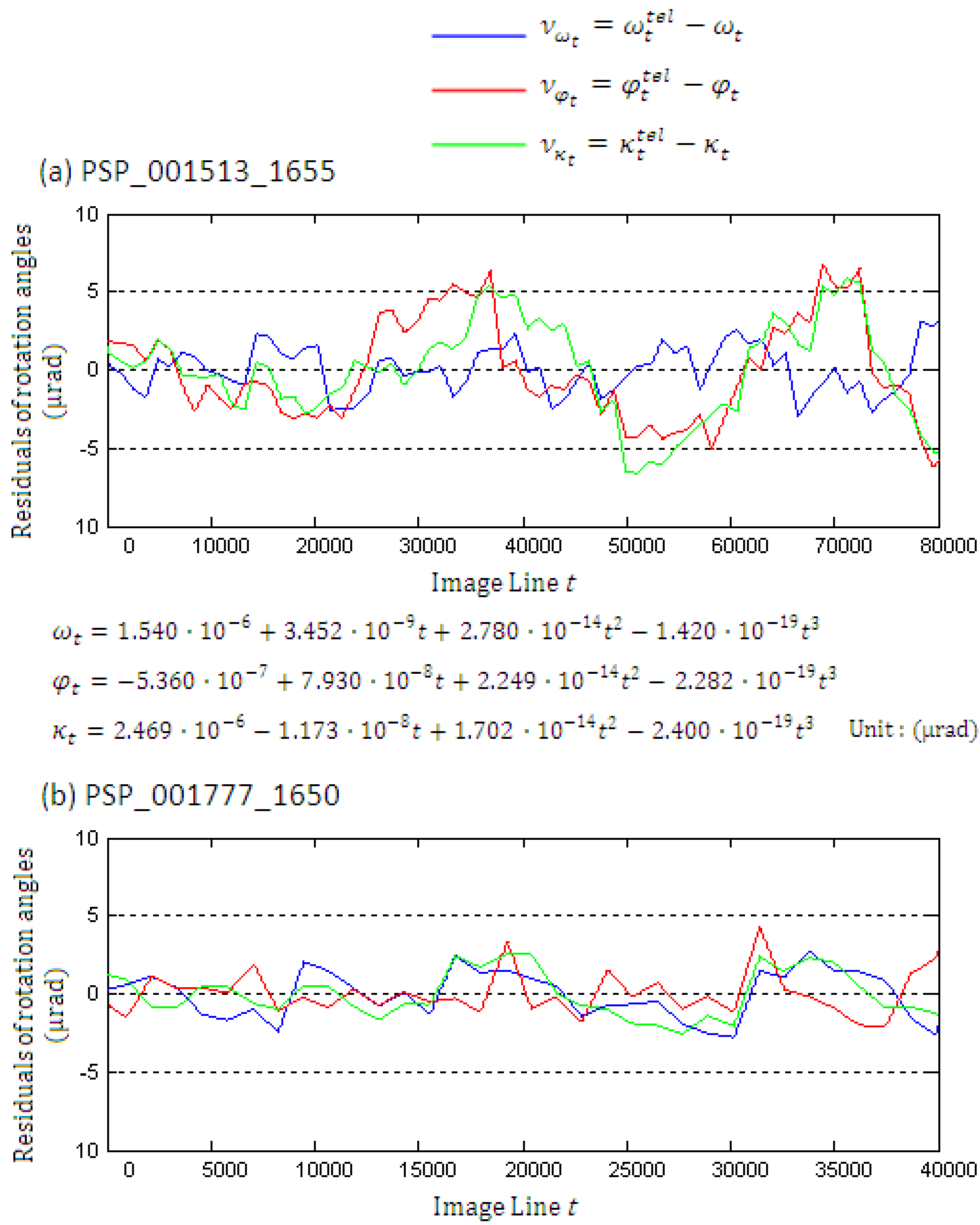

$\nu_{\omega_t} = \omega_t^{tel} - \omega_t$

$\nu_{\varphi_t} = \varphi_t^{tel} - \varphi_t$

$\nu_{\kappa_t} = \kappa_t^{tel} - \kappa_t$

(a) PSP_001513_1655

$\omega_t = 1.540 \cdot 10^{-6} + 3.452 \cdot 10^{-9} t + 2.780 \cdot 10^{-14} t^2 - 1.420 \cdot 10^{-19} t^3$

$\varphi_t = -5.360 \cdot 10^{-7} + 7.930 \cdot 10^{-8} t + 2.249 \cdot 10^{-14} t^2 - 2.282 \cdot 10^{-19} t^3$

$\kappa_t = 2.469 \cdot 10^{-6} - 1.173 \cdot 10^{-8} t + 1.702 \cdot 10^{-14} t^2 - 2.400 \cdot 10^{-19} t^3$ Unit: (μrad)

(b) PSP_001777_1650

$\omega_t = 8.880 \cdot 10^{-7} + 5.255 \cdot 10^{-9} t - 1.547 \cdot 10^{-14} t^2 + 3.397 \cdot 10^{-19} t^3$

$\varphi_t = -3.850 \cdot 10^{-6} + 7.838 \cdot 10^{-8} t - 5.880 \cdot 10^{-14} t^2 + 8.678 \cdot 10^{-19} t^3$

$\kappa_t = 7.326 \cdot 10^{-6} - 9.634 \cdot 10^{-9} t - 1.122 \cdot 10^{-14} t^2 + 1.148 \cdot 10^{-19} t^3$ Unit: (μrad)

Figure 2.6 Differences of orientation angles between telemetry exterior orientation parameters and 3rd-order polynomial fitting result from images a) PSP_001513_1655, (b) PSP_001777_1650, and (c) PSP_007124_1765 (continued)

(continued)

(c) PSP_007124_1765

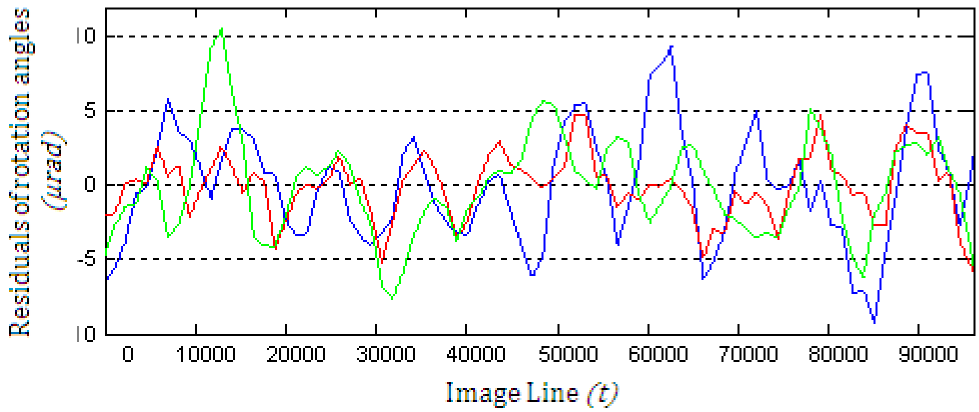

$$\omega_t = -1.806 \cdot 10^{-7} - 1.012 \cdot 10^{-8} t - 1.768 \cdot 10^{-14} t^2 + 1.997 \cdot 10^{-19} t^3$$

$$\varphi_t = -4.311 \cdot 10^{-5} - 7.912 \cdot 10^{-8} t - 2.211 \cdot 10^{-15} t^2 + 4.782 \cdot 10^{-20} t^3$$

$$\kappa_t = -6.191 \cdot 10^{-6} - 8.913 \cdot 10^{-9} t - 1.253 \cdot 10^{-14} t^2 + 8.914 \cdot 10^{-20} t^3 \;\; \text{Unit: } (\mu\text{rad})$$

Figure 2.6 shows the differences of the orientation angles between the telemetry data and the 3-rd order polynomial fitting result for three images, PSP_001513_1655, PSP_001777_1650 and PSP_007124_1765. The residuals for the image pointing parameters in PSP_001513_1655 (Figure 2.6a) are in the magnitude of ±5 μrad. During the 80000-line interval, the maximum differences can be more than 10 μrad, which is equivalent to about 10 pixels in the image space. On the ground, depending on the pixel resolution, 10 μrad equals to about 2.5 to 3 m. The similar variation can be found in other images as well: Figure 2.6b for PSP_001777_1650, and Figure 2.6c for PSP_007124_1765. The residuals of the pointing angles increase in images with more lines. Even for shorter images such as PSP_001777_1650 with 40000 image line, the magnitudes are about ±5 µrad, which translates to about five pixels in image space. This amount is certainly not negligible in high resolution image processing. It indicates that unlike the orbiter position, the image pointing parameters are not completely modeled by the polynomials. Considering the coarse sampling interval (0.1 second) and poor precision (35 µrad) of the initial orientation angles (Kirk et al., 2008), however, the residuals of the third order polynomial model are within reasonable range. In other words, the residuals are not necessarily a non-polynomial pattern, but rather random sampling errors caused by lack of precision.

These residuals may signify the existence of jitter effect, which was also identified in the MOC images, and was also found in HiRISE imagery (Kirk et al., 2007). Jitter is high frequency random patterns that cannot be modeled by, for example, polynomials. The causes of jitter include spacecraft vibrations associated with solar panels or a particular instrument, thermal changes and others. HiRISE stereo observations are usually obtained in high-stability mode by temporarily halting the main sources of spacecraft vibration. In this case, the effects of unexpected motions are at most 1 to 2 pixels with small oscillations of less than 1 pixel in amplitude. However, HiRISE images acquired when other instruments was turned on, showed severe image distortions and blur (Kirk et al., 2008).

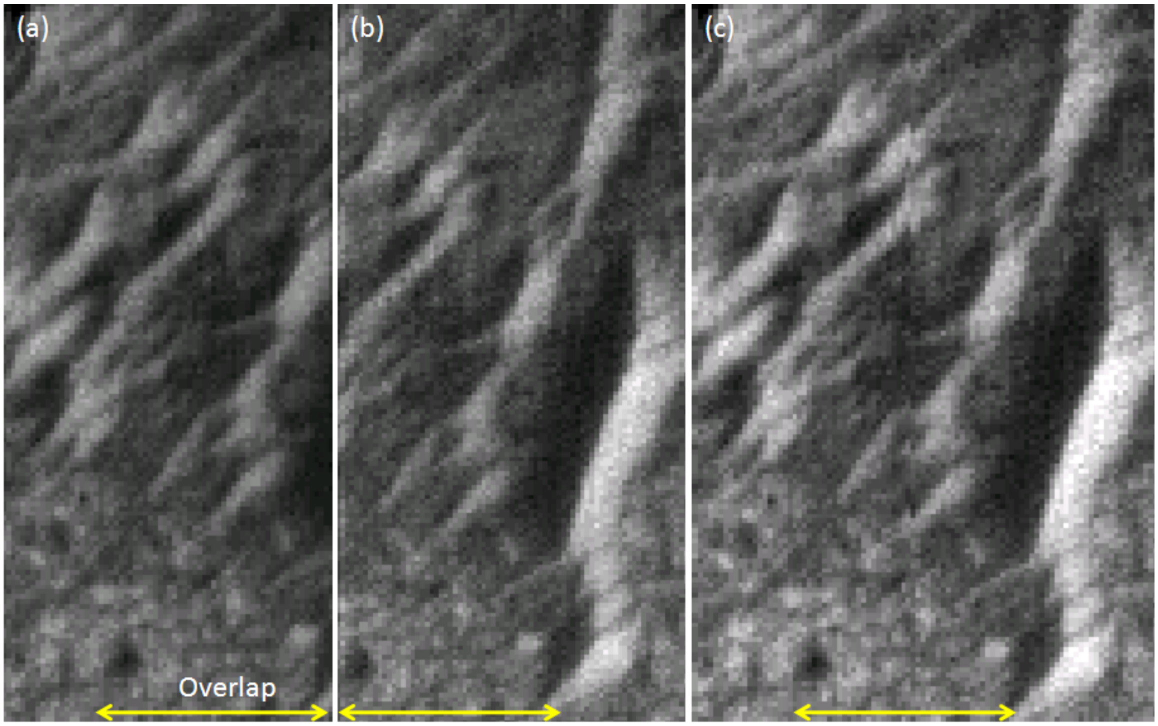

Figure 2.7 Jitter effect shown in PSP_007124_1765. a) Subset of CCD4, b) subset of CCD5, c) image mosaic based on the mean offset between CCD4 and CCD5 images

Figure 2.7 shows the PSP_007124_1765 images, which exhibit noticeable jitter effect. Figure 2.7a and 2.7b are CCD4 and CCD5 images, which share about 48 pixels in the cross-track direction. Figure 2.7c is the image mosaic of the CCD4 and CCD5. In the center, where the boundaries of the two adjacent CCDs are met, there are distinguishable discrepancies of the ground features (Mattson et al., 2009). The image mosaic shown in Figure 2.7c is an overlay of adjacent CCD images based on the mean offset between them. The offset is basically the differences of image coordinates of tie points between adjacent CCDs from matched features in the overlap area.

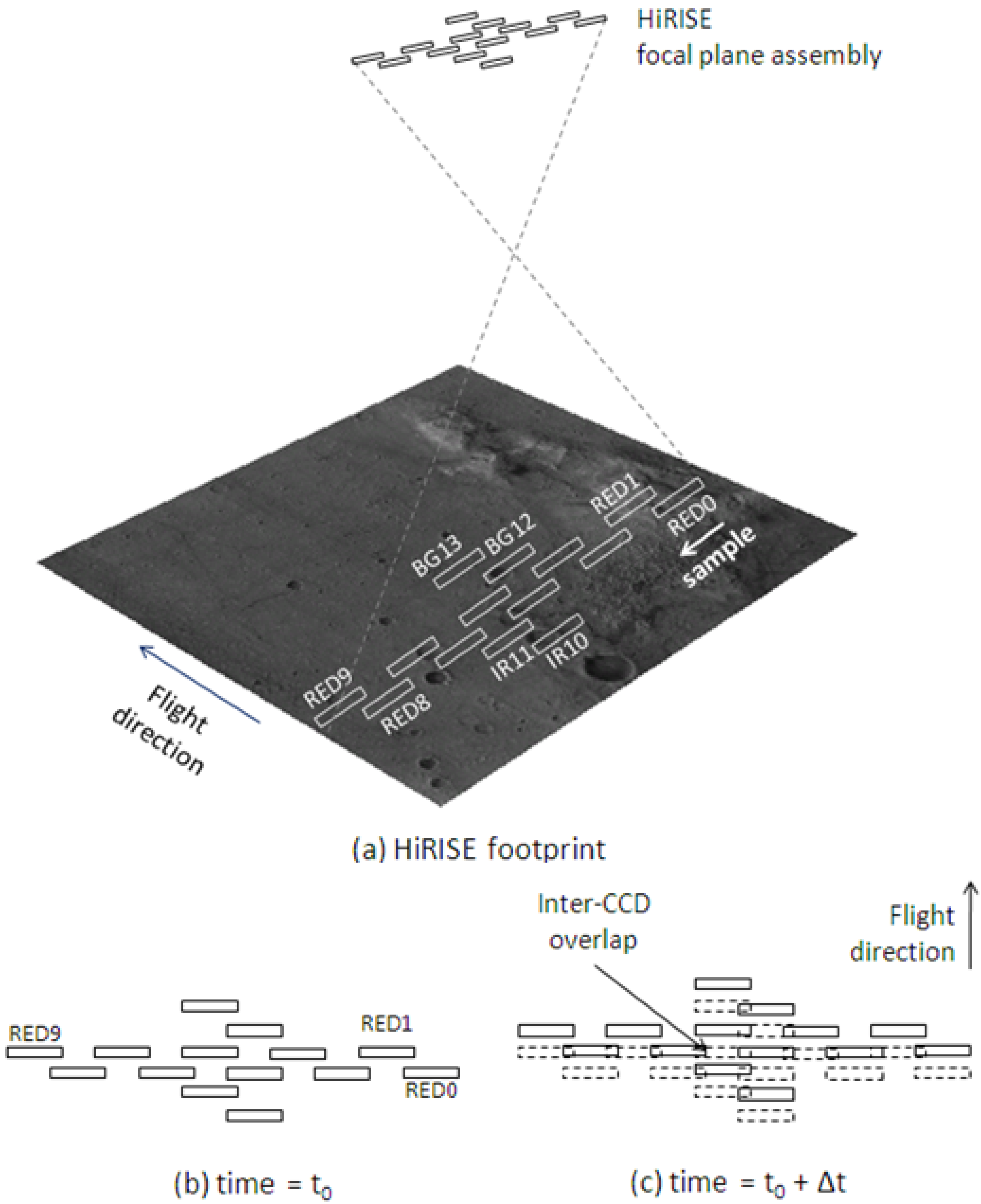

Figure 2.8 Illustration of jitter observation

Not only does the effect of orbital jitter need to be evaluated for topographic mapping capability analysis of the HiRISE camera, but also it should be considered in the sensor model in order to achieve the highest mapping accuracy. Although the angular resolution and sampling interval in SPICE dataset are not precise or dense enough to fully model the jitter movement, the unique design of HiRISE CCD arrangement allows us the glimpse of its effect. As mentioned in Section 2.2, adjacent HiRISE CCDs have about 48 pixels of overlap in the across-track direction and about 7 mm of offset in the along-track direction. Figure 2.8 illustrates how spacecraft jitter can be observed by the inter-CCD overlap.

Figure 2.8a is the footprint of each CCD overlaid on a Martian terrain. Since HiRISE is a push-broom scanner, the footprints swipe through the terrain in the direction of flight. Due to the relative displacement of CCDs in the focal plane assembly, the footprint of RED1 CCD lies ahead of the footprint of RED0 CCD. This creates multiple observation of the same object with adjacent CCDs at different times. Figure 2.8b is the footprint at time t_0, and 2.8c is the footprint at time $t_0+\Delta t$, when the inter-CCD overlap of adjacent CCDs hit the same ground observed at time t_0. The typical time interval between RED CCDs are about 0.05 seconds, which is equivalent to about 550 lines, depending on line rate. In the ideal case, the orbiter would move in constant speed without changing orientation angles. Then the image space coordinates of the same objects in the overlapping CCDs should maintain constant offset. However, due to the irregular movement of the orbiter, the offsets change slightly over time or from line to line. Figure 2.9 shows the offsets in sample direction between adjacent CCDs for the three test images, PSP_001513_1655 (Figure 2.9a), PSP_001777_1650 (Figure 2.9b) and PSP_007124_1765 (Figure 2.9c). Likewise, the offsets in line direction are plotted in Figure 2.10.

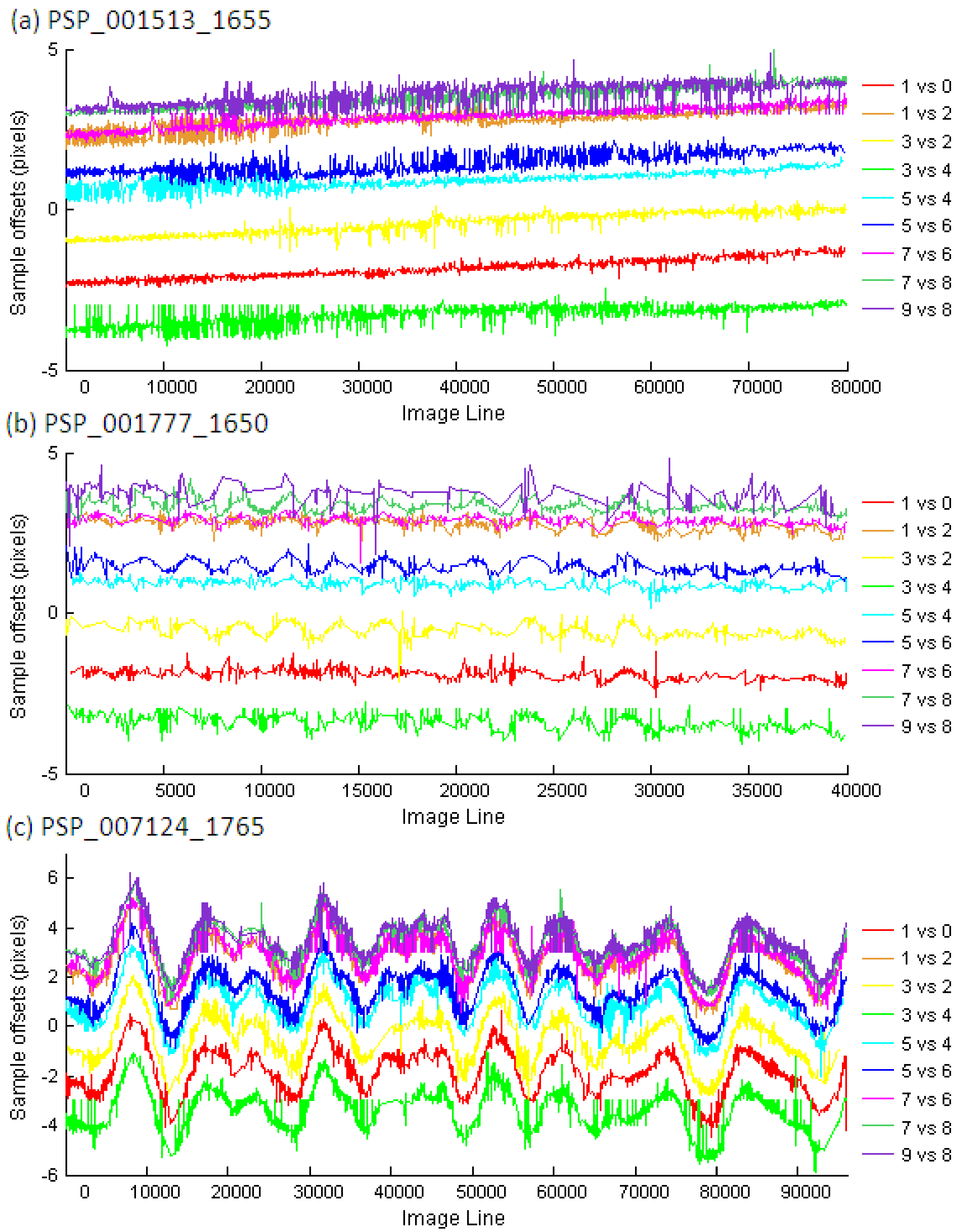

Figure 2.9 Image pixel offsets in sample direction between overlapping RED CCDs

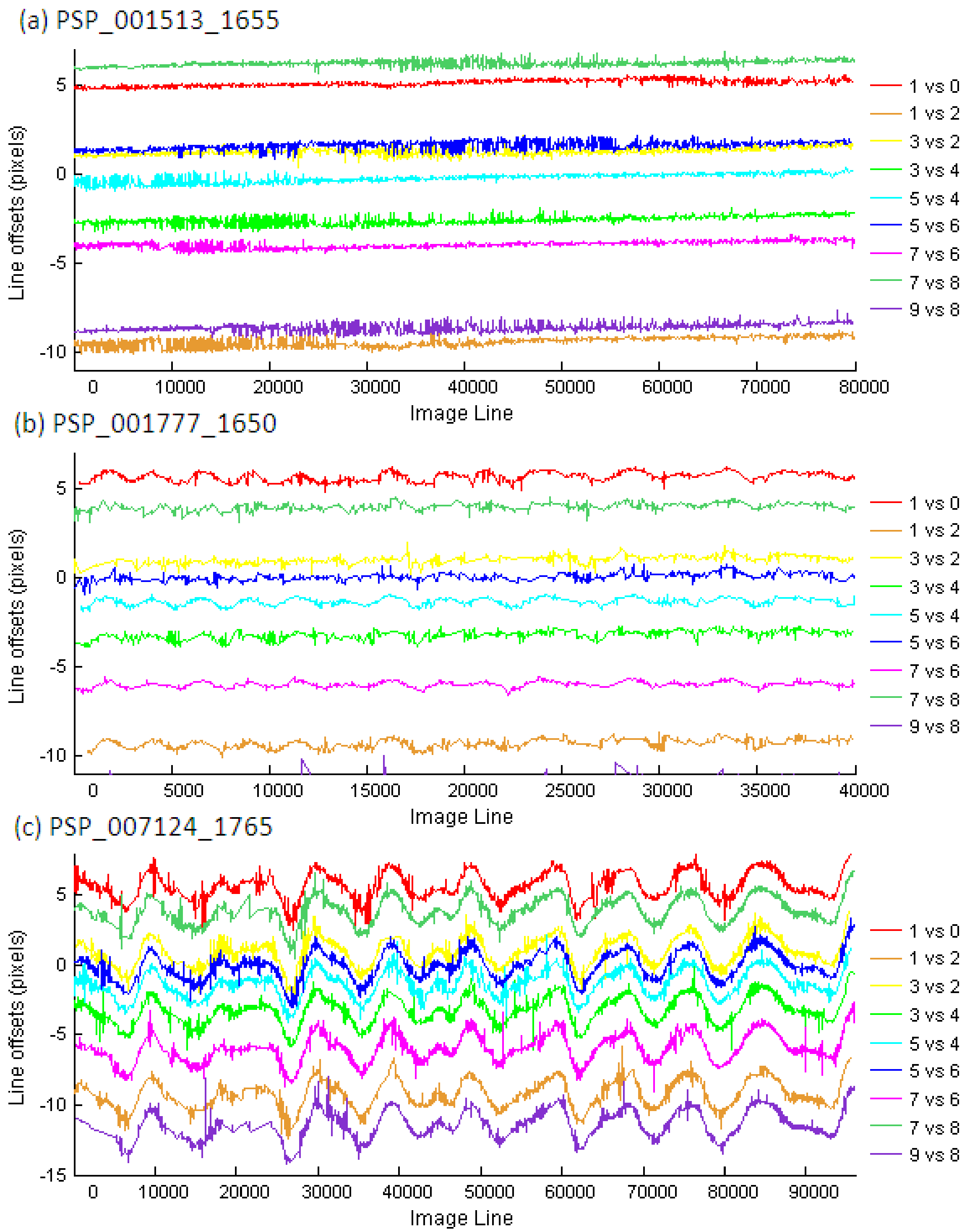

Figure 2.10 Image pixel offsets in line direction between overlapping RED CCDs

The offsets between pixel coordinates of overlapping CCDs are a manifestation of the random movement of the orientation angles, which is shared by the entire focal plane assembly at the same time. Therefore, these offsets are dependent on time or image line in linear scanner like HiRISE. Over image lines, both PSP_001513_1655 and PSP_001777_1650 demonstrate little variation of offsets. The offsets are almost constant, mostly within than 1 pixel from the mean offset and not exceeding 2 pixels in the maximum difference. They are good examples of highly stable image acquisition of HiRISE. On the other hand, PSP_007124_1765 exhibits a severe jitter effect in the magnitude of three to four pixels in the short interval of 10,000 lines, and even reaching several pixels over the course of the entire image lines.

In particular, PSP_007124_1765 image clearly demonstrates how the trends of image pixel offset along the image line are similar to each other. For all three cases, the standard deviation of the offsets from the average fitted curve was about 0.1 pixels. The resemblance of the trend confirms that the offsets are the manifestation of jitter movement, which applies same rotation angles to the entire CCD plane as a function of time.

The HiRISE operations team is working on modeling of the jitter motion and implementation of a solution to adjust the rotation angles to produce with minimal geometric distortions (Mattson et al., 2009). This processing pipeline, named as HiRISE Jitter-Analyzed CK (HiJACK), consists of three steps: interpreting jitter movement in terms of camera pointing angles, incorporating the new pointing data with the existing pointing angles, and resampling the images. The jitter effect is also present in the the Lunar Reconnaissance Orbiter Camera Narrow Angle Camera (LROC-NAC) currently flying onboard the Lunar Reconnaissance Orbiter (LRO). The LRO operation team consisted of the University of Arizona, the USGS, and the Ohio State University, which is working on characterizing and correcting the spacecraft jitter (Mattson et al., 2010)

Image Id	PSP_001513_1655	PSP_001777_1650	PSP_007124_1765
Number of Lines	80000	40000	96000
Rotation Angles	Polynomial Fitting Residuals mean/standard deviation (μrad)		
Roll	0.00/1.36	0.00/1.38	0.00/3.66
Pitch	0.00/3.10	0.00/1.11	0.00/2.03
Yaw	0.00/2.99	0.00/1.39	0.00/3.24
CCD Combination	Sample Offset mean/standard deviation (pixel)		
CCD1 vs. CCD0	-1.88/0.28	-1.91/0.17	-1.75/0.84
CCD1 vs. CCD2	2.74/0.29	2.78/0.17	2.76/0.89
CCD3 vs. CCD2	-0.47/0.33	-0.54/0.22	-0.51/0.95
CCD3 vs. CCD4	-3.28/0.28	-3.38/0.23	-3.36/0.83
CCD5 vs. CCD4	0.91/0.24	0.91/0.14	0.89/0.90
CCD5 vs. CCD6	1.38/0.31	1.44/0.19	1.40/0.90
CCD7 vs. CCD6	2.83/0.30	2.90/0.14	2.79/0.86
CCD7 vs. CCD8	3.46/0.32	3.31/0.17	3.34/0.81
CCD9 vs. CCD8	3.56/0.33	3.71/0.36	3.47/0.82
CCD Combination	Line Offset mean/standard deviation (pixel)		
CCD1 vs. CCD0	5.08/0.18	5.66/0.25	5.76/0.98
CCD1 vs. CCD2	-9.54/0.24	-9.23/0.24	-9.29/1.00
CCD3 vs. CCD2	1.22/0.17	0.97/0.23	0.96/1.01
CCD3 vs. CCD4	-2.59/0.22	-3.25/0.26	-3.26/0.95
CCD5 vs. CCD4	-0.23/0.23	-1.39/0.20	-1.35/0.94
CCD5 vs. CCD6	1.58/0.21	0.02/0.21	-0.03/1.02
CCD7 vs. CCD6	-3.99/0.18	-5.99/0.16	-5.92/1.04
CCD7 vs. CCD8	6.19/0.14	3.97/0.18	3.95/1.01
CCD9 vs. CCD8	-8.63/0.19	-11.68/0.34	-11.35/1.03

Table 2.4 Jitter analysis: Polynomial fitting residuals of the spacecraft pointing angles and offsets of image coordinates of the overlapping CCDs

Table 2.4 shows the statistics of the jitter analysis in the three test images, including the residuals of rotation angle after 3-rd order polynomial fitting and the distribution of such offsets in sample and line directions. Overall, the standard deviations of the rotation angle residuals were similar in all three cases. PSP_001777_1650 had the smallest deviation, followed by PSP_001513_1655 and PSP_007124_1765. The magnitudes of standard deviations in sample and line offsets are in the same order. The residuals of both polynomial fitting residuals and offsets in PSP_001513_1655 were only slightly more than those of PSP_001777_1650, in spite of the number of lines being twice as many. In both images, the standard deviations of offsets were less than 0.5 pixels. This indicates the lack of significant jitter movement in the PSP_001513_1655 and PSP_001777_1650. The offsets in image PSP_007124_1765, a severe case of jitter, showed standard deviation of about one pixel, which is almost three times higher than the previous two images.

The mean offsets are caused by the relative displacement of the adjacent CCDs. Since the relative position of the CCDs is fixed on the HiRISE focal plane, they should be constant in the ideal situation every image. Overall, they have similar values for all three images, especially in sample direction. In the line direction, some of the mean offsets in PSP_001513_1655 are about a few pixels different than those of PSP_001777_1650 and PSP_007124_1765. This may be caused by differences in the readout time gap between CCDs.

Most HiRISE images for topographic mapping products are acquired in high-stability mode. Their jitter effects resemble those of PSP_001513_1655 and PSP_001777_1650. This research focuses on such stable images for rigorous photogrammetric processing. In this case, it is unlikely to find significant jitter effect demonstrated by visible gaps in image mosaic as in Figure 2.7c.

In this chapter, the rigorous HiRISE sensor model is presented in detail, including interior and exterior orientation parameters. The geometric model serves as a basis for the photogrammetric processing of the HiRISE imagery including bundle adjustment and generation of high-accuracy topographic products. The jitter movement in the camera pointing angle is analyzed in the form of relative displacements between the CCDs, which affects the quality of the topographic products. By applying the rigorous sensor model described in this chapter, the effect of the disagreement between the CCDs will be reduced by the bundle adjustment (Chapter 3).

CHAPTER 3

PHOTOGRAMMETRIC PROCESSING OF HIRISE STEREO IMAGES

This chapter describes the photogrammetric processing of HiRISE stereo images including image pre-processing, stereo matching and bundle adjustment. The photogrammetric process is performed to create orbital image networks, the set of orbital imagery connected by tie points and bundle-adjusted exterior orientation parameters. An automatic image matching method is implemented to produce tie points from stereo images. This method uses a coarse-to-fine hierarchical approach of interest point matching and dense grid point matching for topographic products generation. Bundle adjustment, based on polynomial function model, was conducted to improve the accuracy of the exterior orientation parameters and achieve coherence between stereo images. In addition to traditional tie points, inter-CCD tie points between multiple CCDs in a single orbit are used to minimize geometric inconsistencies between HiRISE CCDs. To achieve accurate geopositioning without ground-control points, HiRISE DTM is matched with MOLA MEDGR DTM and PEDR profile after bundle adjustment. Based on the terrain matching results, the position of the HiRISE orbital image network is shifted to ensure consistency with MOLA, the best global Mars terrain model available.

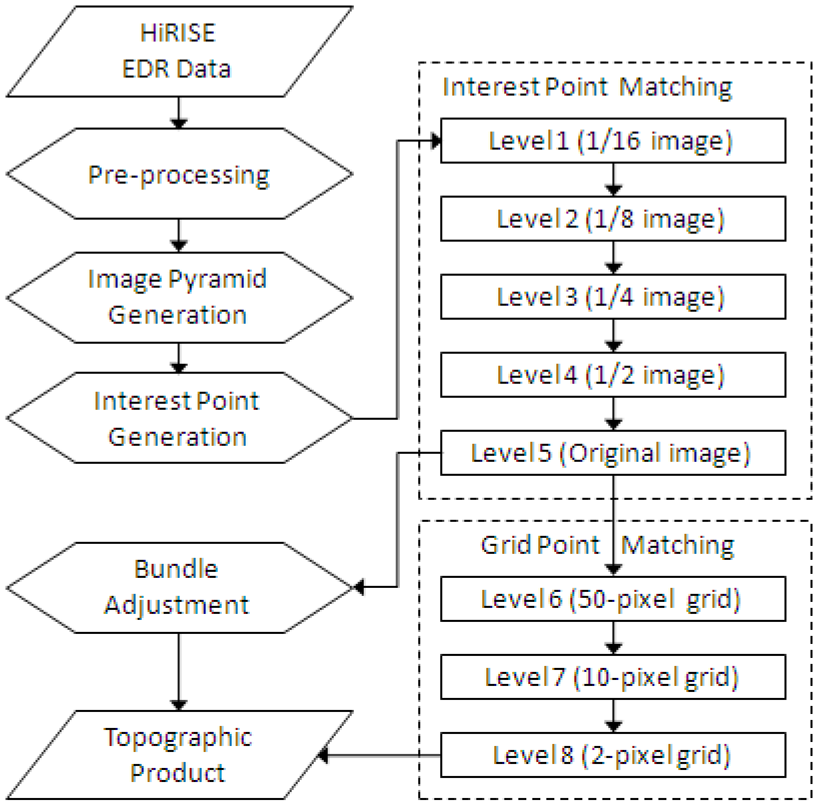

Figure 3.1 Flowchart of the hierarchical stereo matching process

Figure 3.1 shows the overall process of the hierarchical stereo matching. The process starts with the raw dataset (EDR). The pre-processing of the raw images involves radiometric correction, image pyramid construction, and interest point generation. HiRISE stereo matching consists of multiple levels of hierarchical matching: interest point matching from low to high resolution images and grid point matching from coarse to dense grid. After dense grid matching, topographic mapping products are generated.

3.1 Image Pre-Processing and Interest Point Generation

Raw HiRISE images contain systematic noise such as offset in the image data numbers, dark current and column-to-column gain variations (Becker et al., 2007). In HiRISE EDR data sets, the image acquired by each CCD strip (14 in total) is stored as two sub-image strips, each of which is 1024 pixels wide. Brightness values of the two sub-image strips may be inconsistent. The data can be compressed from 14 to 8 bits using piecewise linear mapping via look-up tables (LUTs). Since the mapping used for HiRISE data compression is overall linear, the 8-bit EDR dataset can be directly used for further image processing. The pre-processing of raw image begins with adjusting brightness values of sub-image strips and then combining them together into one seamless image with a 2,048-pixel wide swath. Then radiometric enhancement is conducted to improve the contrast of the images using a linear stretch method (Richards and Jia, 2006). There are also inconsistencies in the signal strength between the across-track CCD arrays, which create dark currents or strip noises at particular columns. Such systematic noise is also removed in the pre-processing stage.

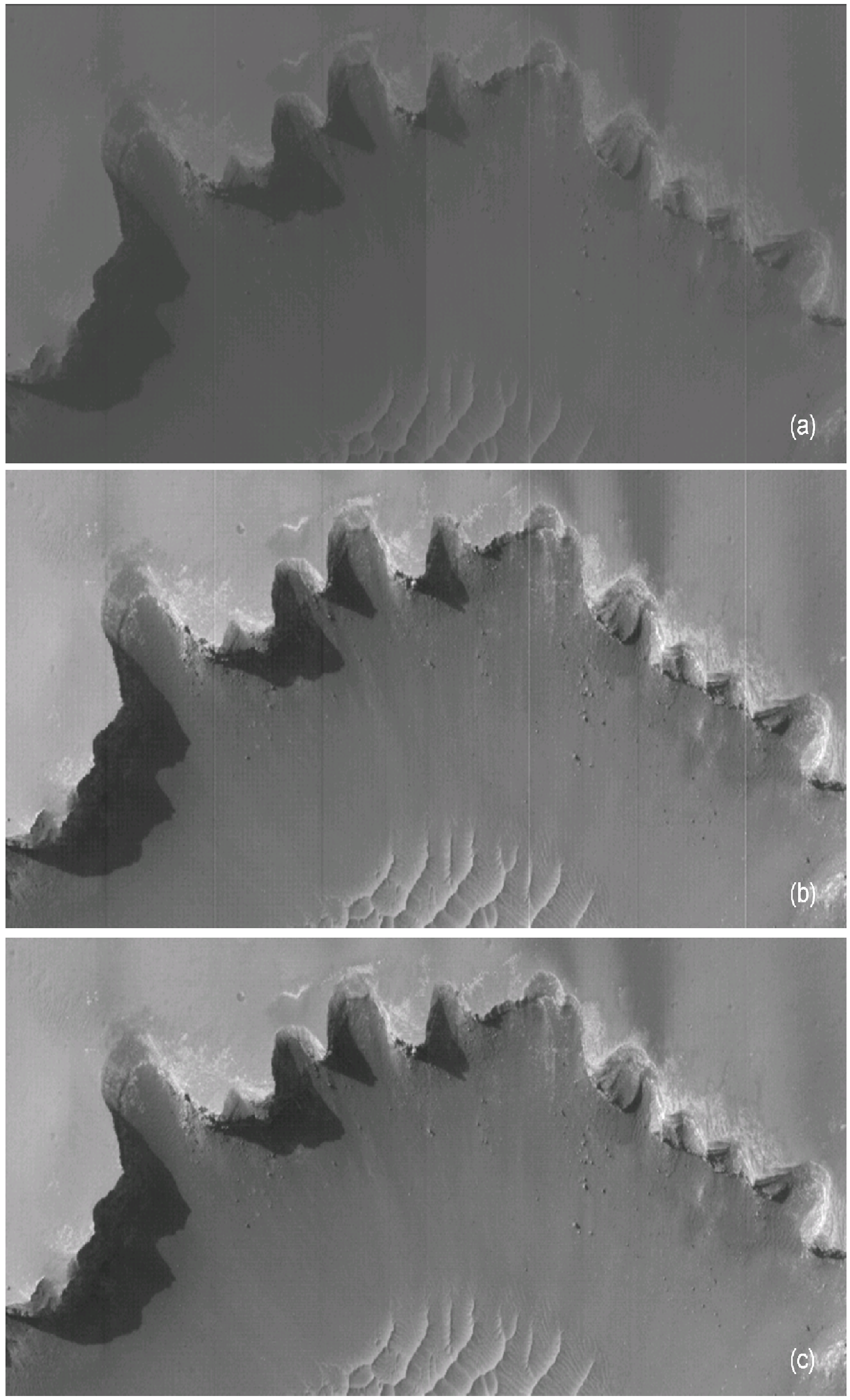

Figure 3.2 Result of image pre-processing (a) Excerpt of raw sub-image strips; PSP_001414_1780_RED5_0.img (left) and PSP_001414_1780_RED5_1.img (right), (b) combined image, (c) image after noise removal

Figure 3.2 is an example of HiRISE raw image pre-processing. Figure 3.2a shows two sub-image strips that are stored as separate image files but in fact, scanned from the same CCD array. The brightness level of the left strip is lower than that of the right one. Figure 3.2b is the merged image of the two strips after brightness adjustment is conducted. In this step, the contrast of the image is also enhanced. The final part of the radiometric enhancement is removal of the strip noises. First, the mean brightness values of each column are calculated. Since strip noises are results from the different sensitivity of CCD pixels, their locations are consistent throughout images. Once the locations of strip noises are confirmed, the brightness values of outlier columns are adjusted to the brightness level of the neighboring pixels. Figure 3.2c is the noise-free image after radiometric enhancement.

After pre-processing, a five-level image pyramid is constructed for further image processing and matching. Starting with the original image, each subsequent level of the image pyramid is created by sub-sampling the previous level image and smoothed by a Gaussian filter (Adelson et al., 1984). Figure 3.3 shows a close-up of a five-level image pyramid generated from PSP_001414_1780 data. In this hierarchical image processing, level 5 represents the original image with 2,048-pixel wide swath. Level 4 has half the size of level 5 image, and its swath is 1,024 pixels. Level 3 is half the size of level 4 and 1/4th of the original image, and so on. In this way, the size of level 1 image is 1/16th of level 5, and the swath is 128 pixels. Lower level images have coarser resolution and details are lost due to smoothing.

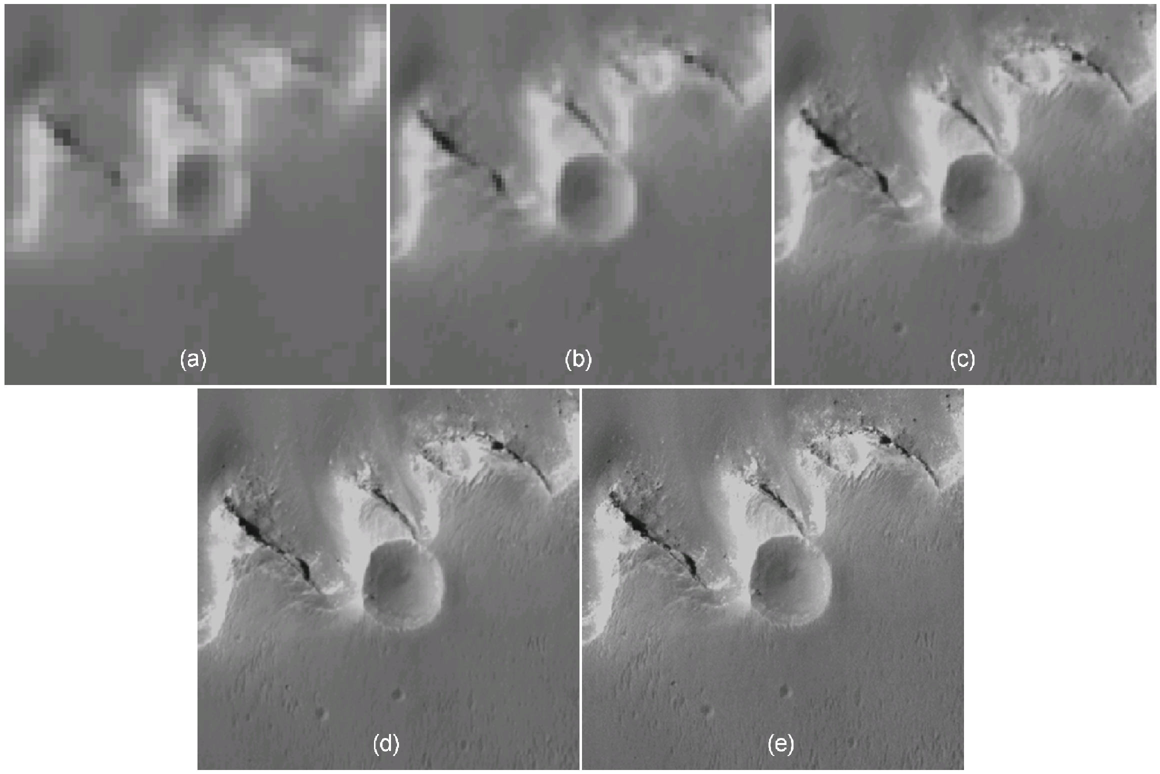

Figure 3.3 Excerpt of image pyramid from PSP_001414_1780 (a) level 1, (b) level 2, (c) level 3, (d) level 4, and (e) level 5

For stereo image matching, interest points are generated by Förstner operator (Förstner, 1986) at every scale of the image pyramid. The corner detector proposed by Förstner uses first-order derivatives and determines corners as local maxima of

$$g' = \frac{{g_x}^2{g_y}^2 - {g_{xy}}^2}{{g_x}^2 + {g_y}^2} \tag{3.1}$$

where g' is the first-order derivative, and g_x, g_y, and g_{xy} denote gradient images,.

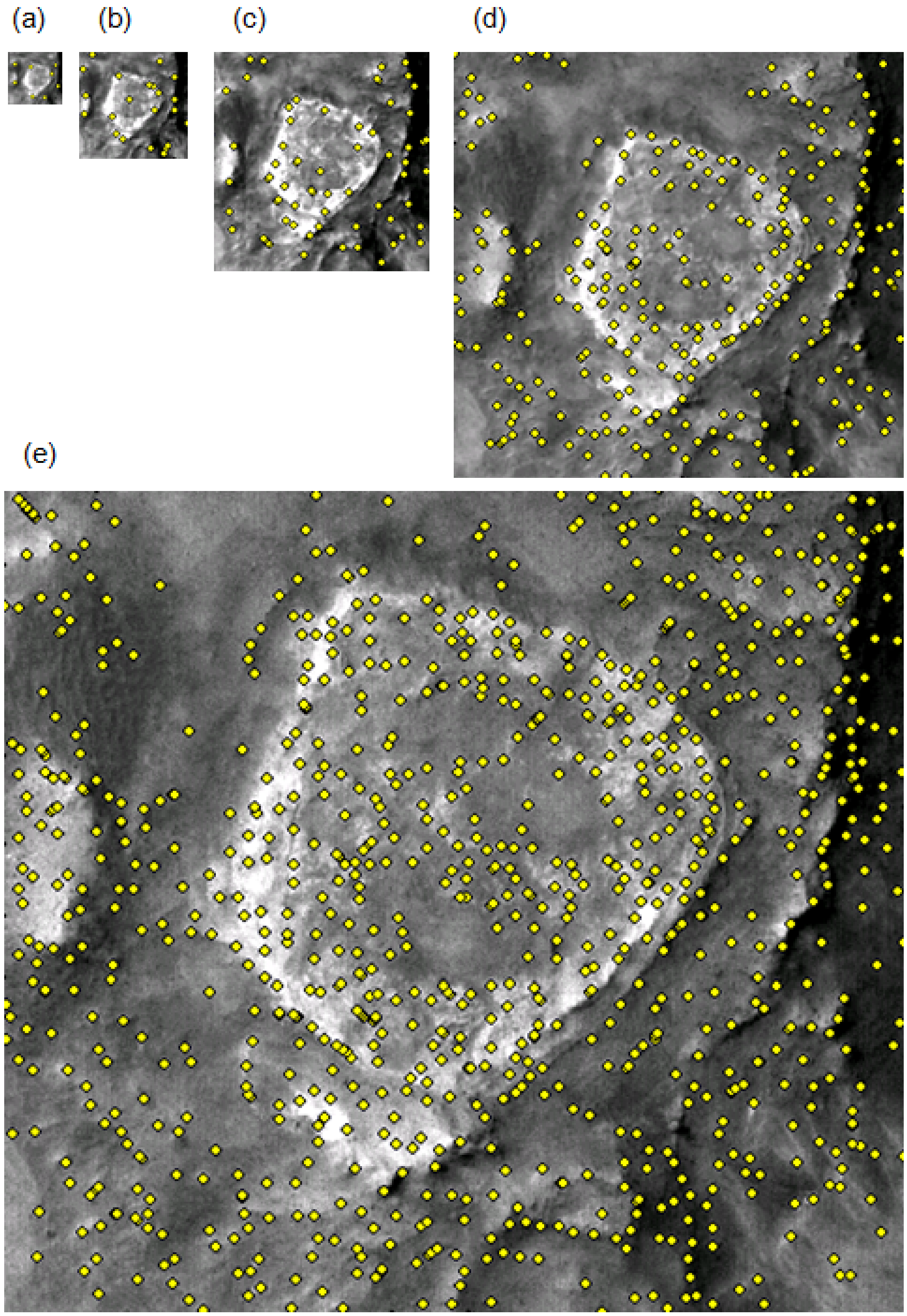

Figure 3.4 Interest points generated from PSP_001777_1650 image pyramid at five levels

(a) level 1, (b) level 2, (c) level 3, (d) level 4, and (e) level 5

Förstner operator generates a series of feature points by identifying distinctive variations of pixel brightness values. The detected feature points, or interest points, reflect the shape of the terrain in the images. Interest points are typically found around shadow, where significant change of brightness values occurs. These points are related to the shape of terrain or objects such as ridges and rocks. However, there are cases where image intensity changes regardless of the existence of terrain features. For example, a dust devil (a strong whirlwind) leaves a dark trails on barren terrain.

Figure 3.4 demonstrates the interest points generated at the five different levels of the image pyramid. Images at lower levels have fewer interest points. Since the Gaussian filter is a low-band pass, high frequency details are lost at lower levels and fluctuations at low frequency are preserved. The prevalence of low frequency information at lower level images is particularly useful in our hierarchical approach. Interest points of the lower level image have more distinguished features than those of the higher level image. Therefore, by starting the image matching process from low level to high level, more distinctive features are matched before features containing high-frequency details.

3.2 Image Matching and Tie Point Generation

To generate high quality topographic products, tie points need to be identified from stereo images as much as possible with best accuracy. In this research, an automatic coarse-to-fine hierarchical stereo matching process is developed to generate and match tie points from raw stereo HiRISE images.

In stereo image matching, cross-correlation coefficients are calculated between a template window and candidate windows in the search area to determine the matching window. Cross-correlation is a standard method to measure similarity of two series. For two series $F(i)$ and $G(i)$, the cross-correlation r can be defined as

$$r = \frac{\sum_{i=1}^{n}[(F(i) - \bar{F})(G(i) - \bar{G})]}{\sqrt{\sum_{i=1}^{n}(F(i) - \bar{F})^2} \cdot \sqrt{\sum_{i=1}^{n}(G(i) - \bar{G})^2}} \tag{3.2}$$

where $i = 1, 2, \ldots, n$, $\bar{F}$ and $\bar{G}$are the means of the corresponding series.

When the correlation coefficient of the matching window exceeds a threshold value, the interest point and the center pixel of the matching window are selected as a matched point. The parameters to determine which matching pair is acceptable can be customized at each level. Among the parameters, the size of template window, search area and the threshold for the correlation coefficient have significant influence on the image matching result (Gallatsatos, 2008). The window size for matching templates is 11 pixels by 11 pixels for the level 1 of the image pyramid, 13 pixels by 13 pixels for the level 2 and 15 pixels by 15 pixels for the rest of the interest point matching and grid point matching. At the first level, search area is the largest as 11 pixels by 11 pixels centered on the estimated location of the conjugate point. As the hierarchical matching proceeds, the search area is decreased accordingly. For level 5 interest point matching and grid point matching, a 3-pixel square search area is enough because hierarchical matching provides a good estimation. Cross-correlation threshold for the interest point matching from level 1 through

4 is set to 0.8, and is lowered to 0.6 for the level 5 through level 8. Selection of optimal values for these matching parameters is discussed in chapter 5.

Matching interest points of stereo images is first conducted on the lowest resolution. The matched points are then transferred to the next level (of higher resolution) where additional interest points are matched. This process repeats itself until it reaches up to level 5, the scale of the original images. At each scale level, the search area for conjugate points in stereo image is confined based on the parallax information from the previous level. As more interest points are generated and matched from lower to higher levels, better knowledge about the parallax information becomes available for search range reduction and quality control of the tie points.

At a subsequent level, points from the previous level are matched again to achieve higher matching precision. A TIN (Triangulated Irregular Network) surface of parallaxes is generated from these matched points using the Delaunay triangulation (Figure 3.5). This TIN is used to estimate the correspondence of additional interest points.

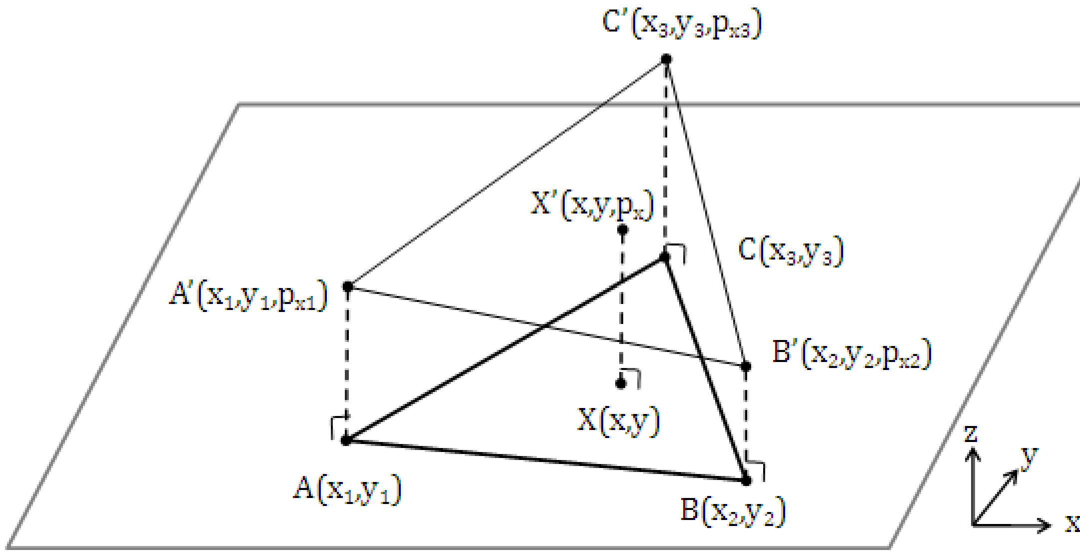

Figure 3.5 Interpolation of x-parallax using TIN surface

For stereo tie points *p* (x, y) and *p'* (x', y'), parallax p_x and p_y are defined as:

$$p_x(x, y) = x' - x \tag{3.3a}$$

$$p_y(x, y) = y' - y \tag{3.3b}$$

where (x, y) is the coordinates of the left image and $(x', \ y')$ is the conjugate coordinates of the right image. If a point $X(x, y)$ is inside of a Delaunay triangle formed by points $\mathrm{A}(x_1, y_1), \mathrm{B}(x_2, y_{12}), \mathrm{C}(x_3, y_3)$, the x-parallax is interpolated based on the TIN surface formed by $\mathrm{A}'(x_1, y_1, p_{x_1}), \mathrm{B}'(x_2, y_2, p_{x_2}), \mathrm{C}'(x_3, y_3, p_{x_3})$. Here, p_{x_1} is $p_\mathrm{x}(x_1, y_1)$, p_{x_2} is $p_\mathrm{x}(x_2, y_2)$, and p_{x_3} is $p_\mathrm{x}(x_3, y_3)$. The x-parallax of point $X(p_\mathrm{x})$ is interpolated as the z-coordinate of point X', which is the intersection between the 3-D plane $\mathrm{A}'\mathrm{B}'\mathrm{C}'$ and the line XX' parallel to z-axis. Parallax in y direction (p_x) can be calculated using the same strategy, only using y-parallax as z-coordinates. Finally, the estimated tie point coordinate (x', y') is defined as:

$$x' = x + p_x \tag{3.3c}$$

$$y' = y + p_y \tag{3.3d}$$

If a point is outside of Delaunay triangles, parallaxes of the nearest points are used for estimation of tie point coordinate.

There are many algorithms for checking if a point is inside a triangle. The simpler and faster algorithm is as follows:

$$a = \frac{[(x - x_1)(y_2 - y_1) - (y - y_1)(x_2 - x_1)]}{[(x_3 - x_1)(y_2 - y_1) - (y_3 - y_1)(x_2 - x_1)]}$$

$$b = \frac{[(x - x_1) - (x_3 - x_1)a]}{(x_2 - x_1)}$$

$If\,(a + b \le 1)\ and\ a \ge 0\ and\ b \ge 0,$
$\quad then\ the\ point\ (x, y) is\ inside\ the\ triangle$

Else, then the point is outside of the triangle

However, this algorithm does not work if the denominator of any of the terms is zero. The more comprehensive version is free from the zero-denominator problem but it is also time-consuming.

The parallax surfaces are formed in image space. The HiRISE image is composed of multiple CCDs, which form separate image spaces. To improve matching performance for points located around the boundary of each CCD, the HiRISE imaging geometry is fully utilized to model points in adjacent CCDs. To make continuous TIN surfaces of parallax, image spaces are stitched together based on the average shift from inter-CCD tie points between overlapping CCDs (Chapter 2).

Automatic blunder detection is performed at each level by eliminating outliers based on the elevation of each point compared to that of the neighboring area. Around every matched point, a 3-D plane is constructed based on 3-D coordinates of the matched points in its local area. Then the standard deviation of the elevation differences from the fitted plane, σ, is calculated. If the elevation difference between the matched point and the 3D plane is less than 2σ, it is accepted as the tie point. If the difference exceeds 2σ, the corresponding point is eliminated. More details about blunder detection are also provided in Chapter 5.

After matching the interest points at level 5, the highest resolution, the interest points are subsequently used to support a further matching process for generating a grid with 50-pixel grid spacing (level 6 in Figure 3.1), and then 10-pixel grid spacing (level 7). To produce a DTM of 1 m ground grid spacing, a 2-pixel grid is consequently defined and points are matched (level 8). To create a sub-meter level DTM, dense matching is performed for every pixel in the images.

3.3 DTM Generation

Given a stereo pair of HiRISE images, 3-D ground coordinates can be calculated from tie points on the stereo images through space intersection based on the collinearity equations. Collinearity equations are based on the fundamental geometric condition that a light ray passes through the perspective center, the ground point in object space, and its corresponding image point (Wolf and Dewitt, 2000). Elements of rotation matrix $\boldsymbol{R}$, $(a_{11}, \cdots, a_{33})$, are formed by the sensor pointing angles (Equation 3.4).

$$\boldsymbol{R} = \begin{bmatrix} a_{11} & a_{12} & a_{13} \\ a_{21} & a_{22} & a_{23} \\ a_{31} & a_{32} & a_{33} \end{bmatrix} = \begin{bmatrix} \boldsymbol{R_1} \\ \boldsymbol{R_2} \\ \boldsymbol{R_3} \end{bmatrix} \tag{3.4}$$

According to collinearity condition, for focal length of the sensor f, object space coordinates of the object $\boldsymbol{P}(X, Y, Z)$ and object space coordinates of the perspective center $\boldsymbol{P^c}(X^c, Y^c, Z^c)$, image space coordinates (x, y) can be determined by projecting the object onto the focal plane (Equation 3.5a). By dividing first and second row by third row in Equation 3.4b, image space coordinates x and y are obtained (Equation 3.5b, 3.5c). Equation 3.5b and 3.5c can be rewritten by substituting the camera focal point $\boldsymbol{P^c}$ to (X^c, Y^c, Z^c), and $\boldsymbol{P}$ to 3D ground coordinates (X, Y, Z), and the rotation matrix $\boldsymbol{R}$ for its elements $(a_{11}, \ldots, a_{33})$ formed by the camera pointing angle.

$$\begin{bmatrix} x \\ y \\ -f \end{bmatrix} = \boldsymbol{R}(\boldsymbol{P} - \boldsymbol{P^c}) = \begin{bmatrix} \boldsymbol{R_1}(\boldsymbol{P} - \boldsymbol{P^c}) \\ \boldsymbol{R_2}(\boldsymbol{P} - \boldsymbol{P^c}) \\ \boldsymbol{R_3}(\boldsymbol{P} - \boldsymbol{P^c}) \end{bmatrix} \tag{3.5a}$$

$$\begin{aligned} x &= -f\frac{\boldsymbol{R_1}(\boldsymbol{P} - \boldsymbol{P^c})}{\boldsymbol{R_3}(\boldsymbol{P} - \boldsymbol{P^c})} \\ &= -f\frac{a_{11}(X - X^c) + a_{12}(Y - Y^c) + a_{13}(Z - Z^c)}{a_{31}(X - X^c) + a_{32}(Y - Y^c) + a_{33}(Z - Z^c)} \end{aligned} \tag{3.5b}$$

$$y = -f\frac{\boldsymbol{R_2}(\boldsymbol{P} - \boldsymbol{P^c})}{\boldsymbol{R_3}(\boldsymbol{P} - \boldsymbol{P^c})} \tag{3.5c}$$

$$= -f\frac{a_{21}(X - X^c) + a_{22}(Y - Y^c) + a_{23}(Z - Z^c)}{a_{31}(X - X^c) + a_{32}(Y - Y^c) + a_{33}(Z - Z^c)}$$

Space intersection from stereo vision is also called forward projection. In photogrammetry, there are two types of solution for space intersection. One is simpler solution using linear least squares, and the other one is iterative method using nonlinear least squares. For each image point $(x, \ y)$, there are two observation equations. In a stereo image pair, two image points generate four equations. To obtain a direct solution of 3-D ground coordinates $\boldsymbol{P}$, the following equation can be formed. Here, a pair of tie points are (x_1, y_1) and (x_2, y_2) from stereo images with focal length f_1 and f_2, camera focal point $\boldsymbol{P^{c\prime}}$ and $\boldsymbol{P^{c}}$", and the rotation matrix $\boldsymbol{R}'$ and $\boldsymbol{R}''$.

$$\begin{bmatrix} \boldsymbol{R_3}x + f\boldsymbol{R_1} \\ \boldsymbol{R_3}y + f\boldsymbol{R_2} \end{bmatrix} \boldsymbol{P} = \begin{bmatrix} (\boldsymbol{R_3}x + f\boldsymbol{R_1})\boldsymbol{P^c} \\ (\boldsymbol{R_3}y + f\boldsymbol{R_2})\boldsymbol{P^c} \end{bmatrix} \tag{3.6a}$$

$$\begin{bmatrix} \boldsymbol{R_3}'x_1 + f_1\boldsymbol{R_1}' \\ \boldsymbol{R_3}'x_1 + f_1\boldsymbol{R_2}' \\ \boldsymbol{R_3}''x_2 + f_2\boldsymbol{R_1}'' \\ \boldsymbol{R_3}''x_3 + f_2\boldsymbol{R_2}'' \end{bmatrix} \boldsymbol{P} = \begin{bmatrix} (\boldsymbol{R_3}'x_1 + f_1\boldsymbol{R_1}')\boldsymbol{P^{c\prime}} \\ (\boldsymbol{R_3}'x_1 + f_1\boldsymbol{R_2}')\boldsymbol{P^{c\prime}} \\ (\boldsymbol{R_3}''x_2 + f_2\boldsymbol{R_1}'')\boldsymbol{P^{c\prime\prime}} \\ (\boldsymbol{R_3}''x_3 + f_2\boldsymbol{R_2}'')\boldsymbol{P^{c\prime\prime}} \end{bmatrix} \Leftrightarrow \boldsymbol{BP} = \boldsymbol{L} \tag{3.6b}$$

$$\boldsymbol{P} = (\boldsymbol{B^T B})^{-1}\boldsymbol{B^T L} \tag{3.6c}$$

The linear least squares solution can be used to estimate initial values for the further nonlinear least squares method. The nonlinear least squares method is based on partial linearization of error equations. The 3-D ground coordinates are updated iteratively until no change can be made.

$$v_x = -a_{11}\Delta X - a_{12}\Delta Y - a_{13}\Delta Z - l_x \tag{3.7a}$$

$$\nu_y = -a_{21}\Delta X - a_{22}\Delta Y - a_{23}\Delta Z - l_y \tag{3.7b}$$

$$\begin{bmatrix} \nu_x \\ \nu_y \end{bmatrix} = \begin{bmatrix} -a_{11} & -a_{12} & -a_{13} \\ -a_{21} & -a_{22} & -a_{23} \end{bmatrix} \begin{bmatrix} \Delta \mathrm{X} \\ \Delta \mathrm{Y} \\ \Delta \mathrm{Z} \end{bmatrix} - \begin{bmatrix} l_x \\ l_y \end{bmatrix} = \boldsymbol{AX} - \boldsymbol{L} \tag{3.7c}$$

$$\boldsymbol{X} = (\boldsymbol{A^T P A})^{-1} \boldsymbol{A^T P L} \tag{3.7d}$$

where a_{ij} (i = 1,2,3; j = 1,2,3) are ratation matrix coefficients, ν_x, ν_y are residuals and l_x, l_y are observed image coordinates.

3.4 Bundle Adjustment of HiRISE Stereo Images

The purpose of the bundle adjustment is the removal of geometric inconsistencies between measurements from the stereo images. In bundle adjustment, the exterior orientation parameters are modified according to the observation equations based on the initial exterior orientation parameters and the tie points. Since no ground control points are available on Mars, additional DTM data is used as control information to achieve absolute positioning of the orbital tracks.

As stated in the previous chapter, the exterior orientation parameters of HiRISE can be modeled as time-dependent polynomial functions (Equation 2.5). Since HiRISE CCDs are fixed on the single focal plane assembly, they share the satellite trajectory and orientation angle at the same moment. Therefore, a single polynomial model can applied to all the CCDs in the HiRISE frame using acquisition time as variables. In this way, bundle adjustment can be accomplished by adjusting only one set of polynomial coefficients.

The unknowns, such as exterior orientation parameters and object point coordinates, are updated iteratively by solving observation equations. In the bundle adjustment of HiRISE stereo images, there are two types of observations. The first type is the observed exterior orientation of each image line based on recorded telemetry data from satellite tracking. The second type is the measured image coordinates of tie points on stereo images. For each image line, there are observed parameters of exterior orientation. Instead of using every image line for observation equations, only selected of image lines are used in the bundle adjustment to improve computational efficiency. Since the exterior orientation parameters are already modeled as polynomial functions, using several equally spaced lines provides enough information to control the relative variance throughout lines. For an image orientation line, the observation equations are:

$$
\begin{aligned}
\hat{X}_t^c &= X_t^{c0} + \hat{v}_{X_t^c} = X_t^c + dX_t^c \\
\hat{Y}_t^c &= Y_t^{c0} + \hat{v}_{Y_t^c} = Y_t^c + dY_t^c \\
\hat{Z}_t^c &= Z_t^{c0} + \hat{v}_{Z_t^c} = Z_t^c + dZ_t^c \\
\hat{\omega}_\mathrm{t} &= \omega_t^0 + \hat{v}_{\omega_t} = \omega_\mathrm{t} + d\omega_\mathrm{t} \\
\hat{\varphi}_\mathrm{t} &= \varphi_t^0 + \hat{v}_{\varphi_t} = \varphi_\mathrm{t} + d\varphi_\mathrm{t} \\
\hat{\kappa}_\mathrm{t} &= \kappa_t^0 + \hat{v}_{\kappa_t} = \kappa_\mathrm{t} + d\kappa_\mathrm{t}
\end{aligned}
\tag{3.8}
$$

where $\hat{X}_t^c$, $\hat{Y}_t^c$, $\hat{Z}_t^c$, $\hat{\omega}_t$, $\hat{\varphi}_t$, $\hat{\kappa}_t$ are the unknown exterior orientation parameters at time *t*, X_t^{c0}, Y_t^{c0}, Z_t^{c0}, ω_t^0, φ_t^0, κ_t^0 are the observed exterior orientation parameters at time *t*, $\hat{v}_{X_t^c}$, $\hat{v}_{Y_t^c}$, $\hat{v}_{Z_t^c}$, $\hat{v}_{\omega_t}$, $\hat{v}_{\varphi_t}$, $\hat{v}_{\kappa_t}$ are the residuals of the exterior orientation parameters at time

t, X_t^c, Y_t^c, Z_t^c, ω_t , φ_t , κ_t are the approximation of the exterior orientation parameters at time t, dX_t^c dY_t^c, dZ_t^c, $d\omega_t$, $d\varphi_t$, $d\kappa_t$ are the correction to the approximation.

The adjustment of exterior orientation parameters are conducted by updating the polynomial coefficients in Equation 2.5; the observed exterior orientation parameters are derived from the polynomial fitting of the initial telemetry data (Equation 2.6). In bundle adjustment, the approximated polynomial coefficients are iteratively replaced by the newly updated ones (Li et al., 2002; 2008a; 2008b).

$$\begin{aligned}
dX_t^c &= 1 \cdot \mathrm{d}a_0 + t \cdot \mathrm{d}a_1 + t^2 \cdot \mathrm{d}a_2 + t^3 \cdot \mathrm{d}a_3 \\
dY_t^c &= 1 \cdot \mathrm{d}b_0 + t \cdot \mathrm{d}b_1 + t^2 \cdot \mathrm{d}b_2 + t^3 \cdot \mathrm{d}b_3 \\
dZ_t^c &= 1 \cdot \mathrm{d}c_0 + t \cdot \mathrm{d}c_1 + t^2 \cdot \mathrm{d}c_2 + t^3 \cdot \mathrm{d}c_3 \\
d\omega_\mathrm{t} &= 1 \cdot \mathrm{d}d_0 + t \cdot \mathrm{d}d_1 + t^2 \cdot \mathrm{d}d_2 + t^3 \cdot \mathrm{d}d_3 \\
d\varphi_\mathrm{t} &= 1 \cdot \mathrm{d}e_0 + t \cdot \mathrm{d}e_1 + t^2 \cdot \mathrm{d}e_2 + t^3 \cdot \mathrm{d}e_3 \\
d\kappa_\mathrm{t} &= 1 \cdot \mathrm{d}f_0 + t \cdot \mathrm{d}f_1 + t^2 \cdot \mathrm{d}f_2 + t^3 \cdot \mathrm{d}f_3
\end{aligned} \tag{3.9}$$

where $(a_0 , \cdots , f_3\ )$ are approximated polynomial coefficients for the exterior orientation parameters.

The second type of observation equations are provided by image tie points. On the stereo images, coordinates of corresponding tie points are measured. From the measured row (line) coordinates of the tie points, time index can be obtained to derive exterior orientation parameters from the polynomial functions (Equation 2.5). Using the calibrated interior orientation and the polynomial model of exterior orientation, a rigorous geometric model is established to connect an image coordinates to the corresponding object coordinates via the collinearity equations.

The ground coordinates of these image tie points are then calculated by space intersection. The observation equations are obtained by plugging in the measured image coordinates, approximate ground coordinates of the tie points and the exterior orientation parameters into the linearized form of the collinearity equations.

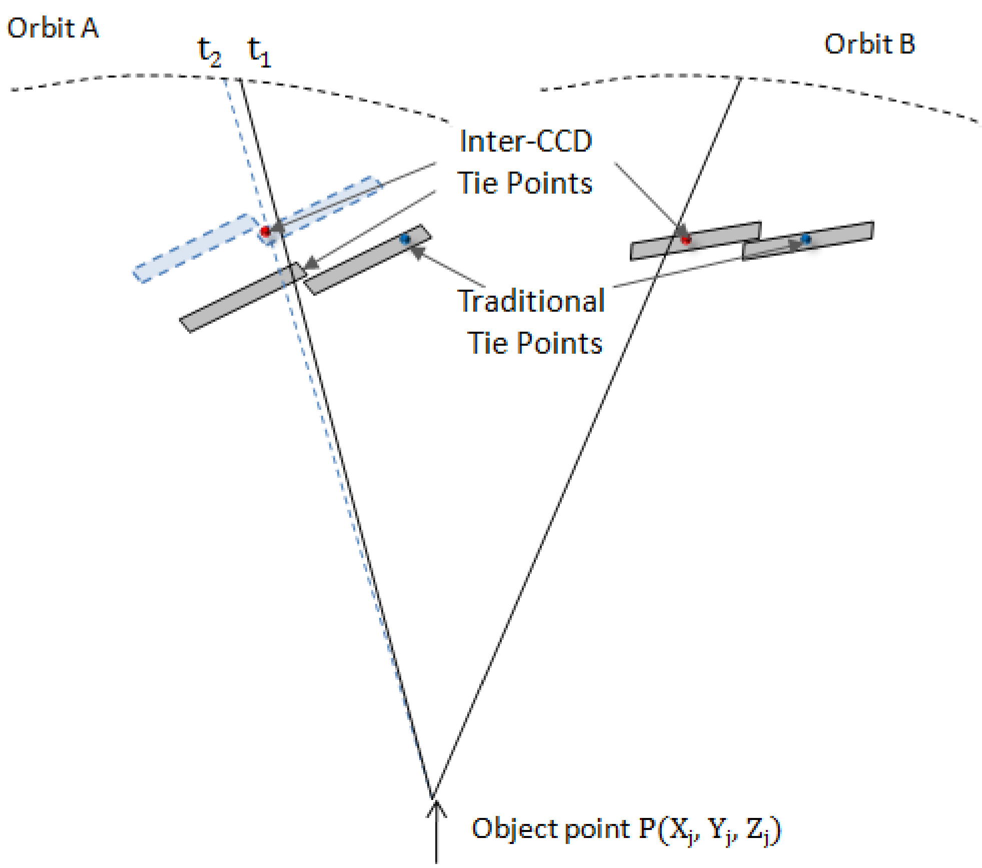

Figure 3.6 Traditional tie points and inter-CCD tie points

Tie points are selected from the matched interest points and checked for even distribution. There are two categories of tie points used in the HiRISE bundle adjustment: traditional tie points and inter-CCD tie points (Figure 3.6). Traditional tie points consist of two corresponding matched points from stereo images. Inter-CCD tie points are traditional tie points plus additional image coordinates of the same object from another CCD of the same image. Since Inter-CCD tie points connect adjacent CCDs in a single HiRISE orbit, this particular measurement can eliminate the internal disagreement between the CCDs. Since HiRISE CCDs are arranged with a certain interval in the along-track direction, inter-CCD tie points are obtained at different times with each other. In Figure 3.6, one tie point on the orbit A is acquired at time t_1, while another tie point of the same object is captured on different CCD at time t_2. In fact, the inter-CCD tie points reflect the change of the orientation between the time t_1 and t_2. As discussed earlier, jitter movement is high-frequency variation of the rotation angles, causing the relative position of image coordinates between overlapping CCDs. Hence, the elimination of the disagreement between overlapping CCDs can contribute to the removal of jitter effect.

3.5 Incorporation of MOLA Control Network

In practice, the HiRISE DTM generated by using only telemetry data may disagree with the MOLA control network by hundreds of meters. After resolving disagreement between stereo images by bundle adjustment, the MOLA DTM and profile are used as elevation control information for approximation of the absolute positioning. Since there is no ground control point available on Mars, it is not feasible to directly connect image points with ground points. In this research, the terrain generated by HiRISE stereo was compared and matched to the MOLA DTM before using MOLA points as vertical control. This correlation-based matching technique treats DTMs as images and matches DTMs according to image correlation. Details on the terrain matching are provided in Chapter 4.

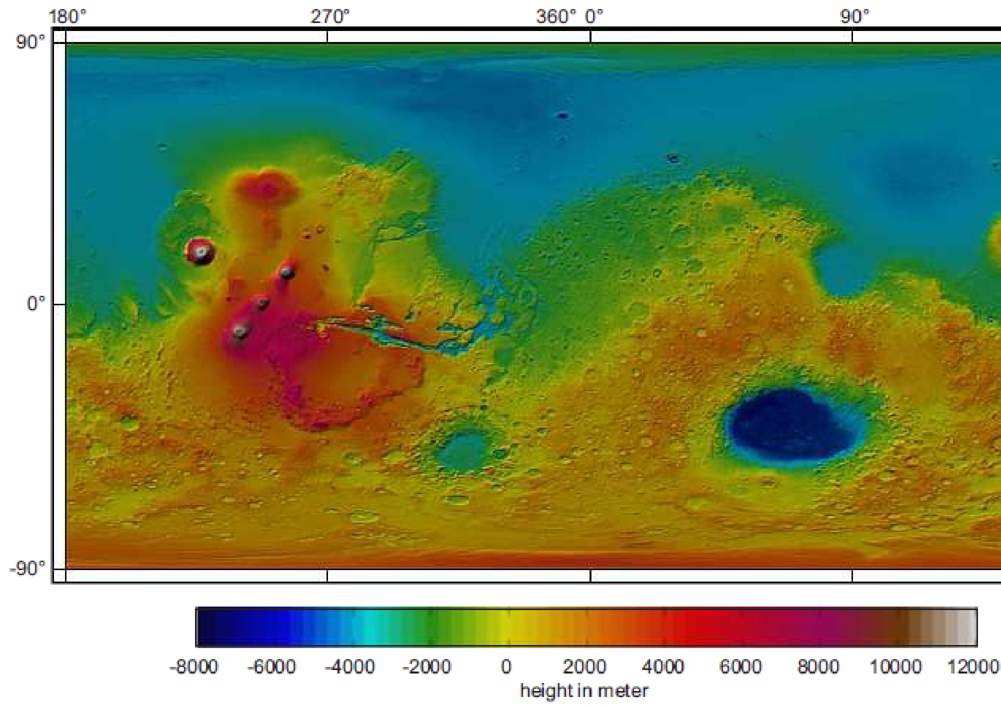

Figure 3.7 MOLA MEGDR DTM

The most detailed MOLA DTM product for a non-polar region is MEGDR with resolution of 128 pixels per degree, which is equivalent to about 463 meters of grid size in equirectangular projection (Figure 3.7). On average, the horizontal accuracy of a MEGDR product is expected to be about 200 m and the vertical accuracy is on the order of 10 m (Gwinner, 2009). The purpose of the terrain matching is to obtain approximated absolute position before further adjustment, based on the actual observation of the terrain elevation from the MOLA PEDR points. Since the horizontal resolution of the MOLA DTM is significantly lower than that of HiRISE imagery (25 cm/pixel), the grid size for the terrain matching is set as 100 m. A MEGDR product is resampled into 100-m grid by bilinear interpolation. HiRISE DTM (Figure 3.8) with the same grid size is generated by Kriging interpolation using 10-pixel grid points.

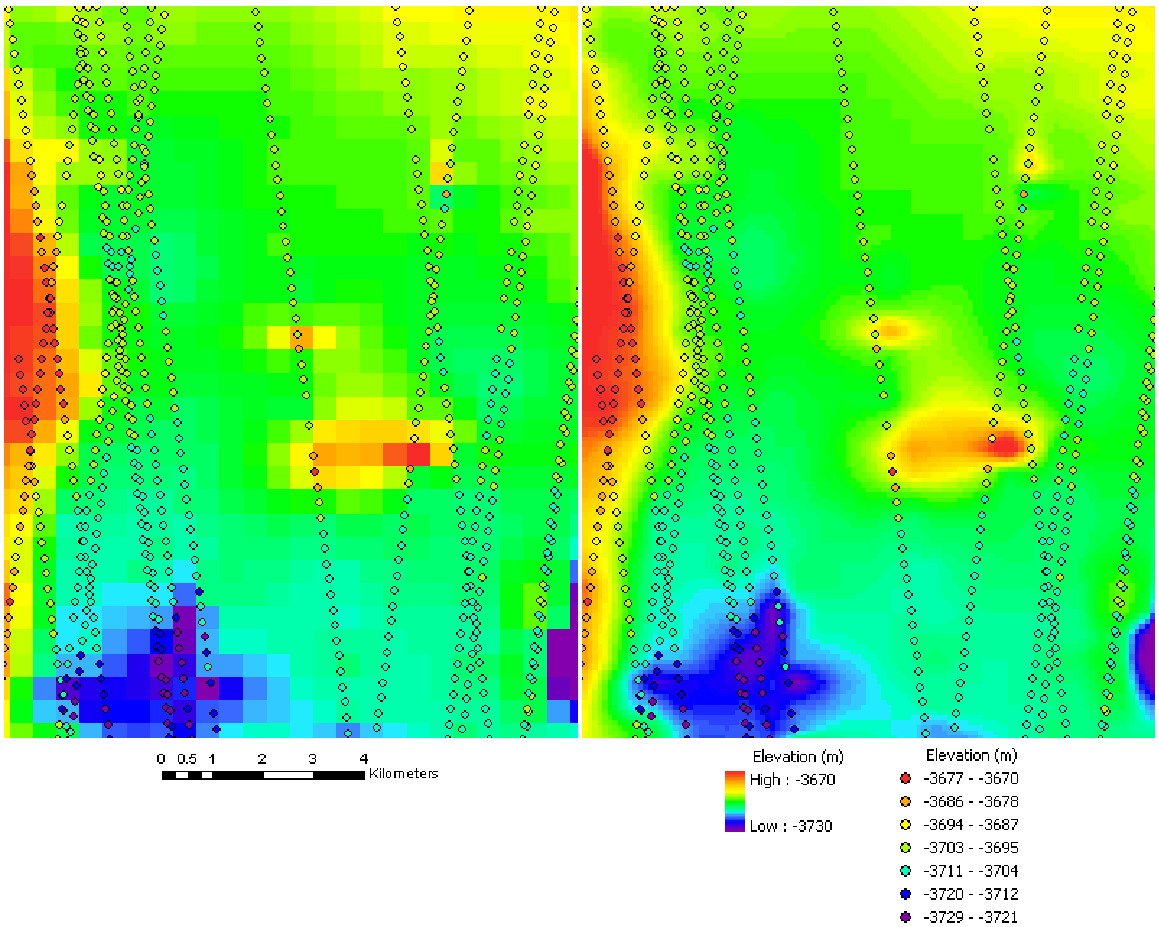

Figure 3.8 MOLA PEDR point data and DTM at the Spirit landing site used for HiRISE vertical control (Left) MOLA MEGDR DTM (463 m/pixel), (right) resampled MOLA DTM (100 m/pixel)

The approximate shift in the object space coordinates is obtained based on the terrain matching between the HiRISE DTM and the MOLA DTM. As can be seen from Figure 3.8, there are areas where the MEGDR DTM is interpolated due to limited coverage of MOLA tracks, especially the Columbia Hills. Therefore, the 3-D coordinates of MOLA PEDR points are matched afterward to conduct more accurate absolute positioning. The DTM-based terrain matching is conducted to obtain to approximate horizontal position and to limit the amount of horizontal shift during the point-based terrain matching. In the example above, the MOLA PEDR points are about 300 m apart from each other. In the terrain match, the position of HiRISE DTM is adjusted up to a few kilometers. In the MOLA point vertical control, the adjustment of horizontal position is confined to 500 m, given that the resolution of MEGDR DTM is 463 m.

Then the trajectories of both stereo orbits are shifted to make the HiRISE DTM consistent to the MOLA DTM. Although there may exist rotations between HiRISE DTM and MOLA DTM, the rotation is assumed to be negligible in this research. For the test area (Chapter 6), the horizontal shift was about 400 m. These shifted satellite positions are used as the initial approximation for further bundle adjustment. For object space coordinates

$$\hat{Z}_k = Z_k^0 + \hat{v}_{Z_k} = Z_k + dZ_k \tag{3.10}$$

where $\hat{Z}_k$ is the unknown elevation of the observed object point k, Z_k^0 is the observed elevation interpolated from the MOLA DTM, $\hat{v}_{Z_k}$ is the unknown residual to the observation, Z_k is the estimated object elevation, and dZ_k is the correction to the estimation. This type is in fact pseudo observation because the interpolated elevation is not direct measurement. To incorporate elevation control in the bundle adjustment, the object coordinates of each observed point are first calculated by the space intersection. Based on the planar coordinate in the object space, the observed elevation Z_j^0 is generated from the four neighboring grid points on the MOLA DTM by bilinear interpolation. Since the coordinates of object points are updated at each iteration of the bundle adjustment, the pseudo observation should also be recalculated.

In this research, the MOLA control network is incorporated for absolute positioning in the two types of terrain matching using MEGDR DTM and PEDR points. The bundle adjustment for HiRISE stereo images is conducted separately. However, there have been efforts for bundle adjustment based on MOLA data. Shan et al. (2005) registered a MOLA profile to stereo MOC images based on an iterative update of exterior orientation using the collinearity equation. However, it is also revealed that there is a nearly constant uncertainty of one MOLA ground spacing distance (about 325 m) along the flight direction in MOC and MOLA registration. After the update of exterior orientation, an uncertainty of 180.8 m in horizontal distance and 30.8 m in elevation difference is also estimated. This amount of uncertainty in registration of MOLA points on the orbital imagery is significantly higher than the known uncertainty of HiRISE exterior orientation parameters to be used as accurate control points. The positional precision of MRO is about 1 to 5 m, and the known precision of the pointing data is 0.035 mRad and systematic errors are considered to be no greater than 0.3 mRad (Kirk et al., 2008). Therefore, the HiRISE exterior orientation is fine-tuned by conducting a separate bundle adjustment using the stereo tie points. Since MOLA laser points cannot be identified in the images accurately, it is not practical to use them as normal ground control points in a bundle adjustment.

In the effort to the bundle adjustment of HRSC based on MOLA control network, Spiegel (2007) and Schmidt et al. (2008) proposed simultaneous adjustment of HRSC interior and exterior orientation based on MOLA DTM as control information. The accuracy of the MEX spacecraft exterior orientation is assumed to be about 1,000 m for position and about 25 mdeg for rotation angles. The resolution of HRSC imagery is 12 m to 15 m, which is much bigger than the resolution of HiRISE imegery (about 30 cm). In their adjustment system, the MEX trajectory is assumed to be affected by systematic shifts and drifts. Shift is constant offset of trajectory from the true satellite position and drift is time derivative of Doppler shift (Katayama et al., 1992). Drift is linearly proportional to the variable and, in this case, time. To compensate these effects in the bundle adjustment, additional observation equations for shift and drift are introduced as

$$\begin{aligned} \hat{X}_t^c &= X_t^{c0} + \hat{X}_0^c + \hat{X}_1^c \cdot t + \hat{v}_{X_t^c} \\ \hat{Y}_t^c &= Y_t^{c0} + \hat{Y}_0^c + \hat{Y}_1^c \cdot t + \hat{v}_{Y_t^c} \\ \hat{Z}_t^c &= Z_t^{c0} + \hat{Z}_0^c + \hat{Z}_1^c \cdot t + \hat{v}_{Z_t^c} \end{aligned} \tag{3.11}$$

where $\hat{X}_0^c$, $\hat{Y}_0^c$, $\hat{Z}_0^c$ are unknown shift, $\hat{X}_1^c$, $\hat{Y}_1^c$, $\hat{Z}_1^c$ are unknown drift.

Although the simultaneous adjustment approach (Spiegel, 2007; Schmidt et al., 2008) showed improvement in height differences between the HRSC object points and the MOLA DTM, the differences were still up to 80 m. Compared to HRSC, HiRISE imagery has higher resolution and better accuracies in exterior/interior orientation parameters.

Moreover, the known accuracy of MOLA DTM is 200 m in planimetry and 10 m in height (Spiegel, 2007). Therefore, the simultaneous adjustment approach based on the MOLA DTM is also an impractical choice for HiRISE bundle adjustment.

3.6 Orthophoto Generation

Using the DTM and the adjusted exterior orientation parameters, an orthophoto can be generated by ortho-rectifying the original HiRISE image. To ortho-rectify the original images, each grid of the DTM with 3-D ground coordinates is back projected onto the HiRISE image using the collinearity equation. The physical coordinates of back projection are transformed to row and column position using the calibrated interior orientation parameters. Since HiRISE is a push-broom sensor, the physical coordinate of the along-track direction is fixed. The image row that provides the physical coordinate of the along-track direction closest to the calibration is selected. Then, the corresponding column position is derived by converting the physical coordinate of the across-track direction into image pixel position. Once the corresponding image pixel for the DTM grid is identified, the pixel brightness value of the same grid on the orthophoto is calculated from the neighboring pixels using bilinear interpolation. Consequently, the orthophoto is defined on the same grid as the DTM.

The orthophoto generation, with a naive implementation strategy, is an inefficient procedure, since all image rows of all CCDs have to be searched to fill one grid on the DTM. To speed up the procedure, a recursive binary search algorithm is performed. The exterior orientation parameters are already sorted, either increasing or decreasing in one direction, at least for the image acquisition period. Instead of starting from the first row of a strip, the search begins at the middle of the strip. By comparing the back projected physical coordinate with the calibrated position, a decision is made about which part of the strip will be searched. The next row to be examined is either in the middle of the upper strip or the lower strip. This recursive procedure is repeated until the optimal row position is identified. To further accelerate the search algorithm, neighborhood search strategy is applied. Since the row positions of the neighboring DTM grids are similar to each other, the DTM grid close to the one with already identified image coordinates needs search for only a small neighborhood of the known row position. Once the row position of the first DTM grid is recursively searched for each CCD strip, the image coordinates of the rest of the grids can be identified very efficiently by the neighborhood search.

CHAPTER 4

ORBITAL AND GROUND DATA INTEGRATION

This chapter describes a new approach developed in this research for integration of orbital and ground image networks. It consists of terrain matching, rock extraction, and rock pattern matching. Orbital image networks are created using the rigorous sensor model (Chapter 2), photogrammetric processing of HiRISE imagery and bundle adjustment (Chapter 3). Ground image networks are constructed as a result of the MER rover localization process based on incremental bundle adjustment. Orbital and ground image networks are constructed separately.

The goal of this research is to link the two image networks within sub-meter level accuracy. The challenges toward integration of orbital and ground image networks are inconsistencies in position, viewing angle and image resolution. Although efforts are made to achieve absolute positioning for both networks, there are still inconsistencies between them caused by several factors. The lack of ground control information on the Martian surface hinders absolute positioning of orbital image networks. The MOLA vertical control network has a horizontal resolution of 463 m. Its accuracy (200 m in horizontal direction, 10 m in vertical direction) is far from the sub-meter level (Gwinner, 2009). Ground image networks are constructed based on combination of localization methods such as dead reckoning, visual odometry and bundle adjustment. However, slippage causes dead reckoning error, and visual odometry is limited due to heavy computational load. Photogrammetric incremental bundle adjustment provides correction to such errors and establishes ground image networks. However, automatic cross-site tie point selection cannot succeed when not enough common ground features are identifiable between rover images taken from different locations. Poor coverage of overlapping area and lack of ground features are the main causes (Wang, 2008). As one of the ways to overcome such positional uncertainty, terrain matching is performed to obtain approximate position of the ground image network relative to the orbital image network based on the similarity between ground DTM and orbital DTM. Terrain matching is a necessary step to confine the search space for further rock pattern matching. Since broader search space can result in higher possibility for false match in rock distribution patterns, terrain matching also functions as measure of quality control.

Integration of the orbital and ground image networks is based on identification of rocks, which are commonly visible ground features from HiRISE images as well as MER Navcam images. Due to the differences in viewing angle and image resolution, individual rocks are not identifiable. Hence, the matching of rocks from orbital and ground imagery relies on the similarity of rock distribution pattern. After matching the distribution patterns of orbital and ground rocks, common rocks are identified from both images networks. Using the rock pattern matching result, the ground image networks are registered to orbital image networks and the position of the rover is adjusted.

4.1 Terrain Matching

In a rover mission, identification of rover positions in orbital images is crucial element for operation as well as for planning. From finding the safest route to locating the target, the information needed for rover navigation is provided by orbital orthophotos and DTMs especially when ground data is not available. HiRISE orbital images do the level of resolution high enough to distinguish the shapes of rocks seen from the ground. No orbital images have similar view direction as ground images. Hence, instead of indentifying common rocks individually, the distribution pattern is used for matching orbital and ground rocks. Even if the initial position of the rover is determined from the extensive manual process, rover track is susceptible to accumulative error from slippage and incremental bundle adjustment. Moreover, due to lack of ground control, the scale of orbital mapping products may differ from that of ground maps. In the long run, these factors lead to a significant discrepancy between orbital and ground image networks. According to the statistical analysis of Sprit rover traverse conducted by OSU Mapping and GIS Lab, the maximum difference between HiRISE orthophoto and bundle-adjusted rover track (with the total length of the rover traverse of 6 km by sol 1899) was about 90 meters (Li et al., to be submitted). After applying 2-D affine transformation to the rover track, the maximum difference to the manually identified rover position on orbital and ground image networks was reduced to 9 meters.

If the rover position from ground image network is 20 meters away from the actual rover position on the HiRISE orthophoto, rock distribution pattern matching with a search range of 15 meters would not provide right answer. However, broadening the search area for rock matching would increase chances of mismatches because the distribution pattern alone cannot distinguish individual rocks. To enhance efficiency and reduce risk of errors in rock matching, 3-D terrain matching is conducted to obtain approximate rover position on the orbital maps. In this research, terrain matching based on the terrain signatures, elevation and slope.

The 3-D terrain matching method treats ground DTM as a moving window on top of orbital DTM and searches at which position their difference is minimized. To compare only the relative variations in elevation, the mean elevation is removed from each DTM. The variance between DTMs represents the difference of the overall shape of the terrain.

$$Cov_{Elev} = \frac{\sum_x \sum_y \left\{\left(Elev_o(x,y) - \overline{Elev_o}\right) - \left(Elev_g(x,y) - \overline{Elev_g}\right)\right\}^2}{n_x \cdot n_y} \tag{4.1}$$

where Cov_{Elev} is the covariance of the orbital and ground DTM, (x, y) are the ground coordinates, $Elev_o(x, y)$ is the elevation of the ground point (x, y) from HiRISE DTM, $Elev_g(x, y)$ is the elevation of the ground point (x, y) from the rover DTM, n_x is the number of grid points in the x direction and n_y is the number of grid points in the y direction.

$Slope(x, y)$, slope for grid point (x, y) is calculated from the DTM grid as follows

$$Slope_x(x,y) = \frac{Elev(x + \Delta d, y) - Elev(x - \Delta d, y)}{2 \cdot \Delta d} \tag{4.2a}$$

$$Slope_y(x,y) = \frac{Elev(x, y + \Delta d) - Elev(x, y - \Delta d)}{2 \cdot \Delta d} \tag{4.2b}$$

$$Slope(x,y) = \sqrt{{Slope_x}^2 + {Slope_y}^2} \tag{4.2c}$$

where $Slope_x$ is the slope of DTM in x direction, $Slope_y$ is the slope of DTM in y direction, Δd is the interval of the slope calculation.

Incorporating slope helps to match distinctive features such as ridges and hills, showing abrupt changes in elevation. The variance of slope is obtained in the same manner as that of DTMs, except for using absolute values:

$$Cov_{Slope} = \frac{\sum_x \sum_y \{Slope_o(x,y) - Slope_g(x,y)\}^2}{n_x \cdot n_y} \tag{4.3}$$

where Cov_{Slope} is the variance of the orbital and ground Slope, $Slope_o(x,y)$ is the slope of the ground point (x,y) from HiRISE DTM, $Slope_g(x,y)$ is the slope of the ground point (x,y) from the rover DTM.

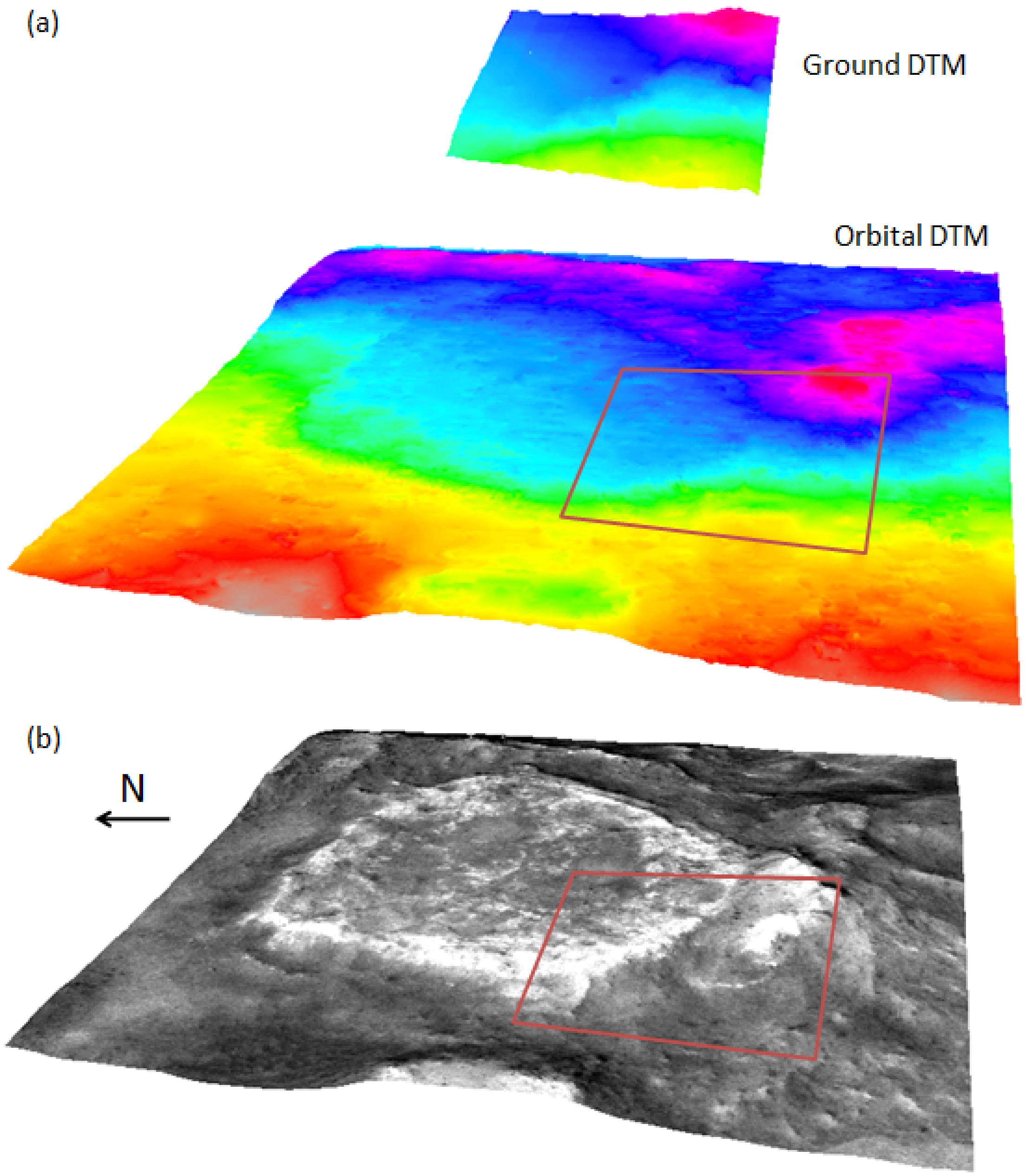

Figure 4.1 3-D view a) ground DTM from rover images taken on sol 1349 and orbital DTM of Home Plate (red rectangle is identified coverage of ground DTM), b) orbital orthophoto of Home Plate, c) ground DTM overlayed on orbital DTM before terrain match, and d) ground DTM overlayed on orbital DTM after terrain match (continued)

(continued)

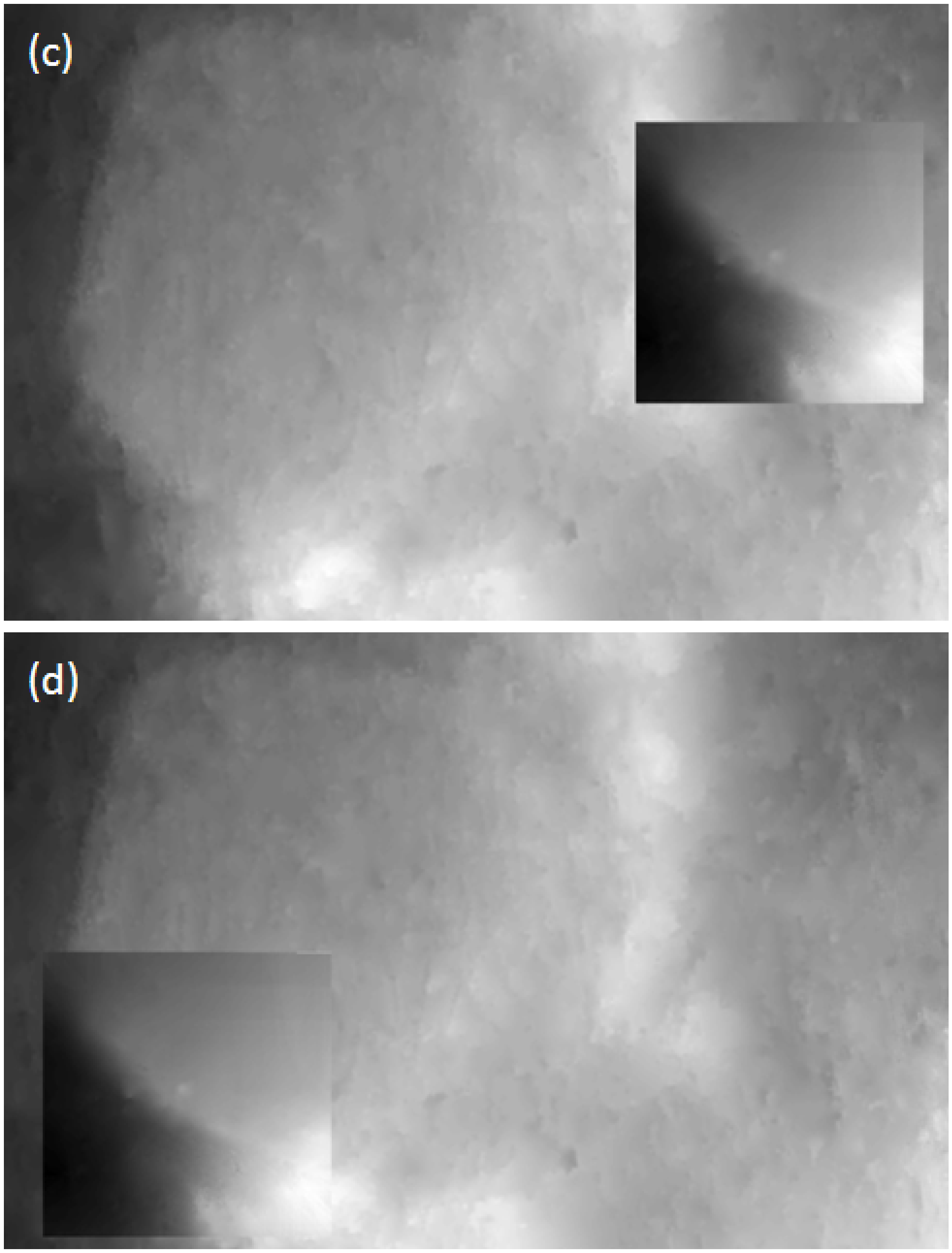

The logic behind terrain matching is the similarity between orbital and ground DTM would be highest at the rover's actual position. In this research, the best fit of ground DTM to the orbital DTM is found where the weighted sum of DTM and slope variance, E, has the minimum value. The weight parameters, w_{DTM} and w_{Slope}, are decided based on the range of each type of covariance. In empirical tests, the range of Cov_{Slope} (unit: meter) as about twice of Cov_{DTM} (unit: degree). Accordingly, the weight parametesr w_{DTM} and w_{Slope} were set to 2 and 1, respectively.

$$E = w_{\mathrm{DTM}} \cdot Cov_{DTM} + w_{\mathrm{Slope}} \cdot Cov_{Slope} \tag{4.4}$$

According to the terrain matching result, a further rock matching process is conducted at the new position of the rover where the variance of the terrain is at the minimum. Figure 4.1 shows the terrain matching example using rover images on sol 1349. Figure 4.1a is the ground DTM generated from photogrammetric processing of Navcam images. In this example, the extent of ground DTM is about 50 m by 50 m. To compare orbital DTM with 1 m resolution and sub-meter resolution ground DTM, they are resampled into 0.3 m grid DTMs. The area covered by ground DTM is the southern part of Home Plate (Figure 4.1b). However, using the separately constructed orbital and ground image networks, the difference between the rover position from telemetry data and the manually identified rover position on the orbital orthophoto was 90 m (Figure 4.1c). Telemetry data refers to downlinked data from the rover including position and orientation information derived from on board observations of wheel odometry, IMU and Sun-finding images (Li et al., 2008c). The rover telemetry data is available at NASA's Planetary Data Systems (http://pds.jpl.nasa.gov/). The search area is set to 100 m squared region centered on the rover telemetry position. After terrain matching, this difference decreased significantly, to 0.22 m (Figure 4.1d). This method can potentially be used for rover localization.

Considering that the resolutions of the DTMs are different, it is neither possible nor necessary to find the exact position. The objective of terrain matching is to obtain a reasonable estimation so that the search area can be reduced for the rock distribution pattern matching (Hwangbo et al., 2008; Li et al., 2007b). However, if the terrain has little variation, as in a flat region, the matching result could be erroneous. In that case, use of terrain matching results as estimation should be limited.

4.2 Rock Extraction

In this section, a rock extraction method using ground and orbital imagery will be provided in detail. To distinguish the image source, rocks detected from rover images are referred to as 'ground rocks', whereas rocks extracted from orbital images are called 'orbital rocks'.

4.2.1 Ground Rock Extraction

Rocks are one of the major features found in rover imagery of the Martian terrain. Gor et al. (2001) used image intensity information to identify small rocks and range information to detect large rocks from Mars rover images. Thompson et al. (2005) developed a rock detection method based on segmentation, feature detection, and classification using texture, color, shape, shading and stereo data from the Zoë rover. Li et al. (2007) proposed new methods of rock modeling from multiple rover sites for autonomous cross-site tie point selection. The strategy was to identify rock peaks and model the surface points as hemispheroid, semi-ellipsoid, cone or tetrahedron. Rocks extracted from cross-site Navcam images then were matched based on the distribution pattern and model parameters (Wang, 2008).

In orbital-ground data integration, the purpose for rock extraction is to identify rocks that are visible from both orbital and ground imagery. Since rocks ultimately serve as tie points between orbital and ground image networks, the size of the rocks is an important factor to consider. As the resolution of HiRISE images is about 30 cm, rocks with diameters less than the orbital pixel resolution have little possibility of being detected from orbit. On the other hand, if a rock is too large, it would not be precise enough to be used as a tie point between orbital and ground image networks. Therefore, rocks to be matched from both orbital and ground images would occupy at least one pixel in the orbital image up to a few pixels.

Typically, rocks are identifiable from orbit because of abrupt changes in image intensities, which make them distinctive from the terrain. It is caused by the shadow of the rocks as well as the albedo of the rocks, which is lower than the terrain. If a rock blends in with its background, there is no way that the rock could be detected from the orbital image. Accordingly, rock extraction in orbital-ground integration should incorporate image intensity as well. Although there is much research of rock extraction, their methodologies vary significantly depending on the type of image source and the purpose of rock detection. For example, HiRISE and MER images are used in this paper to identify common features to link orbital and ground image networks. The objective of rock extraction from MER images in Li et al. (2007b) is automatic cross-site tie point generation between ground imagery. Although both approaches use MER images and implement dense image matching to generate 3-D ground coordinates, the similarity ends there. Li et al. (2007b) select pixels that belong to ground rocks solely based on the 3-D ground coordinates. However, in this research, the foundation of ground rocks extraction is the image intensity, or darkness of the pixel. The most significant difference is usage of geometric model as rock matching criteria, which is the crucial part in Li et al. (2007b), but not applicable this research. Due to the discrepancy between orbital and ground images, in terms of viewing angle and resolution, the size and shape of the detected rocks in one type of imagery were not related to the geometric parameters of the rocks in the other type of imagery. Since the methodology of ground rock extraction in this research is unique from other research and has not been presented thoroughly in publication, detailed description will be provided in this section. Figure 4.2 shows the ground rock extraction process.

From the 3-D point cloud generated by Navcam intra-stereo matching, points that are too close or too far are eliminated. Navcam was originally designed with the intention of imaging the middle range (3~25 m). Points beyond that range have lower positional accuracy. A rock is composed of a continuous surface and a peak that is higher than the terrain surface. Therefore a distinction between the terrain and the rock comes from differences in elevation. To find rock peaks, local peaks with maximum elevation from candidates within a close range (1 m) are identified. The height of a point is defined as the elevation subtracted by that of the lowest point within 1 m. To be considered as a rock peak, the height of local peaks should exceed 22 cm.

Candidate rock points (CRPs) are points close (within 1 m) to these local peaks. CRPs could include points that belong to the terrain as well as rocks. To eliminate terrain points from CRPs, statistics of image intensity are calculated. Points with image intensity less than a certain threshold are accepted as CRPs.

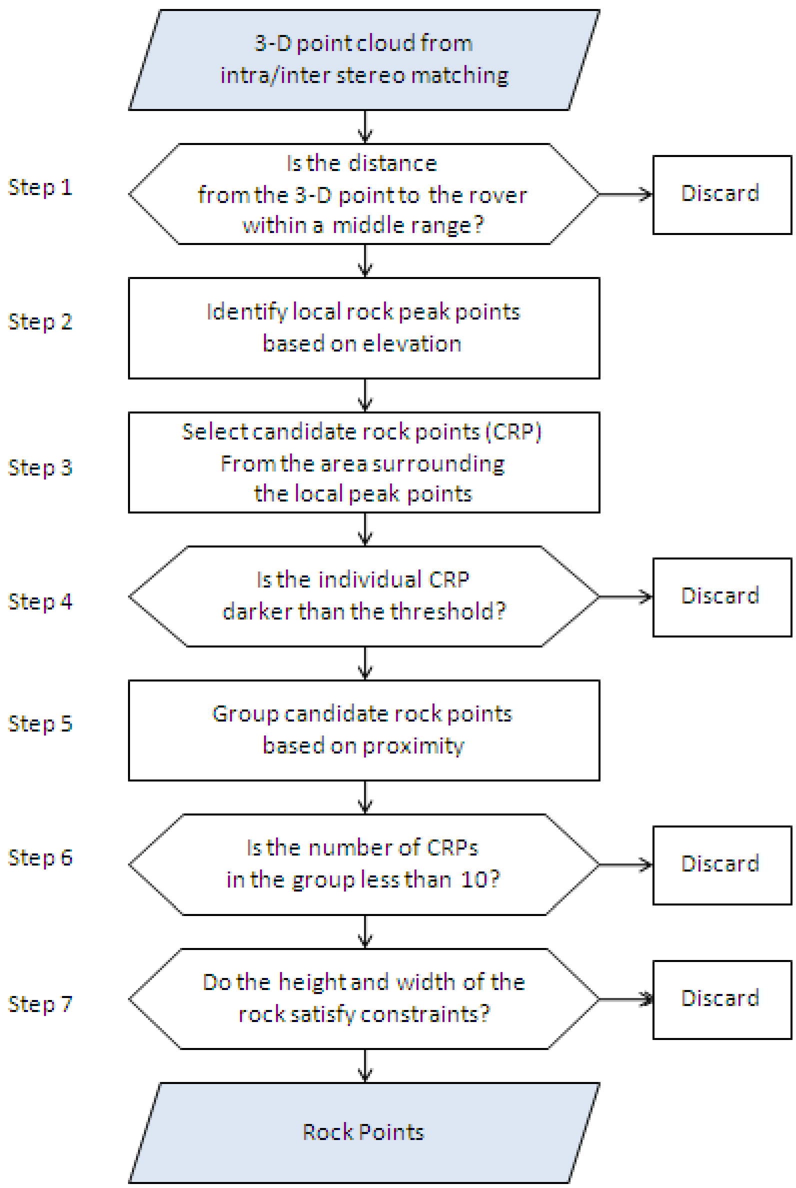

Figure 4.2 Conceptual flowchart of the ground rock extraction process.

Segmentation of CRPs is performed based on proximity in image space. Since local peaks are selected within a range of 1 m, smaller rocks within that range are separated in this step. Each segmented group of CRPs is now called a rock points group (RPG). If the number of CRPs in the RPG is less than ten, it is likely to be very small rock or partial shadow, so these smaller RPGs are eliminated.

Each RPG is modeled as a rock based on height and width. Height is defined as the elevation difference between highest CRP and lowest CRP. Width is the distance between leftmost CRP and rightmost CRP in the image space. The reason for using image space is that object space coordinates behind the visible side of the rock surface are less accurate. To select ground rocks that can be matched to rocks extracted from orbital imagery, size and shape constraints are applied. The RPGs are selected as ground rocks if the height is over 15 cm, the width is between 18 cm and 1 m, and the ratio of height to width is greater than 1/3.

Figures 4.3 through 4.7 show an example of ground rock extraction from a Navcam image at sol 1349. The original Navcam image is shown in Figure 4.3a. After intra-stereo matching using Navcam images, the 3-D coordinate of the matched points are obtained. Based on the position of the rover, the distance between the rover and the rocks are calculated. Among these 3-D points, only those within a range of 3 to 25 m from the rover were selected (Figure 4.3b). The colored pixels represent all the matched image points within the selected range. This step prevents potential errors in rock extraction by eliminating rocks that are too close or far away. In case of close rocks, which can be seen on the bottom of the image, it is difficult to distinguish the top of the rock from the terrain.

The difficulty is caused by the fact that the top part of the rock reflects more light than the side or the bottom, making the image intensity to be similar to that of the terrain. In the case of rocks that are far away, there are simply not enough 3-D coordinates to identify them as rocks.

Based on the 3-D coordinates, local peaks within the 1-m range became candidate rock points (Figure 4.3c). The height of a point is defined as the elevation difference between the point and the lowest point within its 1 m range. The local peaks shown here are the highest points within the range. Bigger rocks in the center show higher lock peak points. Figure 4.3-D shows the points that are below the local peak points within a 1 m range. According to the definition of peak points, all the points surrounding the local peaks in that range are lower than the peak. The combination of the local peak points and the surrounding points form candidate rock points.

Figure 4.4a shows candidate rock points with lower image intensity than a threshold. As can be seen from the original image, rocks are distinguished by the darker brightness values. Due to the angles toward the sun, the side of rocks faces less sunlight than the ground. By applying the constraint, the remaining candidate rock points begin to correspond to actual rocks in the scene.

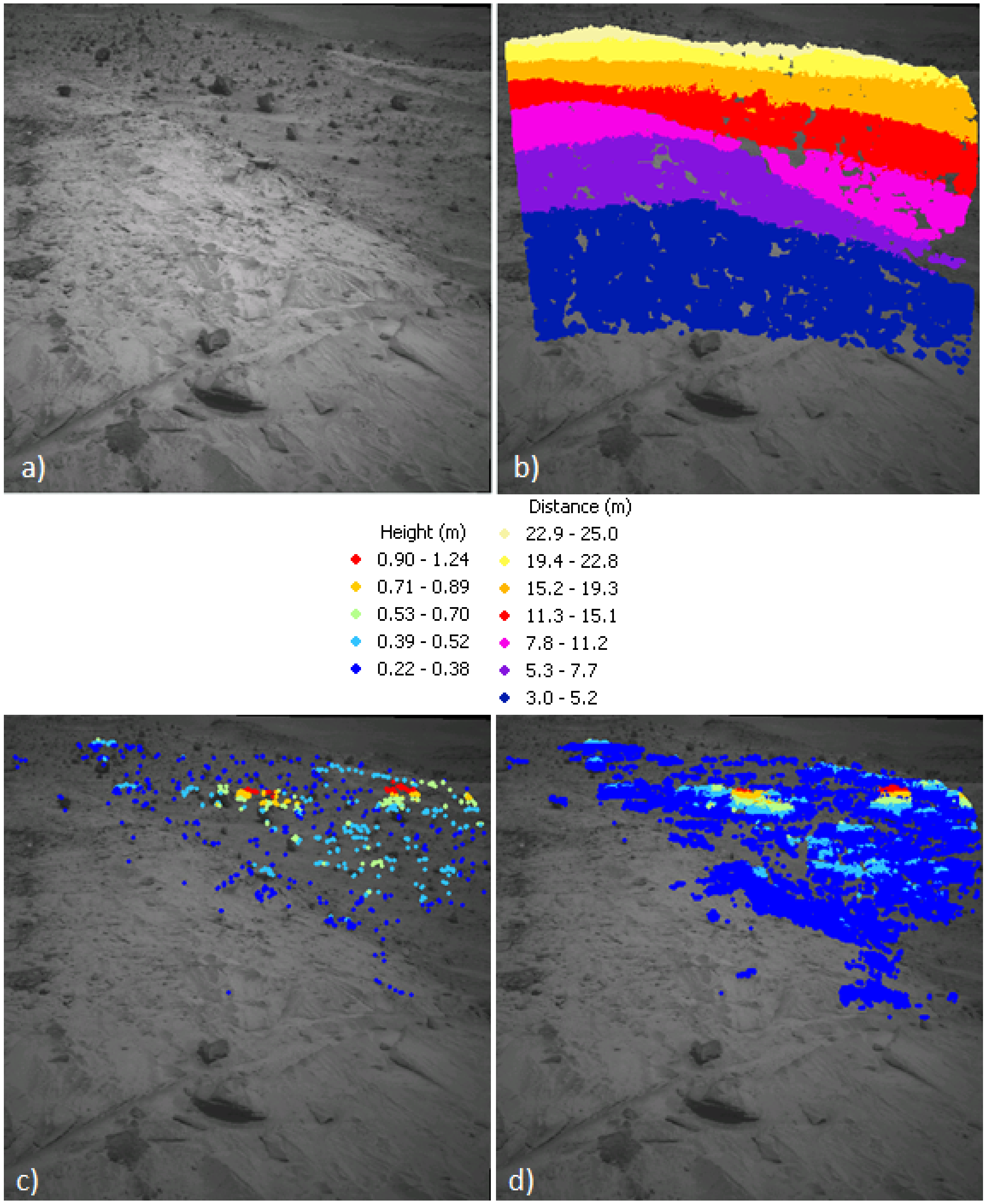

Figure 4.3 a) A Navcam image at sol 1349, b) step 1: 3-D coordinates of matched points between 3 m to 25 m distance from the rover (color indicates distance), c) step 2: local peak points, c) step 3: CRPs below local peak points (color indicates height in c) and d))

To identify and model rocks from the candidate rock points, segmentation is performed based on the connection between the points in the image space (Figure 4.4b). Each segment forms RPG, distinguished by the colors in the figure. There are many smaller segments that belong to rocks but could not be seen from the orbital images because of their size. Since the highest resolution of HiRISE imagery is about 30 cm, rocks that are smaller than that size would not be visible.

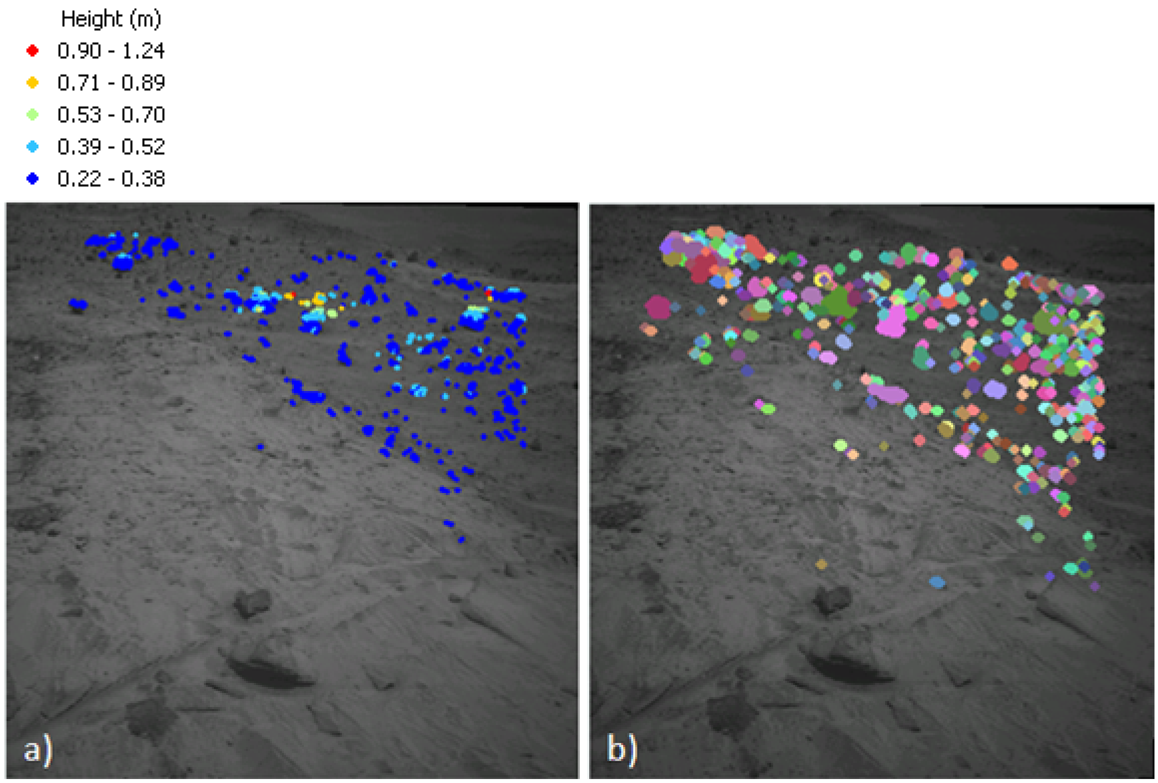

Figure 4.4 Rock extraction result from sol 1349 a) step 4: CRPs with dark image intensity (color indicates height), b) step 5: RPGs from dark CRPs (color indicates individual RPG)

To extract ground rocks that could also be seen from the orbit, RPGs composed of less than 10 points are eliminated (Figure 4.5a). By applying this constraint, only rock point groups that have enough points to model the shapes are selected.

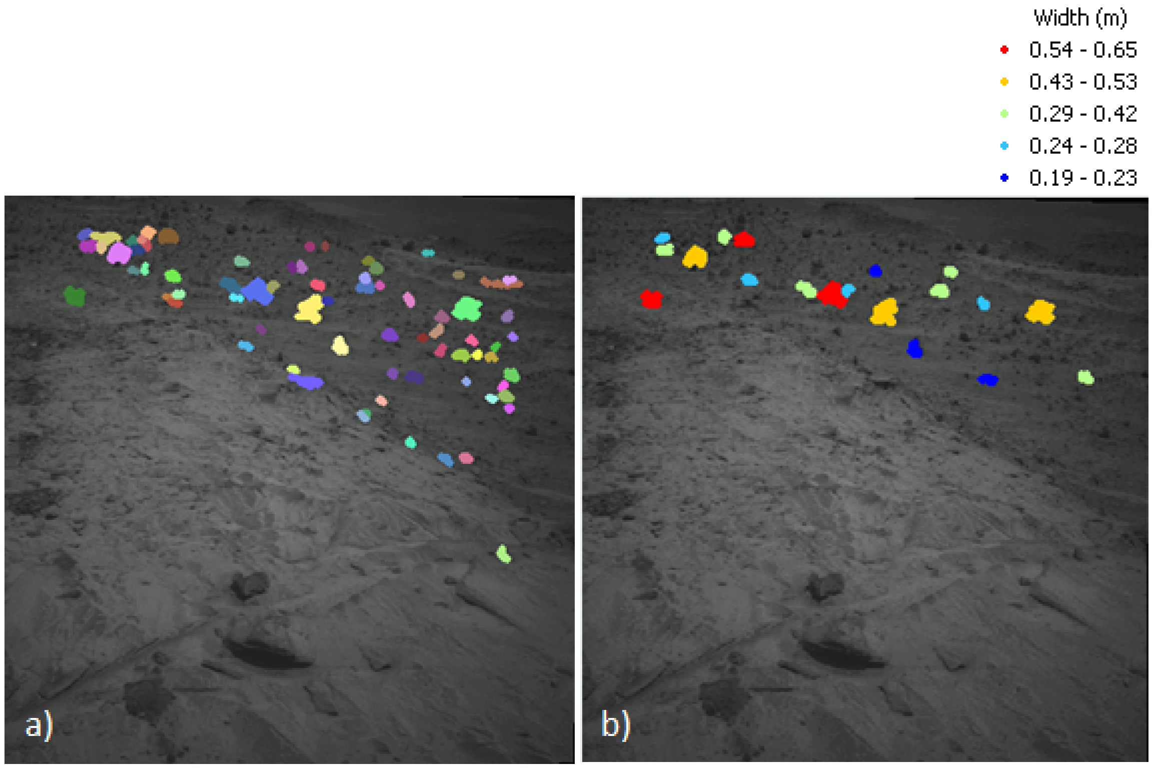

Figure 4.5 Rock extraction result from sol 1349 a) step 6: RPGs with no less than 10 CRPs (color indicates individual RPG), b) step 7: ground rocks satisfying width and height constraints (color indicates width of the rock)

The RPGs, after step 6 elimination, are rocks that can be extracted from ground images. However, not all ground rocks can be visible from orbital imagery. The best resolution of HiRISE images that covers the Spirit rover traverse is about 26.3 cm. Given the orbital image resolution ranging from 25 cm to 30 cm, a certain size constraint is applied to select rocks that are likely to be detected from orbit as well. The RPGs are selected as ground rocks if the height is over 15 cm, the width is between 18 cm and 1 m, and the ratio of height to width is greater than 1/3. The height means the distance between the highest and lowest point of a RPG. The width is defined as the biggest distance in the horizontal direction between all the points within the RPG. The visibility of rocks from orbital imagery is dependent on the shadow, which makes them discernable from the terrain. If a rock is flat, its possibility to be seen from the orbit is decreased. Therefore, RPGs with the ratio of height to width bigger than one third are selected as a rock. These constraints are selected based on manual comparison between rover images and HiRISE images. At the final step, RPGs that satisfy the size and shape constraints are selected as ground rocks. Figures 4.5b shows many small-sized rocks in the close range being eliminated.

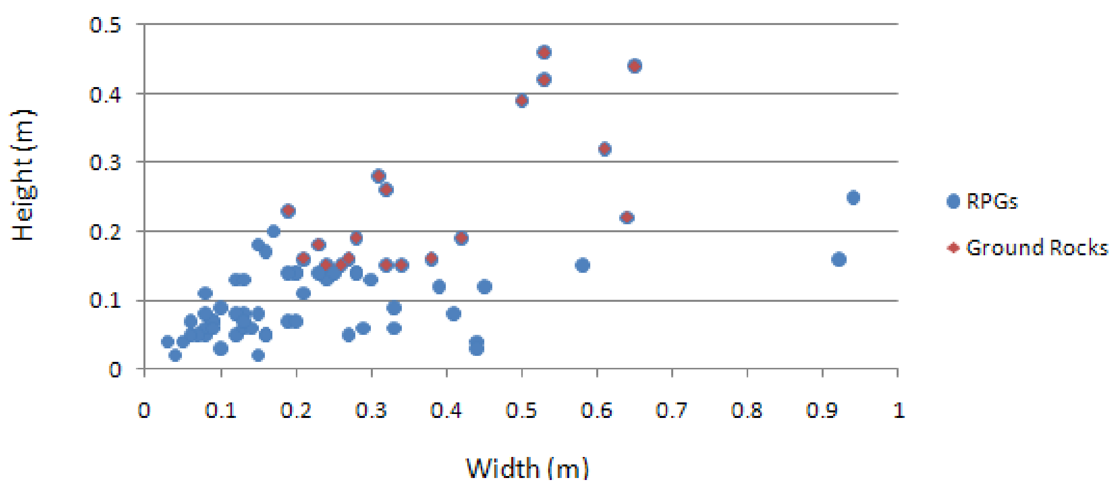

Figure 4.6 Width and height of the RPGs: step 6 results (blue circle) and selected ground rocks at step 7 (red diamond)

Figure 4.6 displays the height and width of the RPGs and final extracted ground rock. The very high resolution of ground imagery enabled extraction of even very small rocks. Out of total 73 RPGs, about 70 % have width less than 30 cm. After eliminating 75 % of the 73 RPGs, 19 of them are accepted as ground rocks.

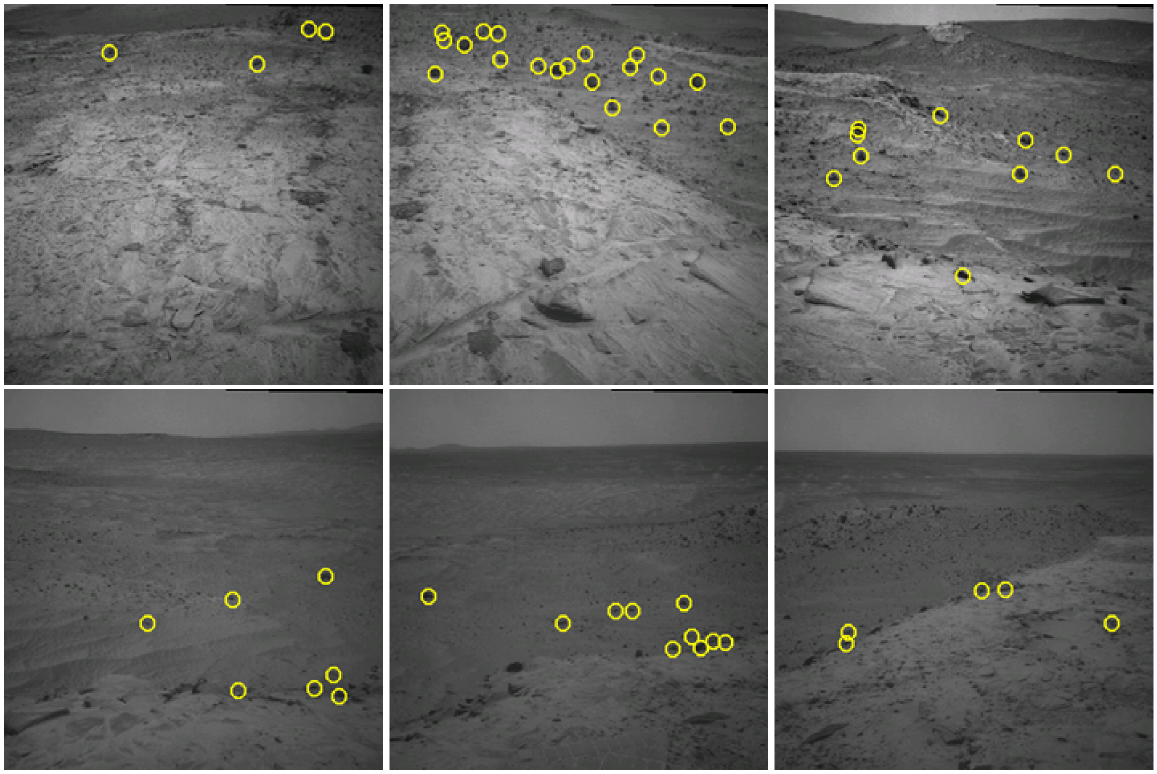

Figure 4.7 Rock extraction results from sol 1349 panoramic Navcam images: the final selected ground rocks circled on the ground image

Figure 4.7 shows the ground rocks extracted from the sol 1349 ground image. From all the Navcam panoramic images, a total of 55 ground rocks area detected. The automatic rock extraction result is consistent with what the human operator selects as rocks. The proposed rock extraction process worked well on the MER Navcam image, judging by the fact that within the target range (3 m ~ 25 m), all the ground rocks were identified as ground rocks. Sol 1349 Spirit rover site has favorable condition; rocks are mostly good-sized and not too close to each other, and their darker tone stands out from the bright surrounding. However, the proposed algorithm can be used to extract ground rocks from other MER images as well.

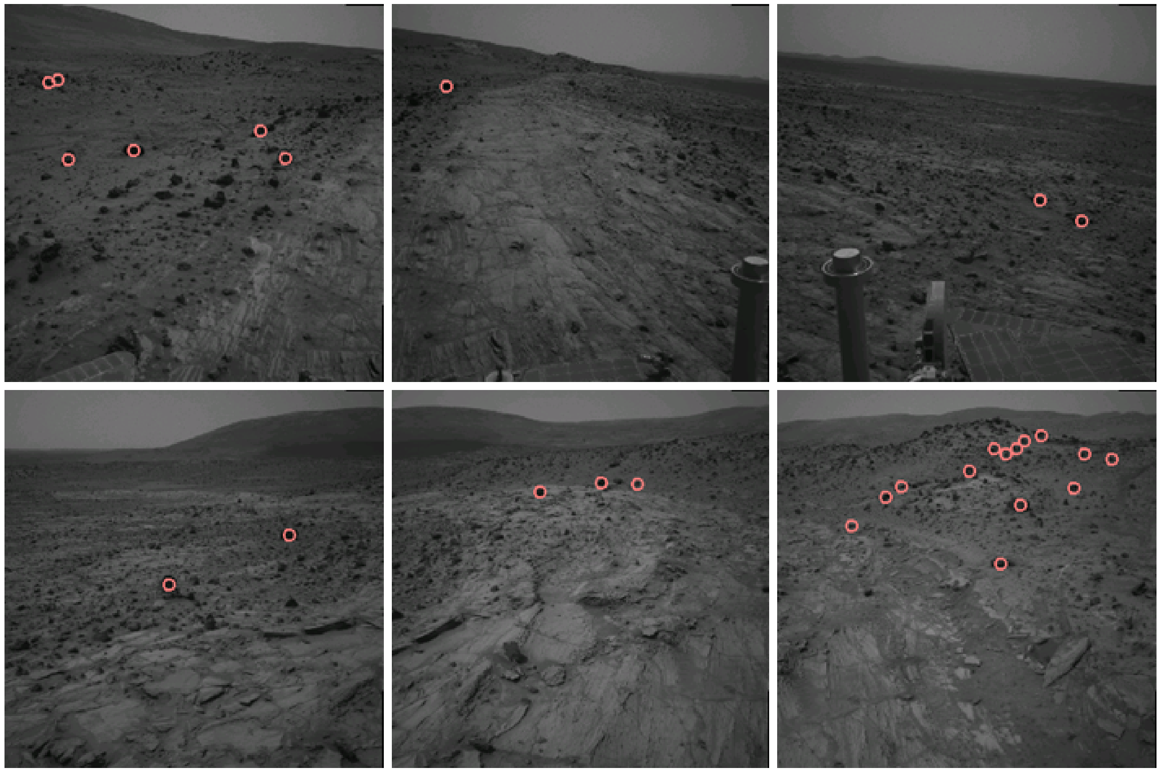

Figure 4.8 Rock extraction results from sol 703 panoramic Navcam images: the final selected ground rocks circled on the ground image

Figure 4.8 is another ground rock extraction example from sol 703 images. This is a more challenging site than the sol 1349 example, because there are numerous small rocks clustered to each other all over the area. All of the extracted rocks in this example are manually identified as ground rocks. Although plenty of rocks were not left out from the selection of 'ground rocks', they were eliminated based on the size and shape constraints to increase matching success with rocks that are extracted from the orbital images.

4.2.2 Orbital Rock Extraction

In orbital imagery, rocks are distinguished from the terrain mainly based on pixel brightness. Since the illumination of the Martian terrain can change based on illumination (sun angles), geology and topography, locally dark pixels are identified by comparing pixel brightness values with those of the neighborhood average. The following procedures were used to extract orbital rocks. Here, an orbital image I contains the pixel values of the HiRISE image after radiometric processing (Chapter 3).

1. Average pixel brightness I_{avg} is calculated by convoluting the average filter M with the orbital image I, so that I_{avg}= M * I. M is a 9 by 9 matrix with every element is 1/81.

2. To obtain relative brightness of image pixels, local brightness of a pixel is calculated by subtracting the average pixel brightness value from the image intensity of the pixel. The local brightness I_{local} is equal to $(I - I_{avg})$.

3. If the subtracted value of I_{local} for a pixel (i, j) is less than $threshold_1$, the pixel belongs to the DarkPixel set:

$$\text{DarkPixel} = \{(i, j) | I_{local}(i, j) < threshold_1\}. \qquad (4.5a)$$

4. However, not all dark pixels are considered as rocks. Rock candidates should meet a certain criterion as a group of rock pixels. For that reason, the elements of the

DarkPixel are then grouped based on proximity, forming connected components CC such that:

$$CC_k = \{(i_c, j_c) | (i_c, j_c) \in \text{DarkPixel},$$
$$i_c' - 1 \le i_c \le i_c' + 1 \text{ and } j_c' - 1 \le j_c \le j_c' + 1 \text{ for } (i_c', j_c') \in CC_k\} \qquad (4.5b)$$

5. If a CC contains at least one pixel whose I_{local} value is less than a $threshold_2$, it becomes a dark connected component (DarkCC). Reasons for not using a single threshold value for extracting rock pixels are twofold: 1) using a less strict $threshold_1$ in the first place eliminates disconnection CCs from dark pixels that actually belong to the same rock, and 2) by applying a stricter $threshold_2$ in a later step, a CC with a very dark pixel is distinguished as a rock:

$$DarkCC_k = \{(i_d, j_d) | (i_d, j_d) \in CC_k, \exists\ I_{local}\,(i_d, j_d) < threshold_2\}\,. \qquad (4.5c)$$

6. The size and shape of a DarkCC are important factors to determining if it can be used as a tie point. For each DarkCC, major and minor axes are defined. Major axis V_{major} is the vector of longest distance in the DarkCC. Minor axis V_{minor} is orthogonal vector to the major axis. For positional accuracy, the maximum width of a DarkCC should not exceed 8 pixels in image space, even when considering the shadow. The ratio of the length of the minor axis to that of the major axis should be larger than 0.3. Using Equation 4.4d, those DarkCC meeting the criteria are selected as orbital rocks (OrbRock).

$$OrbRock_k = \{(i, j) | (i, j) \in DarkCC_k, (i', j') \in DarkCC_k,$$

$$\mathbf{V} = (i' - i', j' - j),\ |\mathbf{V}_{major}| \geq |\mathbf{V}|,\ \mathbf{V}_{minor} \perp \mathbf{V}_{major},\ |\mathbf{V}_{major}| \leq 8,$$

$$|\mathbf{V}_{minor}| \,/\, |\mathbf{V}_{major}| > 0.3\} \qquad (4.5d)$$

The proposed orbital rock extraction method was implemented using an orbital HiRISE image (PSP_001777_1650). The area shown in Figure 4.9 is the south part of Home Plate, particularly where the Spirit rover was at sol 1349. Figure 4.9a is the orbital image I after radiometric processing. By applying 9 by 9 average filter, the local average pixel brightness I_{avg} is obtained (Figure 4.9b). The size of average filter affects the orbital rock extraction outcome. In this research, the filter size is selected based on test results. For the study area, the number of extracted rocks is 22756 for 7 by 7 filter, 27111 for 9 by 9 filter, and 29678 for 11 by 11 filter. Although increased size of filter produced more rocks, many of them were also falsely identified as rocks because it made the local brightness more sensitive. Based on both the quantity and the quality of the rock extraction, 9 by 9 average filter is selected for orbital rock extraction.

The local brightness I_{local}, which is equal subtraction of average brightness I_{avg} from the orbital image I is shown in Figure 4.10a. In this way, the relatively dark pixels can be identified, even when the image intensity of the background is already low. Based on the local brightness I_{local}, DarkPixel sets are obtained by a threshold. Every pixel with I_{local} less than threshold$_1$ is regarded as DarkPixel. In Figure 4.10b, orange and red pixels belong to the DarkPixel sets, which are relatively dark pixels in the neighborhood. I_{local} values of orange pixels are less than threshold$_1$, -12, and red pixels are less than threshold$_2$, -15. DarkPixel sets are segmented into connected components (CC) based on their proximity. However, only if a CC contains no red pixel with I_{local} value less than reshold$_2$, it is selected as a dark connected component, DarkCC. The reason to incorporate two threshold values is to obtain precise configuration of orbital rocks. The pixel brightness values of orbital rocks consist of prominent darker ones and less dark ones surrounding them. If only $threshold_2$ is used for finding DarkPixel, the relatively bright part of the rocks would be lost. On the other hand, using only $threshold_1$ would generate too many false orbital rocks that are actually part of shadow.

Figure 4.11a shows the DarkCC segmentation results after eliminating CCs based on the existence of I_{local} pixel value less than $threshold_2$. Then, the shape and size constraints are applied to DarkCC in terms of the length of major and minor axis. DarkCCs that satisfy those constraints are accepted as orbital rocks that are to be matched with ground rocks.

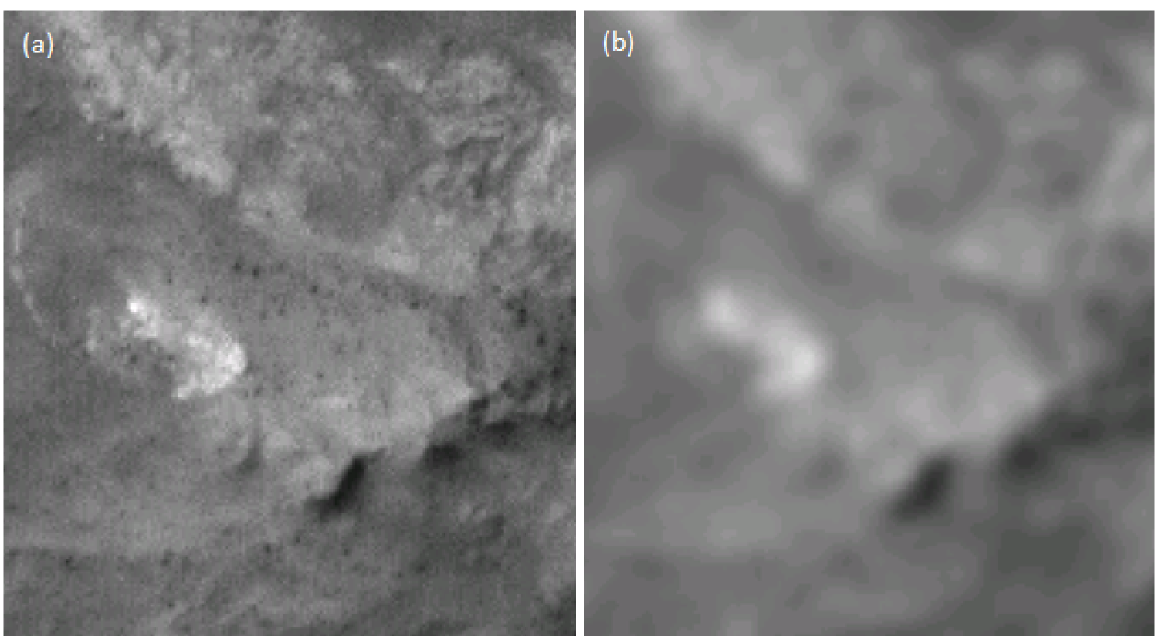

Figure 4.9 HiRISE image of the south part of Home Plate: a) the orbital image I, b) the average pixel brightness I_{avg}

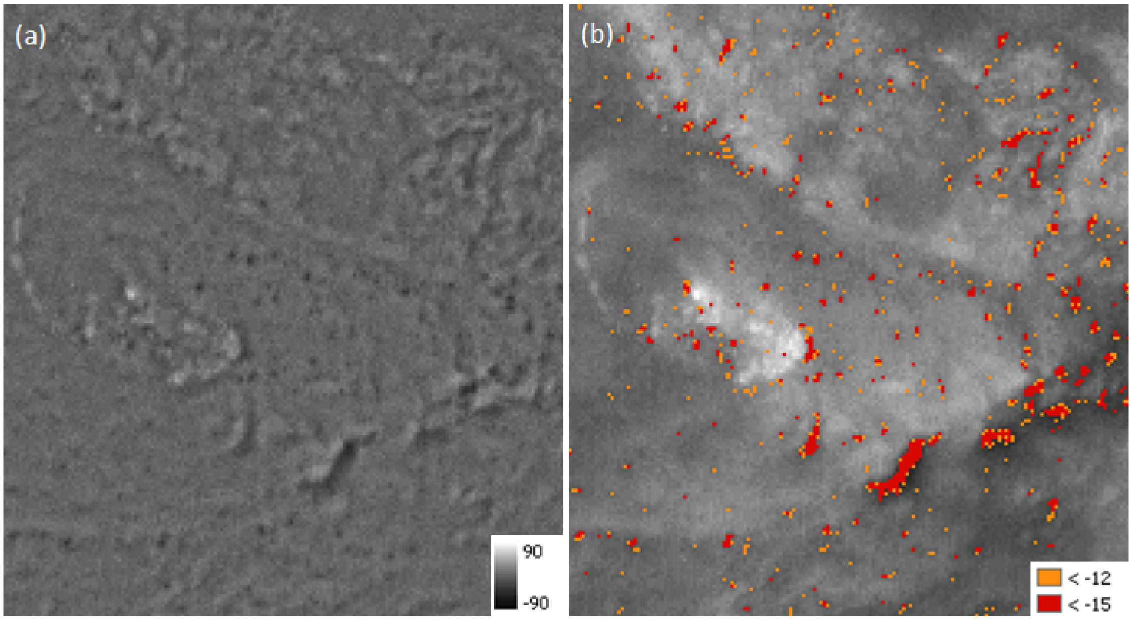

Figure 4.10 a) Local brightness I_{local}, b) the DarkPixel (red and orange pixels) overlaid on the orbital image

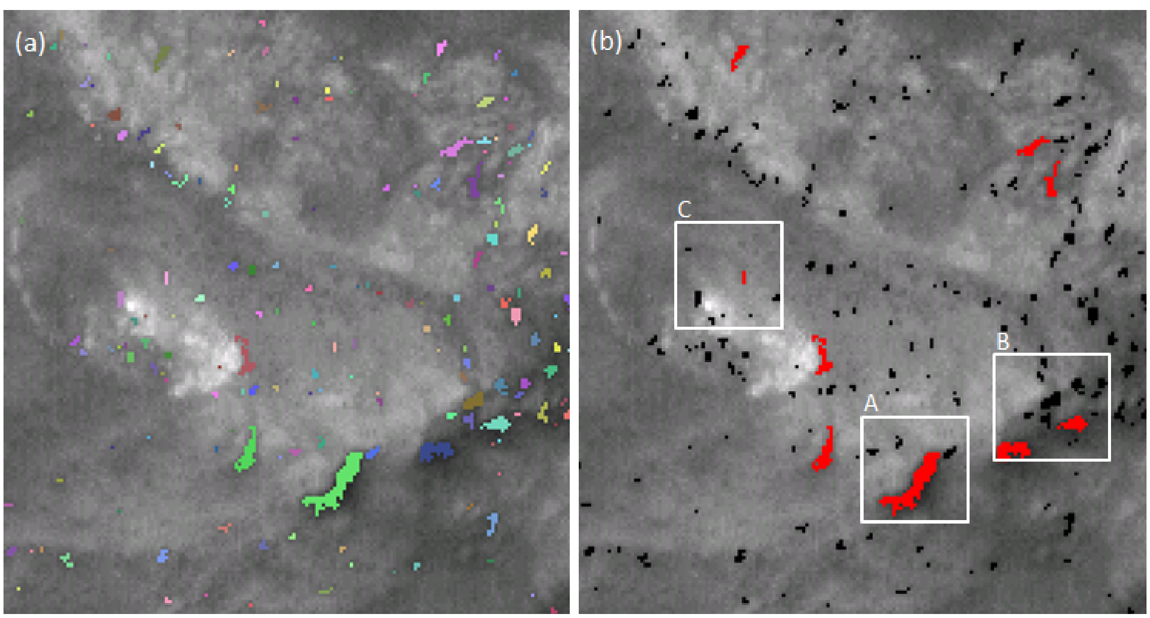

Figure 4.11 a) Dark connected component (DarkCC) with at least one pixel with I_{local} value less than $threshold_2$ (color indicates different DarkCC), b) Orbital rocks (OrbRock) after applying size and shape constraints. (Boxes represent examples in Figure 4.12)

Eight pixels in image space is equivalent to about 4 m in object space. The size constraint on the major axis is applied to eliminate shadows cast from hills and ridges from rocks. Since the extracted orbital rocks will be used as tie points, relatively bigger rocks are excluded for the precision. Figure 4.12 displays the example of DarkCCs with their major axis length and the ratio of the minor axis to the major axis. The examples on the left and middle, the big shadow from small dune is eliminated. Even if these pixels belong to a rock, their size makes it difficult to precisely identify the position of orbital rocks from its shadow. Relatively bigger rocks with the major axis more than eight pixels are also eliminated. In the example on the right, the eliminated DarkCC does not have the typical circular shape of rocks. In experience, it is likely to be either dark ground or shadow on the ridges.

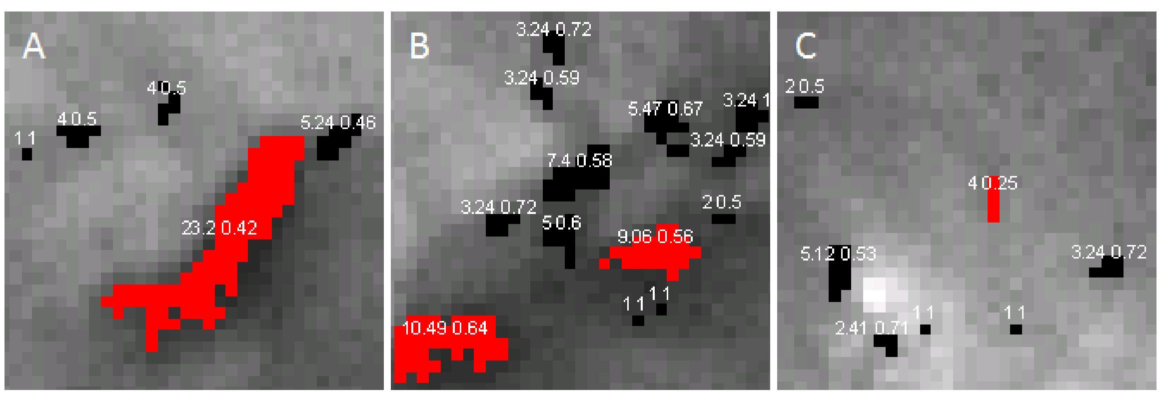

Figure 4.12 Eliminated DarkCC (red) and accepted OrbRock (black). Label indicates the length of major axis and the ratio of minor axis to major axis. (The extent of each example is displayed in Figure 4.11b)

In conclusion, the orbital rocks that can be used as tie points to the ground imagery are identified as connected components of locally dark pixels with at least one prominent darker pixel, small size and relatively round shape. From the test area using PSP_001777_1650 CCD2 image (Figure 4.13), out of 27,297 DarkCCs are generated and 25,963 of them are selected as OrbRocks. The graph in Figure 4.13 shows how the size and shape constraints were affecting the final orbital rock selection. Given that only 5 % of DarkCCs were eliminated, the main component of orbital rock extraction is the image intensity.

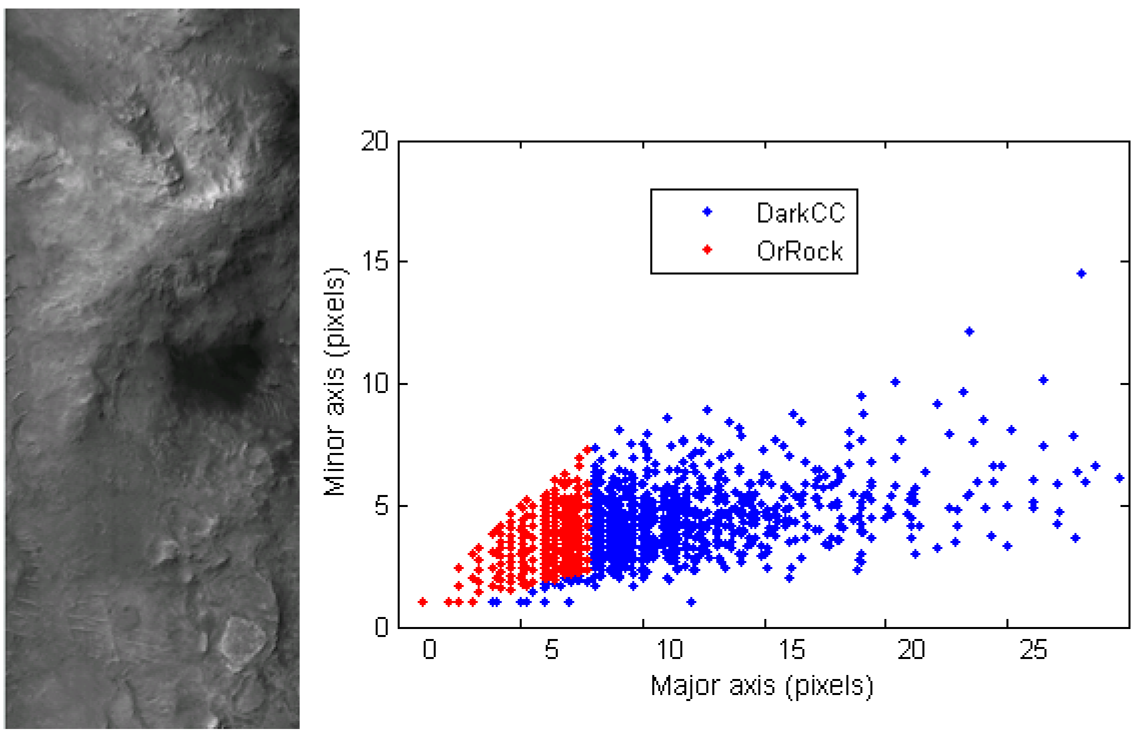

Figure 4.13 Test area of orbital rock extraction (left), Distribution major and minor axis lengths of the DarkCC (blue) and the accepted orbital rocks (red)

The focus of the orbital rock extraction method proposed in this research is obtaining as many orbital rocks as possible, rather than eliminating falsely detected ones. In the ground images, it is possible to determine the size and shape of rocks precisely.

However, the current level of resolution (30 cm per pixel) of HiRISE imagery is not enough for the sizes of the extracted orbital rocks to be representation of the size of rocks identified from the ground images. For example, it is common that two or three small rocks with less than 10 cm in diameter are identified as orbital rocks because of their proximity to each other. Therefore, matching orbital and ground rocks requires an additional method for identifying the correspondence between the two types of rocks.

4.3 Rock Pattern Matching

Once orbital and ground rocks are obtained and terrain matching is completed, rock pattern matching is conducted (Figure 4.13). At this point, it is assumed that the rover position obtained from the rover localization is no more than a certain range from the true location. Since there is no direct connection in size and shape between orbital and ground rocks, only the distribution pattern will determine their correspondence. If the search range for the rock pattern matching is too big, the possibility of matching wrong rocks increases. Therefore, it is important to keep the search range to the minimum. The range is set to 15 m in this research based on the accuracy of the rover localization, which is conducted cumulatively along the rover traverse by applying combination of technologies such as dead reckoning, incremental bundle adjustment, terrain matching and orbital/ground rock pattern matching. Even if one technology fails to provide accurate position, there are still other methods to complement the localization. For example, slippage of the wheels makes the reading of odometer inaccurate, which can be adjusted by bundle adjustment of ground imagery using cross-site rock matching. If there is not enough common coverage between the rover images from different positions, the photogrammetric method cannot be used for rover localization. However, if the terrain covered by ground images shows distinctive shape such as craters, hills or ridges, terrain matching can precisely locate the rover position on the orbital images. If the rover covers only a level terrain with little variation in elevation, the terrain match should not be used for further adjustment of the rover position. However, considering that bundle adjustment successfully corrected the position errors with an accuracy of 0.5% over a 6 km traverse for Spirit rover (Li et al., 2006), frequent updates of rover position on the orbital images could keep the relative positional displacement within, at most, a couple of meters. Still, this small distance could determine success or failure of rover navigation in space mission. That is why there always have been considerable manual efforts to identify ground features in rover images on the orbital topographic products for precise rover localization.

The automatic orbital/ground rock matching starts from configuration of orbital and ground rock pairs within the 15 m range. These pairs are used to determine the translation vectors of the true rover position. Since MER rovers routinely validate their attitudes by finding the sun, the rotation angles of rover images are found to be accurate (Cheng et al., 2005; Li et al., 2007). Therefore, the object-space coordinates generated from rover images and orbital images are assumed to be consistent with each other. Using each vector between the orbital/ground rock pairs, the positions of all the ground rocks are shifted. For each case, the shifted ground rocks are then again paired with orbital rocks if they are within 0.5 m from each other. After comparing the number of orbital/ground rock pairs, the translation vector that produces the most rock pairs is chosen. Based on these sets of matched rock pairs, 2-D affine transformation is performed to complete rover localization. If there are multiple vectors with the maximum number of orbital/ground pairs, the case with minimum residuals in position between matched rock pairs is chosen. Finally, the rover position is adjusted by applying the 2-D affine transformation to the ground image coordinates. Figure 4.14 summarizes the proposed rock pattern matching procedures.

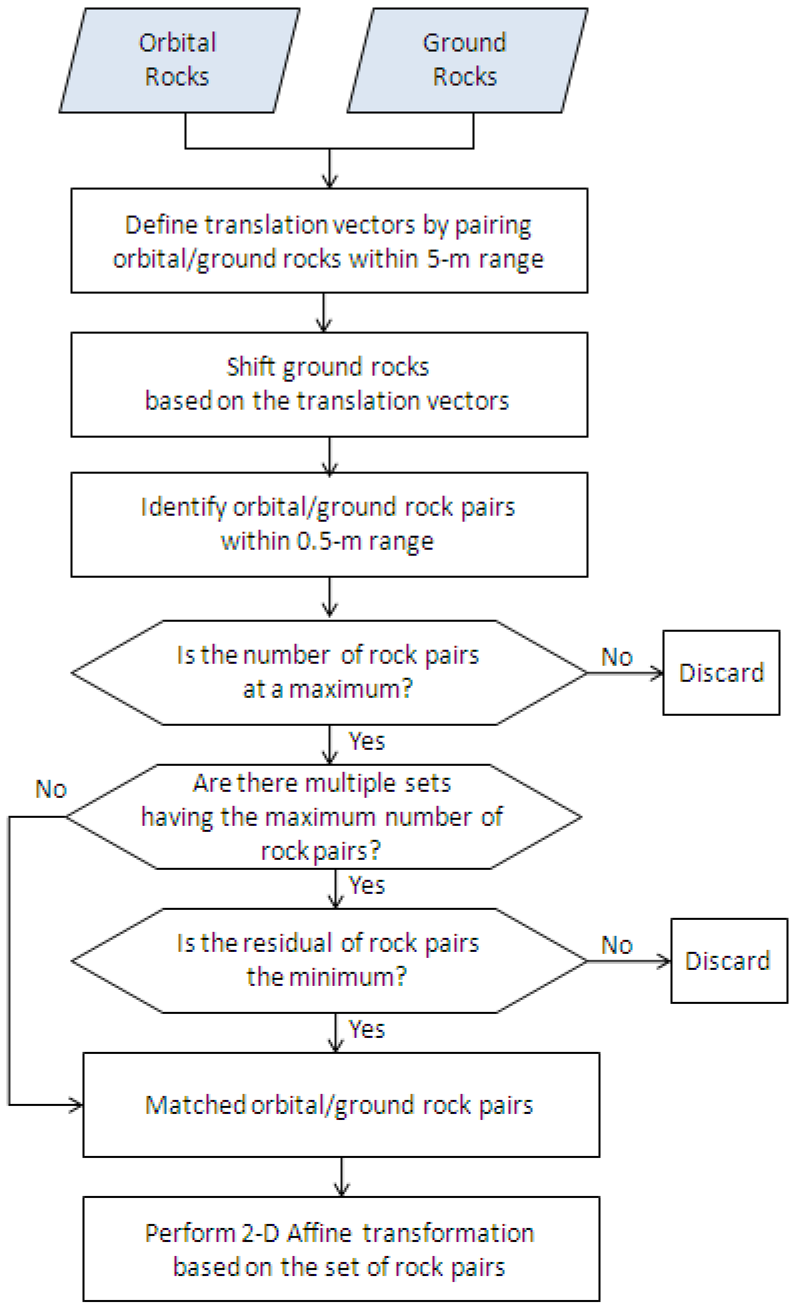

Figure 4.14 Flow chart of orbital/ground rock pattern matching procedure

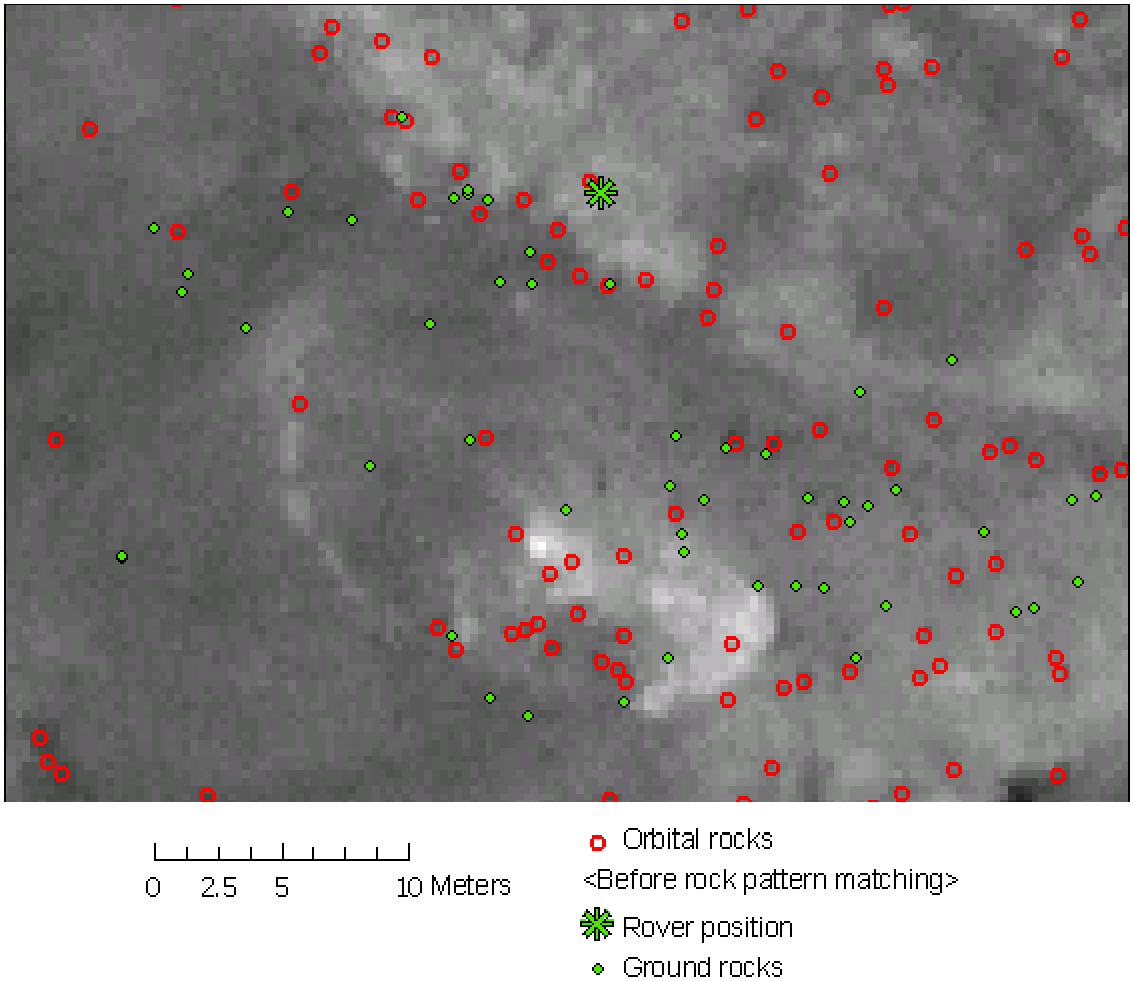

Figure 4.15 Ground rock distributions after terrain matching

Figures 4.15 to 4.17 illustrate how the proposed orbital/ground rock pattern matching works, using the test rover site at sol 1349. In Figure 4.15, the rover position and the ground rocks are overlaid on HiRISE orthophoto based on dead reckoning, incremental bundle adjustment and terrain matching results. As described in the previous section, a total of 55 ground rocks are extracted from sol 1349 Navcam panoramas. The presence of hills and ridges at this site means terrain matching would provide a relatively accurate estimate of the rover position within a couple of meters of residual. Nonetheless, the abundance of both orbital and ground rocks in this area causes challenges for a human operator to figure out their correspondence. The automatic rock pattern matching provides solution for this commonly encountered situation. Using the 15 m search radius, possible translation vectors are calculated based on hundreds of combinations of orbital/ground rock pairs. After applying each translation vector to the ground rocks, the orbital/ground rock pairs that are within 0.5 m are counted.

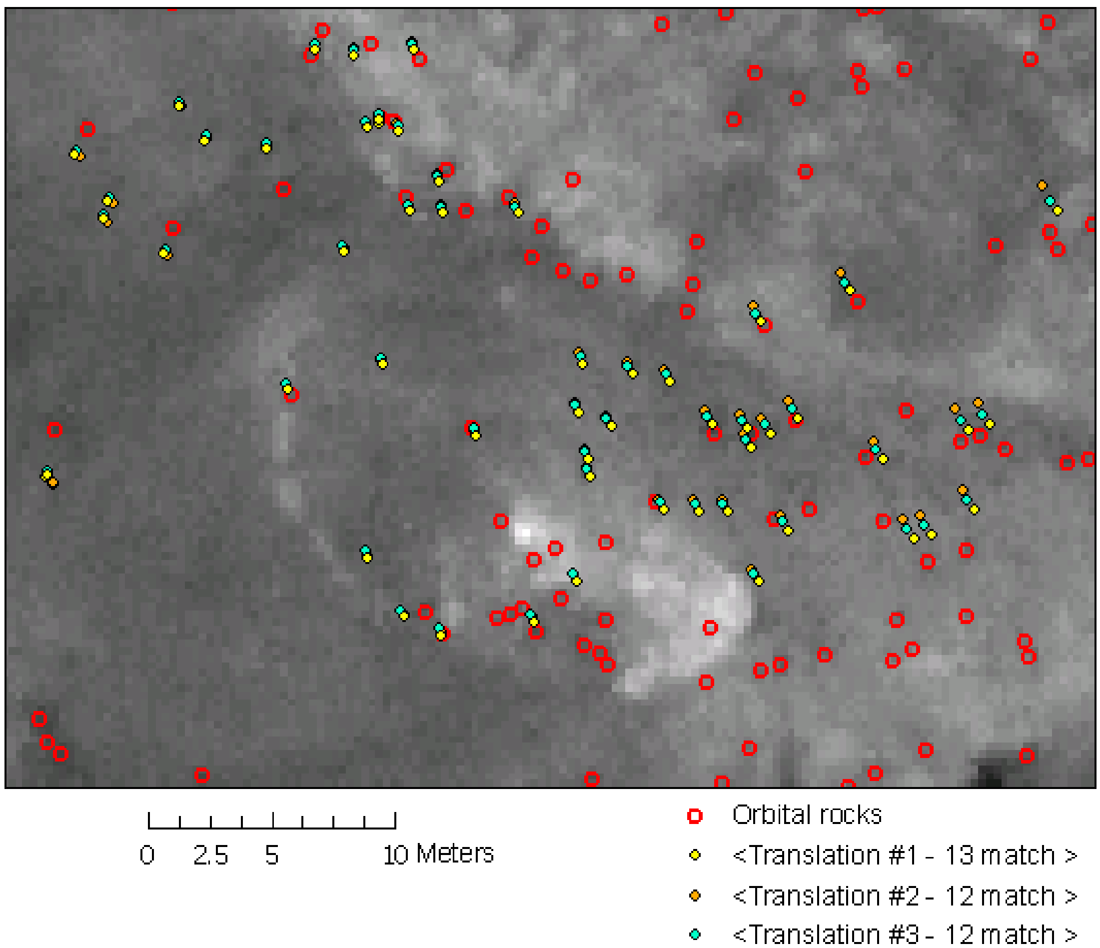

Figure 4.16 Distribution of ground rocks according to the three cases of translation with the most matched orbital/ground rock pairs

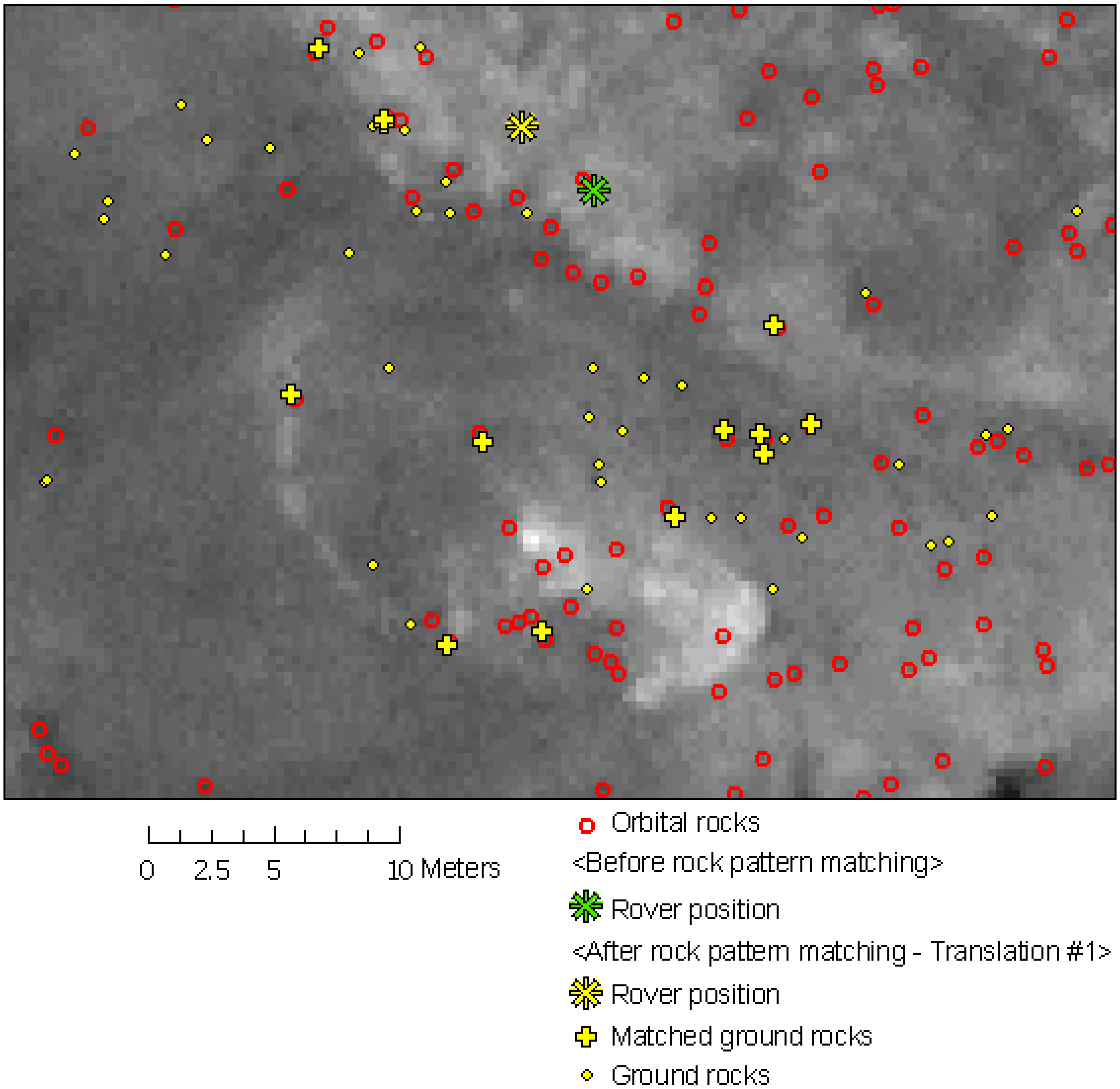

Figure 4.17 Rover localization result after translation and Affine transformation based on orbital/ground rock pattern matching

Figure 4.16 shows the distribution of ground rocks after applying three cases of translation vectors that yielded the highest number of orbital/ground rock pairs. The translation #1 produced 13 matched rocks, while the other two were with 12 matches. According to the rock pattern matching strategy, the translation with the most rock pairs is selected. If there are multiple translation vectors with the most number of matches, the average distance between the rock pairs are calculated so that the one with the minimum displacement is chosen.

After the applying the selected translation to the ground rocks, 2-D Affine transformation is also performed to minimize the residuals between the matched orbital/ground rock pairs. Figure 4.17 shows the positions of the ground rocks and the rover after the translation and Affine transformation. The adjustment of rover position is 3.78 m to the northwest direction.

The test results of the proposed orbital/ground rock matching method using other rover sites will be presented in Chapter 6. The correspondence between the matched ground and orbital rocks is verified from manual identification. The adjusted rover position is consistent with the rover position provided by the MER operation team after labor-intensive procedures. The RMS error of the position of the matched rocks was consistently less than 0.5 m.

Using the proposed method, the rock matching results tested for seven rover sites were successful. However, some guidelines need to be addressed to ensure the quality of the rock matching results for rover localization. There should be a sufficient number of orbital/ground rocks to begin with. In this research, the rock matching is conducted only if the total number of ground rocks is over ten. Also, the distribution of rocks should have a distinctive pattern. It is possible that the selected translation only applies to rocks in a partial area. In such a case, pattern matching may not yield the correct position. Therefore, as a guideline, the distribution of the matched rocks should also be checked.

CHAPTER 5

PARAMETER SELECTION FOR HiRISE STEREO MATCHING

In processing large volume of high-resolution stereo imagery, automation is crucial for generating DTMs and orthophotos economically. The most time consuming and computationally expensive part of orbital data processing is stereo image matching for digital terrain extraction. It involves a variety of parameters, the choice of which can significantly affect the quality of topographic products. Regarding quality of topographic products, there are many aspects to consider: positional accuracy, coverage of matched points and resemblance to the actual terrain. In stereo image matching, no unique set of parameters is optimal because the matching results can vary depending on the input data. This chapter describes parameters selected for high-resolution DTM processing using the HiRISE stereo imagery. The matching parameters such as search window, correlation coefficient threshold and matching window size are discussed. Also, the blunder detection technique, based on 3-D planar fitting, is introduced for eliminating the errors in stereo matching. To assess the performances of the intermediate results in the hierarchical matching process, accuracy and density of tie points at each matching level are analyzed. In this dissertation, tie points refer to conjugate points that belong to same objects in stereo image pair. Tie points are obtained as the result of stereo matching process. The DTM product generated from the automatic stereo matching procedure is compared to the manual matched check points. For the analysis, the automatic stereo matching procedures described in Chapter 3 were performed using a stereo pair of HiRISE images that cover the Columbia Hills area of the Spirit rover landing site (PSP_001513_1655 and PSP_001777_1650).

For planetary surface mapping, the dominant choice for stereo matching software is the BAE Systems SOCET SET for organizations such as USGS (Kirk et al., 2003; 2008), NASA AMES Research Center (Beyer et al., 2010), Arizona State University (Tran et al., 2010). SOCET SET is the best-in-industry photogrammetric software suites for automatic terrain mapping that have been evolved over 20 years. SOCET SET uses the Hierarchical Relaxation Correlation (HRC) algorithm, which is similar to the hierarchical matching in this dissertation. Its early version, Automatic Terrain Extraction (ATE) was based on area-matching, which is the most popular method of stereo matching. Area-based matching uses small windows composed of grey values as matching primitives to perform comparisons over the search area until the best correspondence is reached; cross correlation or Least Square Matching methods can be used. SOCET SET applies Least Square Correlation method (Helava, 1988), while cross correlation is used in this research. Since characteristics of terrain affect the performance of image matching, different strategies were needed for different kinds of terrain. In 1997, SOCET SET included Adaptive ATE, enabling the parameters to be selected from a number of strategies then vary according to the nature of the terrain (Zhang, B., and S. Miller, 1997). For ATE, back–matching is introduced for blunder elimination in terrain, so that point is rejected if the matched point in one image does not coincide with the matched point in other image. Its latest technology, NGATE (Next Generation Automatic Terrain Extraction algorithm) is based on a hybrid approach that uses both image correlation and edge matching (DeVenecia et al., 2007). The problem of area matching is that it assumes the terrain within a matching window is level, which is not always true. Area matching is used to guide and constrain edge matching, and vice versa. Although DeVenecia et al. (2007) reported reduction of about 30 % of manual editing, interactive editing is a crucial part of generating topographic products meeting the National Map Accuracy Standards (NMAS). About horizontal accuracy, NMAS states that "For maps on publication scales larger than 1:20,000, not more than 10 percent of the points tested should be in error by more than 1/30 inch, measured on the publication scale; for maps on publication scales of 1:20,000 or smaller, 1/50 inch." For vertical accuracy, as applied to contour maps on all publication scales, NMAS requires no more than 10 percent of the elevations tested to be in error more than one-half the contour interval (Bureau of the Budget, 1947).

Although the superiority of the SOCET SET photogrammetric suite over the simple area-based matching method is obvious in automatic terrain generation, it is not uncommon for research institutes to develop their own image processing software for specific dataset. The German Aerospace Center (DLR) also developed procedures for HRSC DTM generation including adaptive image preprocessing (Gwinner et al., 2009). Developing all-purpose, all-automatic matching software that can be used for any dataset or terrain is not the objective of this dissertation, nor is to achieve stereo matching results that are comparable to the product of NGATE. For generation of high-quality topographic products meeting NMAS, it is recommended to perform automatic stereo matching using an industry-standard photogrammetry suite such as BAE SOCET SET, Leica Photogrammetry Suite, followed by extensive manual checking and editing. Besides the fact that the cost of such photogrammetry suites requires serious investment, the biggest limitation of using over-the-shelf photogrammetric suite is the lack of flexibility in sensor modeling. It is especially an issue for HiRISE stereo processing in SOCET SET, which provides only generic model of pushbroom scanner. For topographic product generation using SOCET SET, the HiRISE raw imagery was reprojected to a virtual frame to fit it to the generic camera model. This leads to a significant disadvantage in terms of misalignment between adjacent CCDs, resulting uneven terrain surface model. One of the main objectives of this dissertation is to provide a rigorous photogrammetric camera model and a bundle adjustment strategy to resolve the disagreements between the stereo images and between the individual CCDs. The other objective is to establish the connection between orbital images and ground images automatically based on rock extraction and matching for automatic rover localization. In that context, the expectation of stereo matching method used in this research is first to produce evenly distributed tie points for bundle adjustment and second, to generate orthophoto as quickly as possible with no manual editing for rover localization on the orbital map. The expectation for accuracy from 1-m resolution DTM is elevation error to be within 2 meters in 90% of the area.

In Chapter 6, the DTM produced in this research is compared with USGS DTM generated by SOCET SET and manual editing. After co-registration, the elevation difference between them was within ± 5 m and the standard deviation was 0.83 m which means that over 95 % of the DTM elevation was within 2 m from USGS product. The simple area-based matching method in this research benefited from the good stereo geometry and radiometric condition. It should also be noted that the matching strategy and parameters are specifically fine-tuned for HiRISE imagery. On Mars, there is no man-made structure or vegetation. Martian terrain is relatively smooth compared to the lunar surface, which is dominated by impact craters. The matching algorithm in this research is not designed for drastic change of the terrain such as cliffs or handling illumination difference from shadows.

5.1 Selection of Matching Parameters

Controlling the matching parameter setting is important for high-quality DTM generation. Since the stereo matching result is highly dependent on the properties of the input data and the terrain, there is no single set of parameters that is optimal for every occasion. Therefore, it is necessary to discuss the selection of matching parameters specific for HiRISE imagery on Martian terrain. In practice, quality checks for matched points should be conducted to achieve the best possible matching results. Specific modifications of the parameter setting may be needed for a particular dataset. The following sections provide a parameter selection strategy that was used for the DTM generation from the HiRISE stereo imagery.

5.1.1 Window Size for Search Area

As described in chapter 3, coarse-to-fine hierarchical approach is used for automatic stereo matching. The reason for adopting such strategy is to increase matching success rate as well as efficiency. In this research, image parallaxes are defined as the differences in image coordinates between the corresponding points in stereo images (Equation 3.2). In this research, the parallaxes are defined in image coordinates. Therefore, the scale difference between the stereo images affects the magnitude of parallax throughout the extent of the images. The scale of the orbital imagery is directly related to the distance between the orbiter and the targets on the terrain. Figure 5.1a shows the relative orbiter position and imaging geometry for the stereo pair of PSP_001513_1650 and PSP_001777_1655 images. The near-nadir PSP_001777_1655 is closer to the target area by 7 km, which means that the same features on the terrain will occupy more image pixels than in PSP_001513_1650. In the example shown in the figure, the parallax in the top part of the image differs from the parallax in the bottom due to the scale change. The principle of generating DTM from stereo imagery is based on the relationship between the terrain elevation and the image coordinates on the images. Figure 5.1b demonstrates how the terrain elevation affects the parallax in across-track direction. As the terrain gets lower, the parallax increases, and vice versa. Since the terrain (the elevation of the terrain, to be exact) is continuous, the parallaxes also gradually change. Since the baseline of the stereo pair is almost parallel to the x-coordinate in image space, x-parallax shows more association to the variation of terrain elevation than y-parallax. These parallaxes continually increase or decrease along the image space. By using their distribution as a priori knowledge, the approximate position of the corresponding points can be calculated in good precision.

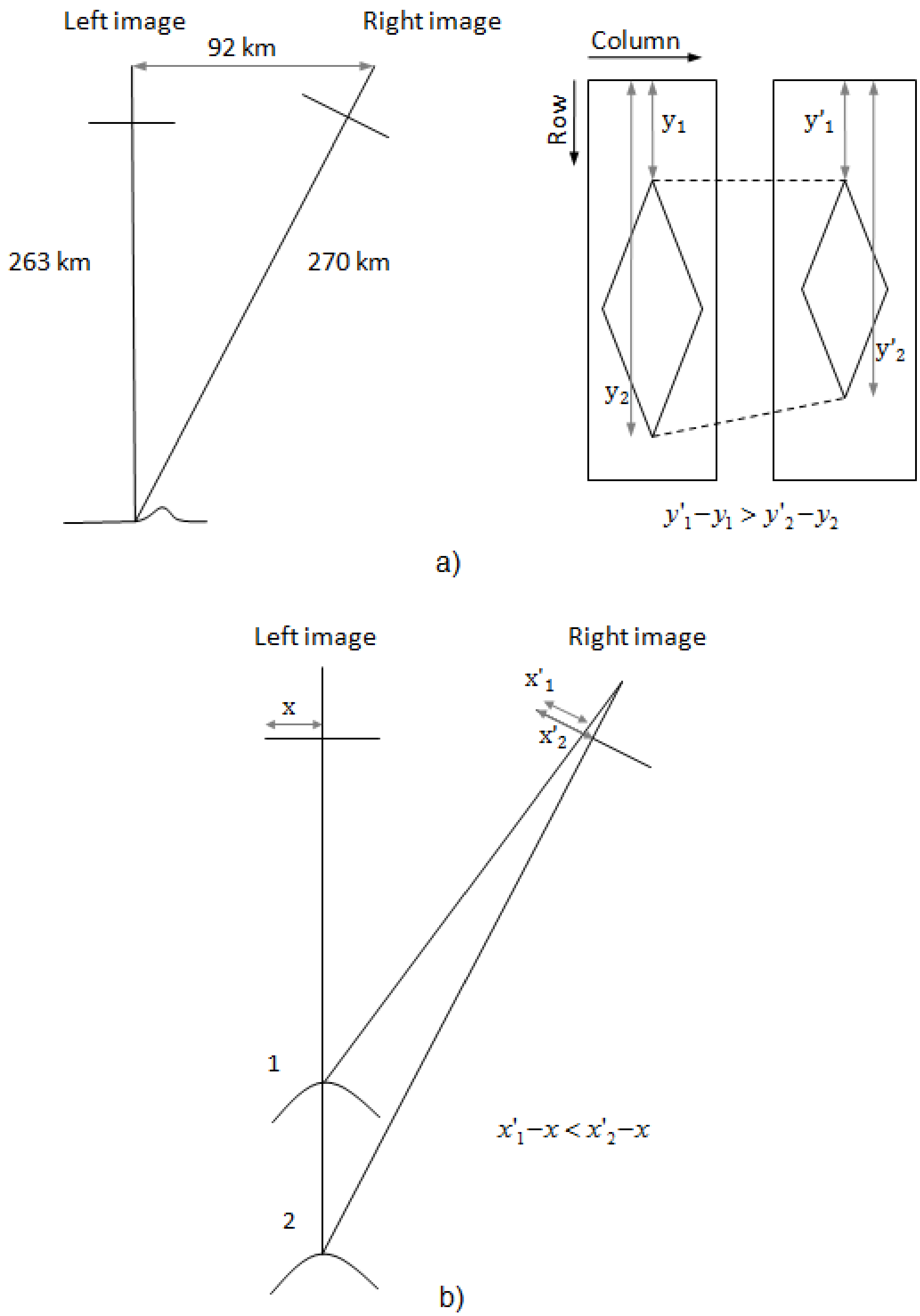

Figure 5.1 a) Relative position of HiRISE stereo and the effect of image scale on parallax, b) the relationship between terrain elevation and parallax in across-track direction

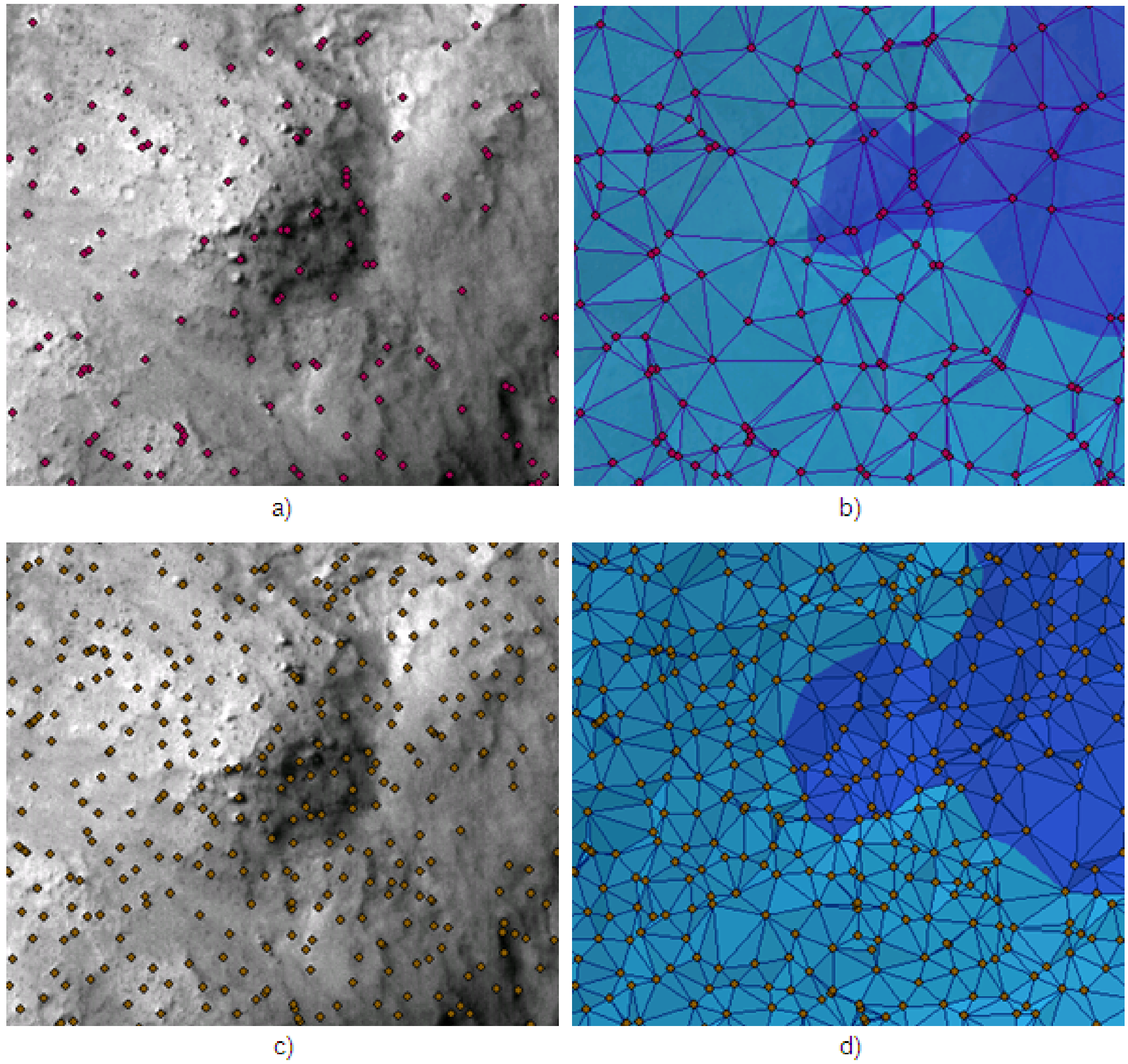

Figure 5.2 a) Level 4 tie points, b) TIN surface of x-parallax from level 4 tie points, c) Level 5 tie points, d) TIN surface of x-parallax from level 5 tie points

Figure 5.2 shows an example of TIN surface formed by tie points at the different hierarchical matching levels. The points in Figure 5.2a and 5.2b are level 4 tie points, whose parallax surfaces are used to estimate the coordinates of the corresponding points for level 5 interest points based on Equation 3.3. By using a priori knowledge of the corresponding points, the search space for automatic stereo matching can be significantly confined, which translates to efficiency in computational load and accuracy by avoiding large blunders. As can be seen from Figure 5.2c and 5.2d, the level 5 tie points form denser and more detailed TIN surface than the previous level. The level 5 TIN surface provides more accurate depiction of the terrain information, which further confines the search space at the next level of the hierarchical stereo matching.

Table 5.1 Average difference of image coordinates between the matched points and the estimation based on the TIN surface. The first numbers are average values (in pixels). The numbers in brackets are standard deviation

Level	x coordinate	y coordinate
1	-0.67 (1.43)	-0.05 (0.66)
2	-0.04 (0.60)	-0.02 (0.47)
3	-0.03 (0.51)	-0.02 (0.43)
4	-0.05 (0.51)	-0.02 (0.42)
5	-0.05 (0.52)	-0.02 (0.46)
6	-0.04 (0.47)	-0.02 (0.44)
7	-0.02 (0.48)	-0.02 (0.43)
8	-0.02 (0.45)	-0.02 (0.42)

In the hierarchical matching, the benefit of using parallax information is fully considered in the selection of search space. To evaluate the accuracy of the estimated coordinates of the corresponding points, the stereo matching result from the test dataset is analyzed in Table 5.1. Except for the initial level, the standard deviations of the differences between the estimated points and the matched points are less than 1 pixel. In fact, the difference is mostly within ±1 pixel, which means the search area of 3 pixels by 3 pixels would be enough in most levels. However rare it may be, 2 or 3 pixels of coordinate differences cannot be ignored. Since distinctive terrain features that result in significant offset from the estimated parallaxes are represented by interest point, their search windows remain larger. However, the search area for grid points can be reduced even further as the grid spacing gets denser. The search window sizes are 3×2 pixels for level 6 and 2×1 pixels window for level 7 and level 8. The search window sizes in this research are presented in Table 5.3.

5.1.2 Threshold of Cross-Correlation Coefficient

For high-quality topographic map production, it is important to generate tie points densely distributed throughout the entire overlapping area of the stereo images. In this research, area-based matching algorithm is used rather than feature-based algorithm. In area-based matching, the gray values of image templates are compared and conjugate image pixels are identified based on similarity in gray value patterns (Zhang, et al., 1995). In the search window, the cross correlation coefficient between the gray values of the pixels is computed against template window. The conjugate point is found if the maximum of the cross correlation coefficients exceeds a certain threshold. If the threshold value is too low, the possibility of mismatch increases. On the other hand, a high threshold could reject correctly matched point because of subtle differences in gray value patterns between the stereo images. DLR is one of the few research institutes that continue to use in-house software for stereo image matching. Gwinner et al. (2009) derived and validated high-resolution digital terrain models from Mars Express HRSC data. Their implementation includes adaptive parameter setting using parameter rules. The size of the search window is adjusted by an epipolar constraint. To find optimal matching threshold values for the HiRISE dataset, the distribution of the correlation coefficients for all of the matched interest points was analyzed.

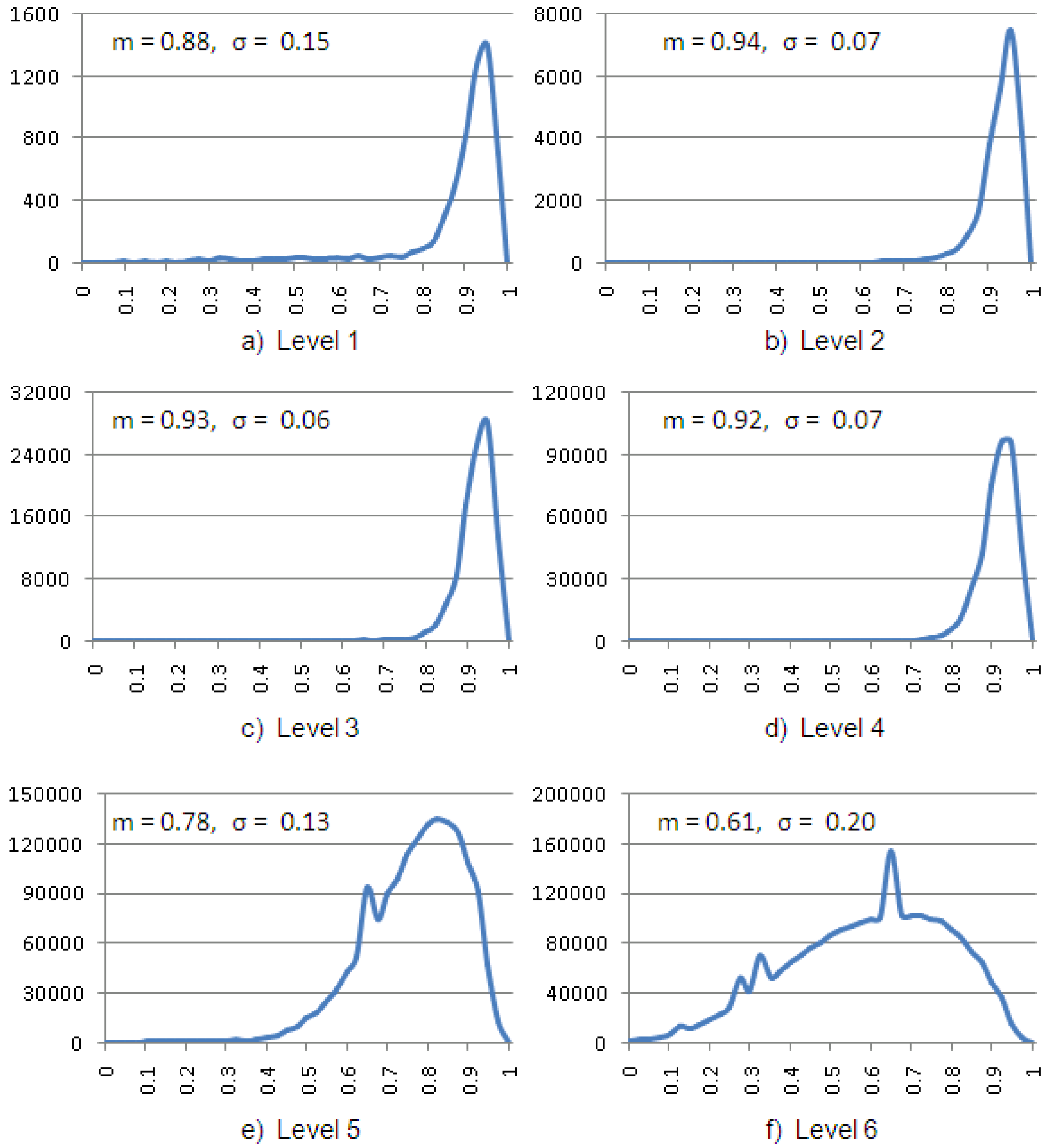

Figure 5.3 Histogram of correlation coefficient values from level 1 through level 6 (x axis: correlation coefficient, y axis: number of points, m: mean of correlation coefficient, σ: standard deviation of correlation coefficient)

Figure 5.3 shows a set of histograms of correlation coefficients for the first six levels of hierarchical matching using the PSP_001513_1650 and PSP_001777_1655 stereo image pair. As defined in Figure 3.1, level 1 through level 4 is based on lower-resolution images from image pyramids. At these levels, histograms of the interest points show a quite clear high correlation curve with mean correlation coefficients closed to 0.9. It is because the conjugate points of interest points extracted from the resampled images are in fact highly distinctive features. Therefore, a threshold value of 0.8 was selected since it is exclusive enough to incorporate only highly correlated pixels without eliminating more than 5 % of the interest points. Original stereo images, in comparison to the resampled images from the previous levels, retain more details. And interest points extracted at this level are generally not as distinctive as the ones from level 1 through level 4. At level 5, where the original images and only interest points are used, the curve has the similar shape as the previous levels. However, the correlation coefficients have lower values with the average of 0.78. A hierarchical matching strategy based on parallax interpolation increases matching accuracies by confining the extent of the search area. After completing level 2 matching, the tie points were already formed along the major features (See Figure 5.8)**.** Image parallaxes, which are directly affected by the elevation, can be interpolated from these feature points. For the HiRISE stereo image matching, the manual check and analysis led to a conclusion that the parallaxes can be accurately approximated up to a pixel in this level of hierarchical matching, based on the interest points depicting the terrain. Therefore, the threshold for the correlation coefficients was lowered to 0.6, which was also used by DLR as correlation coefficient threshold for HRSC stereo image matching, to prevent rejecting too many correctly matched points that have tolerable differences in pixel value patterns (Gwinner et al., 2009).

5.1.3 Window Size for Matching Template

In this research, an area-based matching algorithm is used based on the cross-correlation of template windows of stereo images. A point is represented by the gray value pattern in the template window centered on the point. Anything outside the window is assumed to be irrelevant in image matching. Since selection of the windows influences tie points generation from stereo matching and the resulting topographic products, defining the size of the window is an important issue. Increased window size means more pixels in the neighbor are included in the correlation process. It may subdue the local variation of the elevation, which is represented in the matching result. If the window size is too small, there might not be enough context information for accurate matching. Selection of different matching window sizes, for example 3 pixels versus 50 pixels, would influence the texture of the DTM.

Figure 5.4 shows DTMs of Home plate area of southern Husband Hill of Spirit rover landing site generated from the same dataset (PSP_001513_1655 and PSP_001777_1650) with grid size of two pixels. Three different matching windows are used with size of 11×11 pixels, 15×15 pixels, and 18×18 pixels. Gwinner et al. (2009) also used 13 to 15 pixels of cross correlation window. The grid spacing is two pixels. Considering the ground resolution, the matching window size range from about 2.75 m to 4.5 m. Overall, the DTMs generated from these matching windows are very similar except for subtle details. Global terrain and trends are presented in all three DTMs. All three DTMs show some degree of artifacts in the lower right-hand corner caused by the lack of image texture. A number of techniques, ranging from edge-based matching to smoothing the input image before matching, could produce fewer artifacts than the simple area-based sub-pixel matching used in this paper. The OSU Mapping and GIS Lab has been researching on dealing with matching in low texture regions and reducing the artifacts caused by pixel locking effects. The DTM from the 11-pixel matching window shows the most detailed depiction of the terrain, e.g., the top of the ridge in the north-east part of the area. On the other hand, the one with the bigger matching window (18×18 pixels) also shows artifacts on the lower right-hand corner. However, details of terrain features are also lost to some degree because of the smoothing effect of the larger matching window.

The similar results from the three sizes of matching windows on the DTM production can be observed from the elevation profiles along the same line from Figure 5.4a. In Figure 5.5, the vertical profiles from the three different DTMs from Figure 5.4b, 5.4c, and 5.4d are not visually distinguishable from each other. In this stereo pair, the convergence angle is 19.8°, which translates to a predicted elevation precision of about 0.9 m when RMS matching error is 1 pixel. For matching error of 0.45 pixels, the elevation precision is about 0.45 pixels. The variations between these profiles are well within the range of the expected elevation precision. In other words, matching window sizes of 11 pixels, 15 pixels and 18 pixels do not impose a distinguishable effect in the vertical accuracy of the terrain profile. Hence, the selection of matching window size is subject to the average size and the frequency of terrain features. In this research, the matching window with 15-pixel wide square is selected because the DTM still provides the detail of the terrain without distracting level of noise on the smooth surface.

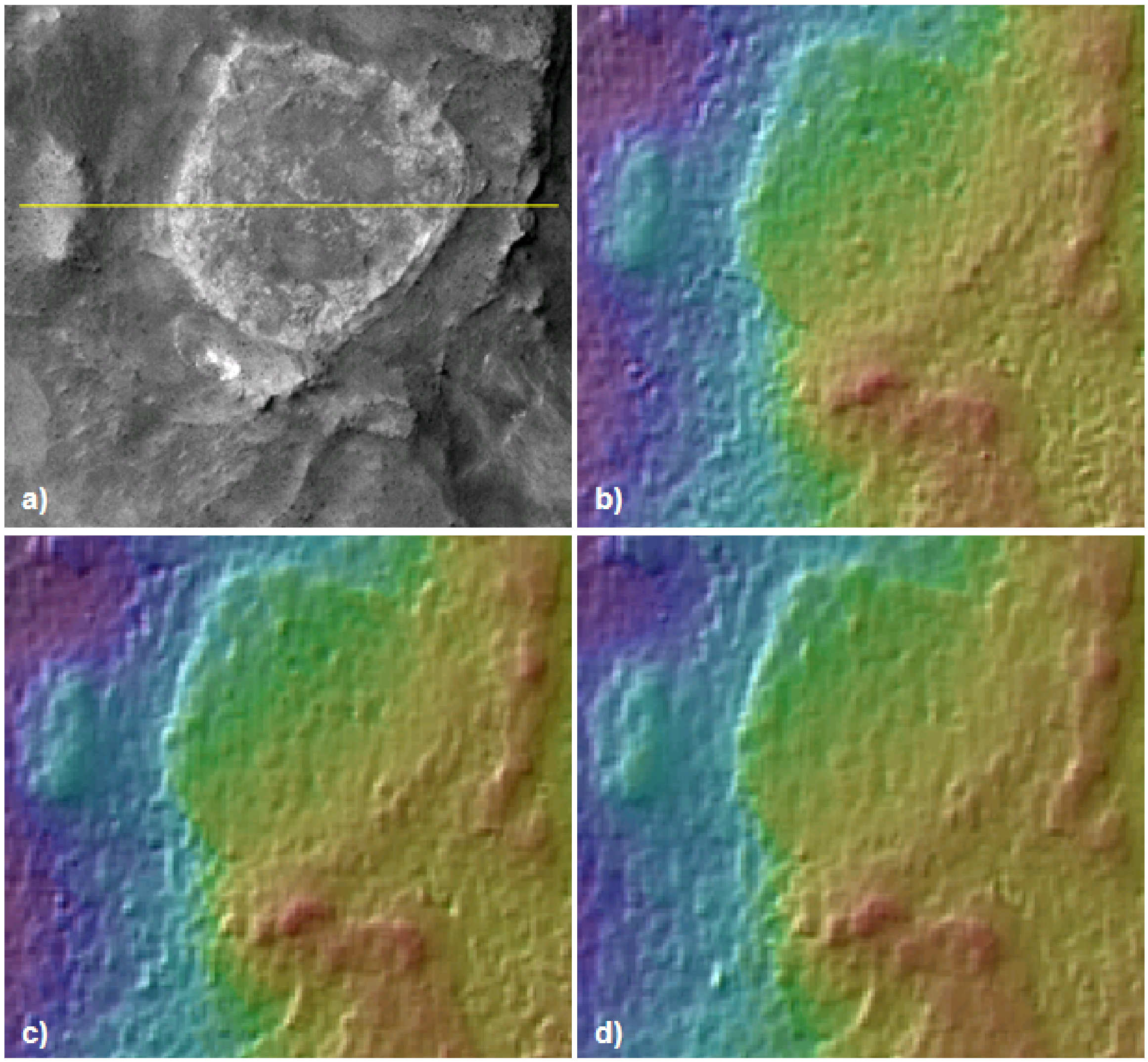

Figure 5.4 Color shaded relief maps of the Home Plae area in Spirit landing site: a) Orthophoto of the area (yellow line is the measurement of terrain profiles in Figure 5.5) DTM generated from b) 11×11 pixels matching windows, c) 15×15 pixels matching window, d) 18×18 pixels matching window

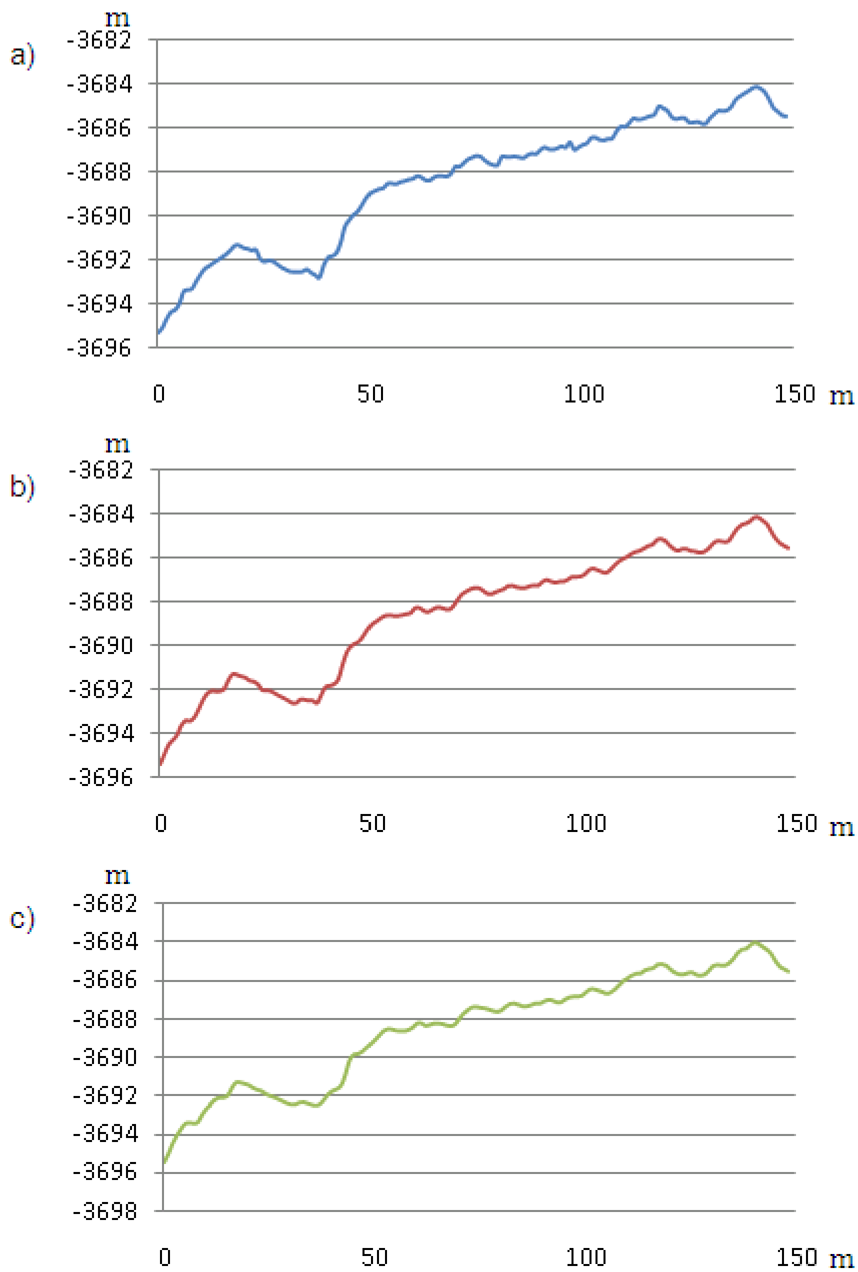

Figure 5.5 Terrain profile from the DTMs generated from a) 11×11 matching windows, b) 15×15 matching window. c) 18×18 matching window. Horizontal axis is the distance (in meter) along the measurement line and vertical axis is the elevation (in meter)

5.2 Selection of Blunder Elimination Criteria

In general, it is agreed that totally automated matching can produce very good results in simple terrain with sufficient gray value variation and adequate image acquisition geometry (Heipke et al., 2007). However, in reality, there are complex situations such as occlusion, shadows, poor texture, atmospheric dust and steep terrain. If the illumination pattern is not exactly the same because of the differences in the viewing angle and the position of the sun, stereo image matching based on cross-correlation coefficient alone could produce matching errors. In order to eliminate blunders from the stereo matching results, outliers are detected based on 3-D plane fitting of object points (Figure 5.6) . Outliers are the values that are statistically far from most others in a set of data. The logic behind the plane fitting is the terrain is continuous and spatially correlated in a small area.

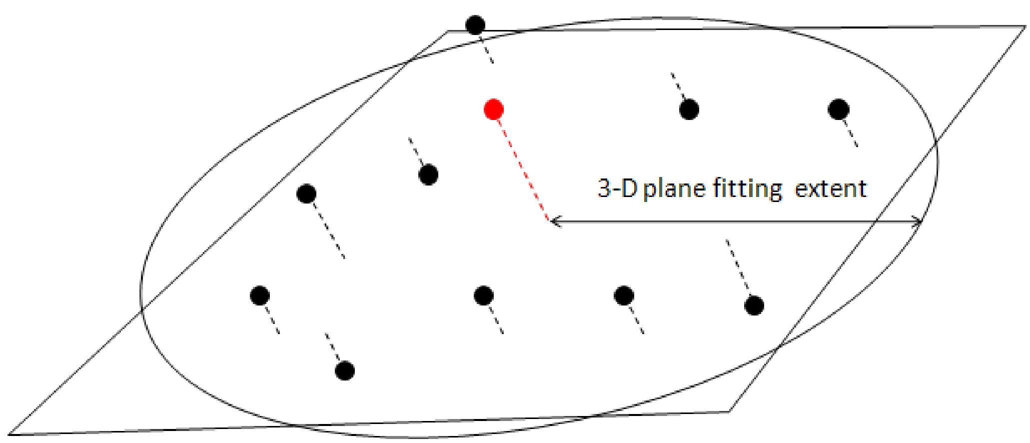

Figure 5.6 3-D plane fitting of object points. Lines represents the offsets, the shortest distance from object points to the fitted plane. Red circle means outlier

In this research, each matched points are tested against the fitted plane from the neighboring object points within a certain distance. Since the spatial distribution pattern of the object points could vary depending on the type of local terrain, the elevation offset from the fitted plane is compared with the standard deviation of the neighboring points. If the offset is outside of 3σ, the matched point is considered as a blunder and discarded from the set of tie points.

Figure 5.7 shows an example of blunder detection and elimination at level 2. Blunder detection is especially critical in the earlier stages of hierarchical matching process. Due to lack of a priori terrain information, the parallax surface is not stable in early matching levels. Since accepted tie points are passed onto the subsequent levels, the success of the automatic stereo matching is directly related to the matching performance at the earlier stages. Figure 5.7a is the interpolated DTM generated from all the matched points before blunder detection. The boxed area in the center clearly indicates abrupt change of the elevation, which was indeed identified as a matching blunder (Figure 5.7c and 5.7d). Compared with a fitted 3-D plane from the surrounding object points, the elevation difference was more than 3σ (σ is the standard deviation of the neighboring points' elevation). After the blunder is eliminated, the unnatural bumps of the terrain were removed as well.

In detecting matching blunders, two parameters need to be considered. One is how to choose neighboring points, which are fitted into 3-D plane. The other is the definition of the outliers compared to the standard deviation of the elevation.

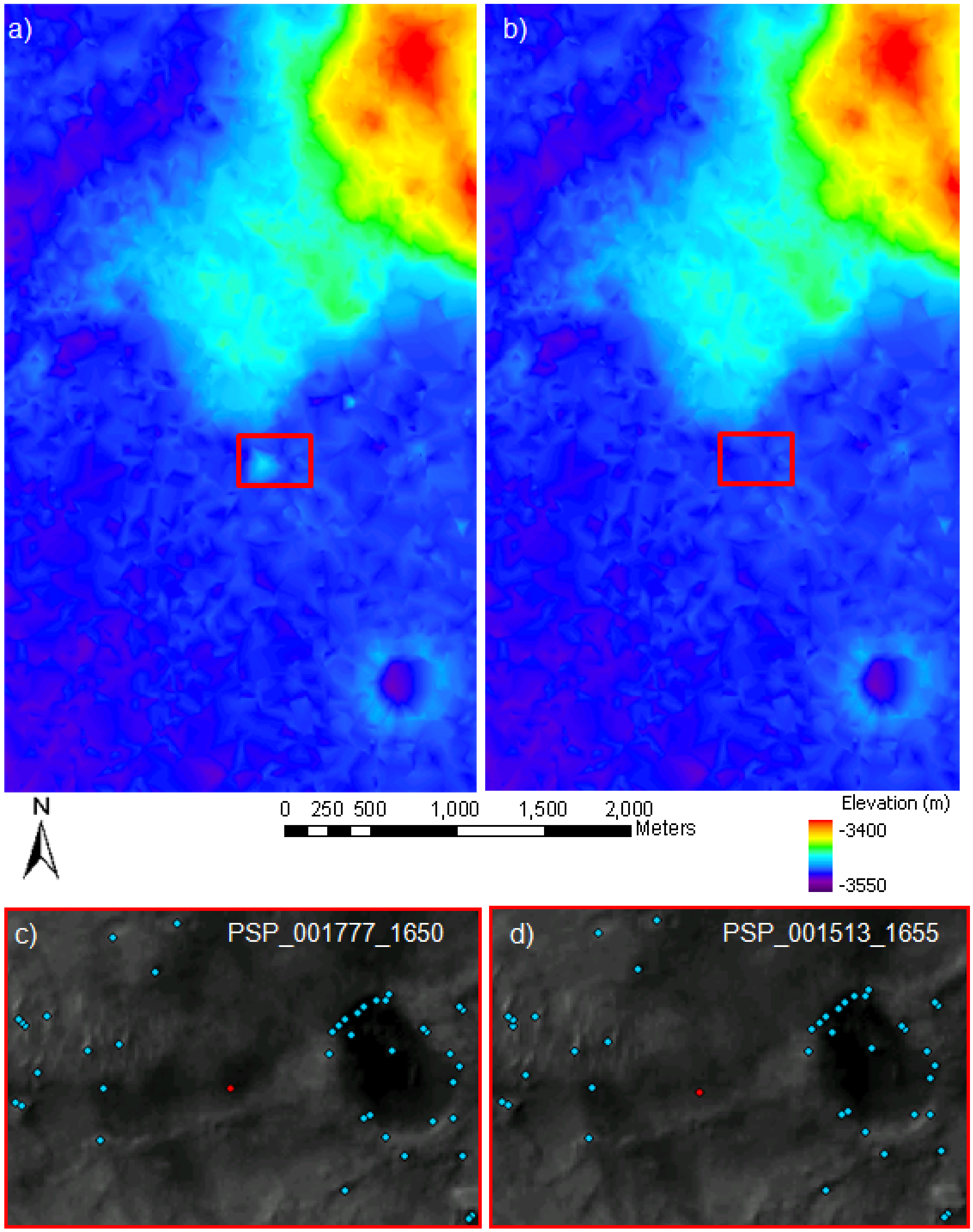

Figure 5.7 Example of blunder elimination at level 1 (blue point: accepted, red point: rejected) a) DTM before blunder detection, b) DTM after blunder elimination, c) matched points on PSP_001777_1650, d) matched points on PSP_001513_1655

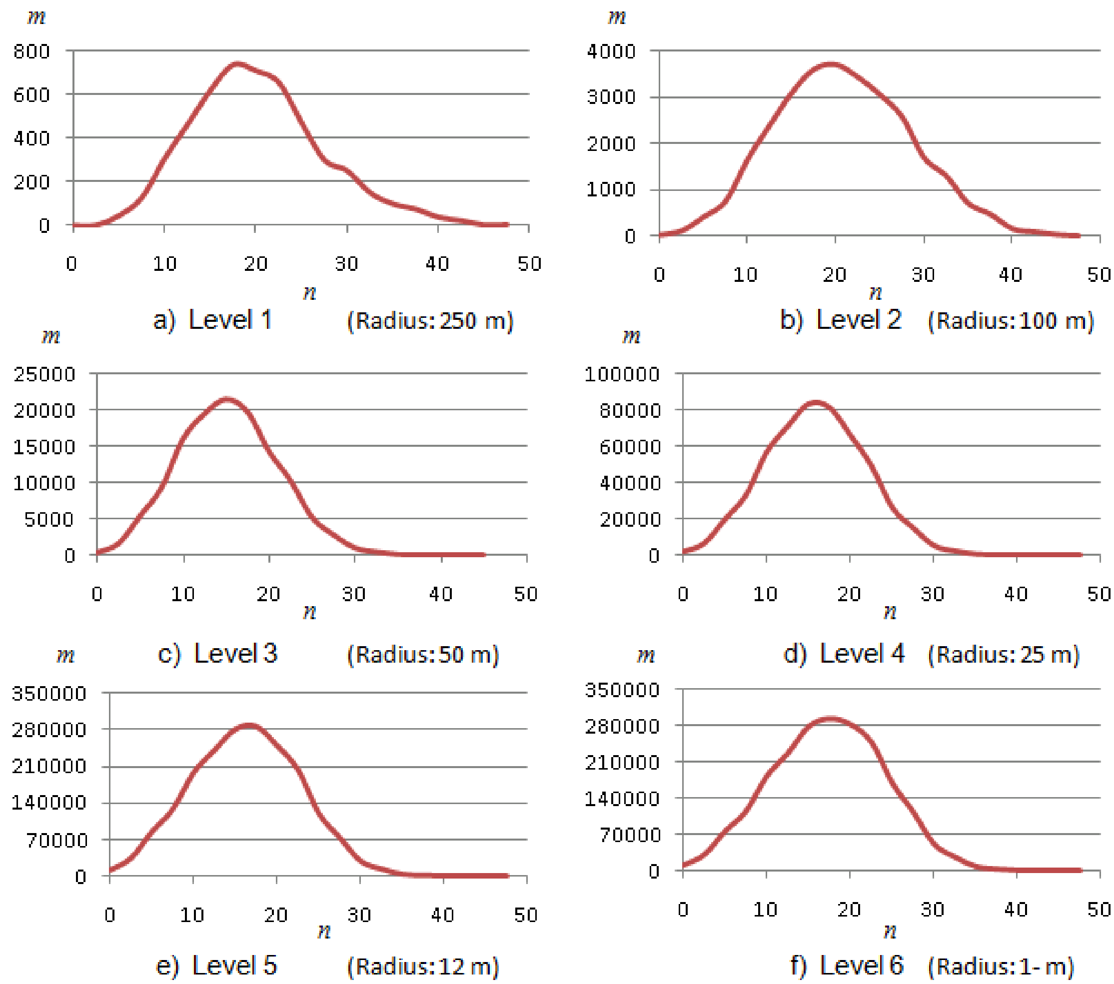

Figure 5.8 Histogram of number of neighboring points for level 1 through level 6. Horizontal axis *n*: the number of neighboring points within the radial distance specified in Table 5.2. Vertical axis *m*: the count of matched points that were tested for blunder based on 3-D plane fitting

In defining the neighboring points, planar distances from the test point are used (Table 5.2). The distances are selected to include about 20 points as neighboring points on average (Figure 5.8). Depending on the density of matched points, the distances decrease toward later stage of hierarchical matching. At level 1, a 250-m radius was searched for the fitting of 3-D plane, while 10-m radius was enough for level 6. Constant values of the distance are used at each matching level for computational simplicity and consistent definition of the neighboring terrain, regardless of the density of matched points. The number 20 was selected to ensure that there are always more than several points in the neighbor. If more than 50 points are included, the 3-D planar fitting of the terrain would mean over-simplification. Using about 20 points, the local terrain variation can be easily fitted into a plane.

By confining search area based on the TIN parallax surfaces, the estimated corresponding points are already in good position. Also, the cross-correlation threshold for the interest points is strictly set to 0.8 at interest point matching levels. These factors reduce the possibility of blunder in stereo matching. Based on statistic analysis on blunder detection, elevation differences within the range of $\pm 3\sigma$ (three times of the standard deviation of elevation) were accepted. The offset (the shortest distance from object points to the fitted plane) of the neighboring points were mostly well within $\pm 1\sigma$ range. However, correctly matched points were often out the range of $\pm 2\sigma$ depending on terrain variation. Although the test dataset (PSP_001777_1650 and PSP_001513_1655) represents typical HiRISE imagery, it is also one in better condition with good imaging geometry, sufficient variation of gray value and little noise in illumination.

5.3 Quality Measurements of Image Matching

According to the discussion in section 5.1 and 5.2, the selected matching parameters for the HiRISE stereo matching of PSP_001513_1650 and PSP_001777_1655 are presented in Table 5.2. They are provided as a general guideline for derivation of high-resolution DTM from HiRISE dataset, thus the selected parameters should be applied with caution according to characteristics of the images to be matched.

Table 5.2 Selected matching parameters for HiRISE stereo image processing

Level	1	2	3	4	5	6	7	8
Match point type	Interest	Interest	Interest	Interest	Interest	50×50 pixels grid	10×10 pixels grid	2×2 pixels grid
Image scale	1/16	1/8	1/4	1/2	1	1	1	1
Matching window size	11×11	13×13	15×15	15×15	15×15	15×15	15×15	15×15
Search window size	11×11	7×7	5×3	5×3	5×3	3×2	2×1	2×1
Correlation coefficient threshold	0.8	0.8	0.8	0.8	0.6	0.6	0.6	0.6
3-D plane radius	250 m	100 m	50 m	25 m	12 m	10 m	6 m	4 m
Plane fitting threshold	3σ	3σ	3σ	3σ	3σ	3σ	3σ	3σ

The size of the matching window is selected based on the empirical observation of average size and frequency of terrain features. For the original scale, the matching window size of 15×15 pixels is selected (section 5.1.3). The size of the search window is reduced from 11×11 pixels in level 1 to 2×1 pixels in level 8 based on the epipolar constraints and TIN surface model (section 5.1.1). The correlation coefficient threshold is set as 0.8 for level 1 through level 4 and 0.6 for level 5 through level 8, based on the distribution of correlation coefficients (section 5.1.2). According to Figure 5.8, there are about 20 neighboring points in the 3-D plane radius, which is sufficient for the plane fitting. At all levels, elevation differences out of the range of ± 3σ were rejected (section 5.2). The quality of the obtained tie points using the described parameters is analyzed based on point density and point accuracy.

5.3.1 Density of Matched Points

The hierarchical matching results of five levels of interest point matching and three levels of grid-point matching are shown in Table 5.3. Since there is no matched point from the previous level at level 1 (1/16 images), the size of search window is set much larger than the other levels due to the lack of detailed terrain information. At level 1, the number of interest points to be matched is 7,246, and 867 points (11.97% out of 7,246) are discarded as a mismatch, due to correlation coefficient values less than the threshold (0.8). Among the 6,379 matched points, 7 points (0.11% out of 6379) are discarded as a blunder based on 3-D plane fitting. At the next level, the final 6,372 points are projected into 1/8 images and rematched based on the new images. 21 points (0.33 % out of 6,372) are discarded based on correlation coefficients, and 6,351 points are rematched on the new image. Again, 30,942 interest points from 1/8 images are matched on the stereo images and except for 2041 (6.6% out of 30,942) unmatched points, 28,901 matched points are newly added at this level. Combining them with 6,351 rematched points, 35,252 points are matched at level 2. After blunder elimination of 43 points (12% out of 35,252), the number of final level 2 points is 35,209. Matching blunder detected by 3-D planar fitting of object points in the first two levels was over 0.1 percent, which is a significantly higher percentage compared to that of subsequent levels (less than 0.1 %). However, as the hierarchical matching proceeds, the blunder is more and more reduced.

From level 2 to level 5 interest point matching, where matched points from the previous levels were re-matched using the higher resolution images, the percent of elimination increased due to the introduction of more detail. As the image size doubled, the number of new interest points quadrupled. The percent of elimination of newly added interest points jumped at level 5 (9.15%). This can be explained by the slight variations of pixel brightness values in the full-scale images that led to a relative decrease in the cross-correlation coefficient values of the corresponding points at level 5. Although the PSP_001513_1655 and the PSP_001777_1650 images are taken only 20 days apart; the viewing angels and the position of the sun are quite different, which affect illumination and pixel brightness values.

Levels 6 to 8 are grid point matching using the same original scale images. Therefore, there is no need to rematch the matched points from precious levels. Since grid points are not as distinguishable as interest points, their cross-correlation coefficients are more influenced by slight variation of pixel brightness values. This leads to the higher percentage of matching error in the grid point matching; 37.67% for 50-pixel grid, 38.92% for 10-pixel grid, and 37.95% for 2-pixel grid. However, DTM errors remained low, indicating that using the parallax surface in the hierarchical process benefited the performance of matching.

Table 5.3 Matching results: number of points and percentage of elimination

Row	Level n	1	2	3	4	5	6	7	8
1	Points matched at $(n-1)^{th}$ level, but not matched at n^{th} level		21 (0.33%)	146 (0.42%)	567 (0.36%)	8121 (1.26%)	n/a	n/a	n/a
2	Points matched at $(n-1)^{th}$ and n^{th} levels		6351	35064	158178	639006	2448341	2653168	7663649
3	New points to match at n^{th} level	7246	30753	126937	501034	1974958	314244	7766683	159330281
4	New points not matched at n^{th} level	867 (11.97%)	1852 (6.02%)	3160 (2.49%)	12064 (2.41%)	165611 (8.39%)	109417 (34.82%)	2756200 (35.49%)	60530051 (37.99%)
5	New points matched at n^{th} level	6379 (88.03%)	28901 (93.98%)	123777 (97.51%)	488970 (97.59%)	1809347 (91.61%)	204827 (65.18%)	5010483 (64.51%)	98800230 (62.01%)
6	Total matched points (row 2 + row 5)	6379	35252	158841	647148	2448353	2653168	7663651	106463879
7	Eliminated points at n^{th} level	7 (0.11%)	42 (0.12%)	96 (0.06%)	21 (0.003%)	12 (0.000%)	0 (0.000%)	2 (0.000%)	65 (0.000%)
8	Final points at n^{th} level	6372	35210	158745	647127	2448341	2653168	7663649	106463814

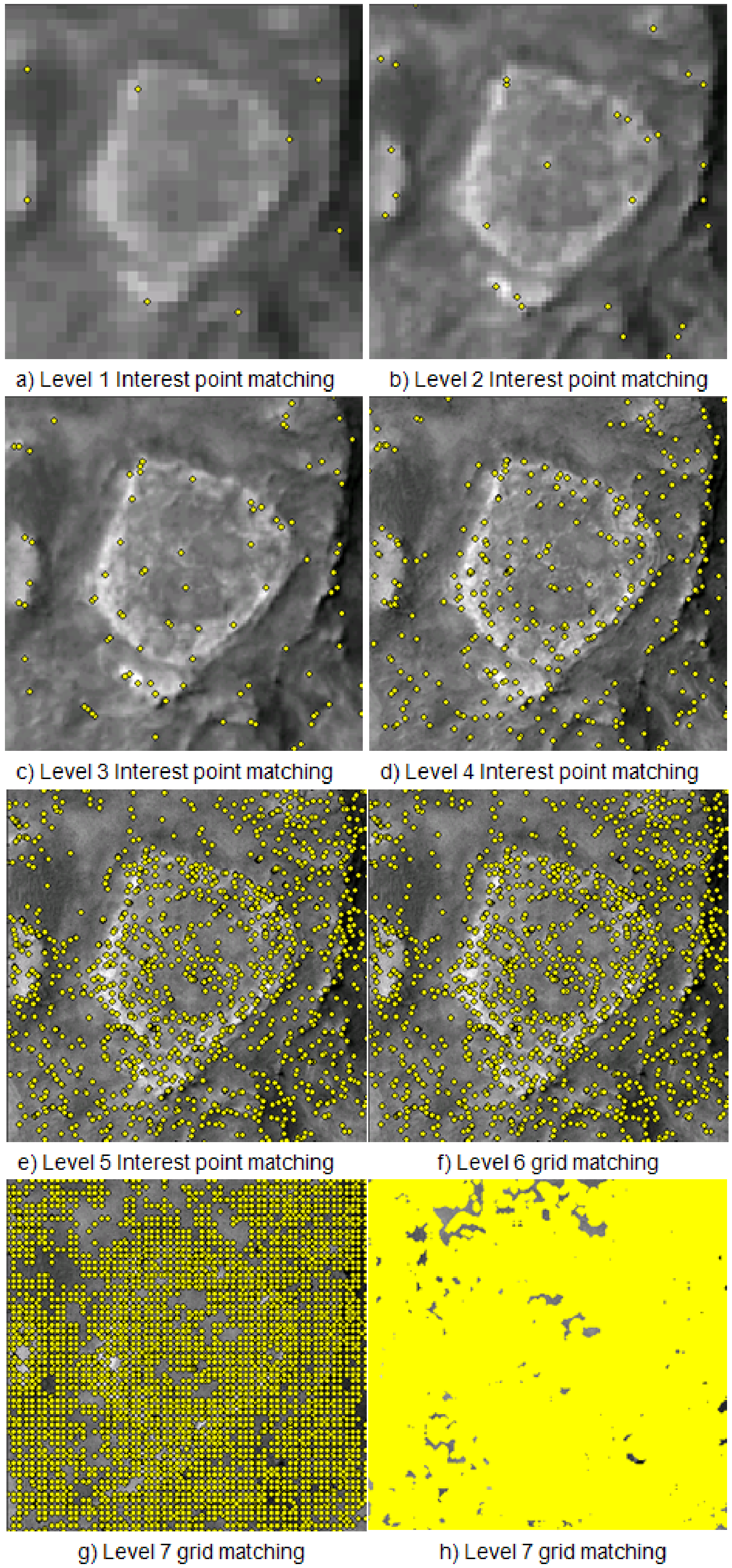

Figure 5.9 Tie points from hierarchical image matching levels

Figure 5.9 shows the coverage of tie points at each hierarchical matching level. Tie points at Level 1 through level 4 are interest points from images of reduced resolution. They provide robust structure of terrain from coarse level with a few feature points to finer level with an increased amount of detail. Although level 5 tie points describe most of the terrain features, area with the no interest points needs to be covered for the completeness of image matching. Therefore, coarse-to-fine grid matching is conducted from level 6 to level 8, where the tie points are obtained with complete coverage, except for featureless areas. With the correlation coefficient threshold of 0.6, the matching success rate for grid points is about 62% to 65%. The rejected points are not necessarily matching errors, but their cross-correlation values are lower due to the inherent difference between the stereo images. There are many reasons why the orbital image of the same area could have unequal distribution of pixel brightness values. The most obvious one is the difference of the sun angles and the viewing angles. Also, the surface of the terrain could be changed due to the wind. The sensitivity of the CCD may differ in each pixel of the array. All of these factors contribute to the low correlation.

Figure 5.10 shows areas with higher matching success rates, and Figure 5.11 shows areas with lower matching success rates. The difference between the two figures is the texture in the images. The areas with higher matching success have distinguishable terrain features and changes in the brightness values. However, the areas with higher rejection rate have little variation in image intensity, and even the same areas show unequal pixel brightness values. For topography product generation, the elevation of the area without matched points is obtained by interpolation. Because the areas where points are not matched are featureless terrain without elevation variation, the interpolation of the unmatched area is acceptable for the scope of this research.

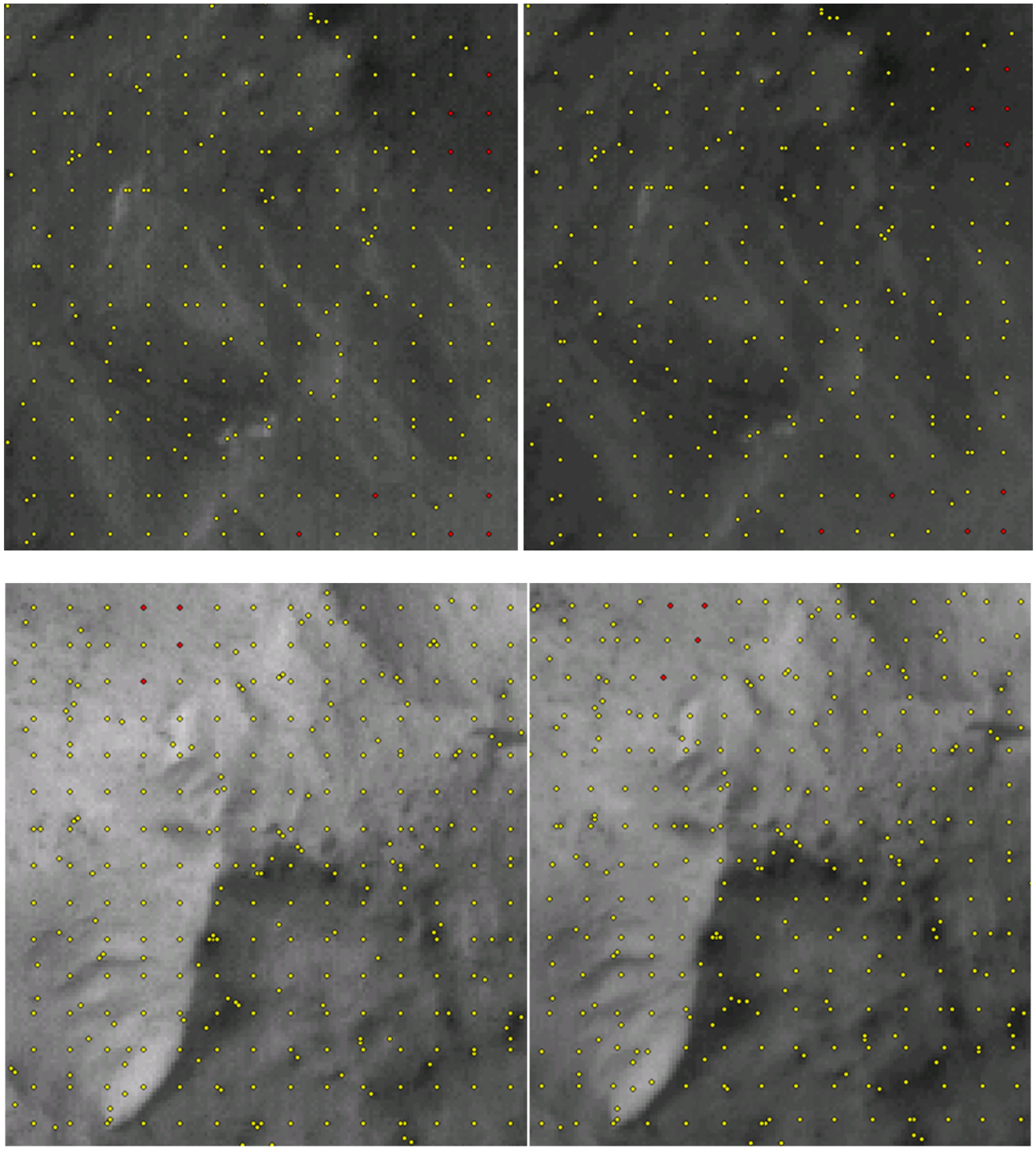

Figure 5.10 Areas with higher matching success rate (Left image: PSP_001777_1650, right image: PSP_001513_1655, red circle: new points not matched at level 7, yellow circle: final points at level 7)

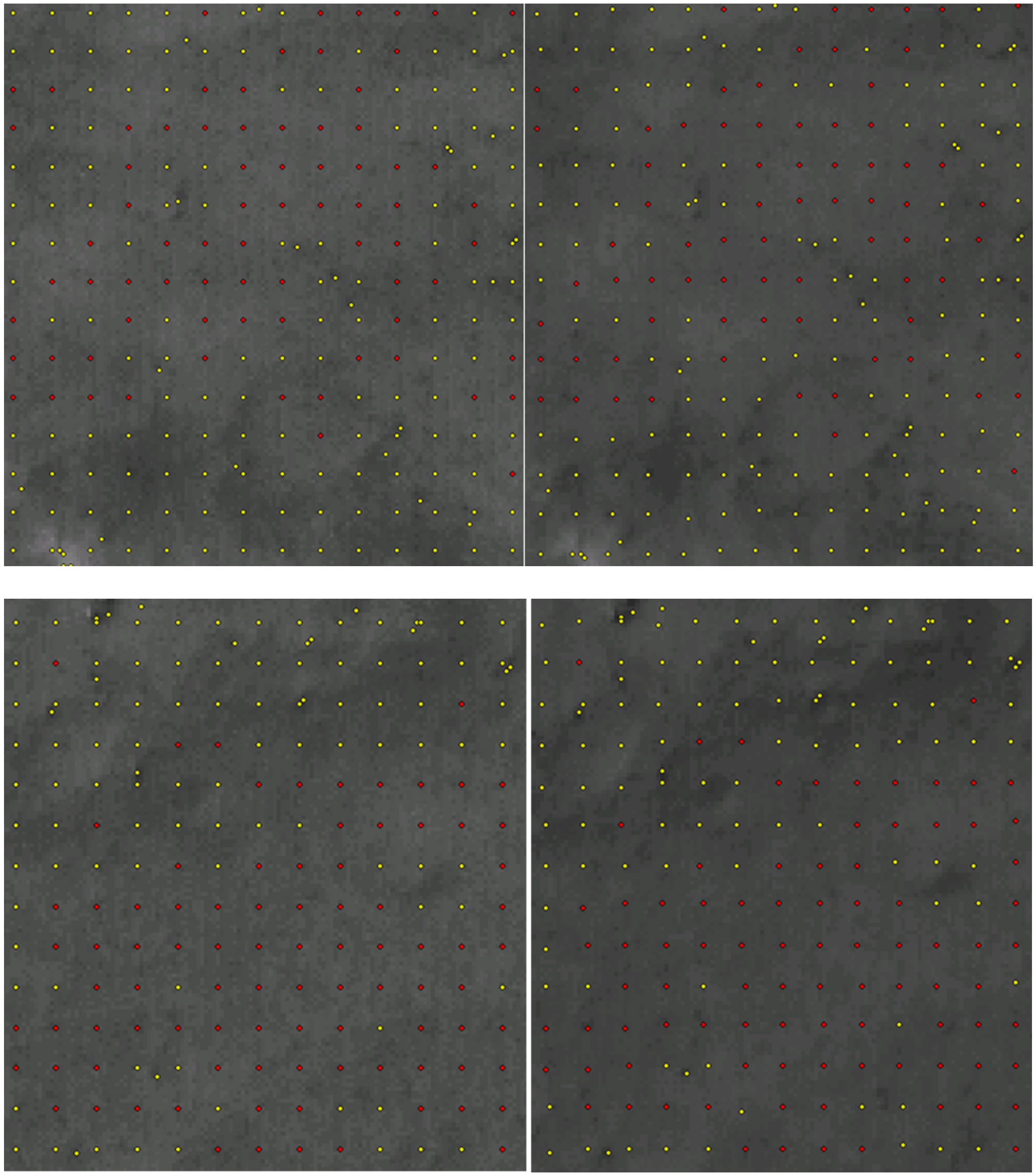

Figure 5.11 Areas with lower matching success rate (Left image: PSP_001777_1650, right image: PSP_001513_1655, red circle: new points not matched at level 7, yellow circle: final points at level 7)

5.3.2 Evaluations of Matched Points

Evaluation of the matched points is conducted at each level of the hierarchical process of image matching. To check the quality of the intermediate matching results, 50 points are randomly selected throughout the entire study area from level 1 through level 7. The automatically matched points were compared with manually matched points to calculate the point distances, called matching residuals. Table 5.4 shows the results of such analysis in terms of the matching accuracy.

Table 5.4 Matching residuals at different levels

Level	Image Scale	Point Type	Residuals (pixel)		
			Mean	Standard Deviation	Maximum
1	1/16	Interest	0.21	0.42	1.41
2	1/8	Interest	0.04	0.20	1
3	1/4	Interest	0.06	0.24	1
4	1/2	Interest	0.08	0.27	1
5	1	Interest	0.11	0.28	1
6	1	50-pixel grid	0.07	0.26	1
7	1	10-pixel grid	0.06	0.25	1

The mean of the residuals at all levels was still less than 0.3 pixels, with the highest at the first level and the maximum residual of 1.41 pixels at the first level. Since the interest points from levels 1 through 4 were transformed onto the next level's higher resolution images and are improved by re-matching, the errors from the previous levels were generally not propagated into subsequent levels. While the mean residuals did not necessarily decrease over the hierarchical process, they remain at a low level.

For the evaluation of the final matching result, the 2-pixel grid points were manually checked for the five test regions with different terrain types (Figure 5.12). Region 1 is a relatively level plain area near the Spirit rover landing center. Region 2 is a crater located northeast of Bonneville Crater along the rover traverse. Region 3 is the summit of Husband Hill. Region 4 is a field of dark, rippled sand dunes on the side of the Inner Basin area of the Husband Hill. Region 5 is Home Plate, a small plateau raised on a valley floor.

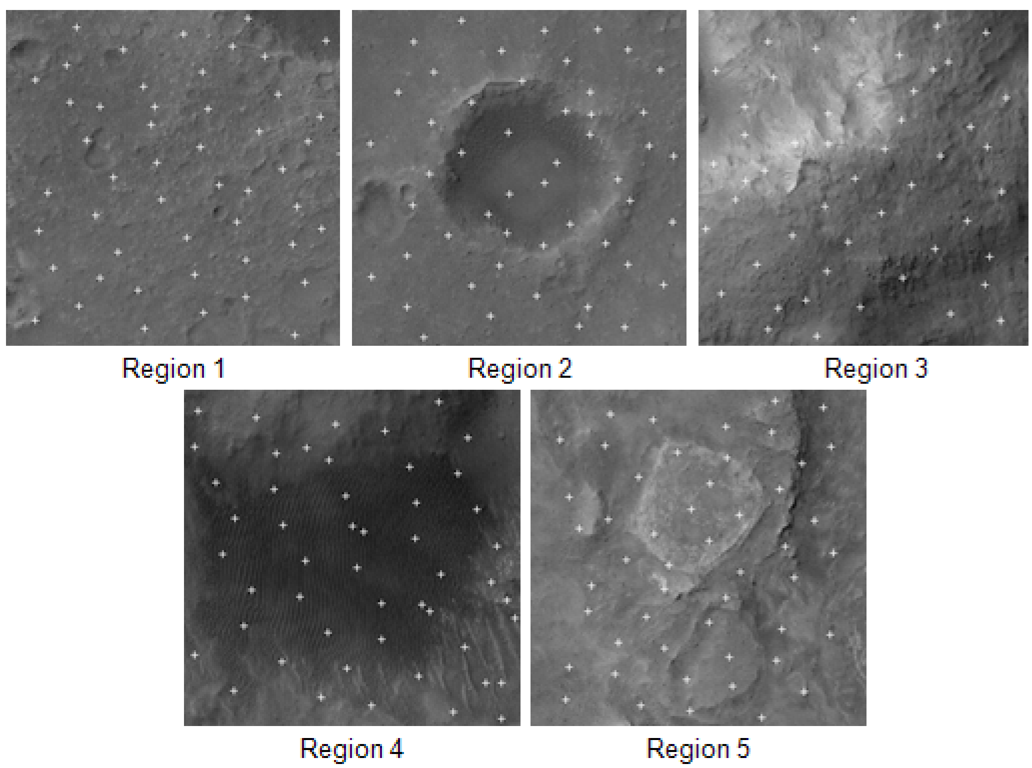

Figure 5.12 Distribution of check points at five test regions

For each region, 50 check points were randomly selected to verify the quality of matching results using manually matched points (Table 5.5). Region 2 (crater) produced the smallest mean residuals, though only slightly lower than Region 1 (level plain). Both regions contain a large number of small rocks that provide distinctive point features beneficial to matching. Region 3 shows a rather less textured area in the north western part; Region 4 mainly shows a striped pattern caused by dunes; and the Home Plate region (Region 5) has rather homogeneous areas by lack of detailed texture. All the check points are in accordance with the manual points with a mean residual around 0.1 pixels for Region 3, 4 and 5, and the maximum residual of 1.41 pixels for Region 4 and 5 because of the repetitive strip pattern and the lack of texture. Overall, the processing results passed the terrain type check very well.

Table 5.5 Matching residuals at level 8 (2-pixel grid) for five test regions

Region ID	Terrain Type	Number of Points	Residuals (pixel) Mean	Standard Deviation	Maximum
1	Level plain	50	0.06	0.24	1
2	Crater	50	0.04	0.20	1
3	Summit	50	0.10	0.3	1
4	Dune	50	0.09	0.30	1.41
5	Flat/Ridge	50	0.11	0.33	1.41

For qualitative assessment of DTMs, shaded relief maps are shown Figure 5.13, for the entire study area and the five test regions. Due to the simplistic nature of the area-based matching in this research, the artifacts with step-pattern in the DTMs are clearly visible in the shaded relief map. The magnitude of such artifacts is less than 1 m in elevation. With convergence angle of 20°, 1 m in vertical direction translates to about 0.3 m in horizontal direction, which is about one pixel in image space. The cause of the step-pattern artifact is the lack of sub-pixel matching capability in the matching method in this research.

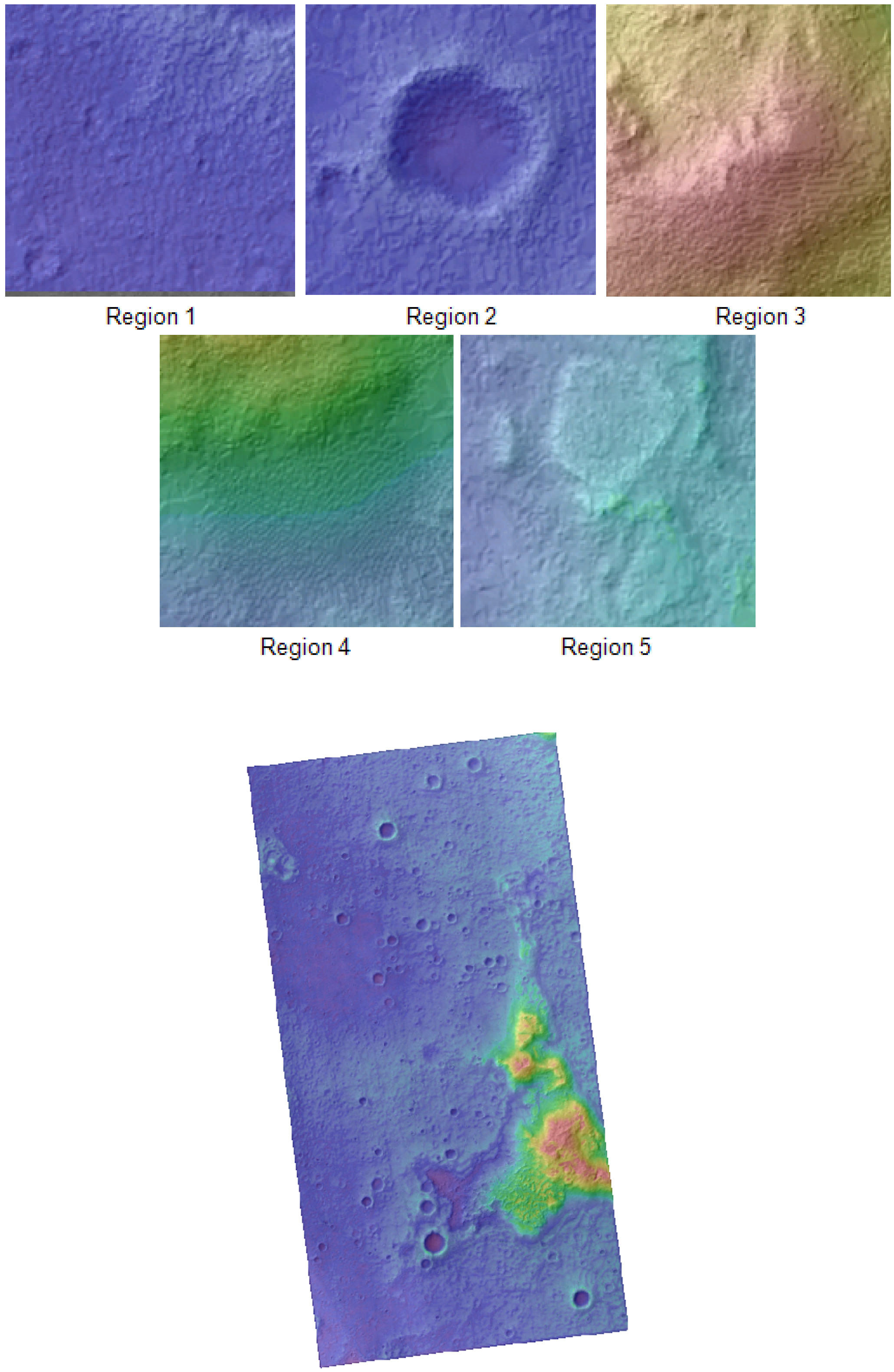

Figure 5.13 Shaded relief map overlaid on HiRISE orthophoto and color DTM

The uncertainty of the DTM generated from the simple area-based image matching is about 1 m in vertical direction. It is intended for fast orthophoto generation if less spatial accuracy is acceptable. The simple DTM generation method used in this research should be used with caution.

5.3.3 Accuracy of Elevation Profile

Finally, a few major topographic features were selected and checked to ensure that these automatically matched points describe the topographic details in a DEM. Six ground features in the area were chosen (Figure 5.14). Feature a) is a ridge located at the summit of the Husband Hill; b) is a line along a sandy dune in the Inner Basin. Feature c) is the eastern part of the boundary of Home Plate;, while d) is positioned across Micheltree Ridge right next to Home Plate. Both features e) and f) are on the northwest side of Bonneville Crater. Along these features, points were manually matched in the stereo images about 3 pixels apart in order to calculate their 3-D coordinates. Then the elevation of each point was compared with the elevation profile from the 0.6-m-resolution DEM generated by the automatically matched points.

Overall, the elevation profiles from both methods showed high levels of correspondence. The differences in elevation between manually matched points and the automatically generated DEM were in the range of ± 0.2 m. The distribution of the differences showed no distinctive pattern for all the six features. The random elevation errors of such magnitude are reasonable, considering that the pixel resolution of the raw images is about 0.3 m.

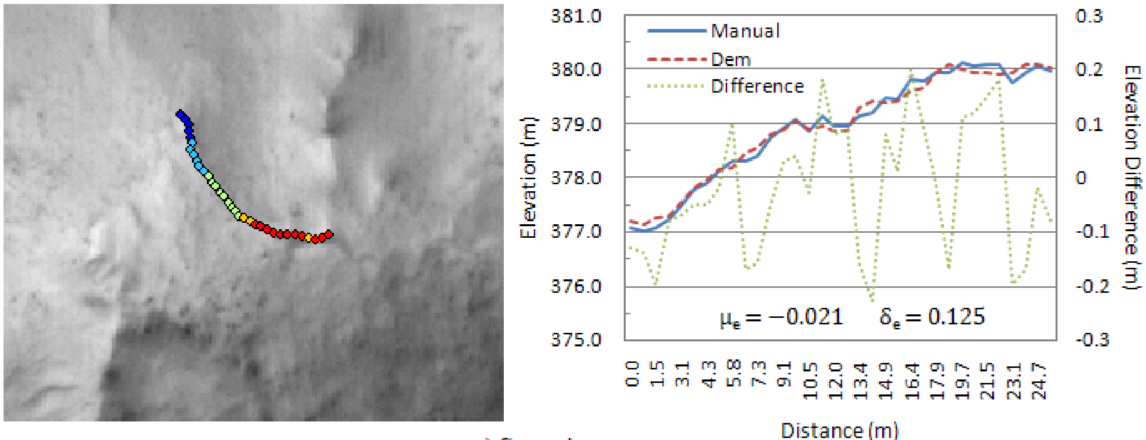

a) Summit

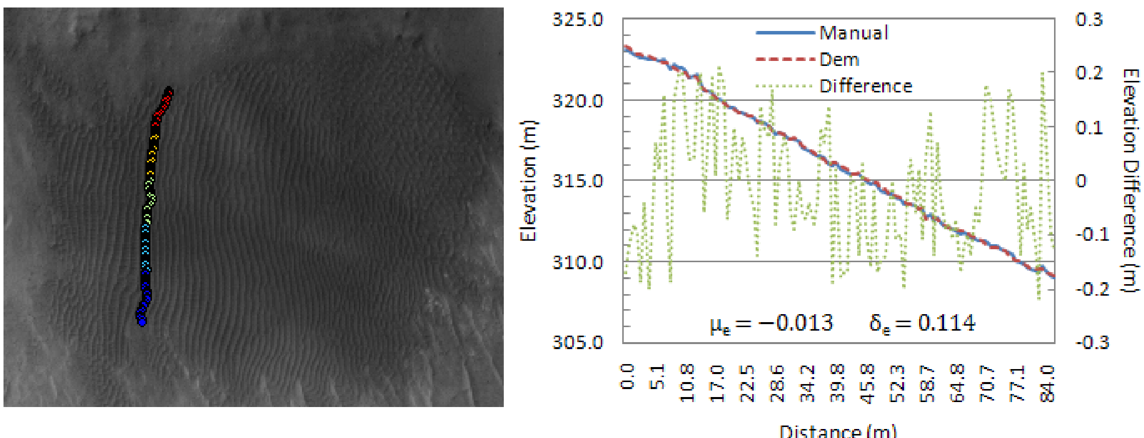

b) Inner Basin

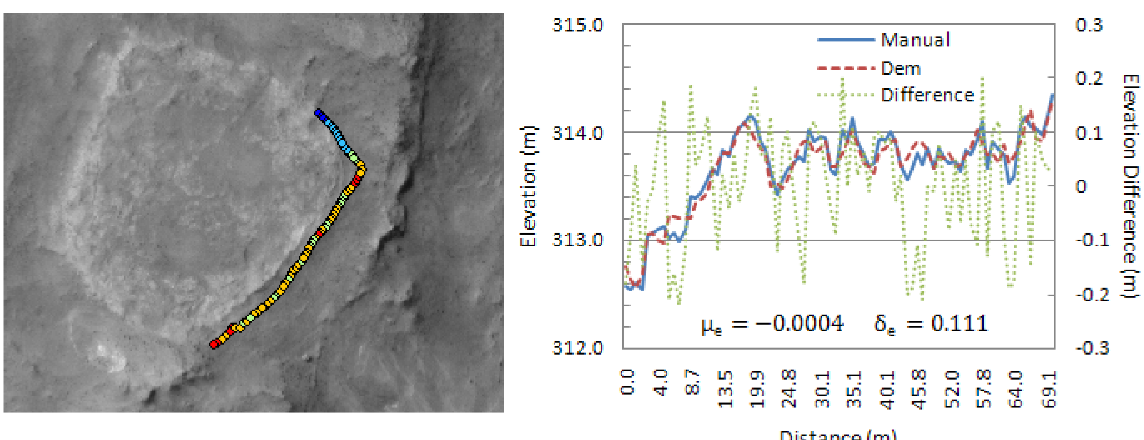

c) Home Plate boundary

Figure 5.14 Elevation profile of automatically generated DEM and manually matched points of six ground features (μ_e = mean of difference, σ_e = standard deviation of difference) (continued)

(continued)

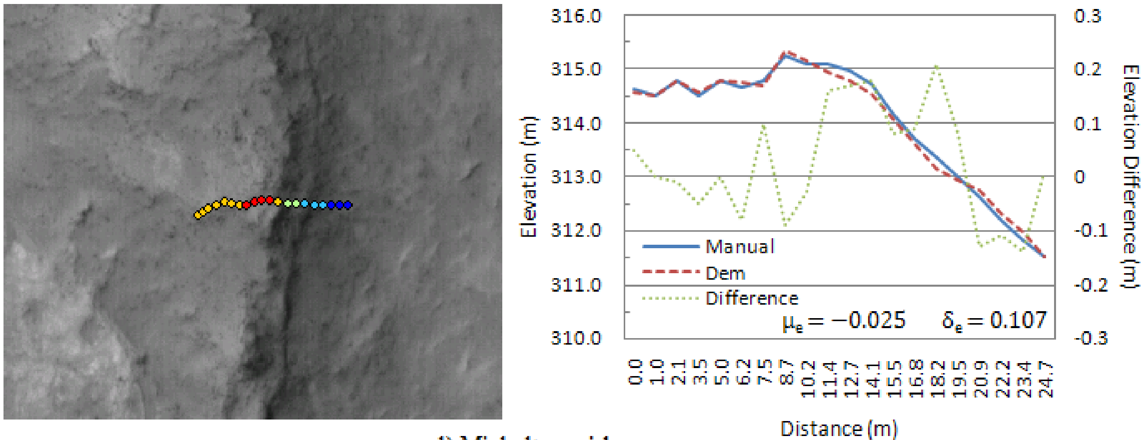

d) Micheltree ridge

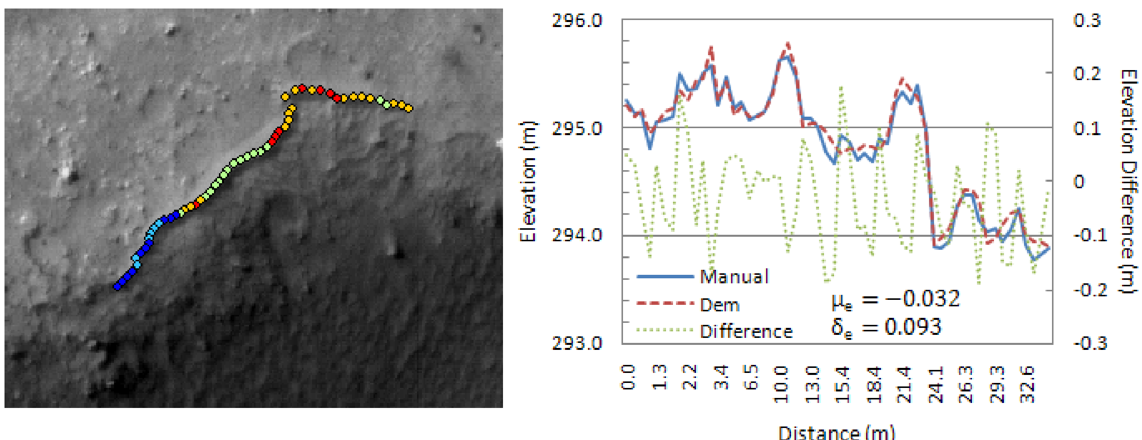

e) Bonneville Crater - ridge

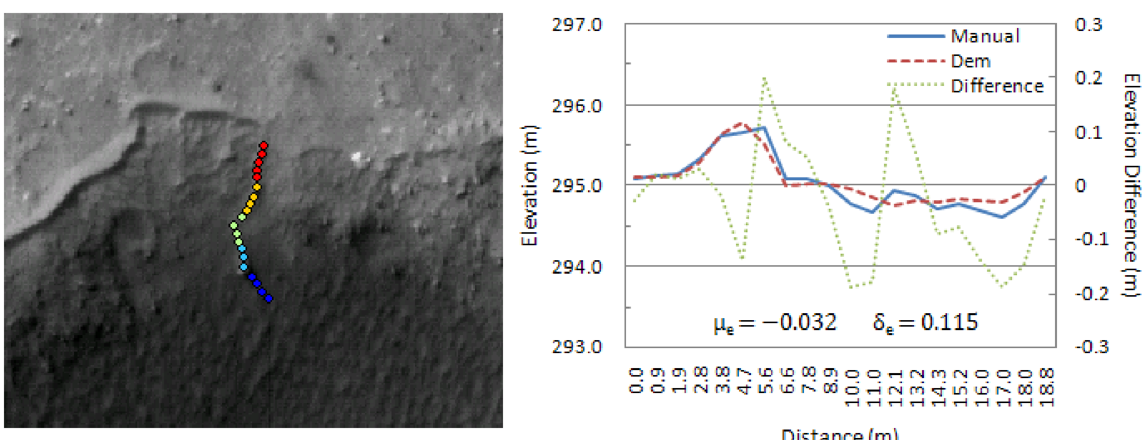

f) Bonneville Crater - slope

In this chapter, parameter selection and quality control for the developed procedures are discussed. Empirical analysis is provided in search for the optimal parameter values. Owing to the coarse-to-fine hierarchical matching, the search window size is reduced as towered the higher image matching levels. The correlation coefficient threshold for interest points for reduced scale images is set as 0.8 based on the distribution of cross-correlation coefficients. For matching original scale images, the threshold is lowered to 0.6. The matching window size is selected based on the average size and the frequency of the terrain. For blunder elimination, 3-D planar fitting of the terrain with an average of about 20 points is performed and any points outside of the range of $\pm 3\sigma$ is eliminated.

For the quality assessment, the distribution of the matched points is analyzed. The areas with distinguishable terrain features and variations in elevation showed high matching success rates. For quick orthophoto generation without manual editing, the terrain elevation of the unmatched area is interpolated in this research. The mean residuals of the matched points are around 0.1 pixels according to the manual assessment. The expected error in elevation of the topographic products is about ± 0.2 m. It should be noted that the stereo matching result is highly dependent on the properties of the input data and the terrain. Therefore, the matching parameters selected in this chapter might not be optimal for other types of imagery or terrain.

CHAPTER 6

IMPLEMENTATION AND PERFORMANCE ANALYSIS

This chapter presents the implementation results of the orbital image processing and integration with the ground image network. The Spirit rover landing site is chosen as the study area. The Spirit rover landing position, which is also the origin of the Local Coordinate System (LCS), is centered at 175.47848 º in longitude and −14.571892 º in latitude (Li et al., 2005). Based on the knowledge of the initial position of the rover, landmarks derived from the MER dataset were used for further horizontal control for integration of orbital and ground image networks.

In this research, the exterior orientation parameters of HiRISE stereo images are bundle adjusted based on the two types of tie points: traditional and inter-CCD tie points (chapter 3). Traditional tie points reduced the back projection residuals between stereo images to less than a pixel. The inconsistency between the overlapping CCDs caused (chapter 2) were not reduced to sub-pixel level until inter-CCD tie points were incorporated into the bundle adjustment system. The effect of using different weight parameters for bundle adjustment is also presented. The global Mars terrain model from MOLA MEGDR DTM as well as 3-D point data from PEDR profile (Smith et al., 1999) are adopted as the control information for absolute position.

The resulting DTM is compared with the DTM created by USGS. After horizontally registering the two DTMs using a 3-D similarity transformation, the vertical differences were calculated. The major differences in elevation came from the vertical jumps between the CCDs. The proposed rock matching method between orbital and ground image networks is tested for seven areas. In the test, the rock extraction and matching could successfully identify the rover positions on the orbital topographic products that were identified manually by human operator.

6.1 Study Area

In testing the proposed strategy for the integration of the orbital and ground image networks, there are two candidates for study area: the Spirit and Opportunity rover landing sites. In this research, the Spirit rover landing site is chosen because of the availability of the incremental ground bundle adjustment results (Li et al., 2006). In case of the Opportunity, ground bundle adjustment could not be conducted on some segments of the traverse because either there were little identifiable landmarks or the rover took long drives without taking appropriate images. In addition, the Spirit rover traverse covers diverse shapes of terrain across the Columbia Hills, which makes this location more desirable for the testing purpose.

Topographic mapping products are generated from the stereo pair of HiRISE images PSP_001513_1655 and PSP_001777_1650, which cover the Gusev Crater landing site of the Spirit rover as shown in Figure 6.1. The coverage of the stereo images includes the areas where Spirit rover landed and explored for the past six years. The

PSP_001513_1655 image was obtained on November 22, 2006. It is centered at 14.6 °S latitude, 175.5°E longitude. It has 27.1 cm/pixel resolution and 80,000 rows. The PSP_001777_1650 image was taken on December 12, 2006. It has a resolution of 26.3 cm/pixel and 40,000 rows. The extent of PSP_001777_1650 image, about 10.5 km × 5.5 km on the ground, is entirely covered by PSP_001513_1655 (Figure 6.1). The two images have a convergence angle of 19.8 degrees.

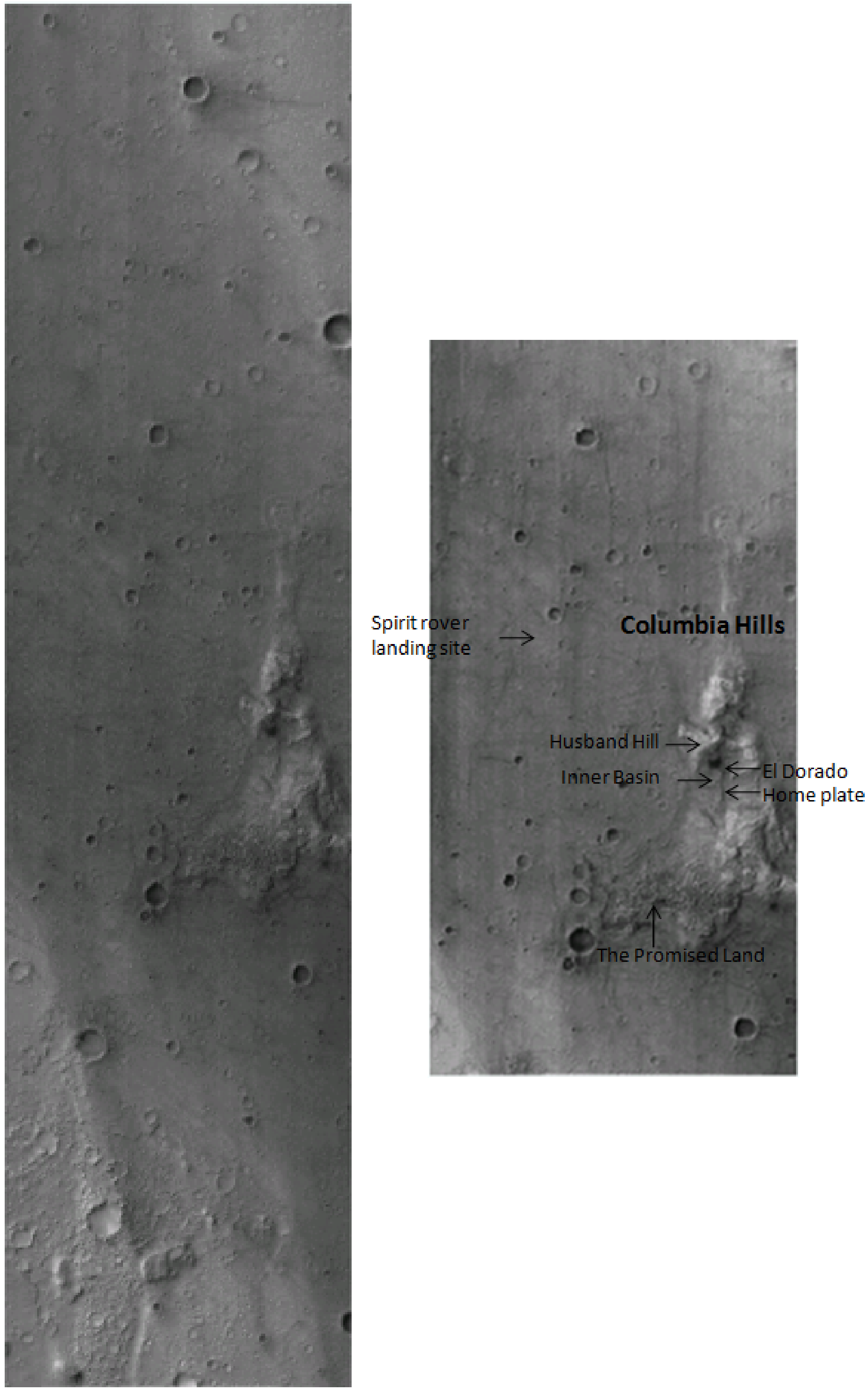

Figure 6.1 HiRISE stereo images at the Gusev Crater landing site: PSP_001513_1655 (left) and PSP_001777_1650 (right)

6.2 Bundle Adjustment of Orbital Images

To generate topographic products with the best accuracy, the inconsistency in the imaging geometry needs to be resolved. In this research, the bundle adjustment is conducted on the HiRISE stereo images to improve the accuracy of the exterior orientation parameters and to achieve the coherence between stereo images as well as between overlapping CCDs. Each HiRISE image consists of ten red band CCD strips. For the best performance of bundle adjustment, evenly distributed tie points are needed. Both traditional and inter-CCD tie points are automatically selected from the matched interest points of the stereo images (Li et al., 2008b). Figure 6.2 shows the distribution of the tie points overlaid on PSP_001777_1650 image mosaic. In Figure 6.2a, 270 traditional image tie points are marked as yellow circles. From matched interest points in the overlapping area between adjacent CCDs of PSP_001777_1650 image, 80 inter-CCD tie points are selected (red circles in Figure 6.2b). Likewise, 80 inter-CCD tie points are chosen from the overlap area of PSP_001513_1655 image (blue circles in Figure 6.2b). Due to severe noise present in PSP_001777_1650 CCD9 image, tie points in the CCD9 are not used in the bundle adjustment process. Among the nine overlap areas between the ten CCDs, the inter-CCD tie points from the overlap between CCD8 and CCD9 were also excluded.

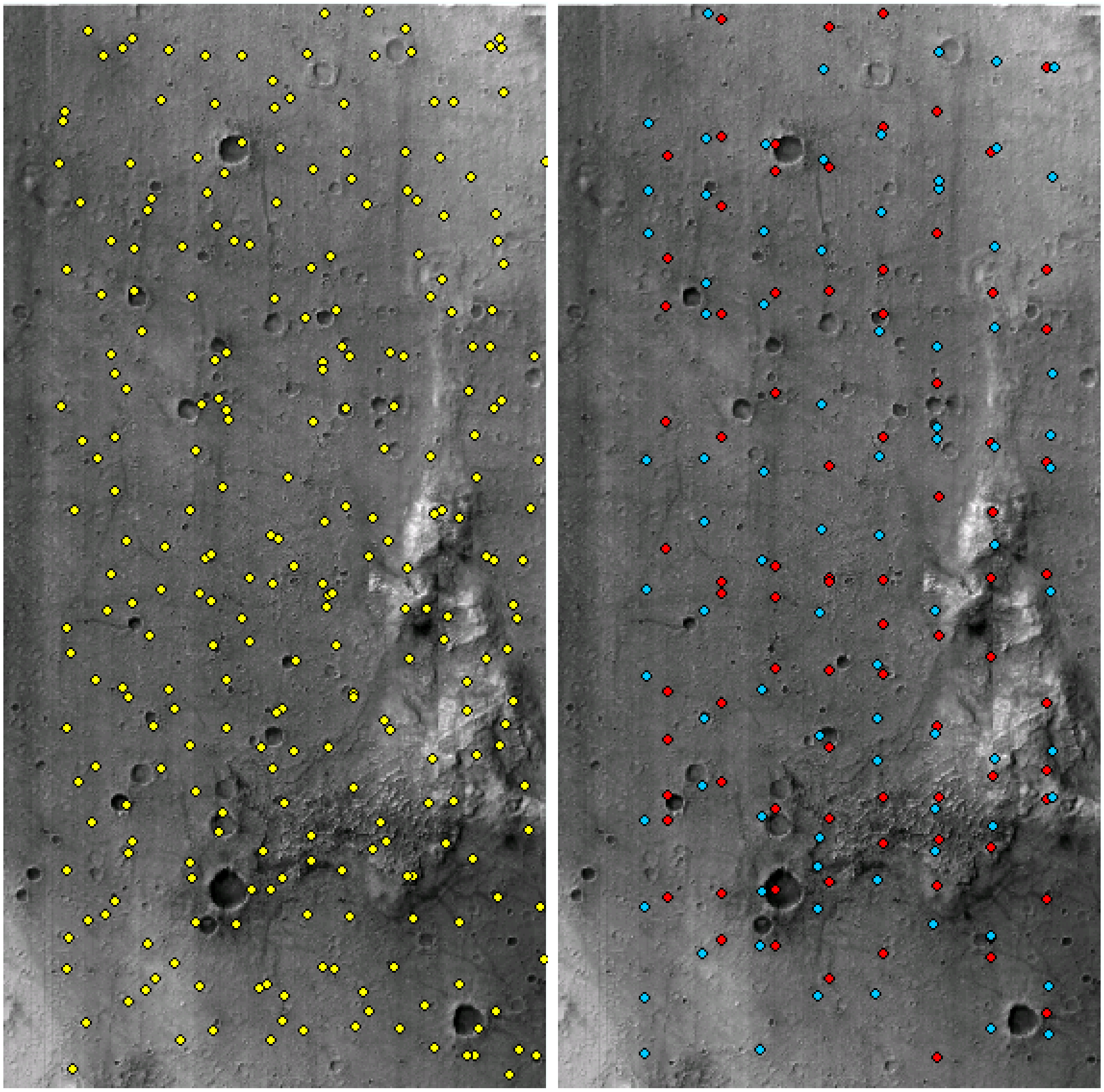

(a) (b)

Figure 6.2 (a) Traditional tie points as yellow circles and (b) inter-CCD tie points from PSP_001777_1650 as blue circles, inter-CCD tie points from PSP_001513_1655 as red circles

As described in chapter 3, the polynomial coefficients of the exterior orientation parameters are adjusted based on the measured image coordinates of the tie points. In the bundle adjustment, total of 430 tie points are used, including 270 traditional tie points

(Figure 6.2a), 80 inter-CCD tie points for PSP_001513_1655 and 80 inter-CCD tie points for PSP_001777_1650 (Figure 6.2b). Since there is no absolute ground truth available on the Martian surface, ground control points could not be used to evaluate the performance of bundle adjustment. Therefore, check points, which were not used in the bundle adjustment process, were selected from matched interest points. The ground coordinates of the check points are obtained by space intersection and back projected on each stereo image. The differences between the back-projected image coordinates and the original measurements are compared to evaluate the performance of the bundle adjustment.

The exterior orientation parameters have their own units. In the bundle adjustment, a least squares system is formed with the *n* observations modeled with zero-mean Gaussian error (Koch, 1999).

$$y = \tau \cdot x + e \text{ where } e \sim (0, \ \Sigma = \sigma_0^2 P^{-1}) \tag{6.1}$$

where y is the n×1 observation vector, x is the true value, τ is the n×1 vector filled with 1, e is the n×1 error vector, Σ is the error covariance matrix, σ_0^2 is a unitless variance component, and P is a weight matrix. The unitless variance component is estimated as

$$\bar{\sigma}_0^2 = \frac{\tilde{e}^T P \tilde{e}}{n - t} \tag{6.2}$$

where $\tilde{e}$ is the residual from the estimation of the unknowns, n is the number of observation, t is the number of unknowns. If the errors are uncorrelated with each other, the weight matrix is defined as

$$P = \sigma_0^2 \begin{bmatrix} 1/\sigma_1^2 & 0 & \dots & 0 \\ 0 & 1/\sigma_2^2 & \dots & 0 \\ \vdots & \vdots & \ddots & \vdots \\ 0 & 0 & \dots & 1/\sigma_n^2 \end{bmatrix} \tag{6.3}$$

The weight of each observation is proportional to the inverse of its variance. Therefore, different weights are assigned to each observation equation to properly account for the quality of the observation to the magnitude of adjustment. Observations with higher accuracy are given higher weight, which is decided based on smaller a priori variance.

For bundle adjustment of HiRISE images, a priori variance of tie point image coordinates is set as half a pixel, or 6 μm based on the expected matching error. The estimated uncertainty of the MRO trajectory is about 5 m for orbits at the beginning of the mission, and within about 1 m for later orbits. As for the rotation angles, the known precision of the pointing data is 0.035 mRad and systematic errors are considered to be no greater than 0.3 mRad (Kirk et al., 2008).

Kirk et al. (2008) reported HiRISE bundle adjustment conducted by the USGS. For the Spirit landing site dataset, the USGS set the variances as 0.5 ° (about 8.727 mRad) for the rotation angles, 100 m for horizontal position, 10 m for vertical position. Such loose weighting for the spacecraft positions and rotation angles was used to resolve the large offset (200-meters shift at the ground level) between MOLA and HiRISE by increasing the amount of adjustment of the exterior orientation parameters. They were expecting to apply tighter weighting of the a priori trajectory and pointing data in future adjustments.

In this research, bundle adjustment of exterior orientation parameters was conducted separately from absolute positioning by MOLA control networks. First, discrepancies between HiRISE stereo images and CCDs are resolved by bundle adjustment with weighting parameters based on a priori accuracy of the position and the orientation. Afterward, the DTM generated after bundle adjustment is matched with the MOLA DTM and points to determine horizontal and vertical shifts of the HiRISE stereo image network. The reason for not incorporating MOLA control into HIRISE bundle adjustment is because there is no accurate, direct correspondence between MOLA points and the image features. The precision of MRO exterior orientation parameters is far better than any dataset used to generate the Mars control network. Increasing the variances for weight parameters allows more adjustment of the observed values, which could also lead to possible loss of precision in the original MRO exterior orientation dataset. Therefore, the known variances of MRO exterior orientation parameters are used for assigning weights in the bundle adjustment system. Furthermore, the bundle adjustment results can vary significantly depending on the control data and weight parameters. For that reason, weight parameters are normally also fine tuned based on the available control data and the expected shift. Using a priori variances as weight parameters, which enables automatic bundle adjustment for generation of vast orbital image networks, has an advantage over manual fine tuning in terms of practicality.

The implementation of bundle adjustment is an iterative process of modifying the polynomial coefficients of the exterior orientation parameters by solving the linearized observation equations. In this research, eight cases of bundle adjustment are tested using different weighting parameters, tie points and control data. The number of iteration is set to 10. Table 6.1 presents the statistical results of the back projection residuals from three types of check points. In the table, ‘A’ stands for traditional tie points, ‘B’ is

PSP_001513_1655 inter-CCD tie points, and 'C' is inter-CCD tie points of image PSP_001777_1650. Before bundle adjustment, the mean magnitudes of back projection residuals were over three pixels and the standard deviations were over two pixels. In other words, there is no sign of major disagreement between the original exterior orientation parameters of the stereo images.

Table 6.1 Statistics of back projection residuals of check points (unit in pixels)

		Variances used for weight			Magnitudes of back projection residuals mean (standard deviation)		
Scenario ID	Bundle adjustment scenario	σ_{X^c} σ_{Y^c} σ_{Z^c} (m)	σ_ω σ_φ σ_κ (mRad)	σ_x σ_y (pixel)	A (pixel)	B (pixel)	C (pixel)
	Without bundle adjustment	-	-	-	3.73 (2.86)	3.37 (2.32)	4.77 (2.93)
1	Without inter-CCD tie points	1	0.3	0.5	0.17 (0.12)	1.39 (0.49)	0.97 (0.35)
2	With all tie points	1	0.05	0.5	0.17 (0.12)	0.52 (0.24)	0.55 (0.25)
3	With all tie points	1	0.1	0.5	0.17 (0.12)	0.52 (0.23)	0.51 (0.24)
4	With all tie points	1	0.3	0.5	0.17 (0.12)	0.52 (0.23)	0.51 (0.21)
5	With all tie points	5	0.3	0.5	0.17 (0.12)	0.52 (0.23)	0.51 (0.21)
6	With all tie points	100	0.3	0.5	0.17 (0.12)	0.51 (0.23)	0.48 (0.21)

Six methods of bundle adjustment were tested using different types of tie points and weighting parameters. Scenario 1 used only traditional tie points, and the variances for weighting parameters are set as 1 m for position, 0.3 mRad for orientation, and 0.5 pixel for image coordinates. In bundle adjustment system, the ratio between weight parameters, rather than their absolute values, really matters. Therefore, the variance for image coordinates is fixed to 0.5 pixel in this experiment.

After bundle adjustment, the mean magnitude of back projection residuals between stereos (A) was significantly reduced to 0.17 pixel, but the mean residuals between inter-CCD overlap were not as drastically reduced. Type B residual in PSP_001513_1655 was still 1.39 pixel, and type C residual was 0.97 pixel. This means that traditional tie points alone are not enough to compensate for the relative disagreement between overlapping CCDs. It should be noted that the type B and C residuals contains not only the misalignment between the CCDs, but also the inconsistencies between the stereo images.

As discussed in Chapter 3, the proposed bundle adjustment for HiRISE image stereo include inter-CCD tie points also. Scenarios 2 through 6 use the same observation equations from both traditional and inter-CCD tie points, although the variances of satellite position and rotation angles were set differently. The tightest weighting is applied in scenario 2, while the loosest in scenario 6. However, the back projection residual, which indicates the effectiveness of bundle adjustment, remains consistent, regardless of the weighting. After bundle adjustment scenario 2 is implemented, the mean magnitude of inter-CCD back projection residuals was 0.52 pixel for type B and 0.55 pixel for type C. Since the image coordinate's precision of tie points is about 0.5 pixel, it is reasonable to say that the disagreement between CCDs is resolved at least up to detectable level. As variances for rotation angles are increased to 0.1 mRad (scenario 2) and 0.3 mRad (scenario 3), the residuals on inter-CCD tie points are slightly improved by 0.01 pixel. When scenario 4 is compared to method 3, looser weighting for position did not further reduce errors. In this case, using the known accuracy of telemetry position for weighting parameters was sufficient for resolving displacement between stereo. Scenario 6 applied much larger position variances (100 m) used by USGS. Compared to scenario 4, looser weighting in position applied to scenario 6 brought the back projection residual down by 0.01 pixel for type B and 0.03 pixel for type C check points.

Although the statistics of residuals are similar in table 6.1, the changes in exterior orientation parameters varied significantly depending on the weighting parameters. In general, the variances for weighting determined the magnitudes of the changes in exterior orientation parameters. The pattern of the change is not exactly predictable. For example, scenario 2 (Figure 6.4) and scenario 3 (Figure 6.5) have a similar trend of change. Scenario 3 has two times bigger variance for rotation angles. However, the rotation angles did not change as much as the position, which increased about three times. In scenario 4 (Figure 6.6), where the variances for rotation angles are three times bigger than scenario 3, the rotation angles increased about twice as much, but the change in position was actually reduced. Scenario 5 (Figure 6.7) has five times bigger variances for position, and its position change went up 25 times bigger than scenario 4, while the rotation angles were about the same. In the bundle adjustment system, orientation parameters are so interdependent on each other. Although bigger variances generally mean more change in exterior orientation parameters, the amount of change is not proportional to the variances. Increasing variance of one parameter impacts other parameters as well. The bundle adjustment that results in scenario 6 (Figure 6.8) is very unrealistic with regard to the amount of changes in exterior orientation parameters. The small back projection residuals before bundle adjustment demonstrate that the original telemetry data is in good shape and the stereo images align relatively well with each other. Scenario 2 through method 6 reduced the residuals to the very similar level, the differences being less than 0.1 pixel. Increasing the variances for weighting does not guarantee produce better results, but could cause unnecessary changes in the exterior orientation parameters instead. Since the disagreement between stereos and CCDs could be resolved even using tightest weighting, it is reasonable to use variances that are consistent with the known accuracies of the parameters. In MRO telemetry data, the uncertainties are 1 m for position, and 0.3 mRad (about 0.017 degree) for rotation angels. Therefore, bundle adjustment was conducted using scenario 4 in this research. After scenario 4 bundle adjustments, the differences of the perspective center positions are smaller than 1 meter and the changes of pointing angles are less than 0.3 mRad.

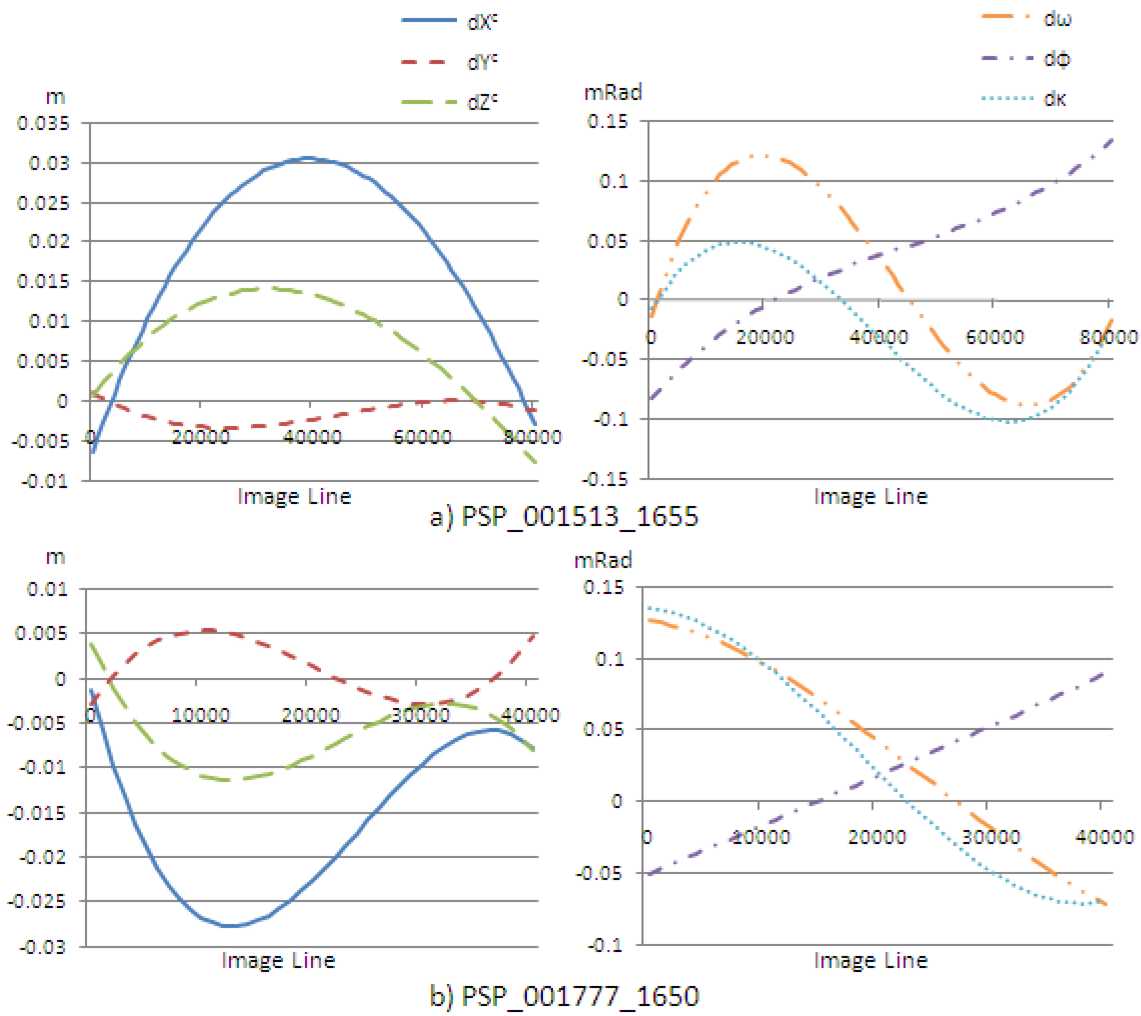

Figure 6.3 Change of orientation parameters after bundle adjustment scenario 1

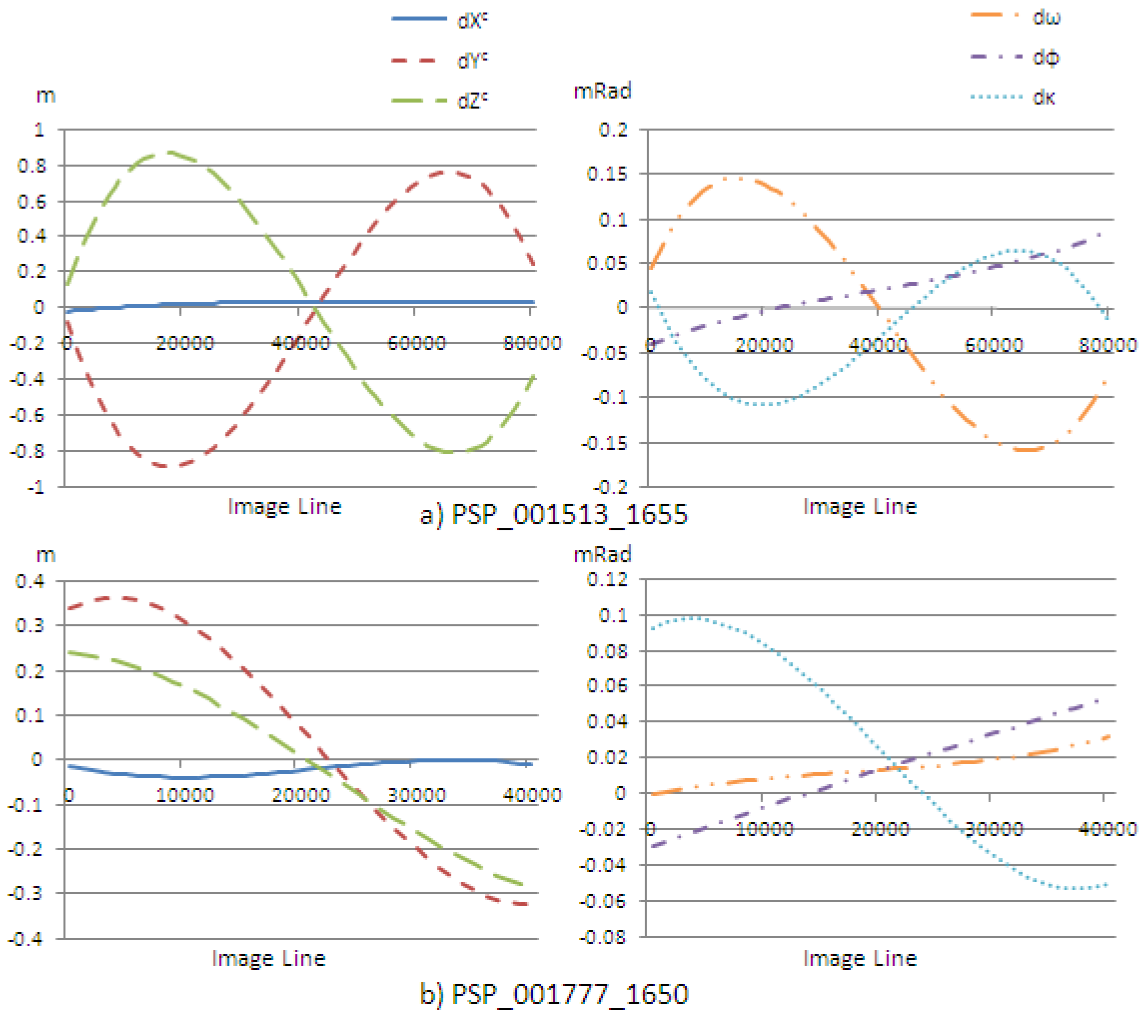

Figure 6.4 Change of orientation parameters after bundle adjustment scenario 2

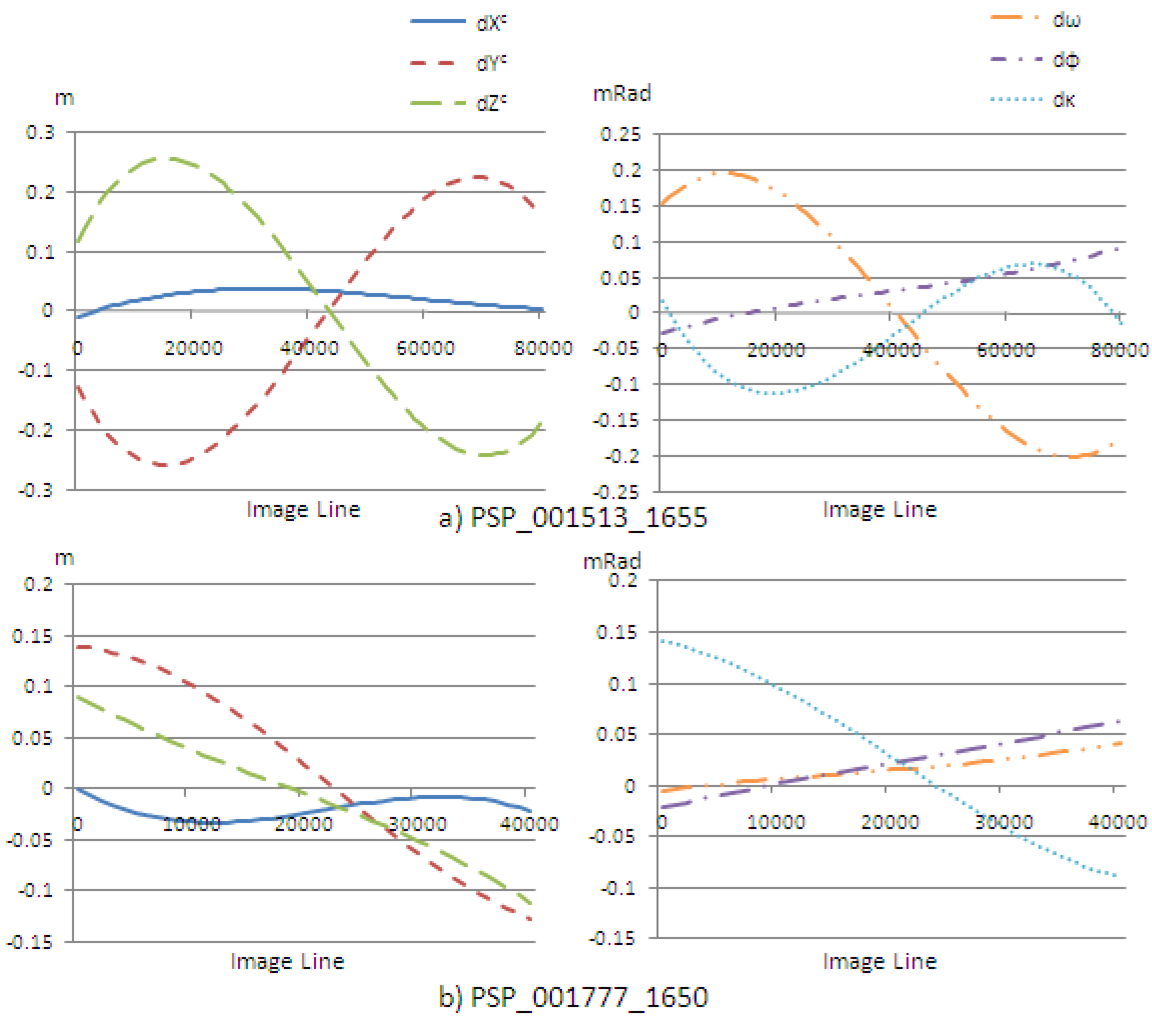

Figure 6.5 Change of orientation parameters after bundle adjustment scenario 3

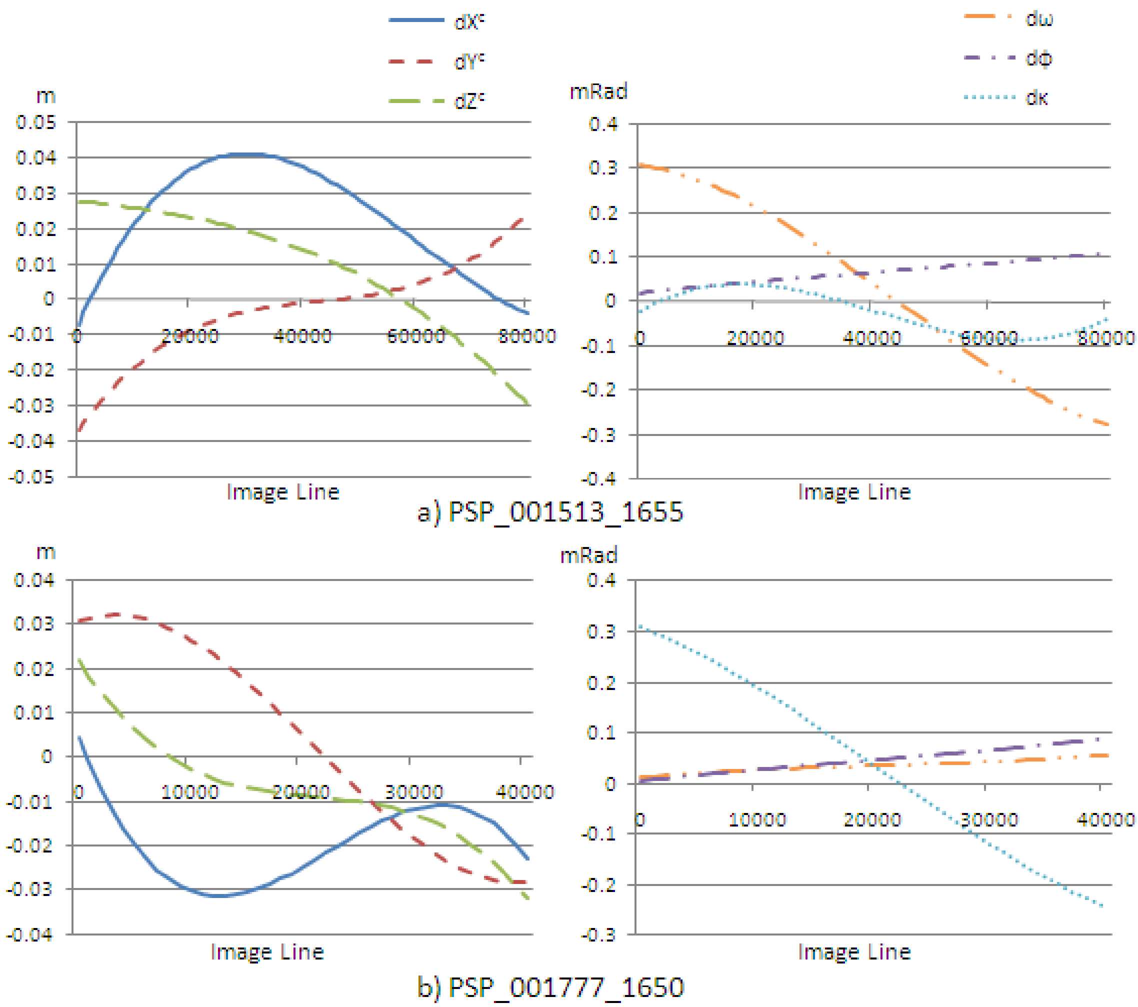

Figure 6.6 Change of orientation parameters after bundle adjustment scenario 4

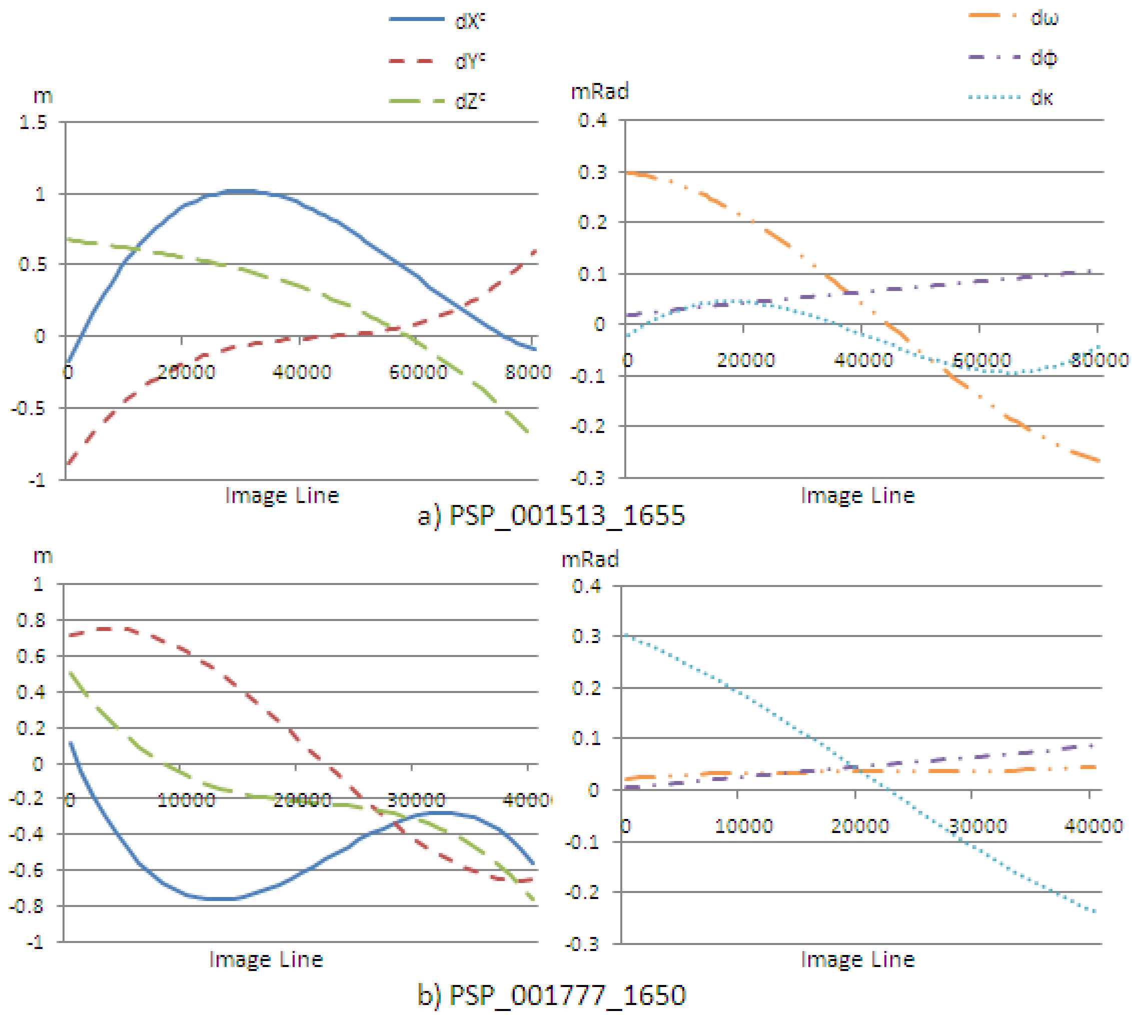

Figure 6.7 Change of orientation parameters after bundle adjustment scenario 5

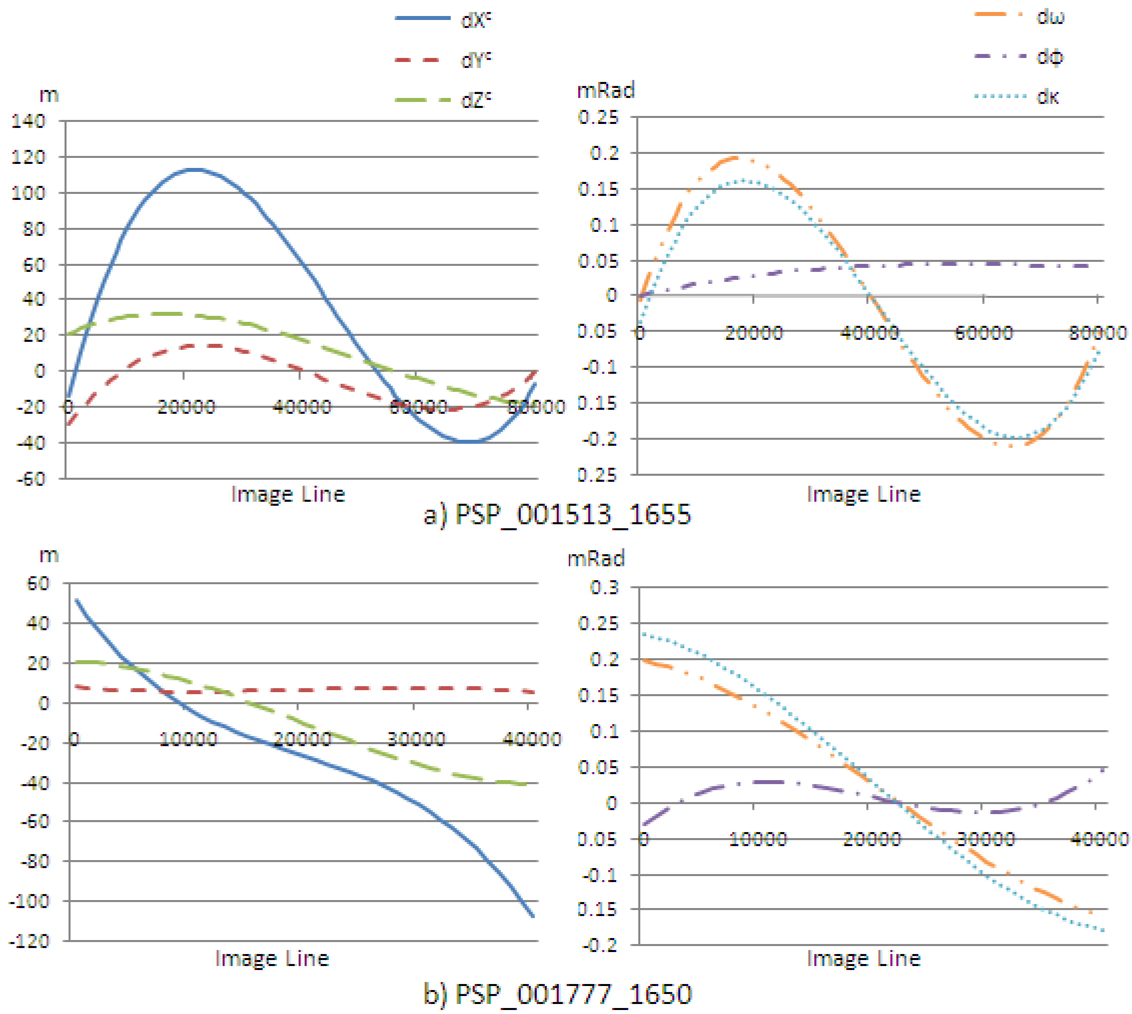

Figure 6.8 Change of orientation parameters after bundle adjustment scenario 6

In Figure 6.9, the back projection residuals of all the check points are displayed as vectors on the PSP_001777_1650 image. Figure 6.9a shows the residuals before the bundle adjustment with the error vector exaggerated by 100 times for legibility. The error vectors here are mainly in the along-track direction. There is a trend in back projection residuals, increasing from south to north direction. The trend is caused by inconsistencies in exterior orientation parameters between the stereo images.

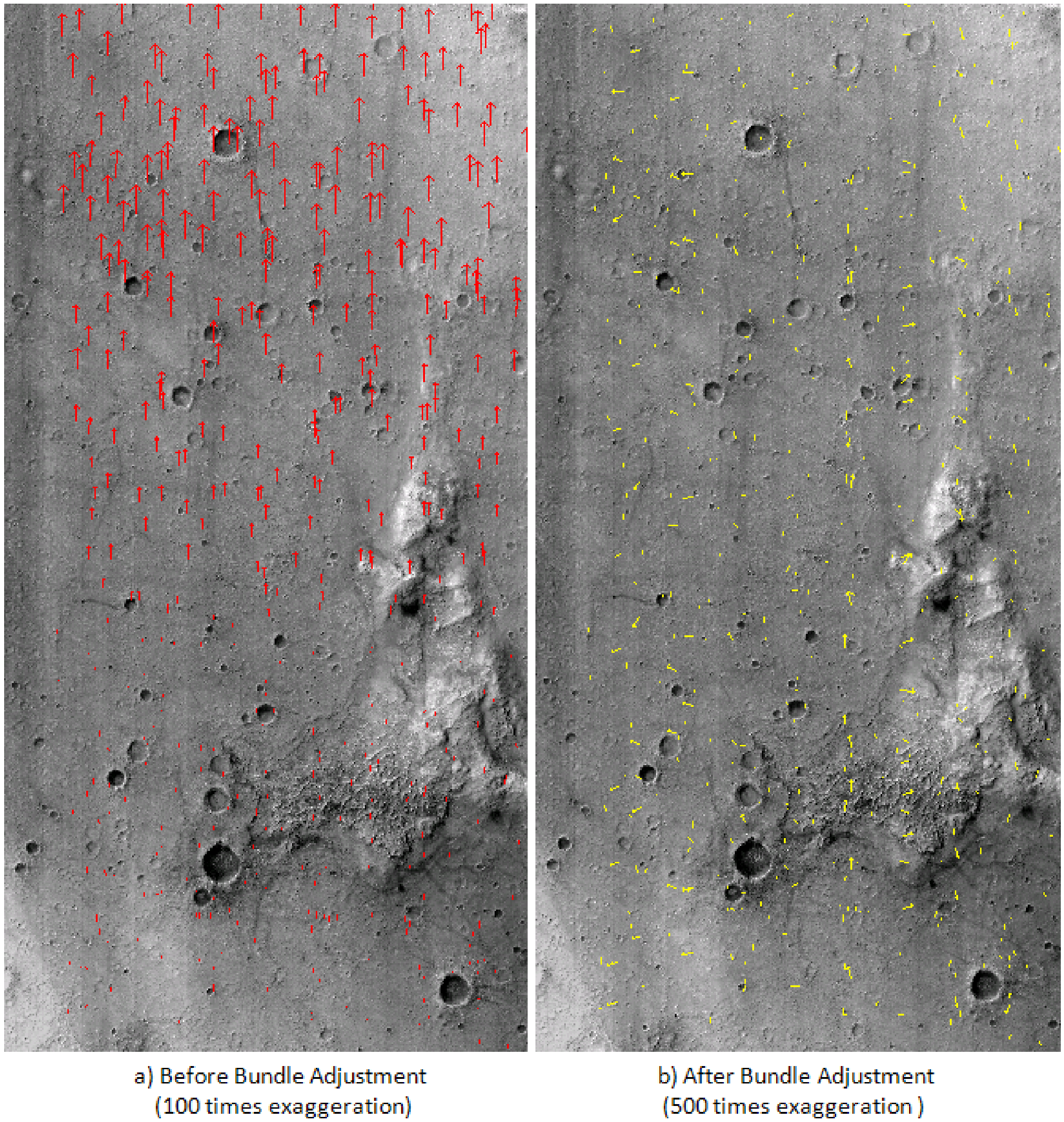

Figure 6.9 Back projection residuals of check points on PSP_001777_1650 image mosaics before and after scenario 4 bundle adjustment

Figure 6.9b shows the residuals after the bundle adjustment with jitter terms incorporated as 500-times exaggerated residual vectors. The significantly reduced error vectors presented in Figure 6.9b and Table 6.1 demonstrate that the inconsistencies between the stereo pairs are successfully removed by the bundle adjustment proposed in this research and that the incorporation of inter-CCD tie points renders better results in the rigorous sensor model.

6.3 DTM and Orthophoto Generation

After hierarchical image matching, about 2.4 million interest points and 104 million grid points were matched. 3-D Ground positions of these points were computed by space intersection using the exterior orientation parameters after method 4 bundle adjustment. Based on these 3-D points, Kriging with a spherical semi-variogram model was conducted to generate a 1-m-resolution DTM of the area covering Spirit rover's entire traverse (Figure 6.10).

The topographic products are generated based on the equirectangular projection, which is also known as equidistant cylindrical projection. The Mars ellipsoid is defined by the International Astronomical Union (IAU) as the Mars IAU 2000 ellipsoid. It has an equatorial axis of 3,396.19 km and a polar axis of 3,376.20 km as (Seidelmann et al., 2002). According to conventional Mars topographic mapping, the geographic location of an object points in equirectangular projection is defined as:

$$x = R(\lambda - \lambda_0)\cos(\phi_1) \qquad (6.1)$$

$$y = R\phi$$

where (x, y) is the geographic location in the equirectangular projection, R is the radius of equatorial axis (3396190 m), λ is the longitude and λ_0 is the longitude of the central meridian of the projection, ϕ_1 is the standard parallel and ϕ is the latitude. In mapping of the test dataset in this research, the central meridian and the standard parallel are both set to 0. In MOLA dataset, elevation of an object point is defined as its distance from the origin of Mars body-fixed frame subtracted by 3,396,000 m. In this research, the same definition is used for topographic product generation.

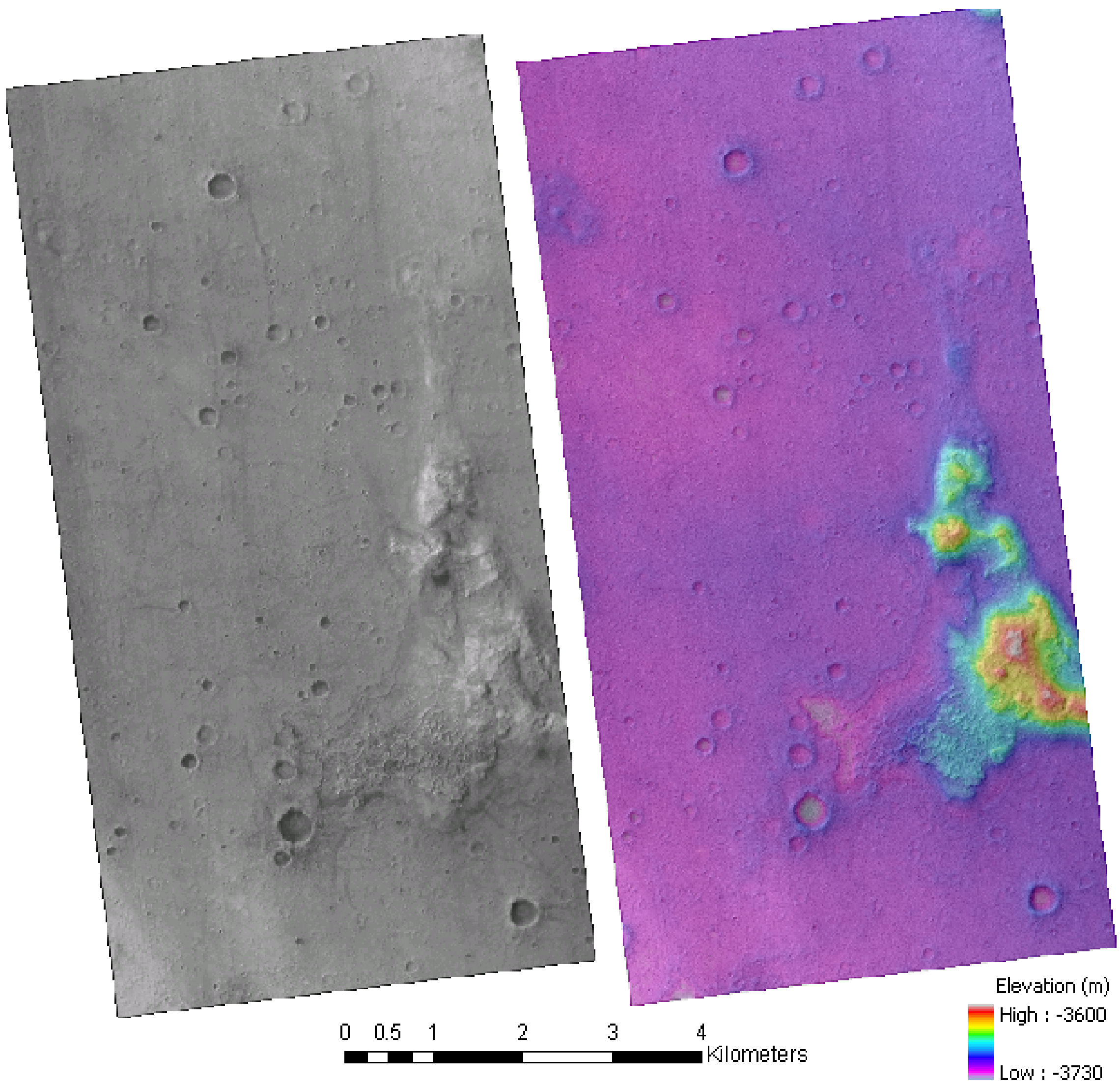

Figure 6.10 HiRISE orthophoto at the Spirit rover landing site (left) and DTM (right)

Using the DTM and the bundle-adjusted exterior orientation parameters, PSP_001777_1650 image was ortho-rectified to generate an orthophoto. For ortho-rectification, each 3-D coordinate of the DTM grid is back projected onto the HiRISE images by plugging in the exterior orientation parameters of each image line into the collinearity equation. After back projection, the physical coordinates of a ray from the object points onto the HiRISE focal plane are transformed to row and column position using the inverse procedure of interior orientation. Once pixel position is identified, the pixel value of the orthophoto is calculated by bilinear interpolation of the neighboring pixels.

The orthophoto generation using a naïve implementation, which fills each grid on the DTM by searching all image lines, is a really slow procedure. To speed up the process, a binary search algorithm is applied. Instead of searching the entire image lines, the search starts from the middle line. Then, a decision is made to search either the upper or lower part of the image by judging which part is closer to the physical coordinates of the back projected pixel. This recursive search stops when the exact row position is identified. To further accelerate the searching algorithm, a neighborhood searching strategy is applied. Since a neighboring DTM grid should also have close pixel position, the search space for a DTM grid is confined to a smaller neighborhood of the row position of the previously searched DTM grid. In this way, only the row index of the first DTM grid of each CCD image strip needs to be recursively searched and the row indices of rest of the girds can be identified in the neighborhood very efficiently. To reach the resolution potential of the HiRISE imagery, a 0.25-meter resolution orthophoto was generated by up-sampling the

DTM from 1 meter resolution to 0.25 meter resolution. Figure 6.11 shows the 3-D view of orthophoto draped onto the corresponding DTM with twice vertical exaggeration.

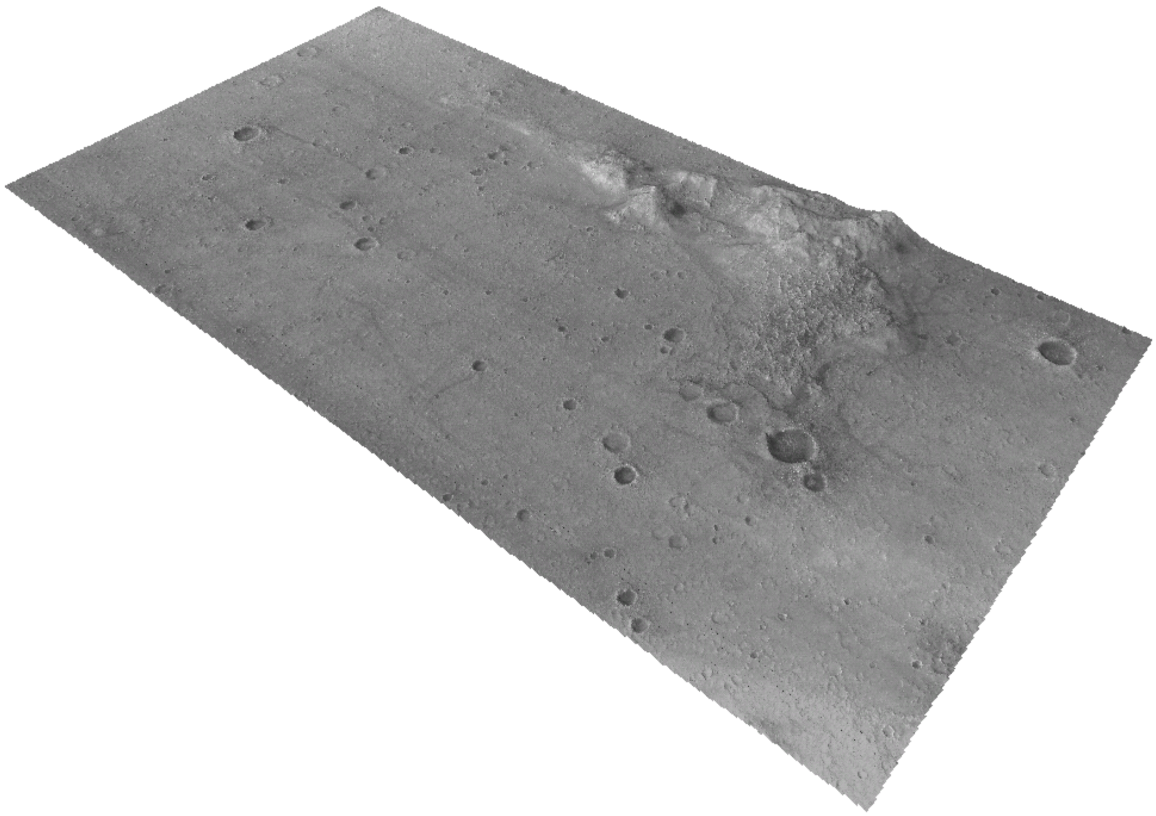

Figure 6.11 HiRISE orthophoto draped on corresponding DTM with twice vertical exaggeration

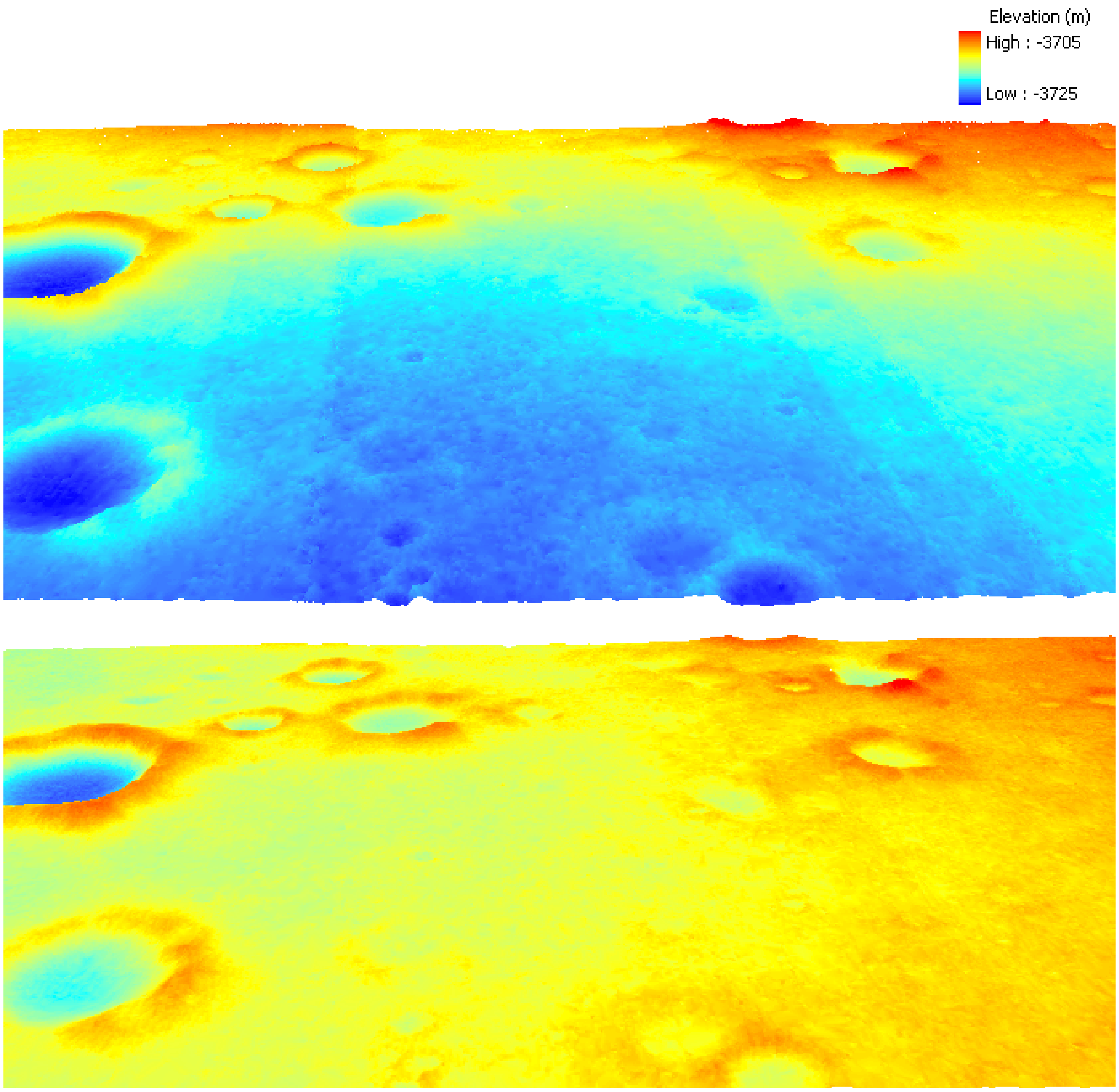

Figure 6.12 3-D surface map of HiRISE DTM with 3x vertically exaggeration. Surface map generated from exterior orientation parameters after method 1 bundle adjustment (top), and method 4 bundle adjustment (bottom)

The bundle adjustment results can be evaluated in the object space. As shown in table 6.1, the ground coordinates calculated using the original telemetry exterior orientation parameters have inconsistencies between the points from overlapping CCDs.

Comparison of the ground coordinates between two inter-CCD tie points on one stereo intersected with the corresponding image point on the other stereo can give us information about such discrepancies. Figure 6.12 shows two DTM surface maps using exterior orientation parameters from method 1 (with traditional tie points only) and method 4 (both traditional and inter-CCD tie points) bundle adjustment. The first one was generated using refined exterior orientation based on bundle adjustment, using only traditional tie points and the second one used exterior orientation adjusted based on both traditional and inter-CCD points. The first surface map has strong artifacts that were caused by geometric inconsistencies between overlapping CCDs. The second surface map shows a seamless homogenous surface even though it is physically generated by different CCD strips. The inconsistencies were not removed by bundle adjustment until inter-CCD tie points were incorporated. The effectiveness of the proposed bundle adjustment with inter-CCD tie points is visually confirmed in the surface map comparison. The average difference of ground coordinates between CCDs was about 1 meter after method 1 bundle adjustment. Using inter-CCD tie points in the method 4 bundle adjustment system, the average difference is reduced to 0.3 meter. The inconsistencies between the overlapping CCDs are successfully removed by incorporating inter-CCD tie points in bundle adjustment.

6.4 Absolute Positioning Using MOLA Control Network

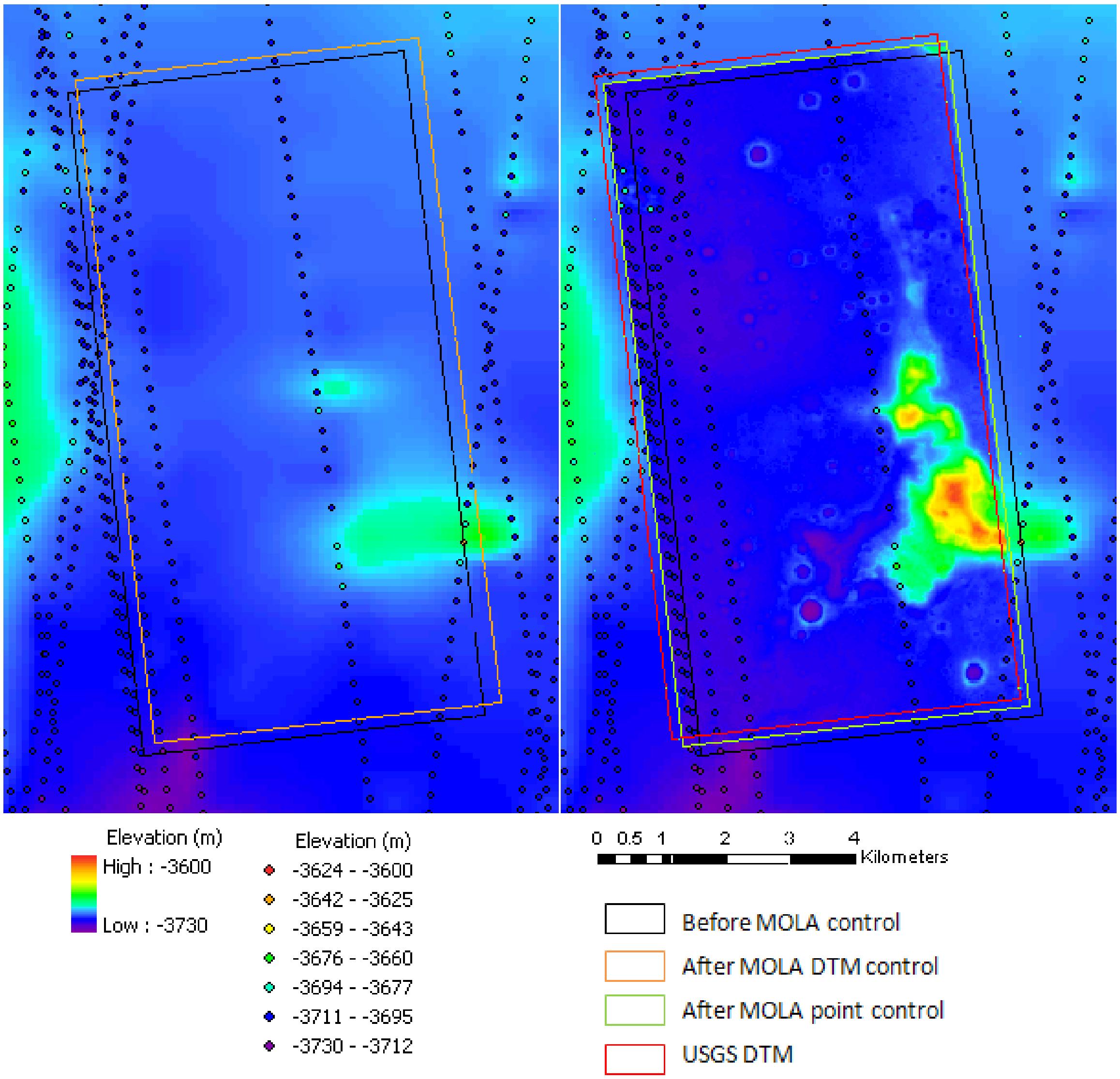

Figure 6.13 Absolute positioning result of HiRISE DTM based on terrain matching to resampled MEGDR DTM (background) and PEDR points (circles). The extents of DTMs are displayed as boxes. The final HiRISE DTM after MOLA point control is overlaid on the right

After removing inconsistencies of exterior orientation parameters between the stereo and CCDs, absolute positioning of HiRISE image is conducted using MOLA control network. According to the proposed absolute positioning method (chapter 3), the HiRISE DTM is first matched to MEGDR DTM, which was resampled to 100-m resolution grid. During the terrain match, the search area was set to 5 kilometers. The amount of horizontal shift from terrain match against MOLA DTM is about 400 m to northeast (Figure 6.13). Based on the initial positioning, the MOLA points from PEDR dataset (shown as regularly spaced circles in Figure 6.13) were further matched with HiRISE DTM. The extent of the second search area is set to 500 m. After the terrain match against the 3-D coordinates from PEDR points, the HiRISE DTM shifted from its original position by 200 m to the west, 100 m to the north, and -232.45 m vertically. In this test dataset, the horizontal shift of HiRISE DTM is less than 230 m, which is well below the search area for the second terrain match. The reason for conducting the terrain match twice–first with MEGDR DTM and then PEDR points–is because the coverage of PEDR dataset is irregular. MEGDR DTM is interpolated elevation data, whereas PEDR data is the actual measurement of the Martian terrain. Therefore, broader terrain matching is conducted with MEGDR DTM to conduct approximate positioning, and later, PEDR points are matched for precise absolute positioning.

The Spirit rover landing position, which is also the origin of Local Coordinate System, is centered at 175.47848 º in longitude and −14.571892 º in latitude (Golombek and Parker, 2004). The location was obtained based on comprehensive rover localization and photogrammetric analysis of various orbital dataset after the landing. In this research, the knowledge of the rover’s landing position is used to validate the absolute positioning result. Later, it is also used as an initial tie point between orbital and ground image networks.

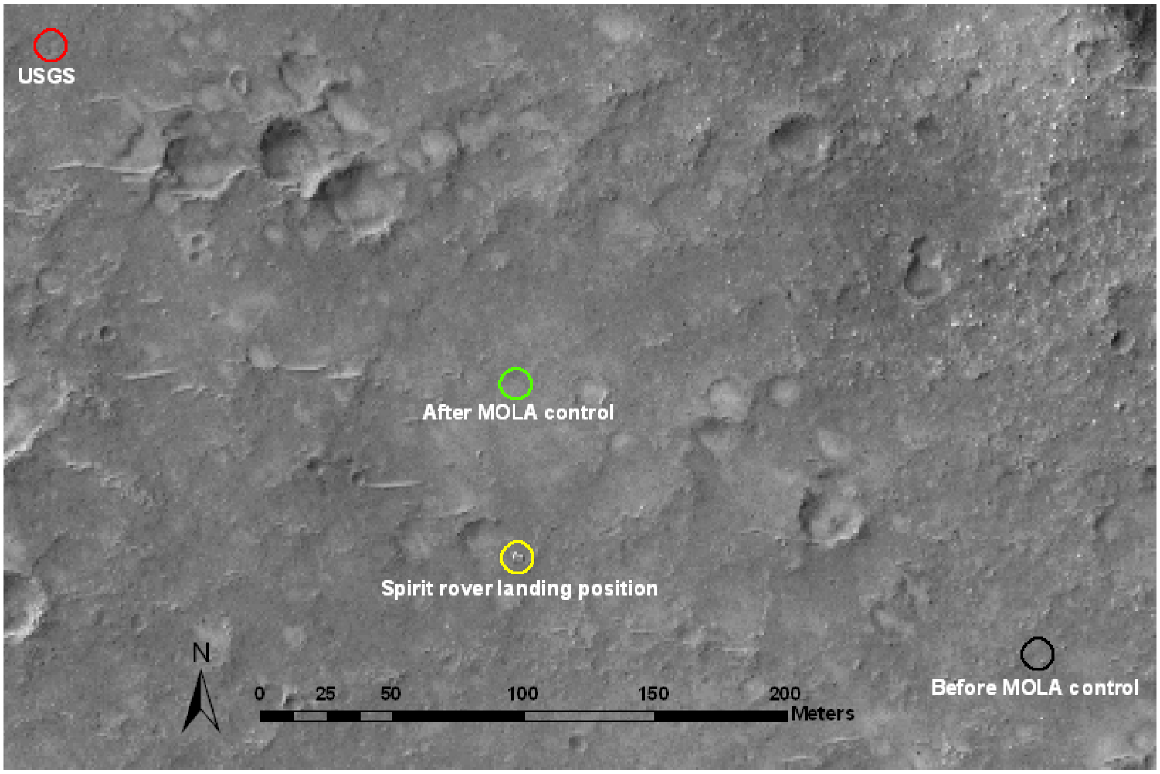

Figure 6.14 The absolute positioning result using MOLA control compared with the known Spirit rover landing position

The origin of Spirit rover traverse can be identified on the HiRISE image since the debris of the landing unit is left on the ground, which is the bright object inside the yellow circle in Figure 6.14. For visual understanding of the result of the absolute positioning presented in this dissertation, the HiRISE orthophoto created in equirectangular projection is shifted so that the debris (yellow circle) represents the known Spirit rover landing position. The Spirit rover landing position in the HiRISE topographic products (generated using the original exterior orientation parameters before bundle adjustment) is displayed as a black circle and about 200 m apart from the known position. After conducting the absolute positioning based on the MOLA control, the displacement is reduced to 65 m. In the USGS orthophoto, the positional difference from the known Spirit rover landing position is about 270 m (shown as red circle in Figure 6.14). Considering that the horizontal accuracy of the MOLA dataset is about 100 m (Smith et al., 2001), the absolute positioning, using MOLA DTM and points, were successful within the accuracy level of the control network.

6.5 Comparison with USGS Products

To check the quality of our DTM and orthophoto, a cross-comparison is conducted with USGS topographic products generated from the same HiRISE stereo images used in this research. For topographic mapping with HiRISE images, the USGS used both the USGS ISIS system and the commercial stereogrammetric software SOCET SET (Kirk et al., 2008). USGS products are directly controlled by the MOLA point data, and the topographic height is referenced to the MOLA areoid. For comparison purposes, the reference of the USGS DTM is set as MOLA DTM, which uses the planetary radius of 3,396,000 m. As seen in Figure 6.13 and Figure 6.14, there is about 230 m of horizontal displacement between the two topographic products. Therefore, a spatial registration between the two DTMs is needed for comparison. A 3-D similarity transformation was performed based on ten evenly distributed control points that were manually selected on the orthophotos (Figure 6.15). This process removes the horizontal displacements. After 3-D similarity transformation, the standard deviation of the residuals of the control points is 0.65 m. The minimum and the maximum residuals in horizontal position were 0.08 m and 0.64 m. Considering the 1-m resolution of the DTMs, the average displacement of less than one grid spacing is reasonable for the DTM comparison. The amount of vertical residual was much larger, ranging from -2.48 m to 1.99 m.

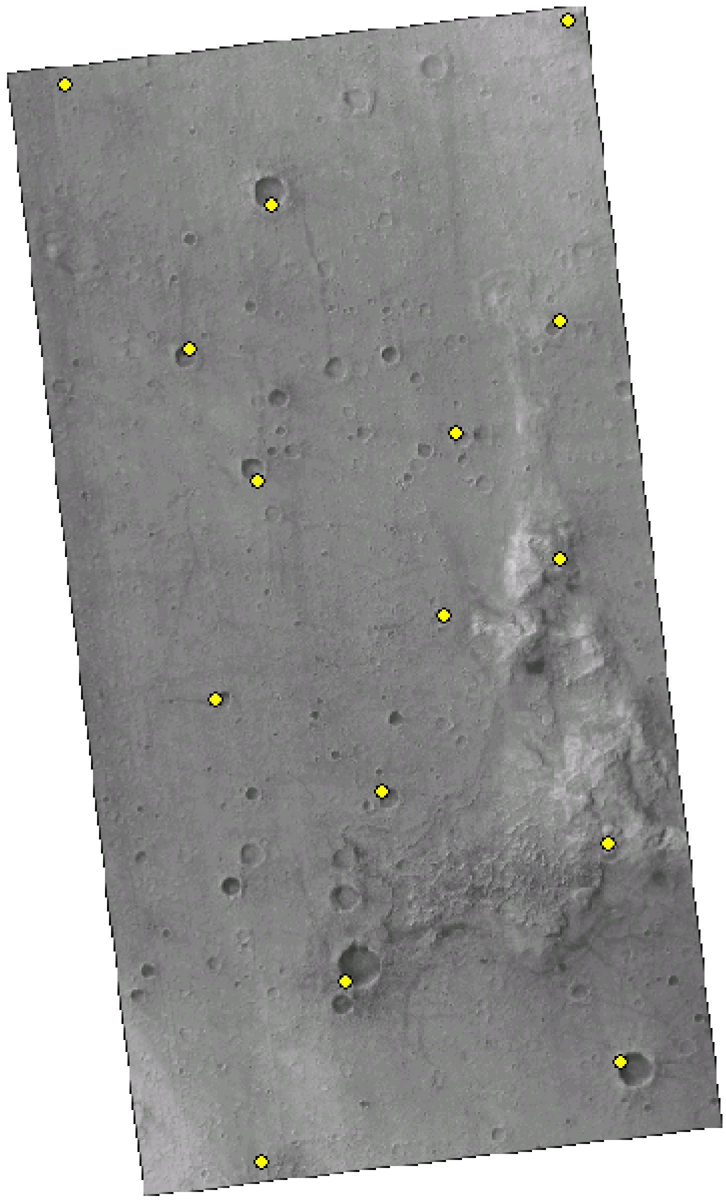

Figure 6.15 Control points for registration of HiRISE orthophoto generated by method 4

bundle adjustment to USGS orthophoto

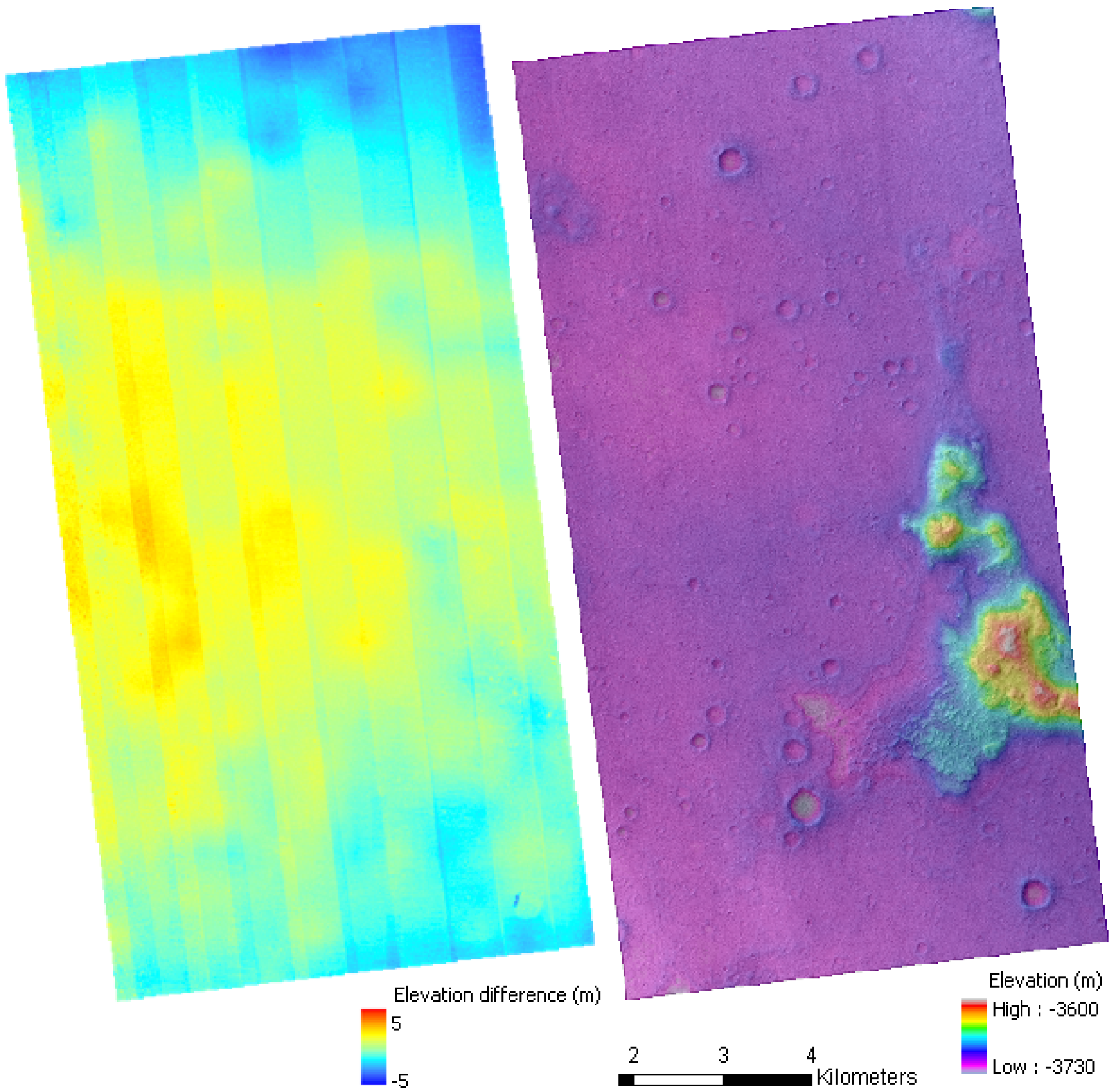

Figure 6.16 Elevation difference between our DTM and USGS DTM

After the horizontal registration, vertical differences were calculated between the two DTMs. Figure 6.16 shows that most areas have differences less than 1 meter. The standard deviation of elevation differences between the DTMs is 0.83 m. There is an obvious trend in the elevation difference, which is likely to be caused by third order polynomial coefficients updated from bundle adjustment. However, the major differences come from the vertical jumps (“cliffs”) that were still present in USGS DTM. There are two red spots indicating large difference between our DTM and USGS DTM. These are interior parts of craters where huge shadows are cast around the crater rims. Due to the change of the sun exposure angle, the two stereo images no longer show the similar distribution pattern of pixel brightness values in the area. Since the simple automatic matching software used in this research accepts only highly correlated points, matched points were lacking in those areas. This suggests that, in such cases where automatically generated tie points are not sufficient enough, manually matched points are beneficial for precision of topographic products.

6.6 Orbital/Ground Rock Matching Along the Spirit Rover Traverse

Seven test sites were chosen to implement the rover localization by orbital/ground rock matching proposed in chapter 4. As presented above, the orbital topographic products are generated by method 4 bundle adjustment and absolute positioning using MOLA control networks. Finally, the horizontal position of HiRISE image network is moved 65 m south so that the origin of the rover traverse could be registered to the official Spirit rover landing position. For planetary surface exploration, the localization of landing position at the beginning of the mission is conducted as top priority and verified rigorously, using every technology available. Therefore, it is reasonable to register the origin of the rover traverse with the HiRISE image network. The proposed method of the rover localization is designed to automatically correct the accumulative offsets between the HiRISE orthomap and the rover traverse obtained from dead reckoning and incremental bundle adjustment.

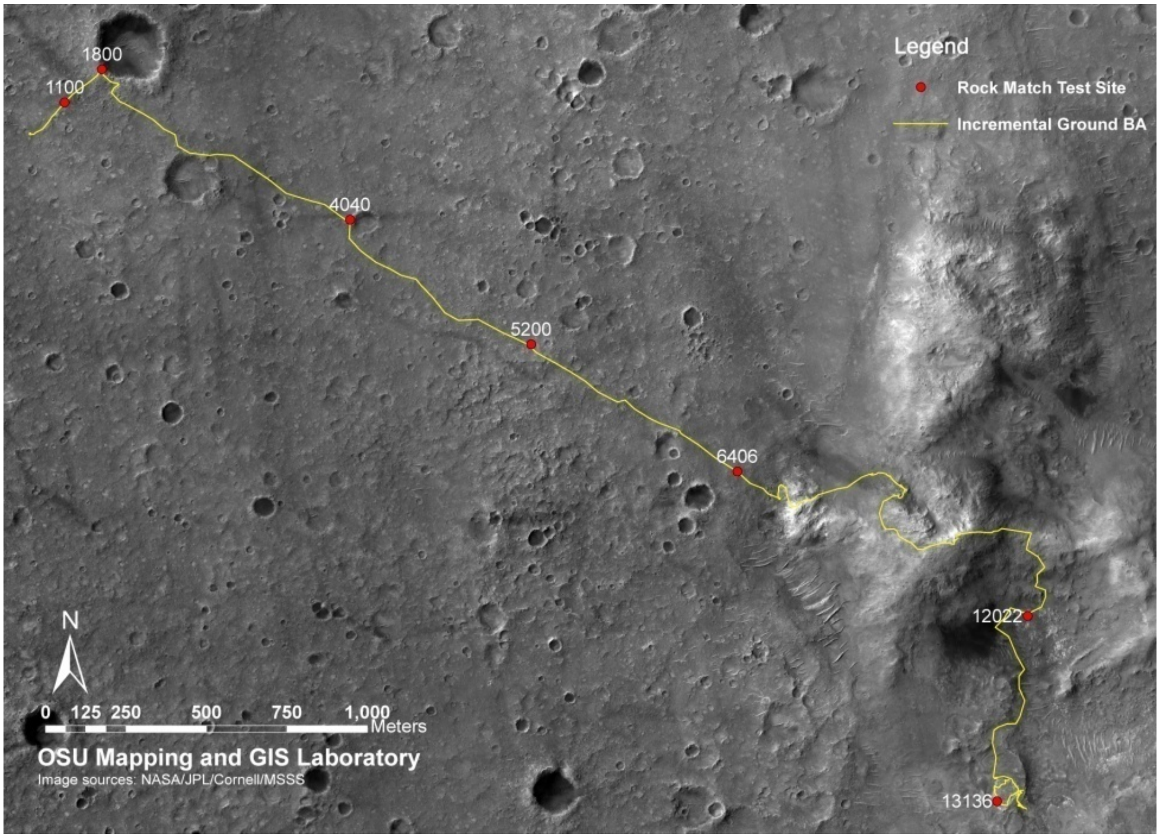

Figure 6.17 Rock matching test sites along the Spirit rover traverse (red dots)

The test sites were selected along the Spirit rover traverse (Figure 6.17). Terrain matching between orbital and ground DTMs, rock extraction and rock pattern matching were conducted at each site. The adjusted rover position was compared with the rover position manually identified on HiRISE orthomap. The rock matching results for the seven test sites are summarized in Table 6.2. Telemetry data from the NASA's Planetary Data Systems were used as the initial rover position. Terrain matching was performed based on the DTMs derived from orbital and ground datasets, and the rover position was updated based on rock pattern matching. In Figure 6.18, the rock matching result of the six test sites are presented, except for the sol 1,349 site already shown in chapter 4.

Table 6.2 Rock matching results from ground imagery

Site	1100	1800	4040	5200	6406	AVLF	AKFF
Sol	51	70	119	132	152	703	1349
Distance from the origin (m)	159.7	309.6	1299.5	2037.3	2802.4	4660.2	5832.7
Number of ground rocks	20	36	23	12	14	30	55
Number of matched ground rocks	10	13	5	6	6	8	13
Percent matched (%)	50.0	36.1	21.7	50.0	42.9	26.7	23.6
Rover position shift after rock pattern matching (m)	(2.05, 0.70)	(1.01, 0.29)	(1.10, 5.73)	(1.25, 1.50)	(-3.80, -10.9)	(1.72, 1.73)	(-2.73, 2.62)
RMS error of the matched ground rocks (m)	0.25	0.21	0.35	0.39	0.28	0.24	0.18

The number of ground rocks extracted from Navcam panorama varied from as little as 12 (sol 132) to 55 (sol 1349), depending on the quantity of rocks meeting the criteria of size, height and image pixel values. After rock pattern matching was performed, the number of ground rocks matched with orbital rocks ranged from 5 to 13, depending on the availability of the corresponding orbital rocks. The ratio of matched ground rocks to extracted rocks ranged from 21.7 % up to 50.0 %. The low match rate is due to the difficulty of the orbital rock detection. The primary reason why rocks clearly visible from the ground are often not detected in the orbital imagery is mainly because image pixel intensity values are not distinguished from the surrounding area. Rover position is adjusted after rock pattern matching and the amount of shift is from 1.1 m to 11.5 m, depending on the effectiveness of terrain matching. The RMS error of the position of the matched rocks was consistently less than 0.5 m. As the number of matched ground rocks increases, the amount of RMS error is decreased.

For all seven test sites, the matched rock pairs and rover positions are consistent with the manual verification. These successfully matched rover sites satisfy the following conditions. First, the number of ground rocks is at least a dozen and no less than five rocks are matched. Ground rocks are spread around the rover and not concentrated on one side only. Although the orbital/ground rock matching rate is low, the ones that are matched are prominent ground features. Therefore, more than four of highly distinguished rock pairs are sufficient enough to identify the rover position on the orbital orthomap.

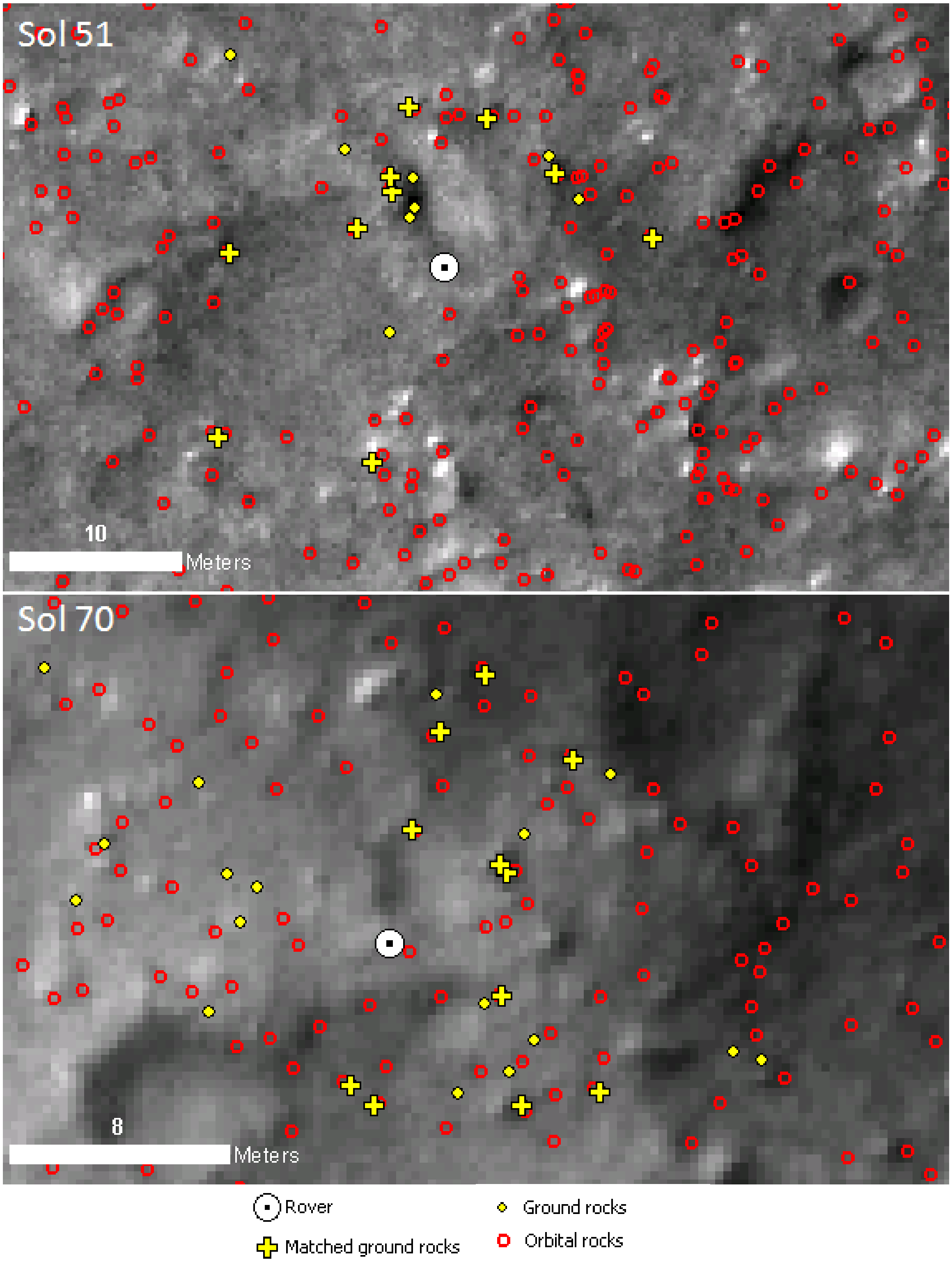

Figure 6.18 Orbital/ground rock matching results overlaid on HiRISE orthophoto

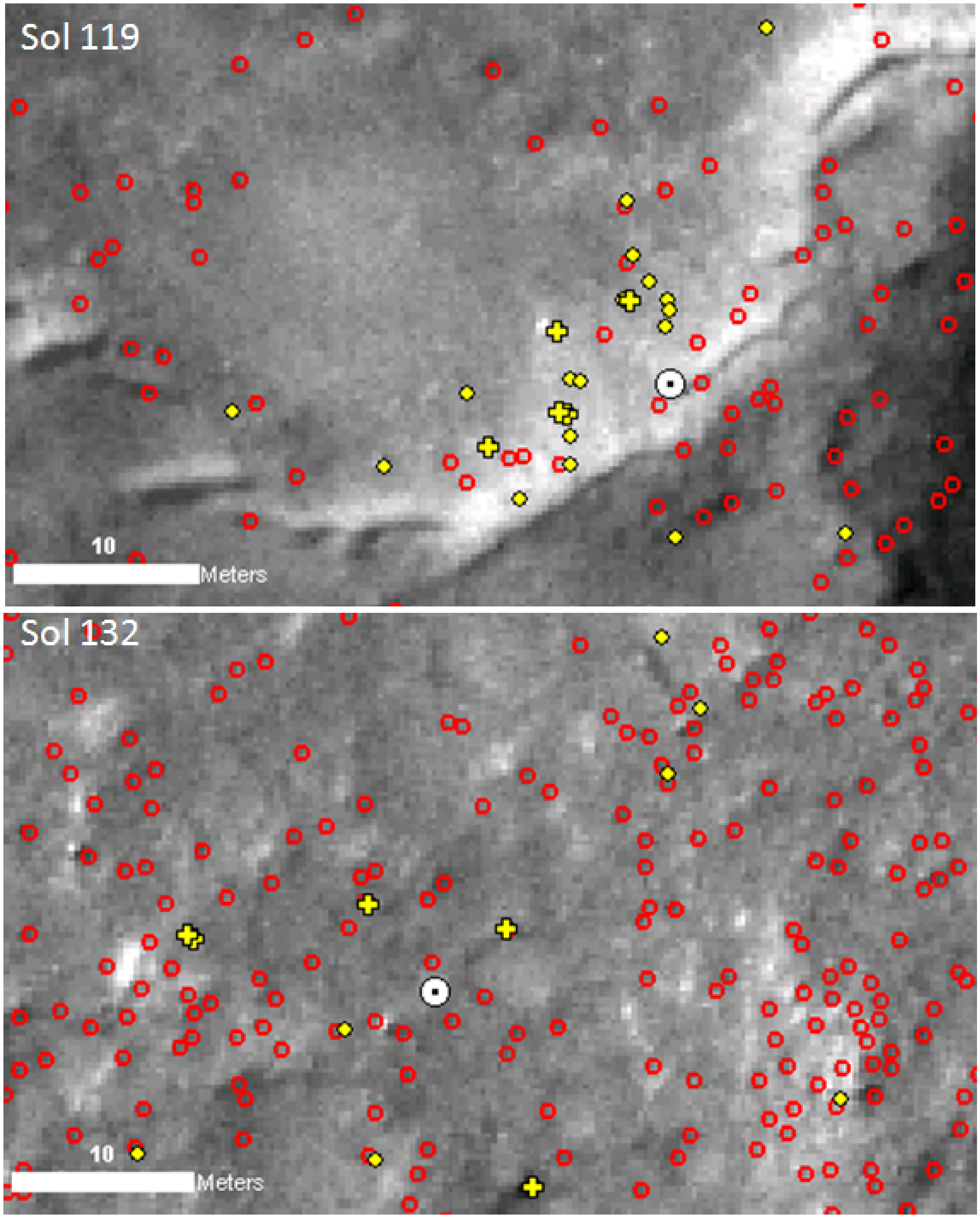

Figure 6.18 (continued)

(continued)

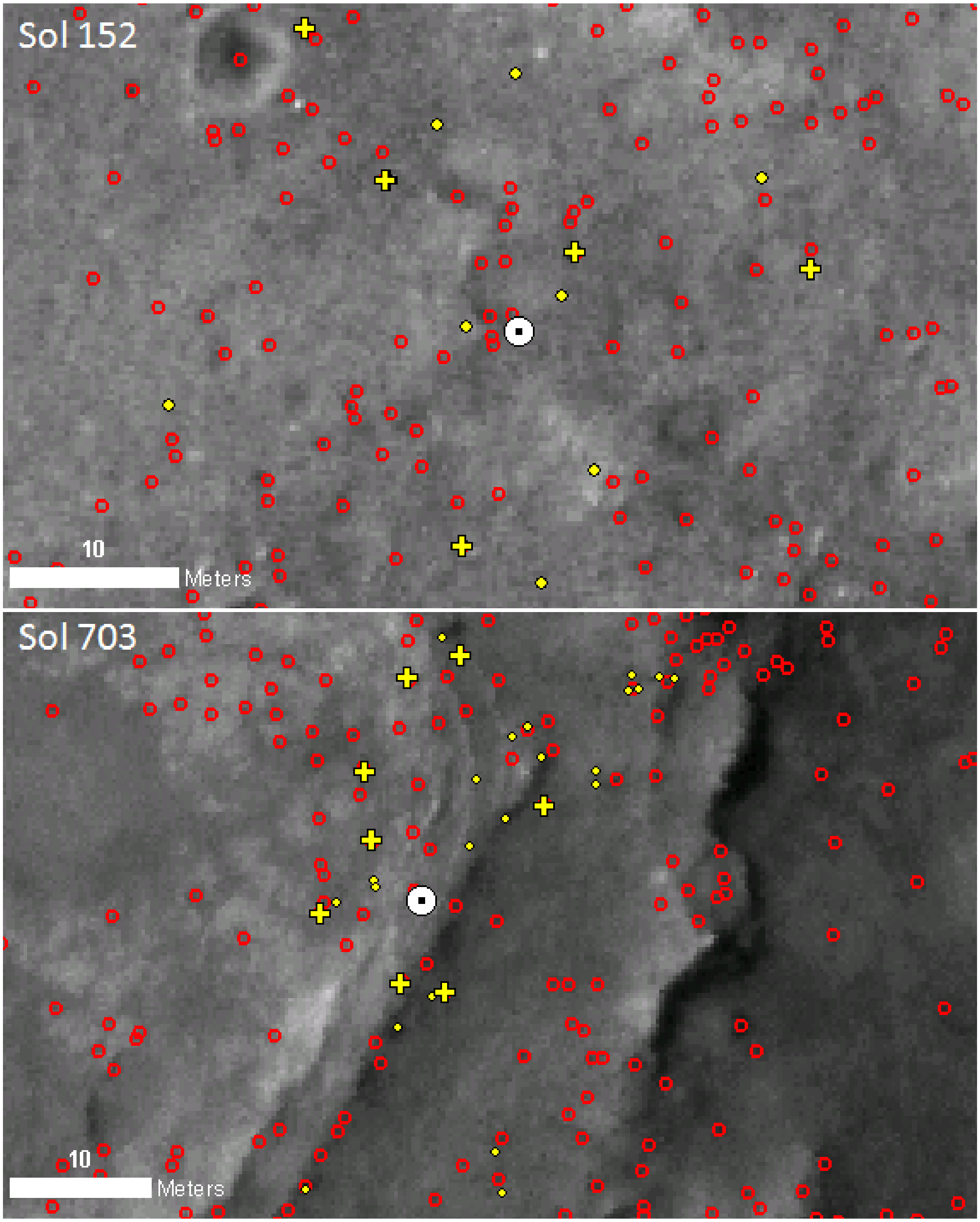

CHAPTER 7

DISCUSSION AND FUTURE RESEARCH

The objectives in this research are twofold. The first is to develop photogrammetric processing methodology for the construction of HiRISE orbital image networks. The second is to develop a new methodology for integration of orbital and ground image networks. The contribution of this dissertation can be divided into the following:

- A framework for orbital image network is developed. Using a HiRISE rigorous sensor model, a bundle adjustment system is developed to resolve misalignment to achieve coherence between stereo images as well as between CCDs in the same image. Also, absolute positioning is conducted by incorporating a MOLA control network in HiRISE orbital image processing.
- A framework to integrate orbital and ground image networks is developed using automatic rock extraction and rock distribution pattern matching to identify common objects from the different types of image networks.
- As a result of HiRISE orbital image processing and integration with MER ground image networks, DTM and orthophoto are generated and rover localization is conducted.

The complexity of the HiRISE sensor geometry raises technical issues that need to be resolved in stereo image processing when it is used for the generation of high-resolution topographic products such as DTMs or orthophotos. In this dissertation, a rigorous sensor model is implemented for HiRISE photogrammetric processing. The reference frames, interior orientation and exterior orientation of HIRISE imagery are defined and described in detail. Also, high-frequency movement of the rotation angle is analyzed based on the relative offsets of image pixels in the CCD overlap area.

For construction of orbital image networks, a bundle adjustment system based on tie points is developed to resolve misalignment of exterior orientation parameters between stereo images and CCDs. Bundle adjustment based on a polynomial function model of exterior orientation parameters was conducted. In addition to traditional tie points, inter-CCD tie points between multiple CCDs in a single orbit are used to minimize geometric inconsistencies between CCDs. The proposed bundle adjustment method based on third-order polynomials reduced mean back projection error of traditional tie points from over 3 pixels to less than 0.2 pixels for the test dataset covering Spirit rover landing site. The back projection residual between inter-CCD tie points was also reduced to about half a pixel. As a result, this method was able to remove the seam line in the DTM. Bundle adjustment without using inter-CCD tie points only reduced the inter-CCD residual to about one pixel, which caused a visible seam line in the DTM. To achieve consistent orbital image network construction without ground-control points, HiRISE DTM is matched with MOLA MEDGR DTM and PEDR profiles after bundle adjustment. Based on the terrain matching results, the position of HiRISE orbital image network is shifted to achieve absolute geopositioning, based on MOLA global Mars terrain model. The absolute positioning result is compared with the Spirit rover landing position visible on the HiRISE image.

In this dissertation, a new framework for integration of orbital and ground image networks is presented. Based on the orbital image network from HiRISE stereo images and a ground image network from MER rover localization process including incremental bundle adjustment, these separate orbital and ground image networks are connected using rock matching. The goal of this research is to link the two image networks within sub-meter level accuracy.

First, terrain matching between orbital and ground DTMs is conducted to obtain approximate rover position on the orbital maps. A rock extraction strategy is developed for orbital and ground imagery to identify rocks that are visible from both types of image source. The ground rock extraction is based on the image intensity and 3-D coordinates. In orbital imagery, rocks are distinguished from the terrain mainly based on pixel brightness. Since rocks ultimately serve as tie points between orbital and ground image networks, the size and shape constraints are applied for rock extraction. Finally, to connect orbital and ground image networks, rock pattern matching is developed based on the extracted orbital/ground rocks. Test results show that this method can effectively extract rocks and adjust rover positions comparable to the labor-intensive incremented bundle adjustment currently used for the MER mission. This technique opens a new possibility for autonomous rover localization performed onboard unmanned vehicles for future space exploration.

A 1-m resolution DTM and a 0.25-m resolution orthophoto are created of the area covering the Spirit rover traverse, based on the rigorous sensor model and bundle adjustment strategy proposed in this research. The DTM generated in this research showed significant reduction of inter-CCD misalignment. The comparison with USGS DTM generated using SOCET SET and manual editing showed standard error of 0.84 m in elevation difference and less than 2 m of residual for 95 % of the area.

Although the proposed methods are successfully implemented in the test site, there are some issues that need to be improved. In this dissertation, a simple area-based matching method is used based on cross-correlation only to generate quick orthophotos without manual editing. However, this method has a problem of pixel-locking: the sub-pixel disparities tending toward their integer estimates, thus resulting DTM with step pattern (Neifian, et al., 2009). To create high-quality DTM that represent the actual terrain, development of new stereo image processing method is needed to reduce the pixel locking.

In this research, absolute positioning is achieved from terrain matching using interpolated MOLA DTM followed by refinement, using MOLA point data. Currently the bundle adjustment is conducted separately from the absolute positioning due to the lack of identifiable MOLA points in HiRISE imagery. In the future, incorporation of MOLA control networks in HiRISE bundle adjustment is desirable to combine the orbital image networks together.

To incorporate the new rover localization technology into autonomous rover navigation, the proposed orbital/ground rock matching process needs to be combined with the incremental bundle adjustment of rover image networks. Rover localization is the sophisticated process of combining many methods including dead-reckoning, visual odometry and incremental bundle adjustment. All of the localization methods have their own advantages and disadvantage depending on the conditions such as the type of terrain and the presence of identifiable features. Further research on decision criteria for all possible scenarios would benefit the development of automated rover navigation by providing strategy for obtaining the optimal localization result from combination of localization methods at various conditions.

APPENDIX

Exterior Orientation Parameter Extraction from SPICE

The space science data on NASA planetary exploration, such as HiRISE exterior orientation parameters, is archived in SPICE information system by Navigation and Ancillary Information Facility (NAIF). The SPICE system includes ancillary data grouped as SPICE kernels and a suite of software, mostly in the form of subroutines that customers incorporate in their own application programs to read the SPICE kernel data and to compute derived observation geometry, such as position, latitude/longitude, and pointing angles. The software is offered in FORTRAN, C, IDL® and MATLAB®. There are plenty of documents and tutorials available in NAIF website about how to use SPICE system (http://naif.jpl.nasa.gov/naif/tutorials.html). This Appendix focuses on extracting HiRISE exterior orientation parameters using C language in Windows environment.

First, the SPICE toolkit in C language should be installed according to the instruction (http://naif.jpl.nasa.gov/naif/toolkit_C_PC_Windows_VisualC_32bit.html). The installation begins with running 'cspice.exe' file and extracting it into a desired location, i.e. C:\HiRISE\. Then the folder structure of the CSPICE system will look like the following picture.

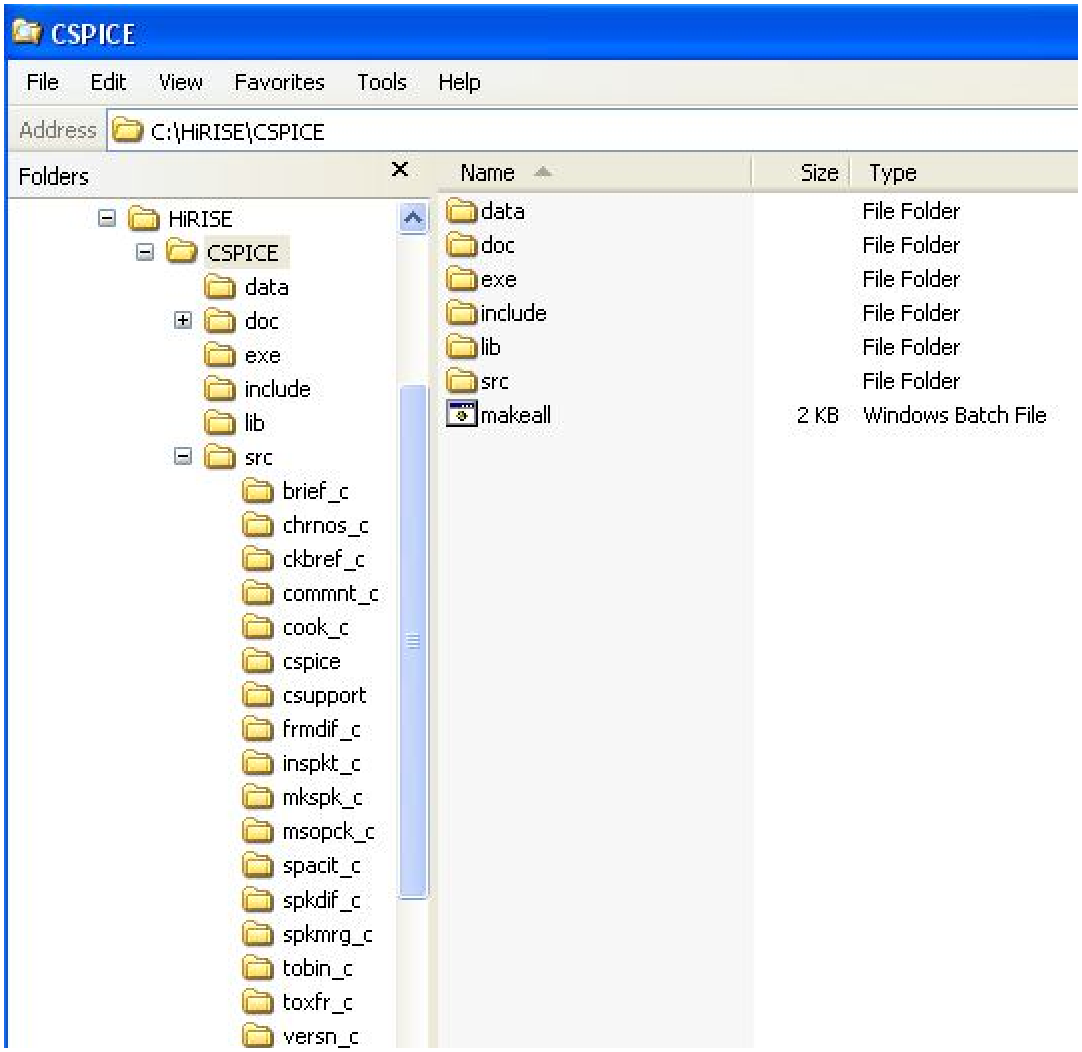

This package is pre-compiled and the libraries could be linked once installed. In some cases, it may be necessary to re-build the toolkit by running the 'makeall.bat' script in the DOS windows command.

```
C:\HiRISE\CSPICE>makeall.bat
```

To compile a native C++ program from the command line, 'cl.exe' compiler should be added to the path. The location of 'cl.exe' file depends on the version of Microsoft Visual Studio. Once the directory containing 'cl.exe' is identified, it can be set to the path. The other way to enable 'cl.exe' is to go to the directory and run the 'vcvars32.bat' script.

Secondly, necessary kernel files should be downloaded from the NAIF website (http://naif.jpl.nasa.gov/naif/data.html).

- Frames Kernel (FK): relationships between reference frames used in geometry computations
- Instrument Kernel (IK): instrument specific information defined in the SPICE
- Planetary Constants Kernel (PCK): orientation of solar system bodies and their physical constants
- Leapseconds Kernel (LSK): tabulation between Coordinated Universal Time (UTC) and ephemeris time (ET)
- Spacecraft Clock Kernel (SCLK): relationship between ephemeris time (ET) and spacecraft clock (SCLK) time
- Camera-matrix kernel (CK): orientation data for a spacecraft or a moving structure on the spacecraft
- SPICE Ephemeris Subsystem Kernel (SPK): ephemeris (trajectory) data for "ephemeris objects" such as spacecrafts, rovers, planets, comets and asteroids.

For organization of the kernel files, it is recommended to create separate folders for each kernel. For example, a typical spice kernel setup will look like the following.

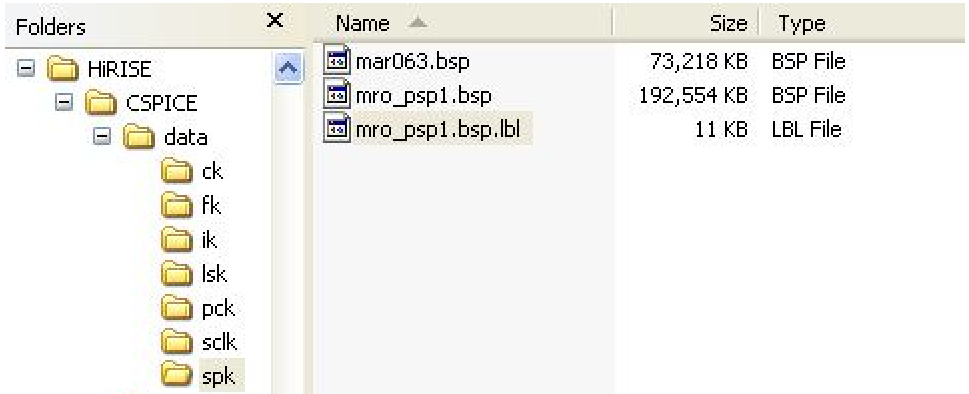

For FK, IK, PCK LSK, and SCLK only the most updated files are needed. CK and SPK store data for a certain period of time. To extract HiRISE exterior orientation, CK and SPK files that include the time of image acquisition are needed. For example, PSP_001777_1650 image was taken on December 12, 2006. The file names of CK indicate the date of data acquisition, such as 'mro_sc_psp_061212_061218.bc'. Satellite SPK files come with label (.lbl) files, which contains the start and end time for the ephemeris data. For this image, the 'mro_psp1.bsp' covers the trajectory of the MRO satellite during the time of the image acquisition, as shown in the following text in the 'mro_psp1.bsp.lbl' file:

```
Approximate Time Coverage
--------------------------------------------------------

     This file covers the following part of the Primary Science Phase
     of the MRO mission (orbits 601 through 2022):

        Start of Interval (ET)               End of Interval (ET)
        --------------------------------     -------------------------
        2006 SEP 12 06:40:00.000             2007 JAN 01 01:01:05.183
```

To extract information from the kernel files, SPICE system needs to load kernels. For this example, a text file 'HiRISE.txt' is created as follows. The file contains the list of the required kernels with the full path information.

HiRISE.txt

```
\begindata
KERNELS_TO_LOAD = (
'C:/HiRISE/CSPICE/data/ck/mro_sc_psp_061212_061218.bc'
'C:/HiRISE/CSPICE/data/spk/mro_psp1.bsp'
'C:/HiRISE/CSPICE/data/spk/MAR063.BSP'
'C:/HiRISE/CSPICE/data/fk/mro_v14.tf'
'C:/HiRISE/CSPICE/data/ik/mro_hirise_v11.ti'
'C:/HiRISE/CSPICE/data/lsk/naif0009.tls'
'C:/HiRISE/CSPICE/data/sclk/MRO_SCLKSCET.00038.65536.tsc'
'C:/HiRISE/CSPICE/data/pck/pck00008.tpc'
)
```

Planetary SPK file is also needed for generation of MRO position regarding to the Mars body-fixed frame. The 'mar063.bsp' file is the kernel for the trajectory of Mars. Each of the FK, IK, LSK, SCLK, and PCK kernel file is the most recently updated ones available in the NAIF website.

The next step is getting image parameters from the header of the EDR HiRISE file. For example, the header of the 'PSP_001777_1650_RED0_0.img' file contains the following information.

```
PRODUCT_ID                        = "PSP_001777_1650_RED0_0"
...
    /* Time at the beginning of the first target image line. */
    START_TIME                    = 2006-12-12T21:53:22.823
    SPACECRAFT_CLOCK_START_COUNT = "850427621:44577"
...
    MRO:DELTA_LINE_TIMER_COUNT       = 131
...
    MRO:BINNING                      = 1
    MRO:TDI                          = 128
...
    LINES              = 40000
```

For generation of multiple exterior orientation files for all 10 CCDs, the 'input.txt' file is created. The first line contains the number of exterior orientation files to generate.

The second line it the directory where the output files are stored. The remaining lines indicate parameters for each exterior orientation file. The first item (i.e. PSP_001777_1650_0) is the output file name. The second item indicates the start time of the spacecraft clock. The following three items are *DLINE*, *BIN*, and *TDI* in Equation 2.4. The last item is the number of lines in the image.

input.txt

```
10
C:\HiRISE\CSPICE\data\
PSP_001777_1650_0 850427621:44577 131 1 128 40000
PSP_001777_1650_1 850427621:41480 131 1 128 40000
PSP_001777_1650_2 850427621:44830 131 1 128 40000
PSP_001777_1650_3 850427621:41480 131 1 128 40000
PSP_001777_1650_4 850427621:44620 131 1 128 40000
PSP_001777_1650_5 850427621:41480 131 1 128 40000
PSP_001777_1650_6 850427621:44701 131 1 128 40000
PSP_001777_1650_7 850427621:41480 131 1 128 40000
PSP_001777_1650_8 850427621:44577 131 1 128 40000
PSP_001777_1650_9 850427621:41308 131 1 128 40000
```

The last step is running C program to extract the HiRISE exterior orientation parameters from the SPICE kernels. Such C programs should be created in '~\CSPICE\src\cook_c\' directory. In this example, 'HiRISE.cpp' was created in the that directory. For simplicity, other input files such as 'HiRISE.txt' and 'input.txt' files are also put into the same folder.

HiRISE.cpp

```
#include <fstream>
#include "SpiceUsr.h"

void GetEO( char *out, char *SCLK, double DLINE, double BIN, double TDI, int LINE )
{
    int     i, j, k, found;
    char    utcstr[30];
    double  LR, et0, et1, et, encsclk, clkout, lt, a1, a2, a3;
    double  pos[3], R[3][3], R1[3][3], R2[3][3], Rt[3][3];

    FILE    *fout = fopen( out, "w" );

    scs2e_c( -74999, SCLK, &et0 );
    LR = ( 74.0 + DLINE/16.0 )/1000000;
    et1 = et0 + LR*(BIN-TDI)/2;
    for( i = 0; i < LINE; i++ )
    {
        et = et1 + i*LR*BIN;

        spkpos_c ( "MRO", et, "IAU_Mars", "CN+S", "MARS", pos, &lt );
        for( j = 0; j < 3; j++ )    pos[j] *= 1000;

        pxform_c( "J2000", "IAU_MARS", et, R1 );
        pxform_c( "MRO_HIRISE_OPTICAL_AXIS", "J2000", et, R2 );
        mxm_c( R1, R2, Rt );
        for( j = 0; j < 3; j++ )
            for( k = 0; k < 3; k++ )
                R[j][k] = Rt[k][j];
        m2eul_c( R, 3, 2, 1, &a3, &a2, &a1 );

        fprintf(fout, "%.12f\t%.12f\t%.12f\t", pos[0], pos[1], pos[2]);
        fprintf(fout, "%.17f\t%.17f\t%.17f\n", a1, a2, a3);
    }
    fclose(fout);
}

int main( int argc, char * argv[] )
{
    int     i, j, count, LINE;
    char    path[50], name[50], out[90], SCLK[50];
    double  DLINE, BIN, TDI;

    furnsh_c( ".\\HiRISE.txt" );

    FILE    *fin = fopen( ".\\input.txt", "r" );
    fscanf( fin, "%d%s", &count, path );
    for( i = 0; i < count; i++ )
    {
        fscanf( fin, "%s%s%lf%lf%lf%d", name, SCLK, &DLINE, &BIN, &TDI, &LINE );
        sprintf( out, "%s%s.txt", path, name );
        GetEO( out, SCLK, DLINE, BIN, TDI, LINE );
    }
    fclose(fin);
    return (0);
}
```

There are two functions in 'HiRISE.cpp' file. The main function calls GetEO function to generate exterior orientation files. Including 'SpiceUsr.h' (line 2) enables the program to utilize many SPICE subroutines. In the main function, the required SPICE kernels are loaded using furnsh_c function (line 43). Then the image acquisition parameters are obtained from 'input.txt' file (line 45-49). By plugging in these parameters to GetEO function, exterior orientation file with the file name 'out' is created (line 51).

In the GetEO function, the spacecraft clock time (SCLK) is converted into the ephemeris time (et0) by function scs2e_c (line 13). The input argument requires the NAIF spacecraft clock ID, which is -74999 for the MRO high precision format clock according to the SCLK kernel. Line 14 through 18 calculates ephemeris time (et) for each image scan line (Equation 2.4).

By plugging in the ephemeris time (et) into spkpos_c function, the position of MRO spacecraft in the Mars body-fixed frame (IAU_Mars) is extracted from the SPK kernel (line 20). Among the input variables, "MRO" is the target body name, "IAU_Mars" is the reference frame of output position vector, "CN+S" is abberation correction method, "Mars" is the observing body name. The output variable, pos is the position of the MRO spacecraft in kilometers and lt is one way light time between observer and target. Since the unit of the position vector is kilometer, the values of pos is multipled by 1000 to obtain the position in meter. Line 23 through 29 extracts the orientation angle. The function pxform_c returns the rotation matrix that transforms position vectors from the one frame to another. The first variable is the frame to teansform from, and the second variable is the frame to transform to, the third variable is the ephemeris time and output is stored in the fourth variable, a 3×3 rotation matrix. The function mxm_c multiplies two 3×3 matrices from the first and second variables and return the multiplied product as the third variable. Therefore, line 23 through 25 can be rewritten as:

$$\vec{v}_{\mathrm{IAU\_Mars}} = \mathrm{R1} \cdot \vec{v}_{\mathrm{J2000}} \qquad \text{(line 23)}$$

$$\vec{v}_{\mathrm{J2000}} = \mathrm{R2} \cdot \vec{v}_{\mathrm{HiRISE}} \qquad \text{(line 24)}$$

$$\vec{v}_{\mathrm{IAU\_Mars}} = \mathrm{R1} \cdot \mathrm{R2} \cdot \vec{v}_{\mathrm{HiRISE}} = \mathrm{Rt} \cdot \vec{v}_{\mathrm{HiRISE}} \qquad \text{(line 25)}$$

$$\vec{v}_{\mathrm{HiRISE}} = \mathrm{Rt}^{\mathrm{T}} \cdot \vec{v}_{\mathrm{IAU\_Mars}} = \mathrm{R} \cdot \vec{v}_{\mathrm{IAU\_Mars}} \qquad \text{(line 26-28)}$$

The m2eul_c function is used to obtain the rotation angles in the form of roll, pitch and yaw. The first variable is a rotation matrix to be factored. (3, 2, 1) are the rotation axes of the 'factor' rotations. The last three variables are third, second, and first Euler angles in radians. Therefore, the rotation matrix R is equivalent to rotating around x-axis by a1, y-axis by a2, and then z-axis by a3. The output files are consisted of six exterior orientation parameters (position in meter and rotation angles in radians) for each line (line 31-32). The detailed explanation of each function is provided in the source codes located in the '~\CSPICE\src\cspice\' folder.

Finally, HiRISE.cpp file can be compiled by running cl command with the cspice.lib library (located in C:\HiRISE\CSPICE\lib\). After compilation, the executable file 'HiRISE.exe' is created. Executing HiRISE.exe file will generate exterior orientation files in the output directory specified in the input text file.

```
C:\HiRISE\CSPICE\src\cook_c>cl HiRISE.cpp ..\..\lib\cspice.lib
Microsoft (R) 32-bit C/C++ Optimizing Compiler Version 15.00.21022.08 for 80x86
Copyright (C) Microsoft Corporation.  All rights reserved.

HiRISE.cpp
C:\Program Files (x86)\Microsoft Visual Studio 9.0\VC\INCLUDE\xlocale(342) : war
ning C4530: C++ exception handler used, but unwind semantics are not enabled. Sp
ecify /EHsc
Microsoft (R) Incremental Linker Version 9.00.21022.08
Copyright (C) Microsoft Corporation.  All rights reserved.

/out:HiRISE.exe
HiRISE.obj
..\..\lib\cspice.lib

C:\HiRISE\CSPICE\src\cook_c>HiRISE
```

REFERENCES

Abshire, J.B., X. Sun and R.S. Afzal (2000). Mars Orbiter Laser Altimeter: Receiver Model and Performance Analysis, *Applied Optics*, 39 (15), 2449-2460.

Acton, C.H. (1999). SPICE products available to the planetary science community, *Lunar Planet. Sci.XXX*, Abstract 1233 (CD-ROM).

Adelson, E.H. C.H. Anderson, J.R. Bergen, P.J. Burt, and J.M. Ogden (1984). Pyramid methods in image processing, *RCA Engineer*, 29 (6), 33-41.

Agarwal, S. (2006). Rock extraction, modeling and matching for the automation of Mars rover localization. Master Thesis, The Ohio State University, Columbus, OH.

Albee, A., R. Arvidson, F. Palluconi, and T. Thorpe (2001). Overview of the Mars Global Surveyor mission. *Journal of Geophysical Research*, 106 (10), 23291–23316, doi:10.1029/2000JE001306.

Albertz, J., M. Attwenger, J. Barrett, S. Casley, P. Dorninger, E. Dorrer, H. Ebner, S. Gehrke, B. Giese, K. Gwinner, C. Heipke, E. Howington-Kraus, R.L. Kirk, H. Lehmann, H. Mayer, J. Muller, J. Oberst, A. Ostrovskiy, J. Renter, S. Reznik, R. Schmidt, F. Scholten, M. Spiegel, U. Stilla, M. Wählisch, G. Neukum, and the HRSC CoI-Team (2005). HRSC on Mars Express – Photogrammetric and Cartographic Research, *Photogrammetric Engineering & Remote Sensing*, 71 (10), 1153–1166.

Archinal, B.A., R.L. Kirk, T.C. Duxbury, E.M. Lee, R. Sucharski, and D. Cook (2003). Mars Digital Image Model (MDIM) 2.1 Control Network, *ISPRS Working Group IV/9 Workshop "Advances in Planetary Mapping 2003"*, Houston, TX, March 2003.

Archinal, B.A., E.M. Lee, R.L. Kirk, T.C. Duxbury, R.M. Sucharski, D.A. Cook, and J.M. Barrett (2004). A new Mars Digital Image Model (MDIM 2.1) control network, *XXth ISPRS Congress*, Istanbul, Turkey, July 2004.

Arvidson, R.E., R.C. Anderson, P. Bartlett, J.F. Bell III, D. Blaney, P.R. Christensen, P. Chu, L. Crumpler, K. Davis, B.L. Ehlmann, R. Fergason, M.P. Golombek, S. Gorevan, J.A. Grant, R. Greeley, E.A. Guinness, A.F.C. Haldermann, K.

Herkenhoff, J. Johnson, G. Landis, R. Li, R. Lindermann, H. McSween, D.W. Ming, T. Myrick, L. Richter, F.P. Seelos IV, S.W. Squyres, R.J. Sullivan, A. Wang, and J. Wilson (2004). Initial localization and physical properties experiments conducted by Spirit at Gusev Crater. *Science*, 305 (5685), 821-824.

Beyer, R.A., B. Archinal, Y. Chen, K. Edmundson, D. Harbour, E. Howington-Kraus, R. Li, A. McEwen5, S. Mattson, Z. Moratto, J. Oberst, M. Rosiek, F. Scholten, T. Tran, M. Robinson, and the LROC Team (2010). LROC stereo data- results of initial analysis, *41st Lunar and Planetary Science conference*, Woodland, Texas, Abstract 2678.

Cheng, Y., A. Johnson, and L. Matthies (2005). MER-DIMES: A Planetary Landing Application of Computer Vision, 2005 *IEEE Computer Society Conference on Computer Vision and Pattern Recognition*, 1, 806-813.

Cheng, Y., M.W. Maimone, and L. Matthies (2006). Visual Odometry on the Mars Exploration Rovers. *IEEE Robotics and Automation Magazine,* 13 (2), 54–62.

Christensen, P.R., B.M. Jakosky, H.H. Kieffer, M.C. Malin, H.Y. McSween, Jr., K. Nealson, G.L. Mehall, S.H. Silverman, S. Ferry, M. Caplinger, and M. Ravine (2004). The Thermal Emission Imaging System (THEMIS) for the Mars 2001 Odyssey Mission, *Space Science Reviews*, 110, 85-13.

Devencia, K., S. Walker, and B. Zhang (2007). New Approaches to Generating and Processing High Resolution Elevation Data with Imagery. *Photogrammetric Week*, 17 (5), 1442-1448.

Di, K., F. Xu, R. Li, L. Matthies, and C. Olson (2002). High Precision Landing Site Mapping And Rover Localization By Integrated Bundle Adjustment of MPF Surface Images, *International Achieves of the Photogrammetry, Remote Sensing and Spatial Information Sciences (IAPRS)*, 34 (4), 733-737.

Di, K., F. Xu, J. Wang, S. Agarwal, E. Brodyagina, R. Li, and L. Matthies (2008a). Photogrammetric Processing of Rover Imagery of the 2003 Mars Exploration Rover Mission, *ISPRS Journal of Photogrammetry and Remote Sensing*, 63 (2), 181-201.

Di, K., J. Wang, S. He, B. Wu, W. Chen, R. Li, L.H. Matthies, and A.B. Howard (2008b). Towards Autonomous Mars Rover Localization: Operations in 2003 MER Mission and New Developments for Future Missions, *The XXI Congress of The International Society for Photogrammetry and Remote Sensing*, Beijing China, July 3-11, 2008. (DVD-ROM).

Estlin, T., D. Gaines, C. Chouinard, F. Fisher, R.Castano, M. Judd, R. Anderson, and I. Nesnas (2005). Enabling autonomous rover science through dynamic planning and scheduling. *Proceedings of the IEEE Aerospace Conference*, Big Sky, Montanna, March 2005.

Fabris, M., and A. Pesci (2005). Automated DEM extraction in digital aerial hotogrammetry: precisions and validation for mass movement monitoring, *Annals of Geophysics*, 48 (6), 973-988.

Förstner, W. (1986). A feature based correspondence algorithm for image matching, *Intl. Arch. Photogrammetry and Remote Sensing*, 26 (3), 150–166.

Gaddis, L.R., R.L. Kirk, J.R Johnson, L.A Soderblom, A.W. Ward, J. Barrett, K. Becker, T. Becker, J. Blue, D. Cook, E. Eliason, T. Hare, E. Howington-Kraus, C. Isbell, E.M. Lee, B. Redding, R. Sucharski, T. Sucharski, P.H. Smith, and D. T.Britt, (1999). Digital mapping of the Mars Pathfinder landing site: Design, acquisition, and derivation of cartographic products for science applications. *Journal of Geophysical Research*, 104 (E4), 8853-8868.

Galiatsatos, N., D. Donoghue, and G. Philip (2008). High resolution elevation data derived from stereoscopic CORONA imagery with minimal ground control: an approach using Ikonos and SRTM data, *Photogrammetric Engineering & Remote Sensing*, 74 (9), 1093–1106.

Goldberg, S.B., M.W. Maimone, and L.H. Matthies (2002). Stereo vision and rover navigation software for planetary exploration, *Proc. IEEE Aerospace Conf.*, Big Sky, MT, 2002.

Golombek, M., and T. Parker, (2004). Lander localization, MER Project Memorandum (one for Spirit, one for Opportunity), JPL/NASA.

Gor, V., R. Castano, R. Manduchi, R.C. Anderson, and E. Mjolsness (2001). Autonomous rock detection for Mars terrain, *AIAA Space 2001 Conference and Exposition*, Albuquerque, NM, August 2001.

Gwinner, K., F. Scholten, M. Spiegel, R. Schmidt, B. Giese, J. Oberst, C. Heipke, R. Jaumann, and G. Neukum (2009). Derivation and Validation of High-Resolution Digital Terrain Models from Mars Express HRSC-Data, *Photogrammetric Engineering & Remote Sensing*, 75 (9), 1127–1142.

Heipke, C., J. Oberst, J. Albertz, M. Attwenger, P. Dorninger, E. Dorrer, M. Ewe, S. Gehrke, K. Gwinner, H. Hirschmuller, J.R. Kim, R.L. Kirk, H. Mayer, J.-P. Muller, R. Rengarajan, M. Rentsch, R. Schmidt, F. Scholten, J. Shan, M. Spiegel, M. Wahlisch, G. Neukum, and the HRSC Co-Investigator Team (2007), Evaluating planetary digital terrain models: The HRSC DTM test, *Planetary and Space Science*, 55 (14), 2173 – 2191, doi:10.1016/j.pss.2007.07.006.

Heleva, U.V. (1988). Object space least square correlation, *Photogrammetric Engineering & Remote Sensing*, 54 (6), 711-714.

Katayama, M., A. Ogawa, N. Morinaga (1992). Carrier synchronization under Doppler shift of the nongeostationary satellite communication systems, *IEEE Int. Symp. Information Theory Applicat. (ICCS/ISITA)*, Singapore, 466-470.

Kirk, R.L., et al., (1999). Digital photogrammetric analysis of the IMP camera images: Mapping the Mars Pathfinder landing site in three dimensions. *Journal of Geophysical Research*, 104 (E4), 8869-8888.

Kirk, R.L., B.A. Archinal, E.M. Lee, M.E. Davies, T.R. Colvin, and T.C. Duxbury (2001). Global Digital Image Mosaics of Mars: Assessment of Geodetic Accuracy, *32nd Lunar and Planetary Science Conference*, Houston, TX, March 12-16.

Kirk, R.L., E. Howington-Kraus, B. Redding, D. Galuszka, T.M. Hare, B.A. Archinal, L.A. Soderblom, and J.M. Barrett (2003). High-resolution Topomapping of Candidate MER Landing Sites with Mars Orbiter Camera Narrow-angle Images, *Journal of Geophysical Research*, 108 (E12), 8088, doi:10.1029/2003JE002131.

Kirk, R.L., E. Howington-Kraus, M.R. Rosiek, J.A. Anderson, B.A. Archinal, K.J. Becker, D.A. Cook, D.M. Galuszka, P.E. Geissler, T.M. Hare, I.M. Holmberg, L.P. Keszthelyi, B.L. Redding, W.A. Delamere, D. Gallagher, J.D. Chapel, E.M. Eliason, R. King, and A.S. McEwen (2008). Ultrahigh resolution topographic mapping of Mars with MRO HiRISE stereo images: Meter-scale slopes of candidate Phoenix landing sites, *Journal of Geophysical Research*, 113 (E00A24), doi:10.1029/2007JE003000.

Koch, K. (1999). Parameter estimation and hypothesis testing in linear models, 2nd editiion. *Springer*, New York/Berlin etc.

Kuschel, M., J. Oberst, E. Hauber and R. Jaumann (1999). An Image Map of the Mars Pathfinder Landing Site. *ISPRS WG IV/5: Extraterrestrial Mapping Workshop "Mapping of Mars 1999"*, July 23-24, 1999, Caltech, Pasadena, CA.

Lefort, A., P.S. Russell, N. Thomas, A. S. McEwen, C.M. Dundas, and R.L. Kirk (2009). Observations of periglacial landforms in Utopia Planitia with the High Resolution Imaging Science Experiment (HiRISE), *Journal of Geophysical Research*, 114 (E04005), doi:10.1029/2008JE003264.

Li, R., G. Zhou, N.J. Schmidt, C. Fowler, and G. Tuell (2002). Photogrammetric Processing of High-resolution Airborne and Satellite Linear Array Stereo Images for Mapping Applications. *International Journal of Remote Sensing*, 23 (20), 4451-4473.

Li, R., K. Di, L.H. Matthies, R.E. Arvidson, W.M. Folkner, and B.A. Archinal (2004). Rover localization and landing site mapping technology for 2003 Mars Exploration Rover mission. *Photogrammetric Engineering & Remote Sensing*, 70 (1), 77-90.

Li, R., S.W. Squyres, R.E. Arvidson, B.A. Archinal, J. Bell, Y. Cheng, L. Crumpler, D. J. Des Marais, K. Di, T.A. Ely, M. Golombek, E. Graat, J. Grant, J. Guinn, A. Johnson, R. Greeley, R.L. Kirk, M. Maimone, L.H. Matthies, M. Malin, T. Parker, M. Sims, L.A. Soderblom, S. Thompson, J. Wang, P. Whelley, and F. Xu (2005). Initial results of rover localization and topographic mapping for the 2003 Mars Exploration Rover mission. *Photogrammetric Engineering & Remote Sensing*, 71 (10), 1129–1142.

Li, R., B.A. Archinal, R.E. Arvidson, J. Bell, P. Christensen, L. Crumpler, D.J. Des Marais, K. Di, T. Duxbury, M. Golombek, J. Grant, R. Greeley, J. Guinn, A. Johnson, R.L. Kirk, M. Maimone, L.H. Matthies, M. Malin, T. Parker, M. Sims, S. Thompson, S. W. Squyres, and L.A. Soderblom (2006). Spirit Rover Localization and Topographic Mapping at the Landing site of Gusev Crater, Mars, *Journal of Geophysical Research*, 111 (E02S06), doi:10.1029/2005JE002483.

Li, R., R.E. Arvidson, K. Di, M, Golombek, J. Guinn, A. Johnson, M. Maimone, L.H. Matthies, M. Malin, T. Parker, S.W. Squyres, and W.A. Watters (2007a). Opportunity rover localization and topographic mapping at the landing site of Meridiani Planum, Mars. Mars, *Journal of Geophysical Research*, 112 (E02S90), doi:10.1029/2006JE002776.

Li, R., K. Di, A.B. Howard, L. Matthies, J. Wang, and S. Agarwal (2007b). Rock modeling and matching for autonomous long-range Mars rover localization. *Journal of Field Robotics: Special Issue on Space Robotics*, 24 (3), 187-203.

Li, R., K. Di, J. Hwangbo, and Y. Chen (2007c). Integration of Orbital and Ground Images for Enhanced Topographic Mapping in Mars Landed Missions, *Annual NASA Science Technology Conference*, College Park, MD, June 19-21.

Li, R., K. Di, J. Hwangbo, and Y. Chen (2008a). Rigorous Photogrammetric Processing Of HiRISE Stereo Images and Topographic Mapping At Mars Exploration Rover Landing Sites, *39th Lunar and Planetary Science Conference*, League, TX, Abstract 1864.

Li, R., J. W. Hwangbo, Y. Chen, and K. Di (2008b). Rigorous Photogrammetric Processing of HiRISE Stereo Images for Mars Topographic Mapping. *XXI ISPRS Congress*, July, 3-11, 2008, Beijing, China.

Li, R., B. Wu, K. Di, A. Angelova, R.E. Arvidson, I. Lee, M. Maimone, L.H. Matthies, L. Richer, R. Sullivan, M.H. Sims, R. Greenberger, and S.W. Squyres (2008c). Characterization of traverse slippage experienced by Spirit rover on Husband Hill at Gusev crater, *Journal of Geophysical Research*, 113 (E12S35), doi:10.1029/2008JE003097.

Maki, J. N., J.F. Bell, K.E. Herkenhoff, S.W. Squyers, A. Kiely, M. Klimesh, M. Schwochert, T. Litwin, A. Johnson, M. Maimone, E. Baumgartner, A. Collins, M. Wadsworth, S.T. Elliot, A. Dingizian, D. Brown, E.C. Hagerott, L. Scherr, R. Deen, D. Alexander, and J. Lorre (2003), Mars Exploration Rover engineering cameras, *Journal of Geophysical Research*, 108 (E12), 8071, doi:10.1029/2003JE002077.

Maimone, M., A. Johnson, Y. Cheng, R. Willson, and L. Matthies (2004). Autonomous navigation results from the Mars Exploration Rover (MER) mission. *Proceedings of the 9th International Symposium on Experimental Robotics (ISER)*, Singapore, June 2004.

Maimone, M.W., P.C. Leger, and J.J. Biesiadecki (2007). Overview of the Mars Exploration Rovers' Autonomous Mobility and Vision Capabilities, *IEEE International Conference on Robotics and Automation (ICRA) Space Robotics Workshop*, Roma, Italy, 14 April 2007.

Malin, M.C. and K.S. Edgett (2001). Mars Global Surveyor Mars Orbiter Camera: Interplanetary cruise through primary mission. *Journal of Geophysical Research*. 106 (10), 23429–23570.

Matthies, L., E. Gat, R. Harrison, B. Wilcox, R. Volpe, and T. Litwin (1995). Mars microrover navigation: performance evaluation and enhancement. *Autonomous Robots*, 2 (4), 291-311.

Matthies, L., M. Maimone, A.Johnson, Y. Cheng, R. Willson, C. Villalpando, S. Goldberg, A. Huertas, A. Stein, and A. Angelova (2007). Computer Vision on Mars. *Int. J. Comput. Vision* 75 (1), 67-92.

Mattson, S., A. Boyd, R.L. Kirk, D.A. Cook, and E. Howington-Kraus (2009). HiJACK: Correcting spacecraft jitter in HiRISE images of Mars, *European Planetary Science Congress*, Potsdam, Germany, September 2009, 4, EPSC2009-604-1.

Mattson, S., M. Robinson, A. McEwen, A. Bartels, E. Bowman-Cisneros, R. Li, J. Lawver, T. Tran, K. Paris, and the LROC Team (2010). Early assessment of spacecraft jitter in LROC-NAC., *41st Lunar and Planetary Science conference*, Woodland, Texas, Abstract 1871.

McEwen, A. S., E. M. Eliason, J.W. Bergstrom, N. T. Bridges, C. J. Hansen, W. A. Delamere, J. A. Grant, V. C. Gulick, K. E. Herkenhoff, L. Keszthelyi, R. L. Kirk, M.T. Mellon, S. W. Squyres, N. Thomas, and C. M. Weitz (2007). Mars Reconnaissance Orbiter's High Resolution Imaging Science Experiment (HiRISE), *Journal of Geophysical Research*, 112 (E05S02), doi: 10.1029/2005JE002605.

McGlone, J.C., E.M. Mikhail, J. Bethel, and R. Mullen (2004). *Manual of Photogrammetry,* American Society of Photogrammetry and Remote Sensing.

Nefian,A.V., K. Husmann, M.J. Broxton, V. To, M. Lundy, and M. Hancher (2009). A Bayesian Formulation for Sub-pixel Refinement in Stereo Orbital Imagery", *IEEE International Conference on Image Processing*.

Neumann, G.A., Abshire, J.B., Aharonson, O., Garvin, J. B., Sun, X., and Zuber, M. T., (2003). Mars Orbiter laser Altimeter pulse width measurements and footprint-scale roughness, *Geophys. Res. Lett.*, 30 (11), 1561.

Olson, C.F. (2000). Probabilistic self-localization for mobile robots. *IEEE Transactions on Robotics and Automation*, 16 (1), 55–66.

Olson, C.F., L.H. Matthies, M. Schoppers, and M.W. Maimone (2003), Rover navigation using stereo ego-motion, *Robotics and Autonomous Systems*, 43 (4), 215-229.

Richards, J. A. and X. Jia, 2006. *Radiometric Enhancement Techniques*, 4th Ed. Berlin, Springer.

Rieder, R., H. Wänke, T. Economou, and A. Turkevich (1997). Determination of the chemical composition of Martian soil and rocks: The alpha proton X ray spectrometer. *Journal of Geophysical Research*, 102, 4027–4044.

Saunders, R.S., R.E. Arvidson, G.D. Badhwar, W.V. Boynton, P.R. Christensen, F.A. Cucinotta, W.C. Feldman, R.G. Gibbs, C. Kloss Jr., M.R. Landano, R.A. Mase, G.W. McSmith, M.A. Meyer, I.G. Mitrofanov, G.D. Pace, J.J. Plaut , W.P. Sidney, D.A. Spencer, T.W. Thompson and C.J. Zeitlin, (2004). 2001 Mars Odyssey mission summary, *Space Sci. Rev.* 110 (1), 1–36.

Schmidt, R., M. Spiegel, C. Heipke, A. Dumke, G. Neukum and the HRSC Co-Investigator Team, (2008) Operational determination of tie points and bundle adjustment of HRSC images of the mars express mission, *XXI ISPRS Congress*, July, 3-11, 2008, Beijing, China,1025-1030.

Scholten, F., K. Gwinner, T. Roatsch, K. Matz, M. Wählisch, B. Giese, J. Oberst, R. Jaumann, G. Neukum, and the HRSC Co-Investigator Team (2005). Mars Express HRSC Data Processing – Methods and Operational Aspects, *Photogrammetric Engineering & Remote Sensing*, 71 (10), 1143–1152.

Shan, J., J-S.Yoon, S. Lee, R. Kirk, G. Neumann, and C. Acton (2005). Photogrammetric Analysis of the Mars Global Surveyor Mapping Data, *Photogrammetric Engineering and Remote Sensing*, 71 (1), 97-108.

Smith, P. H., M.G. Tomasko, D. Britt, D.G. Crowe, R. Reid, H.U. Keller, N. Thomas, F. Gliem, P. Rueffer, R. Sullivan, R. Greeley, J.M. Knudsen, M.B. Madsen, H.P.

Gunnlaugsson, S.F. Hviid, W. Goetz, L.A. Soderblom, L. Gaddis, and R. Kirk (1997). The imager for Mars Pathfinder experiment, *Journal of Geophysical Research*, 102 (E2) , 4003–4026, doi:10.1029/96JE03568.

Smith, D. M.T. Zuber, H.V. Frey, J.B. Garvin, J.W. Head, D.O. Muhleman, G.H. Pettengill, R.J. Phillips, S.C. Solomon, H.J. Zwally, W.B. Banerdt, and T.C. Duxbury (1998). Topography of the Northern Hemisphere of Mars from the Mars Orbiter Laser Altimeter. *Science*, 279 (5357), 1686-1692.

Smith, D.E., M.T. Zuber, S.C. Solomon, R.J. Phillips, J.W. Head, J.B. Garvin, W.B. Banerdt, D.O. Muhleman, G.H. Pettengill, G.A. Neumann, F.G. Lemoine, J.B. Abshire, O. Aharonson, C.D. Brown, S.A. Hauck, A.B. Ivanov, P.J. McGovern, H.J. Zwally, and T.C. Duxbury (1999). The Global Topography of Mars and Implications for Surface Evolution, *Science*, 284 (28), 1495-1503.

Smith, D.E., M.T. Zuber, H.V. Frey, J.B. Garvin, J.W. Head, D.O. Muhleman, G.H. Pettengill, R.J. Phillips, S.C. Solomon, H.J. Zwally, W.B. Banerdt, T.C. Duxbury, M.P. Golombek, F.G. Lemoine, G.A. Neumann, D.D. Rowlands, O. Aharonson, P.G. Ford, A.B. Ivanov, C.L. Johnson, P.J. McGovern, J.B. Abshire, R.S. Afzal, and X. Sun (2001). Mars Orbiter Laser Altimeter: Experiment summary after the first year of global mapping of Mars, *Journal of Geophysical Research*, 108 (E12), 23689-23722, doi: 10.1029/2000JE001364.

Smith, P. H., L. Tamppari, R.E. Arvidson, D. Bass, D. Blaney, W. Boynton, A. Carswell, D. Catling, B. Clark, T. Duck, E. DeJong, D. Fisher, W. Goetz, P. Gunnlaugsson, M. Hecht, V. Hipkin, J. Hoffman, S. Hviid, H. Keller, S. Kounaves, C.F. Lange, M. Lemmon, M. Madsen, M. Malin, W. Markiewicz, J. Marshall, C. McKay, M. Mellon, D. Michelangeli, D. Ming, R. Morris, N. Renno, W.T. Pike, U. Staufer, C. Stoker, P. Taylor, J. Whiteway, S. Young, and A. Zent (2008). Introduction to special section on the Phoenix Mission: Landing Site Characterization Experiments, Mission Overviews, and Expected Science, *Journal of Geophysical Research*, 113 (E00A18), doi:10.1029/2008JE003083.

Spero, D.J. (2004). A review of outdoor robotics research. Technical report MECSE-17-2004. Department of Electrical and Computer Systems Engineering, Monash University, Melbourne, Australia, November 2004.

Spiegel, M. (2007). Improvement of Interior and Exterior Orientation of the Three Line Camera HRSC with a Simultaneous Adjustment. International Archives of Photogrammetry, *Remote Sensing and Spatial Information Sciences*, 36 (3/W49B), 161–166.

Squyres, S.W., R.E. Arvidson, E.T. Baumgartner, J.F. Bell III, P.R. Christensen, S. Gorevan, K.E. Herkenhoff, and G. Klingelhöfer, M.B. Madsen, R.V. Morris, R. Rieder, and R.A. Romero (2003). The Athena mars Rover Science Investigation, *Journal of Geophysical Research*, 108 (E12), 8062, doi:10.1029/2003JE002121.

Thompson, D.R., S. Niekum, T. Smith, and D. Wettergreen (2005). Automatic Detection and Classification of Geological Features of Interest, *Proceedings of the IEEE Aerospace Conference*, Big Sky Montana, March, 1995.

Tran, T., E. Howington-Kraus, B. Archinal, M. Rosiek, S.J. Lawrence, H. Gengl, D. Nelson, M.S. Robinson, R. Beyer, R. Li, J. Oberst, S. Mattson, and the LROC Science Team (2010). Generating digital terrain models from LROC stereo images with SOCET SET, *41st Lunar and Planetary Science conference*, Woodland, Texas, Abstract 2515.

Wang, J. (2008). Modeling and matching of landmarks for automation of Mars rover localization. Ph.D. Dissertation, The Ohio State University, Columbus, OH.

Wolf, P.R. and B.A. Dewitt (2000). *Elements of photogrammetry with applications in GIS*. 3rd ed., McGraw-Hill, Boston.

Wu, S. (1979). Photogrammetric Portrayal of Mars Topography. *Journal of Geophysical Research*, 84 (B14),1955-1959.

Xu, F. (2004). Mapping and localization for extraterrestrial robotic explorations. Ph.D. Dissertation, The Ohio State University, Columbus, OH.

Yoon, J., and J. Shan (2005). Combined adjustment of MOC stereo imagery and MOLA altimetry data, *Photogrammetric Engineering and Remote Sensing*, 71 (10), 1179–1186.

Zhang, B., and S. Millter (1997). Adaptive Automatic terrain Extraction, *Proceedings of SPIE,* 3072, 27-36.

Zhang, Z., R. Deriche, O. Faugeras, and Q. Luong, (1995). A robust technique for matching two uncalibrated images through the recovery of the unknown epipolar geometry, Artificial Intelligence, *Special Volume on Computer Vision,* 78 (1-2), 87-119.

Zitová, B., J. Flusser, J. Kautsky and G. Peters (2000). Feature point detection in Multiframe images, *Czech Pattern Recognition Workshop 2000,* Peršák, Czech Republic, February 2–4.

Zurek, R. W., and S. E. Smrekar (2007). An overview of the Mars Reconnaissance Orbiter (MRO) science mission, *Journal of Geophysical Research*, 112 (E05S01), doi:10.1029/2006JE002701.